Micropipette Manipulation for the Production and Characterisation of Microparticles in Biomaterials Discovery

Submitted by
Charlotte A Henshaw

Thesis submitted to the University of Nottingham for the degree of Doctor of Philosophy.

June 2022

Abstract

The use of microparticles for biological applications is increasing, and with it, the need for specialised microparticles. While one of the major advantages of microparticles is the ability to fine-tune properties, such as chemistry and morphology to best serve an application, achieving this usually relies on lengthy trial-and-error processes.

Micropipette manipulation techniques have proven to be valuable tools in studying cell mechanics, protein dehydration and material characterisation. The techniques permit the study of simple and complex multicomponent systems from an alternative perspective to traditional techniques. Utilising these techniques droplets and particle forming systems can be studied on the microscale and in real time. Thus, providing improved understanding of microparticle formation and aiding in particle design and optimisation. The hypothesis for this work was that micropipette manipulation techniques can be employed to understand and improve formation of bio-instructive microparticles.

In this thesis, micropipette manipulation techniques were used to study a series of microparticle systems. To better enable this application, methods were developed to improve or extend existing analysis practices. The new routines allowed for a reduction in measurement error to the limit of detection, improved efficiency, and increased processing capabilities. Additionally new methods were developed for analysing droplet microstructure.

i

A comprehensive assessment of the impact of the most widely utilised microparticle materials, poly(vinyl alcohol) (PVA) and poly(D, L lactic acid) (PDLLA), on solvent/water interfaces was conducted using the static equilibrium interfacial tension method. The polymers were treated as additives to two solvent/water combination base systems (dichloromethane (DCM) and ethyl acetate.) From this assessment empirical equations were derived for calculating the interfacial tension for given concentrations of the polymers. The maximum interfacial tension for DCM/water to remain as stable drops during particle formation was determined as approximately 11.1 mN m^{-1}. Droplet dissolution was assessed for both base solvents with a range of PDLLA/PVA concentrations. The diffusion coefficients for the base solvents in water were $17 \pm 3.8 \times 10^{-6} \, cm^2 \, s^{-1}$ (DCM) and $10.1 \pm 0.28 \times 10^{-6} \, cm^2 \, s^{-1}$ (ethyl acetate). Negligible change was seen for the addition of polymer to either phase. Comparisons to the Epstein-Plesset model and the activity-based model for dissolution were conducted for both solvents for the range of PDLLA concentrations concerned. Dissolution followed the curve of the Epstein-Plesset model but deviated from the expected final size given by the activity-based dissolution model.

A series of novel, bio-instructive surfactants were assessed for their use in particle formation through the polymerisation of monomer droplets produced using droplet microfluidics. The effectiveness of the different surfactants was determined using static equilibrium interfacial tension measurements. Different core monomers, polymer architecture and hydrophilic and hydrophobic components were considered. Optimum concentrations of surfactants were taken into droplet microfluidics for optimised particle production. Flow maps were generated mathematically using the optimised compositions and showed good

agreement with the stable regions found experimentally. Investigations of material transfer between the monomer drop and the surroundings showed unusual behaviour by the monomer for which a mechanism is proposed to explain such behaviour.

A dual surfactant system for enabling the production of biodegradable microparticles using droplet microfluidics was investigated and the concentrations optimised for performance and application criteria. The particles produced using PDLLA in ethyl acetate formed secondary droplets both inside and on the surface of drop as dissolution occurred. By varying the concentrations of surfactant, core polymer and continuous phase saturation, the morphology of these particles could be manipulated. Using EGPEA-mPEGMA it was possible to generate a topography, reproducible between single particles studies and high volume microparticle production, that could be controlled by adjusting surfactant concentration.

The studies presented here demonstrate the improved understanding of selected microparticle formation systems through the application of micropipette manipulation techniques. Characterisation of novel biomaterials was conducted which in turn allowed the optimisation of bio-instructive microparticles through droplet microfluidics.

Publications and Conference Proceedings

<u>Manuscripts published</u>

Henshaw, C.A.; Dundas, A.A.; Cuzzucoli Crucitti, V.; Alexander, M.R.; Wildman, R.; Rose, F.R.A.J.; Irvine, D.J.; Williams, P.M. Droplet Microfluidic Optimisation Using Micropipette Characterisation of Bio-Instructive Polymeric Surfactants. *Molecules* **2021**, *26*, 3302. https://doi.org/10.3390/molecules26113302

<u>Conferences/Meetings attended</u>

1. CA Henshaw, FRAJ Rose, MR Alexander, PM Williams (2021).

   Poster presentation – Micropipette Manipulation Techniques: The Key to Understanding Microparticle Production. 11th Liquid Matter Conference – online platform (Prague)

2. CA Henshaw, FRAJ Rose, MR Alexander, PM Williams (2020).

   Poster presentation – Micropipette Manipulation Techniques: The Key to Understanding Microparticle Production. 11th World Biomaterials Congress – online platform

3. CA Henshaw. A Dundas, FRAJ Rose, MR Alexander, PM Williams (2020).

   Poster presentation – Informing Microfluidics Processing Using Micropipette Manipulation. Next Generation Biomaterials Discovery Annual Workshop.

4. CA Henshaw. A Dundas, FRAJ Rose, MR Alexander, PM Williams (2019).

   Poster presentation – Informing Microfluidics Processing Using Micropipette Manipulation. Polymer Research Symposium, University of Nottingham

5. CA Henshaw. A Dundas, FRAJ Rose, MR Alexander, PM Williams (2019).

   Poster presentation – Informing Microfluidics Processing Using Micropipette Manipulation. School of Pharmacy, School Research Event, University of Nottingham

6. CA Henshaw, FRAJ Rose, MR Alexander, PM Williams (2019).

   Poster presentation – Micropipette Manipulation of Microparticle Components: An Insight into "Golf Ball" Particle Formation. Next Generation Biomaterials Discovery Annual Workshop.

Acknowledgements

This work would not have been possible without the support of many people. Firstly, thank you to my supervisors, Professor Felicity Rose, Professor Morgan Alexander and especially, Professor Phil Williams. Thank you for sharing your time and knowledge with me. The support and guidance have been invaluable both to the project and my development as a researcher.

Thank you to the School of Pharmacy and the EPSRC Next Generation Biomaterials Discovery Program Grant for providing the platform and opportunity to pursue my doctoral studies and for giving me the chance to meet so many wonderful people.

I am grateful to the collaborators who shared this journey with me: Dr Adam Dundas for his microfluidic knowledge, help, and for his endless optimism, Dr Valentina Cuzzucoli Crucitti for her wisdom and producing the surfactants and Dr Anders Utoft for guiding me in the "art" of micropipette manipulation. Also, thank you Professor Derek Irvine for your knowledge and support and to Professor David Needham. Thank you to the nmRC for use of their facilities and help in imaging individual particles we all crossed our fingers had not got lost on the way across campus. A special thank you to Dr Chris Parmenter for conducting FIB-SEM on my behalf and to Dr Zouxin Zhou, Centre for Additive Manufacturing, for conducting viscosity measurements.

Over eight years at Nottingham I have met many people that have helped to shape me into the person and scientist I am today. A special place in my heart will always belong to my Physics family. Thank you to my C15 office buddies

Whether its late-night calls when I've been upset, helping prepare for exams with equation flash cards or a puppy, a craft, and a cup of tea as a break. Thank you for all you have done and sacrificed for me, I wouldn't have made it without you.

COVID-19 Impact Statement

The COVID-19 pandemic had a substantial impact on the progress of this research. When the University was closed for lockdown, there was no laboratory access from March until August. As the third of my four years I was at the peak time for experimental work.

I had been in the middle of a series of experiments in collaboration with another PhD student, understanding their new surfactants and building a set of characterisations which were to be a key part of the project. This work was halted by the pandemic. The collaborator had to submit during this time and so upon returning to the University this work could not be completed as originally intended. Instead, these studies were altered so more detailed studies were undertaken on materials that were already available.

When the lockdown happened, I had been in the process of getting access and training to facilities to carry out testing of the micropipette manipulation findings on bench scale particle productions. However, due to restrictions when returning I was unable to follow this through. Access to such facilities was limited to those already working there. To overcome this, I worked with those able to conduct some of these tests on my behalf, however, this prevented the full realisation of these studies and instead other areas had to be identified to investigate.

I worked with my supervisors to organise work that could be conducted whilst away from the University. The focus during this time became computational work, enabling me to focus on some of the more complex aspects of the analysis and models. The previous year, due to family illness, I had spent some time away from the laboratory and begun such work as a contingency to optimise the time then.

As someone with an existing anxiety disorder, the impact of the pandemic with the disruption to routine and general uncertainty, had a considerable impact on my mental health. This resulted in periods in which focus, and productivity were very low. During this time, I kept in touch with my supervisors and planned with them to minimise the impact to the work and to my health.

Table of Contents

List of Figures

List of Tables

List of Abbreviations

AFM	Atomic Force Microscopy/Microscope
ANOVA	Analysis of Variance
CMC	Critical micelle concentration
DCM	Dichloromethane
DMAEMA	2-(dimethyl amino)ethyl methacrylate
EA	Ethyl Acrylate
EGDPEA	Ethylene glycol dicyclopentenyl ether acrylate
EGPEA	Ethylene glycol phenyl ether acrylate
EP	Epstein-Plesset
HMDA	1,6-hexanediol diacrylate
HPhOPA	2-hydroxy-3-phenoxypropyl acrylate
IFT	Interfacial Tension
mPEGMA	poly(ethylene glycol) methyl ether methacrylate
O/W	Oil in Water
PDLA	poly(D-lactic acid)
PDLLA	poly(D,L-lactic acid)
PLA	poly(lactic acid)
PLGA	poly(lactic-co-glycolic acid)
PLLA	poly(L-lactic acid)
PVA	poly(vinyl alcohol)
ROI	Region of Interest
SD	Standard Deviation
SEM	Scanning Electron Microscope/Scanning Electron Microscopy
THFuA	Tetrahydrofurfuryl acrylate
ToF-SIMS	Time-of-Flight Secondary Ion Mass Spectrometry
VB	Viscous Boundary
W/O	Water in Oil
W/O/W	Water in Oil in Water

List of Symbols

A	Area
c	Concentration
c_I,	Concentration at the interface
C_s	Saturation concentration
C_0	Initial concentration
$Ca_{i/c/d}$	Capillary number of phase I (continuous, c or dispersed, d.)
D	Coefficient of Diffusion
J	Flux
P	Pressure
$Q_{i/c/d}$	Flow rate of phase I, (continuous, c or dispersed, d.
R	Radius of drop
t	Time
γ	Interfacial tension
η	Viscosity
ρ	Density

Chapter 1: General Introduction

Chapter 1 - General Introduction

1.1 Micropipette Manipulation: An Overview

Micropipette manipulation techniques were first developed by Evan Evans and his group in the 1970s to study the mechanics of red blood cells,[1–3], white blood cells and lipid vesicles.[4–7] At its simplest, a micropipette is a glass capillary with specific taper, with an internal diameter below 1 mm for which the internal pressure can be controlled. The geometry of the micropipette can be varied to suit the application. Micropipette aspiration remains a crucial technique for studying cell and membrane mechanical properties, however, it is the development and employment of micropipette manipulation for the study of interfaces, emulsions and microparticles that are of interest to this work.

Microparticles, their precursor emulsions and their associated properties are predominantly assessed in bulk, with bench-scale experiments limited by both the volume and timescales of the processes such that effects can only be seen once processing is complete.[8,9] Micropipette manipulation techniques offer a unique ability to conduct studies on such systems at the appropriate scale and visualise formation in real-time.

In this thesis, two forms of micropipette manipulation are used: interfacial tension (IFT) measurements utilise a single tapered micropipette, whilst single particle studies, used to assess the droplet and particle formation, require two long, thin micropipettes with almost parallel walls. Figure 1-1 demonstrates these two techniques. In each case, micropipette manipulation studies take place in a chamber mounted above an inverted microscope.
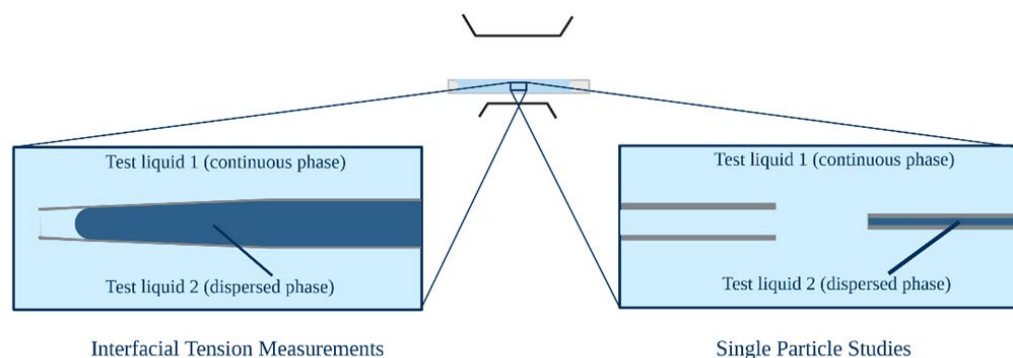
Figure 1-1 Schematic overview of micropipette manipulation techniques. Experiments are conducted in a glass chamber in an inverted microscope set-up. Interfacial tension studies use a single tapered micropipette, whilst single particle studies use two long, thin almost parallel micropipettes.

1.1.1 Micropipette Manipulation for Interfacial Tension Measurements

The first use of the micropipette technique for IFT measurements, as described and used in this work, was published in 2001 in a two part paper, with the first showing the proof of principle and validating the methods,[10] and the second extending its use to assess the equilibrium and dynamic interfacial tensions for phospholipids across a range of temperatures.[11] Since then, the technique has been used to assess a range of liquid/air and liquid/liquid interfaces under the influence of various alcohols, salts and other surface active species. [12–14] It has even been used to study the interfacial behaviour of lung surfactants (both natural and synthetic).[15] Since its first use, the method for measuring dynamic interfacial tension has changed considerably,[10,12,13] whereas the equilibrium interfacial tension measurements, including the analysis methods, have remained the same.

1.1.2 Micropipette Manipulation for Single Particle Studies

Single particle studies using micropipette manipulation methods vary somewhat in their methods, with some using single pipettes,[16] and others as many as three.[17] Most instances use parallel pipettes, though tapered ones are preferred for studies measuring interfacial tension directly from the drop.[18]

Single particle, or rather single drop studies, have been carried out to measure the diffusion of a range of common organic liquids in water and vice versa. Initial studies on aniline/water systems were crucial in developing the methodology as well as the Epstein-Plesset model for use on liquid drops.[19] Since then, studies have gone on to measure the diffusion of various organic solvents in single, binary and tertiary systems,[12,20] assess the effect of the chain length on the diffusion of alcohols and alkanes,[21] and describe the dissolution of solute containing drops[17,22] whilst developing further the methodology and mathematical descriptions.

The technique is not limited to solvent diffusion. Single particle studies have allowed the development of Microglassification™, a process of drying protein in highly concentrated particles through dehydration in alcohol, to give lower water content than conventional methods, without degrading the protein.[23–25]

Micropipette manipulation has been successfully used to understand the ageing of a droplet interface. Studies completed on water drops dispersed in crude oil saw that over time bitumen adsorbed to the interface from the oil. While freshly formed drops merged when brought into contact, aged drops did not. It was concluded that the adsorbed bitumen provided steric stabilisation.[9] The studies

also showed a bitumen shell remained when the water was removed, creating a crinkled film. For harder interfaces, such as waxy shells formed from phospholipids, both diffusion[16] and the mechanical strength have been successfully assessed.[26]

Perhaps some of the most exciting studies are those concerning phase separation. Studies carried out using micropipette manipulation offer a unique perspective for observing this phenomenon. Real-time phase separation within or across the surface of a drop has been observed and the kinetics studied. So far, this has been applied to drops containing a drug as a phase separating component,[27,28] and across the surface of lipid microparticles.[29]

Between 2009 and 2012, a series of studies were performed on biodegradable particles containing antibiotics. Initially, the idea was to incorporate fusidic acid into poly(lactic-*co*-glycolic acid) (PLGA) or poly(3-hydroxybutyric acid-*co*-3-hydroxyvaleric acid) (PHBV) microparticles to provide controlled release of the drug to the site of orthopaedic operations, by integrating the particles into the cement used to secure the joint replacement. The particles were prepared using solvent emulsion evaporation, with a dispersed phase comprised of either PLGA or PHBV and fusidic acid in dichloromethane (DCM), with an aqueous phase containing poly(vinyl alcohol) (PVA) to provide stabilisation.

The final particles displayed unique morphologies, whereby the fusidic acid separated from the polymer during solvent removal to form fusidic acid protrusions (domes) on the surface. This was studied further using single particle techniques to assess the separation in real time. The use of a different core

polymer changed the separation and structures observed. The size of the domes could be controlled by the relative concentrations. [27] This work was extended by assessing drops containing both fusidic acid and rifampicin. While fusidic acid produced large protrusions on the surface, rifampicin separated to create small dimples. Adjusting the ratio of the two drugs allowed fine control over the morphology. Single particle studies allowed the phase separation to be understood in terms of solute concentration. It was also found that washing the particles to remove the drug created golf ball/dimpled particles whose morphology could be readily adjusted.[28] This led to an alternative use for the particles: forming scaffolds for tissue engineering.[30,31]

1.2 Fundamental Concepts

1.2.1 Interfaces

Two immiscible fluids are separated by an interface. The interface behaves somewhat like an elastic skin stretched over the two phases, resisting further any expansion and always trying to contract. While the bulk phases on either side remain homogenous; their properties reflecting that of the individual phase, the interface behaves very differently with its own set of properties.[32–34]

There are two ways to consider the interface and its associated properties. The first is that the interface is a region where the transition between phases is smooth and so the properties of the phases also transition smoothly through this region. The system is effectively broken into three separate regions. The other view is to mathematically define the interface as having zero width. All properties are constant up to this point when assessed from either of the bulk phases. The

difference in any given property between the model and reality is then termed the surface excess and attributed entirely to the interface. This is much simpler in terms of calculation, but has a great dependency on where the interface is placed.[32]

1.2.1.1 Interfacial Tension

The surface, or interfacial, tension, represents the extra energy that results from having two immiscible phases in contact. It is described by

$$\gamma = {}^F\!/_{dx}$$

Where γ is the interfacial tension and F is the force acting on the interface perpendicular to unit length, dx. The interface acts as under a contractile force, resisting the increase in area. Therefore, as a free energy, for constant temperature and pressure, it can be written as

$$G = \gamma A$$

Where G is the Gibbs free energy and A is the area of the interface. It should be noted that this breaks down for high viscosity systems, as the rearrangement of molecules is too slow.[35] As γ is positive, systems will try to minimise their surface area in order to minimise the total energy. The source of this energy is unfavourable interactions between molecules of the two phases. Being surrounded by the same species, or at least those of a similar nature, a molecule in bulk has a complete set of favourable interactions. However, at an interface, half of the possible interactions are replaced with unfavourable interactions,

causing an increase in energy such that the energy of the interface is greater that of the bulk.[35]

In the case of water, molecules form hydrogen bonds with neighbouring water and/or other polar molecules and ions, causing rearrangement that results in an energetically favourable system. If the neighbouring molecule is non-polar, for example a long-chain hydrocarbon, these arrangements are interrupted. The water molecules then try to minimise unused bonds, causing the interface to contract. Similarly, a drop of oil placed in a bulk aqueous phase will always adopt a spherical shape as it tries to minimise its area. It can be understood from this that the separation of the phases to minimise the number of opposing molecules is favourable.[32]

A material that is soluble in one phase may find it thermodynamically favourable to adsorb at the interface rather than remaining in bulk. These molecules are generally amphiphilic – they have one part which is polar and so interacts well with the aqueous phase and another part which in non-polar and so is favoured by the organic phase. By arranging themselves into a monolayer at the interface they reduce the number of unfavourable interactions and therefore the total energy of the system.

Given an adequate efficiency and high enough concentration of the amphiphilic species, it will continue to adsorb at the interface until the interfacial energy matches the energy in bulk. The migration of such species to the interface is controlled by diffusion, but in order to leave the interface again they must overcome an energy barrier, making them reasonably stable at the interface.[32,35]

1.2.1.2 Surfactants

For systems that need to retain a high surface area, the free energy needs to be lowered by reducing the interfacial tension. Carefully selected amphiphilic materials – surfactants – added to one or both phases permit this reduction, increasing the stability of the interface. Surfactants are categorised as one of the following: anionic, cationic, zwitterionic and non-ionic. Surfactants of the last form are used throughout this work. Within this, the ratios of hydrophilic (polar) to hydrophobic (non-polar) known as the hydrophilic-lipophilic balance (HLB) cover a wide range, as do the surfactant origins – natural polymers and proteins, synthetic etc. and therefore the shape and size of the molecules.[33,35]

Generally, as surfactant concentration is increased, the IFT falls smoothly toward a lower limit,[32] as in Figure 1-2. For low surfactant concentrations (blue region in Figure 1-2) this relationship is approximately linear, with the corresponding surface excess concentration scaling linearly with concentration. Large changes in IFT can be seen with a relatively small concentration of surfactant.[33,36] As the concentration increases further and the lower limit is reached, the IFT values become independent of the concentration indicating surfactant molecules can no longer adsorb to the interface. Instead, molecules aggregate in the bulk phase, with those able to form micelles doing so. This is the critical micelle concentration. For species that do not form micelles the term "effective micelle concentration" can be used.
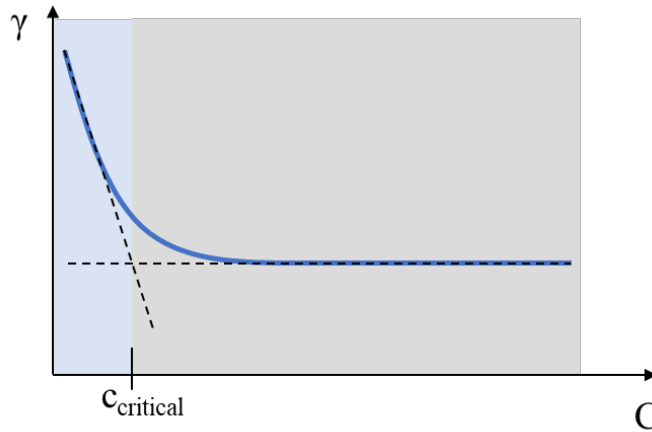
Figure 1-2 Interfacial tension decreases smoothly with increasing surfactant concentration (blue region) up to the critical micelle concentration $c_{critical}$. Beyond this interfacial tension is independent of surfactant concentration (grey region.)

This concentration value helps to describe the efficiency and effectiveness of a surfactant. More broadly, the surfactant is assessed by the bulk concentration that is required to achieve a specific reduction in IFT and the maximum possible IFT reduction. Unfortunately, while the HLB can provide some assistance as to selecting the right surfactant for a specific system, the complex nature of surfactants means it is not always possible to link the structure to the behaviour in the system. As a result, surfactant selection requires a deal of experimentation.[33]

1.2.2 Emulsions

In order to produce microparticles an emulsion usually must first be formed. Emulsions are a mix of at least one immiscible material dispersed as drops of 1 μm or greater inside another. The systems are inherently thermodynamically unstable, with the immiscible phases wanting to separate to minimise the total

area in contact with the other phase. As such, emulsions rely heavily on surfactants to maintain stability long enough to satisfy their purpose.[32,33]

Emulsions can be formed through dispersion or condensation techniques. Dispersion requires the mechanical shearing of one phase within the other phase. This is a high energy process. As the first phase is sheared, the drops become smaller so the total interfacial area drastically increases, increasing the unfavourable energy.[32,33,35] There are several techniques available to form emulsions, such as high speed mixing, microfluidics, sonication or passing through a small cap as in an homogeniser.[32] Condensation methods involved a third phase that both the emulsion phases are miscible in which is gradually removed.[35]

An alternative emulsion mechanism is spontaneous emulsification. This requires a very low IFT and is unlikely to be sustained throughout the whole sample. A more detailed discussion on this mechanism is given is Chapter 4, where its occurrence is utilised.

Prior to forming the emulsion, it is important to know which will be the continuous phase and which the dispersed, and crucially, how this is going to be ensured. The volume fraction, production method and choice of surfactant all play a role in determining whether the emulsion is water-in-oil (W/O) or oil-in-water (O/W).[33] These also help determine the size of the emulsion drops which, depending on the production methods, can have a very wide distribution.[32] The emulsions considered in this work are all O/W. Multiple emulsions such as water-in-oil-in-water (W/O/W) are often utilised for producing complex

microparticles. These are only considered here in the context of reviewing microparticle properties, morphology, and production.

1.2.2.1 Emulsion Stability

The mixing of two immiscible liquids causes a large increase in energy. In order to minimise this, drops will merge until the interfacial area is at its minimum – that is until they are completely separated. There are several mechanisms by which an emulsion will separate.

- Creaming – Drops will rise to the top of the emulsion before merging.

- Flocculation – Due to a difference in density between the phases. Drops come together into large groups and merge.

- Coalescence – Merging of two small drops when they come into contact. The interface ruptures and the drops become one large drop.

- Otswald Ripening – The difference in pressure between large and small drops means small drops are more soluble in the surrounding media. As a result they will dissolve into the continuous phase and diffuse to the larger drops, resulting in growth of the large drops.[33]

Depending on drop size and the density difference between the phases, any or a combination of these events can take place while the dispersed phase of the emulsion is still liquid; stopping the successful formation of particles.[32]

Separation can be combatted through the careful selection of emulsifier/surfactant. As well as lowering the interfacial tension, and therefore

the thermodynamic drive to coalescence, surfactants can prevent drops merging by:[32]

•   Electric stabilisation – Repulsive forces between charged or polar groups. Rearrangement of molecules in the continuous phase close to the drops occurs due to polarisation or charges on the drop surface. This leads to series of layers of altering positive/negative charges or polar orientations, causing a wider barrier known as double layer repulsion. [32,34]

•   Steric stabilisation – Projections from the drop surface physically stop drops from touching. This is a key process when using polymeric surfactants, where the loops and tails protruding from the drop significantly hinder the approach of neighbouring drops. As well as a physical barrier, it is also entropically unfavourable for the drops to get too close as the configuration of the protruding chains become limited, leading to an increase in energy and in osmotic pressure, in turn causing more solvent to be drawn in so forcing drops apart. Polymeric stabilisers have a large effective thickness, providing a physical barrier against drop coalescence.[34]

•   Viscosity – Higher viscosity leads to slower movement. The number of collisions between drops is inversely proportional to the viscosity of the continuous phase. Large (macromolecule) surfactants in the continuous phase increase its viscosity and so decrease the likelihood of coalescence. [32,33]

•   Marangoni Flow – As drops approach there is drainage of the liquid between them. Surfactant molecules in the continuous phase are moved causing

an increase in interfacial tension. In response, more surfactant molecules are drawn into the space, reducing interfacial tension again and preventing coalescence.[32,33]

Some or all of these techniques can be applied to the pre-particle emulsion system in order to maintain stability. This is achieved by careful selection of the surfactants and phase materials themselves.

1.2.3 Diffusion and Dissolution

All particles in a liquid experience Brownian motion. The special fluctuations arising from this are small, on the μm order, and as the process is random, the net motion is zero. This movement constitutes the diffusion of a particle within its own material – self diffusion. Conversely, when an energy imbalance exists, such as a chemical potential difference caused by a concentration gradient, the molecule will move to equilibrate this difference.[37] This can be within its own phase, for example octanol adsorbing to the water/octanol interface on expansion of the interfacial area,[12] or through a second phase, as for solvent extraction.

All solvent evaporation and extraction methods of particle formation require the dissolution of solvent from a drop into the continuous phase (in the system studied in this work, it is organic solvent transferring into the aqueous phase). As such, assessing this movement using single particle studies can provide valuable insights into this stage of particle production.

1.3 Micropipette Measurement Techniques

1.3.1 Interfacial Tension Measurement Techniques

Interfacial tensions can be readily measured using a variety of methods. Traditional techniques, such as Wilhelmy Plate and de Noüy Ring use very large volumes of material to obtain the value. Drop based methods, such as pendant drop, sessile drops, and growing and oscillating drops use less of the dispersed phase, but still require a relatively large amount of material. These methods can obtain values very quickly and are simple to use but have their limitations.[38–43]

For drops on the picolitre scale that contain surface-active species, the IFT can differ significantly from tension measured on a macroscale interface. This is because the surface area, and so coverage of surface-active materials, change drastically between those scales. As the scale of interest for microparticle forming emulsions is that of picolitre drop, it is important to assess the interface on this scale.[9,43–47]

The techniques mentioned above deal with drops no smaller than microlitres and some only flat surfaces. Conversely, IFT measurements using micropipette manipulation techniques are taken on the same scale as the drops. Another consequence of this reduced scale is a drastic decrease in the amount of material needed. A measurement is carried out with less than 2 µL to 3 µL of the dispersed phase in the pipette, though in practicality a few hundred microlitres are needed during the set-up of the experiment.

1.3.2 Micropipette Manipulation for Interfacial Tension Measurements – Theoretical Basis

If an interface is curved a pressure difference between the two sides must exist. What holds this interface in equilibrium is the interfacial tension.[32] This is described by the Young-Laplace equation,

$$P_1 - P_2 = \Delta P = \gamma \left(\frac{1}{R_1} + \frac{1}{R_2} \right)$$

where P_1 and P_2 are the pressures acting either side of an interface, which has radii of curvature R_1 and R_2, respectively. Alternatively, when the interface is spherical such that $R_1 = R_2$:[11,33]

$$\Delta P = \frac{2\gamma}{R}$$

The foundational assumptions for this model are that the interface is both real and finite, the pressure is neither infinite nor zero and neither is the radius of curvature of the interface. Several groups have developed techniques to measure interfacial tensions using Laplace pressure and capillary methods on the micro- to picolitre scales. These either consider pressure changes when transitioning into different sized channels,[48] or the deformation of droplets or bubbles inside or held on a micropipette.[49–51]

Laplace pressure and capillary action, the tendency for a liquid to rise inside a narrow tube, form the basis of IFT measurements using micropipette

manipulation.[14] A glass tube with a diameter of a few hundred microns placed vertically on the surface of water will begin to fill with the water. This will continue, with the water preferentially wetting the glass and displacing the gas from the surface, until the adhesion forces balances by the downward force from the weight of the water in the tube. The flow is determined by the interfacial tensions, geometry of the tube and gravity. The tensions cause the water/air interface to adopt a specific contact angle with the glass. This angle changes for different interfacial tensions, allowing the tension values for that system to be determined. Figure 1-2 A shows the situation for a vertical capillary, where the interface reaches an equilibrium height, h. The balance of adhesion and gravitational force can be written as

$$\pi R^2 \rho g h = 2\pi R \gamma \cos \theta$$

Equation 1-5

where ρ is the density of the liquid, and the other values are as defined in diagram A in Figure 1-2. This can be rearranged for calculation of interfacial (surface) tension:

$$\gamma = \frac{R \rho g h}{2 \cos \theta}$$

Equation 1-6
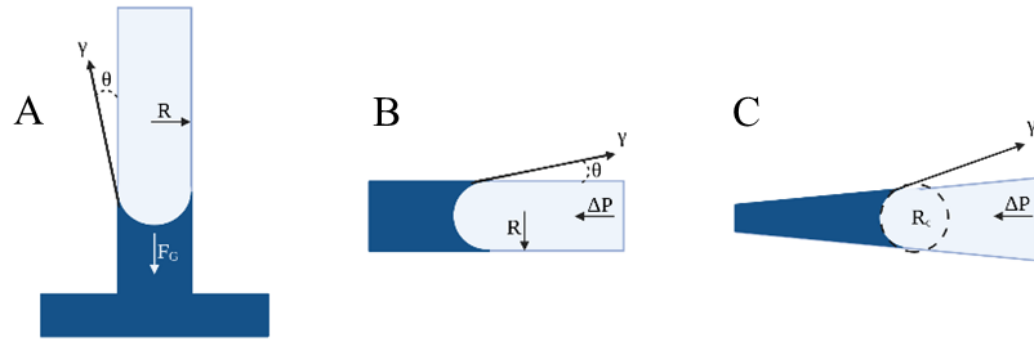
Figure 1-3 Capillary action force balances providing a stationary liquid/air interface for (A) vertical capillary, (B) horizontal capillary and (C) a tapered capillary, showing the forces acting. In a vertical capillary (A) gravity causes the weight of the liquid to balance the height rise whilst in horizontal capillaries (B and C) an external pressure is required.

When the capillary is placed horizontally gravity can no longer act against the capillary action. In this situation, the liquid continues to flow into the capillary unless balanced by an external pressure, ΔP, as in Figure 1-2 B. This results in a change to Equation 1-6 such that

$$\gamma = \frac{\Delta P R}{2\cos\theta}$$

<div align="right">Equation 1-7</div>

Smaller radii tubes require a higher opposing pressure, however there is still only one pressure and one contact angle for each tube size/fluids combination.

To overcome this limitation, tapered pipettes are used. As seen from when two capillaries of different diameters are combined, the liquid flows until the pressure, caused by the different radii, is balanced.[33] By using a tapered pipette the need for contact angle measurement is removed. Instead, this parameter is accounted for by the taper of the pipette and the change in radius of curvature for different systems, as shown in Figure 1-2 C. The equation for calculating interfacial tension, therefore, collapses back to the form of Equation 1-4. Every

position, and so every radius the interface meets, requires a different pressure to hold the interface at equilibrium. As a result, multiple measurements can be made for that interface in the same pipette, and IFT can be verified in one test.[52]

A liquid in contact with a solid substrate forms a characteristic contact angle to that substrate. This predominantly occurs in one of two states: Wenzel or Cassie-Baxter. The different states arise from the texture of the substrate. In the Cassie-Baxter state air is trapped in grooves on the surface, resulting in a more hydrophobic surface and so a greater contact angle. In the Wenzel state the liquid can settle into the grooves, displacing the air, and resulting in increased surface wettability.[53,54] It is possible, when using two liquids passing over the same surface that one becomes trapped in the groves, influencing the contact angle of the second liquid with the solid surface. The use of tapered pipettes for interfacial tension measurements removes the contact angle dependence from the force balance, returning it to Equation 1-4. A precaution to avoid any remaining influence of wetting phenomena is that a spherical cap of the interface is examined, rather than including portions close to the substrate, ensuring the shape measured is determined only by the two fluids. This is discussed in later chapters.

The diffusion of surfactant to the interface is often very fast and therefore difficult to capture. Most methods for measuring dynamic interfacial tensions are limited by larger area requirements or the range of times they can measure over – those designed for early lifetime measurements cannot be extended for slower adsorptions.[43,52] Micropipette manipulation methods, specifically the

Micropipette Interfacial Area-expansion Method (MIAM), are able to overcome these limitations.[13] Such measurements are made on interfacial areas the same scale as those of picolitre drops, and so additionally benefit from small volume requirements. Although the technique does not reach the lower time scale limits of some methods,[43] adsorption under 1 second can be assessed and it can be extended for long adsorptions of minutes and even hours.

1.3.3 Epstein-Plesset Model for Droplet Dissolution

In 1950, Paul S. Epstein and Milton S. Plesset developed a model describing the dissolution of a stationary gas bubble as it dissolves into the surrounding liquid.[55] This was then tested by Duncan and Needham using micropipette manipulation techniques, first for air bubbles in water and then on liquid-liquid systems.[16,19]

To apply this model to a system the following criteria and assumptions need to apply:[16,19,22,55]

•	The bubble or drop must be stationary – This allows the assumption that the interface velocity is zero whilst the drop shrinks, and so convection can be ignored.

•	The surrounding material can be considered an infinite medium – The volume of the surrounding phase must be much greater than the solubility limit for the diffusing material and the distance to any boundary must be much greater than the size of the drop.

•	The initial concentration of the diffusing material in the surrounding phase must be known.

- Steady state approximations are valid so long as drops are given enough time to form (<0.1 seconds.)

- Direct and accurate measurements of the drop radius as a function of time must be obtainable.

The radius of curvature of small drops (less than 100 μm radius) introduces a Laplace overpressure which depends on the interfacial tension. However, it was shown by Duncan and Needham that this can be neglected when dealing with a liquid-liquid system.[19] It should also be noted that depending on the solubility there will be diffusion of the surrounding liquid into the drop. However, this is extremely difficult to measure. Based on the volume of the drop, the maximum amount of continuous phase material that can enter the drop should be small enough to be within measurement error.[16]

Consider a drop of material *"A"* placed/formed in surrounding, immiscible medium, *"B"*. Mass transfer between the two phases will begin instantly, driven by a chemical potential gradient. The rate at which the drop will shrink depends on how quickly the *"A"* material can move away from the drop interface which in turn depends on how quickly it can move in material *"B"*. This is determined by the strength of the chemical potential gradient, described by the difference between the concentration of *"A"* in *"B"* at the interface and at an infinite distance away from the interface. The concentration of *"A"* in *"B"* at any given position and time is $c = c(r,t)$.

The change in concentration with time is described by Flick's second law of diffusion. In spherical coordinates, as for a drop this is written:

$$\frac{\delta c}{\delta t} = D\nabla^2 c = D\left(\frac{2}{r}\frac{\delta c}{\delta r} + \frac{\delta^2 c}{\delta r^2}\right)$$

Where D is the diffusion coefficient. The boundary conditions arising from the criteria noted above are that the interface is in equilibrium with the drop. At the interface, $r=R$, and the concentration of "A" in "B" is at saturation level, c_s. Far from the drop at $r=\infty$, the concentration of "A" in "B" is the same as prior to drop formation, c_0. This allows Equation 1-8 to be written as[16]

$$\left[\frac{\delta c}{\delta t}\right]_{r=R} = (c_0 - c_s)\left(\frac{1}{R} + \frac{1}{\sqrt{\pi Dt}}\right)$$

The mass transfer out of the drop is proportional to flux, J, through the interface. This is the number of particles, Q, passing through a thin area, A, per unit of time:

$$J = \frac{d\left(Q/A\right)}{dt}$$

Writing in terms of mass change with time:

$$\frac{dm}{dt} = -4\pi R^2 J$$

Or alternatively,

$$\frac{dm}{dt} = 4\pi R^2 \rho \frac{dR}{dt}$$

Where ρ is the density of the diffusing phase. Equating Equation 1-11 and Equation 1-12 gives an alternate expression for flux,

$$\frac{dR}{dt} = -\frac{J}{\rho}$$

where both R and t can be measured in a laboratory setting.

The definition of flux given by Flick's first law of diffusion is

$$J = -D\frac{\delta c}{\delta t}$$

Equating the terms in Equation 1-14 to those in Equation 1-9 and Equation 1-13 gives

$$\frac{dR}{dt} = \frac{-Dc_s(1-f)}{\rho}\left[\frac{1}{R} + \frac{1}{\sqrt{\pi Dt}}\right]$$

where $f=c_0/c_s$. This is the Epstein-Plesset (EP) model describing the dissolution of a drop of one pure material into another.

Modifications have been made to account for multicomponent drops, keeping a mass transfer approach.[20] However, this required that all components are homogeneously mixed and all undergo dissolution into the phase *"B"*. This breaks down as different components have different fluxes and so the area

fraction at the interface representing each component does not remain constant.[56]

To overcome this, an activity-based approach was taken which accounts for a solute present in the drop.[22]

For a drop formed of a solute and dissolving material *"A"*, the concentration of the solute will increase as the dissolution of *"A"* progresses. Consequently, the activity of *"A"* decreases. In this situation, the concentration of *"A"* in *"B"* at the interface is no longer at the saturation concentration, so c_s must be replaced with c_i, the concentration at the interface. In turn, *1-f* in Equation 1-15 is replaced with $f_i–f$ where $f_i = c_i/c_s$. The assumption that the drop is in thermodynamic equilibrium still holds, such that the concentration of *"A"* at the interface and just outside the drop is the same as the concentration of *"A"* inside the drop. The modified equation is therefore:

$$\frac{dR}{dt} = \frac{-Dc_s(f_i - f)}{\rho}\left[\frac{1}{R} + \frac{1}{\sqrt{\pi Dt}}\right]$$

Equation 1-16

As with a pure drop, the flow of material will continue until the chemical potentials balance, that is when $f_i-f=0$ (or $f=1$ for pure drops). Unlike f, which describes the starting/infinite conditions so is constant, f_i changes with time. Therefore, in order to apply the model, $f_i(t)$ must be determined.[22]

As the flow of material stops when $f_i=f$, f_i can be found by measuring the final *"A"* concentration of drops undergoing dissolution into material *"B"* which has been partially pre-saturated with material *"A"*. Details of this process in a

practical sense are given in Chapter 4 where this is applied. The equation describing $f_i(t)$ is entirely empirical.

An additional requirement is placed on drops of more than one component (e.g., a dissolving material and a solute) that the materials in the drop must rearrange faster than the interface is receding such that the concentration at the interface is the same as that throughout the drop. If this is not the case, dissolution will be slowed down by a build-up of solute at the interface.[22,56]

Further modifications to the EP model have been made to account for the material lost during formation of the drop and for the area of the drop blocked by the pipette itself which cannot undergo dissolution properly. It was determined that the volume change during formation was negligible in the work presented in this thesis, but the area modification was needed.

1.4 Microparticles

The small size, vast material range and ability to be specifically tailored to a given application make microparticles a highly useful tool in a wide range of areas. The applications range across industries with interest in personal care products,[57,58] in coatings,[59] catalysis and synthesis processes,[18] pharmaceutical and healthcare products,[60,61] namely controlled drug delivery and release,[62–68] and cell biology applications[69,70], including delivery.[71–73] The use of microparticles as carriers has been considered since the 1970s.[64,74] As such, a large volume of research has been conducted on the encapsulation of various active pharmaceutical ingredients[62,64,74,75] leading to a number of approved and

marketed microsphere formulations for conditions such as prostate cancer, endometriosis and diabetes.[28]

An important and growing area of interest for the use of microparticles is tissue engineering.[60,69,76–80] Traditionally, cell culture is performed on flat, rigid surfaces, such as well plates. However, this is far removed from the reality cells experience in their natural environments. Cells take cues from their environments, such as stiffness, roughness and curvature of surfaces in contact, which then dictates the cell behaviour. Using cell sheets or aggregates to build larger tissues often results in hypoxia and reduced viability, while pre-formed 3D scaffolds lack the complexity needed to replicate the extra cellular matrix.[79]

Microparticles have been shown to be effective support structures for a wide range of cell types; with culture on and in microparticle complexes (e.g. sintered microparticles to form a scaffold),[30,31] free microparticles [77,78,81–83] and even suspension cells.[60,84] Microparticles have been shown to have a number of positive affects in tissue engineering, compared to traditional culture platforms, including improved cell adhesions, promoting vascularisation and improving viability.[78,79,85,86] They are also able to modulate immune response, such as macrophage polarisation,[66,81] and promote differentiation into a specific cell type.[30,60,77,86,87] These abilities are finely controlled through a combination of microparticle properties. These properties can be split roughly into chemistry, morphology and deliverables.[78,79]

Particle chemistries dictate the fundamental behaviour of the particle, such as whether it degrades, its hydrophobicity/hydrophilicity, and its stiffness.

Microparticles of PLA will have a similar stiffness to bone[65] and so produce a different response to a microparticle made of gelatine, though both have been used for the delivery of peptides and TGF-β.[62,88] Whilst PLA and its related copolymers are often selected because they are biologically inert, bio-instructive materials can be incorporated into microparticles to great effect. This can be achieved by forming the particles with these materials, either as the core,[89] surfactant,[90] or in conjunction with another material in the same phase.[70]

A series of microparticles were produced to assess the bacterial response to bio-instructive materials discovered in 2D. These materials, found using high-throughput screening, were found to drastically decrease or increase the attachment of selected bacteria.[91–94] Microparticles were formed using one such material as the core, with PVA to stabilise,[89] or with surfactants formed using the bio-instructive chemistry.[90] In both cases, the materials performed better than controls, exhibiting the same trends as in 2D. In the first type, however, the effect was impacted by PVA.[89,90] This is because the surface chemistry of a particle is key in determining the response of the interacting cells.[79,93]

Alternatively, the selected chemistry can be applied to the surface after production.[30,76] An example of this is the formation of PLGA spheres and irregularly shaped microparticles by H. Thissen *et al.*[76] The irregular shaped particles were made by simply crushing spherical particles. Both types were then treated with ammonia plasma and had collagen adsorbed to the surface. They were tested in the context of regeneration of articular cartilage, with both the

shape and surface chemistry changing the proliferation of cells whilst maintaining phenotype.

The size, shape, and structure of a particle, including the surface-to-volume ratio and the level of porosity and/or existence of secondary compartments, have great effect on the adhesion and proliferation of cells as well as their phenotype, and in the case of stem cells, the final differentiation.[78,79] Texturing of surfaces, such as dimpling, has produced significant effects even when the overall structure is 2D.[95]

An example of this is microparticles with "golf ball" like surfaces. These are produced through the separation of multiple components in the dispersed phase. The separating components are miscible with the dispersed phase solvent but not with one another. This results in phase separation occurring as the solvent is removed, forming pockets of the second material in the main polymer microparticles. Both fusidic acid, as in a study by M. Alvarez-Paino, *et al*. and 2-methylpentane as used by Kuk Young Cho's group have been used as this phase.[27,28,30,96] The particles have small bumps covering the surface which are removed by washing (fusidic acid) or evaporation (2-methylpentane) to leave behind a dimpled surface. M. Alvarez-Paino, *et al*. were able to extend this further by altering the ratio of fusidic acid and poly($_{D-L}$-lactic acid) (PDLLA) in the dispersed phase to produce large fusidic acid domains, which after removal left irregular, angular particles.

Cells from two cell lines – MCF-10A and HEK293 – where cultured on the particles formed with 2-methulpentane and smooth surfaced particles as a

control. For both cell types they saw high cell adhesion to the dimpled particles, with cells almost covering the entire surface and very low adhesion on the smooth particles. They hypothesised that the increase in adhesion was due to the increase in surface area to volume ratio. Human immortalised mesenchymal stem cells (hMSCs) were cultured on smooth, dimpled, and angular particles in the studies by M. Alvarez-Paino, *et al*. In this case, cell attachment was higher on all microparticles than on a 2D control, with the dimpled particles showing lower attachment than the smooth and angled particles in this case. The difference in adhesion was seen even when the number was normalised to the surface area, showing texture had a significant effect. Here they hypothesised the difference in attachment was due to increased numbers of attachment points on the textured microparticles.

Both groups also showed the texture had significant impact on cell morphology. Cells spread on the smooth microparticles but were round or elongated on the textured particles. This is in agreement with the results from Kuk Young Cho's group, that cells stretched on the dimpled particles, with the dimples appearing to act as anchor points.[30,31,85,96] For the human immortalised mesenchymal stem cells, there was an increase in markers showing osteogenesis for textured particles compared to the smooth ones.

So-called "fuzzy" microparticles,[86] whose surface appears as a dense covering of fine strands – similar in appearance to a pompom – have been formed from PLGA/PLGA-b-PEG. The surface texture could be controlled by different

heating conditions post-production and the deposition of dopamine. These showed significant promotion of bone regeneration in post-surgery *in vivo* tests.

Complex surface structures, such as pollen-inspired particles,[97] deep "wrinkles"[59] and even spikes[98] can be formed through single emulsions, either by traditional or droplet-microfluidic approaches, by varying polymer and copolymer ratios or with the addition of a separating phase. Complex pore systems can be created using multiple emulsions.[71,99,100]

Extensive studies have been conducted for the encapsulation of active pharmaceuticals, with the aim of achieving controlled release.[63,64] The same principles can be applied to particles in tissue engineering to delivery growth factors such as TGF-β and BMP-2,[87,88,101,102] proteins,[74] serum [101]and even oxygen.[79]

Chemistry, topography, and the use of encapsulates can be combined to produce very specific particles, tailored to the application at hand.

1.5 Emulsion Solvent Evaporation

Emulsion solvent evaporation, ESE, is the most common way to prepare polymer microparticles and microspheres, as carriers or for their many other roles. Often chosen because it is a simple and well-defined method, it allows a large number of particles to be made in a reasonably short amount of time and can be made more or less complex as required.[74,103–107] Briefly, a polymer is dissolved in an organic solvent, with any other oil soluble materials required. It is then emulsified with an aqueous phase to form drops, before hardening into the final

particle.[104] Single (O/W or W/O) emulsions, double emulsions (W/O/W or O/W/O) or multiple emulsions can be formed depending on the structural and encapsulation requirements. For example, most hydrophobic drugs are formed in a O/W emulsion whereas proteins require W/O/W double emulsion.[63,71,87,108]

No matter how complex the formulation, ESE can be broken down into two stages: emulsification, and solvent elimination. The first stage involves the breakup of the dispersed phase into microdroplets through shear. This stage determines the size and distribution of the final particles, with the stirring rate, and therefore shear, known to have a great impact on this. Increasing the stirring rate drastically decreases the size of the droplets and so the particles.[109] The drops need agitation to continue throughout the next stage in order to avoid aggregation.[104]

The second stage is solvent elimination. This can be done via evaporation, in which solvent diffuses from the dispersed phase into the continuous phase, before evaporating from the surface, or by solvent extraction. In this method, the emulsion is quenched by adding it to a large volume of fresh continuous phase material (e.g. water in most cases.)[63,103] In solvent evaporation, the evaporation rate controls the solvent saturation in the continuous phase and therefore the rate of solvent transport from the droplets.[104] In the extraction method it is the ratio of the two volumes of continuous phase – initial and quenching – that control the transfer rate.[110] In both cases the rate is also dependent on the solvent used.

Solvent elimination and final hardening control the morphology of the particles, any phase separation behaviour and, where applicable, encapsulation and release

behaviour.[103,111,112] Understanding solvent transport behaviour therefore allows control over these properties. For example, increasing the solvent evaporation rate through increased ambient pressure during the production of Lidocain loaded PLA particles produced smaller, smoother particles with lower encapsulation efficiency than under standard conditions.[113] Shanquin Liu, *et al*. produced polystyrene particles with a varied density of pores by varying the rate of solvent evaporation and the ratio of the phase separating materials. [100]

Solvent evaporation is also key for microparticles produced using droplet microfluidics. Depending on the channel size, concentration of solvent, drop size and density the solvent transport may begin as soon as drops are produced. It is more likely, however, that the small channel size will lead to quick saturation of solvent in the continuous phase, restricting the removal of solvent until the drops reach the collection beaker, or at least wider tubing.[58]

Residual solvent is a concern, especially where the particles will be in used in a biological setting, due to the toxicity to cells. The result is that in practice a third stage in the process is required. The whole process can then be described as: i) droplet formation in second phase, ii) solvent transfer into second phase and iii) final drying to remove all solvent.[104]

Solidification can be divided into three stages:[28]

• Solution state – dominated by mass transfer of the solvent into the continuous phase. Concentration of the solute(s) increases but movement in the drop remains free.

• Gel state – mass transfer continues but the drop viscosity has increased dramatically, slowing, or preventing movement inside the drop. This gelation point is known as the viscous boundary. Once this is reached the removal of the remaining solvent is slow and difficult.

• Glassy state – only once all solvent is removed from the particle is it in its final solid state.
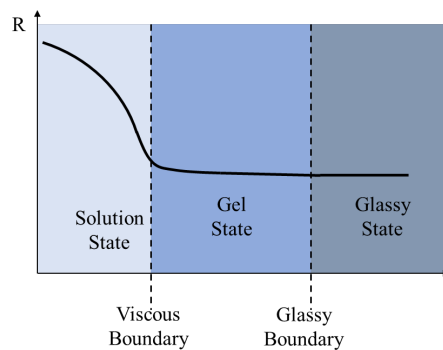
Figure 1-4 An example dissolution curve (radius as a function of time) showing the three stages of solidification: solution state, gel state and glassy state are separated by the viscous boundary and the glassy boundary

1.5.1 The Viscous Boundary

The viscous boundary onset depends on the size and composition of the drop. The approach to the viscous boundary can be easily observed with drops which have internal features – such as phase separated components or bubbles – by following their movement. Alternatively, it is identifiable on a plot of radius as a function of time as being the beginning of the inflection, where the curve starts to plateau.[28]

1.6 Droplet Microfluidics

1.6.1 Background

Microfluidic devices are systems which comprise multiple phases in confined (< 1 mm) flows. They vary greatly and are useful in a range of applications such as emulsion systems, organic synthesis and bioanalysis, with the "lab-on-a-chip" format offering wide-ranging possibilities to run analysis in parallel while only requiring small amounts of material.[114] Droplet-based microfluidics is common in many biotechnology applications, such as the encapsulation of single cells and genes.[115] The same principles can be applied to the production of polymer microparticles.

Droplet microfluidics is considered to be the most effective method of particle production.[58] Initially developed from membrane emulsification methods,[116] microfluidic devices for the production of monodisperse droplets were first established in 2001.[115] They offer the ability to manipulate individual droplets and exert unprecedented control over drop formation and system properties. Droplet-based microfluidics is based on the competition between the inertial and interfacial forces, with the choice of geometry and flow parameters shifting the balance between one or the other to generate the desired flow pattern.[117,118]

Droplet microfluidics overcomes many of the disadvantages of emulsion solvent evaporation methods whilst being high yield and low cost.[114,115,119] ESE methods suffer a lack of uniformity in the flow and hence in the breakup of droplets, leading to high polydispersity, with a coefficient of variance often around 40%.[118,120] Droplet microfluidics offers fine processing control and constant

flow, which provides drops with such low coefficients of variance that populations can be described as monodisperse.[116,118] Additionally, ESE relies on high shear to break up the drops which can limit the materials or objects eligible for encapsulation and may not provide uniform dispersions inside the drops.[114] Droplet breakup in high shear systems is too quick for drops to be properly stabilised, so a higher surfactant concentration is required to avoid recoalescence.[120]

Monodisperse drops and particles are required for particle-based displays, photonic materials, therapeutics, high performance fillers, and for consumer and personal care, as well as tissue engineering and scaffolds, since these applications require uniformity and predictable behaviours. As such, formation through microfluidics is preferable in these cases.[117]

Drops and particles produced using ESE methods are generally spherical as they are constrained by interfacial energy minimisation. To move away from this shape or create more complex particles, even simple double emulsions, multiple stages, and extensive processing is required, increasing energy, materials and cost. This is not the case with microfluidic devices, as chips can be designed or combined such that drops of specific shape and microstructure, with multiple compartments, can be created in one process.[119] The size of the drops can be manipulated by changing the flow whilst maintaining the desired morphology.[121] This level of control has led to claims that microfluidic devices have revolutionised the field of emulsions and created a new class of colloids.[119]

1.6.2 Microfluidic Devices

Devices for droplet-based microfluidics come in many forms and materials. Commonly chip-based designs are produced from glass or PDMS, allowing for the precise control of geometries that is required to enable droplet production. Geometries include T-sections/junctions, flow focussing and hydrodynamic focussing, membrane and EDGE, concentric junctions, and coaxial flow. Figure 1-3 depicts the most common geometries, T-junction (A), Flow-focussing (B) and Coaxial (C).[117,118] In addition to fixed chip set-ups, the devices can be made from separate pieces similar to the micropipettes. [121,122]
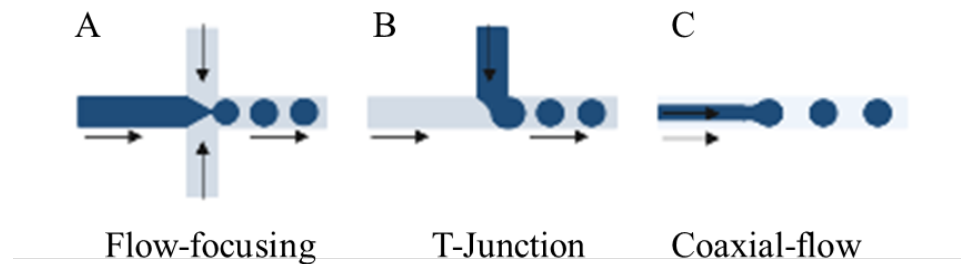
Figure 1-5 The of the most common geometries for droplet microfluidics. (A) flow-focussing, (B) T-junction and (C) coaxial-flow (co-flow).

The different devices and geometries have their own advantages and disadvantages, so it is important to choose the right one for the application at hand. The focus here will be the flow-focussing device. As seen in Figure 1-3 A, four channels form a cross shaped junction. The dispersed phase travels in a single channel at flow rate Q_d, to the junction. The continuous phase is split between two channels which approach the junction from opposite directions, meeting the dispersed phase at right angles with flow rate, Q_c. The dispersed

phase is pinched off by the two impinging continuous phase feeds causing the dispersed phase to break into droplets as the phases all flow into the remaining 4th channel. Flow-focussing devices are good for scaled-up production as they can easily be run in parallel and are more stable than T-junctions over a longer time scale. However, this design requires more extensive optimisation of geometry and flow parameters to yield regular sized drops.[116]

1.6.3 Key Forces in Droplet Microfluidics

Reducing the length scale of a system to the microscale causes a large surface area to volume ratio, in turn increasing the importance of interfacial and viscous forces, and negating effects caused by gravity. Viscosity, interfacial tension and wetting are key to understanding and controlling the formation of drops inside a microfluidic device.[118,123]

When two, non-miscible phases flow together there are a range of instabilities which are either absolute or convective. Interfacial tension creates instabilities that undulate, eventually leading to the breakup of flow into drops. Whether this occurs, or how the instability continues, is a balance between the interfacial tension working to minimise the area between the phases, the viscosity which supresses growth and the inertia of the fluid that acts to keep it flowing onwards. In most cases concerning microfluidic devices the inertia is ignored. As a fluid is confined the interfacial forces dominate. The complexities of flow fields, non-consistent interfacial tensions etc. are however, beyond the scope of this work.[117,118,124]

1.6.4 Surfactants in Droplet Microfluidics

Drops are formed in milliseconds, or less, which means that the time for transport competes with formation time. Even though the drops are of the order of picolitres, many surfactants take longer to diffuse to the interface than the formation time allows. The consequence of this is that the amount of surfactant at the surface during and instantly after droplet production may be lower than that at equilibrium, and so the interfacial tension may be higher and the system less stable than measurements would suggest. As such, a higher concentration of surfactant is often needed in these systems. It has been reported that commercial surfactants do not fulfil the needs of systems utilising these microfluidic devices.[115,124]

Surfactants are, of course, critical for droplet formation but also further complicate the system by altering the rheological properties of the interface compared to the bulk and changing flow.[115] It should also be noted that rather than improving the stability, surfactants can also cause additional instabilities. An example of this is "tip-streaming", where the flow of the drop causes the surfactant to concentrate at one end of the drop, causing an interfacial tension gradient that can lead to further drop breakup, or coalescence at the low surfactant end.[118] This can be turned into a useful feature, allowing a bimodal distribution of drop sizes that can be controlled with careful tuning of flow

rates.[57] As mentioned above, the rate of formation means drops are not stabilised immediately and so recoalescence may occur if droplets collide.[124]

1.6.5 Flow Regimes

1.6.6 Flow maps and stability predictions

The flow behaviour of immiscible fluids in a microfluidic device belongs to one of a series of flow regimes. There is some variation in the names, and the exact description of the various regimes across the literature. Nonetheless, they are broadly classified as dripping or jetting, where dripping simply describes any pattern where stable drops are formed and jetting is characterised by the flow of two distinct streams.[117] Figure 1-4 shows how these flows appear in a flow-focussing device using the conventions followed throughout this thesis.[57,90,118,124]
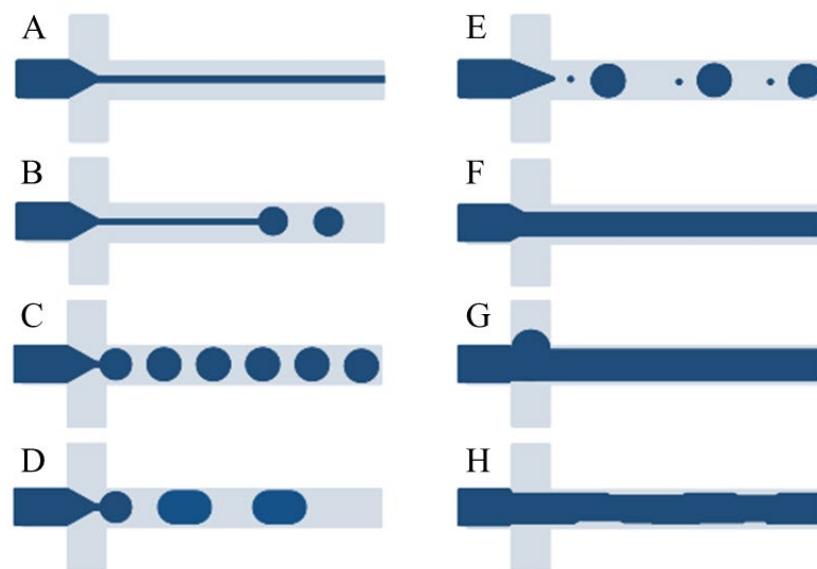
Figure 1-6 Flow regimes in a flow-focusing device. (A) threading, (B) jetting, (C) dripping, (D) large dripping, (E) satellite drops, (F) tubing, (G) displacement of the flow and (H) wall wetting.

- Threading is defined by a stream of the dispersed phase which is stable over long distances ($l \gg h$, where l is the stability length and h is the height of the channel)

- Jetting comprises a stream, as for threading, but in this case the stream breaks up a short distance from the junction ($l < 20h$). This can allow access to smaller drop sizes than standard dripping patterns.

- Dripping produces drops at or near the junction. The size and location of breakup can vary. As the drop size becomes comparable to the diameter of the channel, the drops become deformed. This is "large dripping" and if drops become too large, they can become unstable.

- Satellite drops are secondary drops produced in addition to the main drop. These are generally much smaller than the main drop.

- Tubing is a viscous dominated flow with a much wider dispersed phase stream than the jetting and threading regimes. This often leads to wetting.

- Displacement is the movement of the dispersed phase into one of the continuous phase channels as well as, or instead of, into the outlet. This happens when the flow rates of the continuous phase are not exactly balanced, with the stronger flow pushing the dispersed phase into the channel of the weaker flowing material.

- Wetting occurs when the dispersed phase wets the walls. It is difficult to regain a stable flow once this has occurred.

Regimes can be broken down further based on the specifics of the system.

1.6.6.1 Capillary Numbers

Given the wide range of flow behaviours that can be exhibited, it is useful to have a way to describe and predict the behaviour of a system. It is common to describe a system using the dimensionless value, capillary number, Ca:

$$Ca_i = \frac{\eta_i Q_i}{\gamma A}$$

where γ is interfacial tension between the two phases and A is the area of the exit channel. The capillary number is calculated for each phase, i, using the corresponding viscosity, η, and flow rate, Q. This parameter clearly shows the balance between the two driving forces: viscous and capillary, and allows one to easily see the importance of the physiochemical properties of the materials.[118,123]

The capillary numbers can be used to create a flow map to visually compare the parameters producing different flow regimes. Figure 1-5 A shows an example of one such map from T. Cubaud and T. Mason, where the regimes have distinct boundaries such that the behaviour could easily be predicted based on the properties. Unfortunately, a universal flow map is not possible due to the difference between viscous-stress based transitions and capillary number transitions so a new map must be made for each dispersed phase/continuous phase combination.[117,118]

Flow maps can also be produced using the flow rates or flow ratios. This is more intuitive for making adjustments to a system and visualising the impact of flow; however, it does not allow for comparison between different systems.

Two key assumptions are used to generate the maps, no matter the method. The first is that the interfacial tension remains constant. In practice this is only true for systems with either no surfactant or very high levels. Secondly, inertial forces can be neglected owing to low Reynolds numbers.[124]
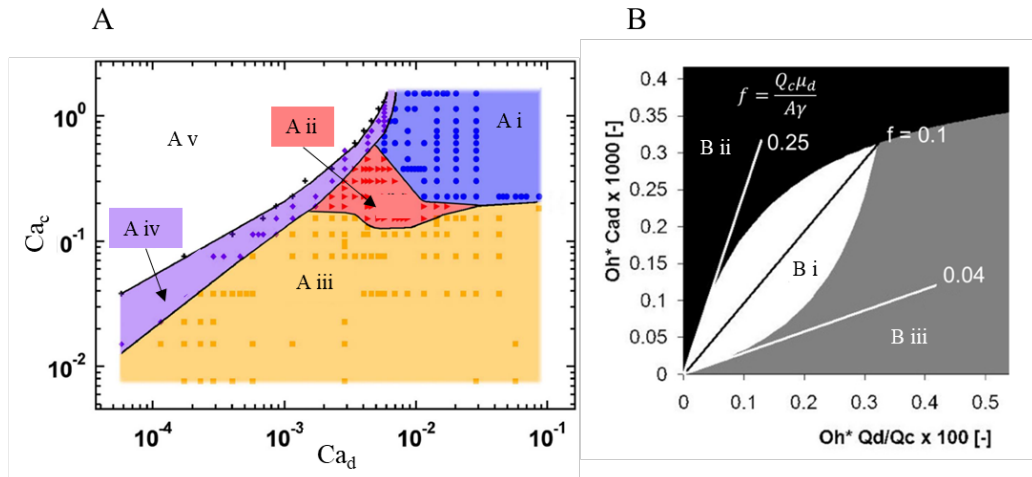
Figure 1-7 Flow maps created using the capillary number (A) and Ohnesorge numbers (B). (A) is adapted from Capillary Threads and Viscous Droplets, T. Cubaud and T. Mason, 2008. Distinct flow regimes were identified as A, i) threading, A, ii) jetting, A, iii) dripping, A, iv) tubing and A, v) displacement. Calculations are for a glycerol/PDMS oil system.[118] (B) is adapted from Single Microparticles to Microfluidic Emulsification, K. Kinoshita, et al., 2016. The flow map represents all combinations of liquid properties, channel size and flow rate. The region B, i) denotes combinations which will lead to uniform spherical particles, B, ii) gives non-uniform particles and instabilities and B, iii) produces droplets larger than the exit channel.[8]

Some general rules have been developed based on the capillary numbers. At low Ca (<0.01), the geometry dominates as the viscosity is not high enough, therefore there is low flow and squeezing occurs. As Ca increases (>0.1) the stream becomes hard to break up. This can result from a high viscosity or a high continuous flow rate leading to jetting type behaviours.[124]

In order to produce droplets both the continuous and dispersed phase flow rates, Q_c and Q_d respectively, need to be low. The transition between jetting and

dripping happens between capillary values of 0.1 and 1, though a wider range of 0.001 and 10 has been suggested. [117,122,124,125]

It is possible to generate drops outside of the region suggested by the capillary limit, though it acts as a reasonable guide to determine appropriate parameters for the set-up.[57,117,122]

1.6.6.2 De Bruijn Equations and Ohnesorge Numbers

A set of equations specific to flow-focussing devices were laid out by de Bruijn in the patent *Process for Preparing Monodisperse Emulsions*.[126] From these equations the flow rates required to produce identical, spherical drops can be calculated as follows.

The flow rate for the continuous phase is given by

$$Q_c = f \frac{\gamma A}{\eta_c}$$

where A is the cross-sectional area of the exit channel, γ is the interfacial tension and η_c is the viscosity of the continuous phase. The value f is an empirical constant which is varied between 0.04 and 0.25, outside of this range the droplets are no longer stable. The regions in Figure 1-5 B visualise this condition. Comparing Equation 1-17 and Equation 1-18 it can be seen that f is effectively the capillary number.

The range of stable flow rates for the dispersed phase can then be calculated using the flow rate ratio, satisfying the condition:

$$\frac{Q_d}{Q_c} = \frac{0.00272}{Oh_c Oh_d}$$

where Oh_c and Oh_d are the Ohnesorge numbers for the continuous and dispersed phase respectively, calculated using

$$Oh_i = \frac{\eta_i}{\sqrt{\rho_i \gamma R}}$$

where η_i and ρ_i are the viscosity and density respectively, γ is the interfacial tension and R is the radius of the exit channel. Systems meeting these criteria should produce spherical, monodisperse drops.[8,126]

1.6.7 Manipulating Drop Size

Varying the flow rates within the dripping regime allows the droplet size to be controlled. For systems with a narrow range of stable flow rates there may only be small variations possible, whilst for other systems this becomes a very valuable tool. The change in size is proportional to the amount of material flowing, though other factors, such as channel geometry, complicate the development of predictive equations.[57,118]

Low continuous phase flow rates increase the likelihood of drop coalescence, as does the change in channel width as the drops transition from the chip to the connecting tubes since drops that are close whilst still solidifying are more likely to merge.[57]

1.7 Polymers for Microparticle Production

1.7.1 Materials for the Microparticle Core

Throughout this work the word "biocompatibility" is used in discussion of material characteristics. Though definitions vary, in this case it defines materials whose presence in a body/tissue is tolerated and causes no toxicity.

For most biological applications, the core of the microparticle must be non-toxic and biodegradable, and there should be a thorough understanding of the degradation behaviour and cellular response.[66] The most common core materials are poly(lactic acid) (PLA) and the related copolymer poly(lactic-co-glycolic acid) (PLGA) owing to their biocompatibility, physiochemical suitability and processability. These polymers can be made into virtually any shape through methods such as injection moulding and 3D printing. They can be used for microsphere formation and microencapsulation by employing emulsion solvent evaporation, solvent extraction, spray drying and microfluidics.[64,74,127]

PLA has been used successfully in tissue engineering for scaffolds, bone screws and anchors, temporary and long-term implants as it has a similar elastic modulus to bone, as well as the controlled delivery of therapeutics, proteins and small molecule drugs. Multi-encapsulation and the freedom to create complex shapes allow the devices and particles to be multifunctional.[64,74]

PLA is a linear, aliphatic biopolymer. It is easily derived from corn or sugar cane, making it a low cost and easily accessible material.[127] It exists in two forms: poly(L-lactide) and poly(D-lactide). The physiochemical properties of the two forms are nearly identical, however, the L form is crystalline, whilst the D form

is completely amorphous.[63] By combining the two forms in different portions the thermal, rheological and degradation behaviour can be controlled. These can be manipulated further by changing the molecular weight and polydispersity.[66,128]

PLA degrades through hydrolysis into lactic acid monomers, which are easily removed by the body through metabolic pathways.[127] The rate of degradation is crucial for drug delivery and can be controlled through particle morphology (dimensions, porosity, etc.) as well as the properties of the polymer (molecular weight and polydispersity, L to D ratio)[74]

The disadvantages of PLA are that it is hydrophobic, has low cell adhesion, is slow to degrade and, although being inert is advantageous is some situations, its lack of ability to direct cell differentiation is limiting in many cases. Additionally, despite it and its degradation by-products being nontoxic, the acids can cause inflammation at the site.[127] The alternative is to use naturally occurring biopolymers, such as complex sugars. However, these are not as easy to control, limiting their applications in other ways.[63]

1.7.2 Solvent Selection

The organic solvent(s) used in microparticle formation must meet the following criteria: low boiling point, high volatility, low toxicity, be partially miscible in water and of course, solubilise the polymer(s) required.[75,106]

Dichloromethane (DCM) is commonly used in microparticle formation due to its high volatility and ability to solubilise most polymers of interest. However, it is toxic. As such there is a trend to move towards ethyl acetate, a much less toxic

option. Ethyl acetate is around 4.5 times more soluble in water that DCM. Rather than being an advantage, this can make particle formation harder to achieve. The sudden loss of solvent upon addition to the continuous phase can lead to polymer precipitation and formation of fibre-like agglomerates rather than particles. [75,106]

1.7.3 Surfactants

Surfactants are required to stabilise the interface during drop formation. As the surfactant remains once the drops have hardened into particles, biocompatibility of the surfactants is as crucial as that of the core material.

Polymeric surfactants come in a wide array of structures, shapes, sizes, and chemistries. They can be linear or branched and be a homopolymer, formed of a single repeating unit, such as PVA, or a mix copolymer, a mix of two or more units as for the bio-instructive surfactants assessed in this work. Copolymers can be formed in a random arrangement of the different units or have a block of each chemistry.[34] Diagram A in Figure 1-6 shows a random arrangement in a comb-graft surfactant, where the backbone is the hydrophobic component and hydrophilic chains protrude.[90] In contrast, Figure 1-6 B shows a surfactant with block architecture, *A-B*, where the hydrophilic and hydrophobic components are separated. An example droplet, showing how each surfactant presents at the interface is also shown.
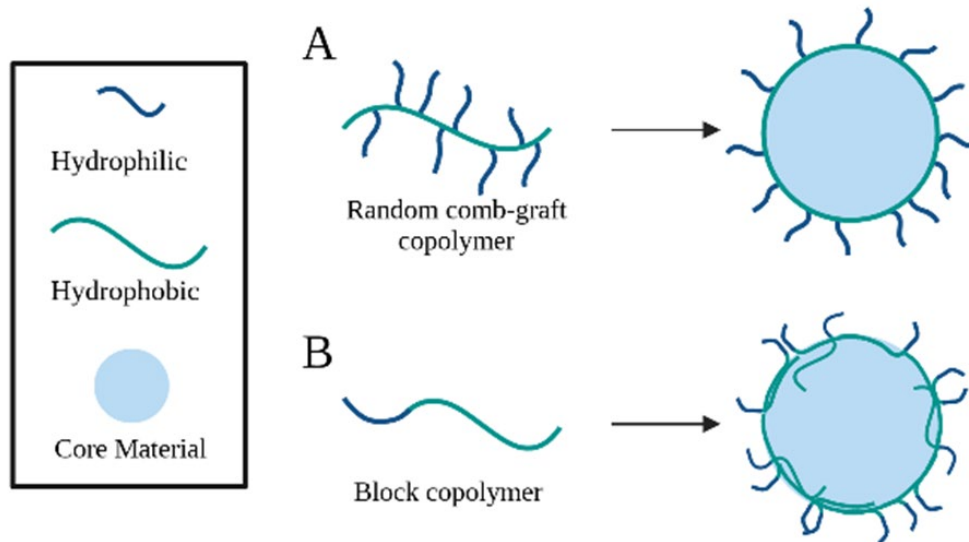
Figure 1-8 Surfactant architecture of (A) comb-graft copolymer chain and a depiction of this surfactant on a final particle, and (B) block copolymer of the A-B form accompanied by a resulting particle. Not to scale.

Polymer chains have many interactions with the interface. Though individually these are weak, the total number makes the adsorption strong. The nature of the block architecture allows larger loops and protrusions between the phases.[33]

Poly(vinyl alcohol) (PVA) is the most common surfactant used in particle systems utilising core materials such as PLGA and PLA. PVA is a semi crystalline polymer, soluble in water and not soluble in organic solvents. Altering the level of hydrolysis varies the solubility and the ability to adhere to hydrophilic surfaces.[75] The ability of PVA to stabilise emulsions depends on its concentration as well as the molecular weight of the PVA used.[75] Higher molecular weights are more effective surfactants than low molecular weights.[36]

Whilst polymeric surfactants are not always able to provide a great reduction in IFT, relying more on their effectiveness as a mechanical and/or thermodynamic

barrier, PVA is able to reduce IFT between the liquid phases even in small volumes.[33] PVA will always migrate to the interface as it has a very high energy in the bulk. Significant reductions in IFT can be achieved with concentrations as low as 0.1w/v%, as the water will strongly move to the bulk. IFT as a function of concentration has no minimum value, though changes at high concentrations are minimal. An effective CMC has been shown for PVA to be approximately 1.1 % (w/v).[36] The properties of the resulting particle depend on the concentration of PVA used. Higher PVA concentrations reduce the IFT more, leading to smaller particles. However, this also increases the thickness of PVA on the particle.[75]

PVA is very difficult to remove from a particle's surface. As the organic solvent is removed the vinyl chains become interconnected with the core polymer matrix. The amount of residual PVA increases for organic solvents with increased miscibility in water, for example more PVA will remain in particles produced using ethyl acetate than with DCM. While this is not a problem for many applications - indeed it is often required when using PLA to improve wetting between particles and media – when the core material is bio-instructive PVA screens its effects.[75]

Studies have been carried out to form microparticles with a core material which had shown very low levels of bacteria attachment.[89] PVA was used to stabilise droplet formation. After several washes with PBS, PVA remained in a non-uniform coating. 2D tests showed different attachment levels with and without PVA. In other work the PVA coating on particles has been shown to limit their

uptake by macrophages, and, by protecting the inner polymer (in this case poly(D-L-lactide-co-glycolide) from enzyme entry, reduced the degradation rate.[109]

There is a clear need for alternative surfactants that are able to meet the biological requirements of the final application, as well as the physiochemical requirements for particle production.

1.7.4 Discovery and Use of Bio-instructive Materials

Most materials used in biological applications are modified from related or earlier materials with a chain of compromises on different properties.[93] High-throughput screening has been shown to be invaluable in the search for bio-instructive materials. Originally developed to aid in drug discovery, material development fields began using high throughput screening platforms in 2004.[92] They allow for the synthesis, processing, and assessment of vast numbers of materials in parallel. Since it is the surface properties of materials that dictate the biological response, 2D microarrays containing small spots of thousands of different polymers can yield vast quantities of data, quickly and without the need for high quantities of materials or high costs.[93,129] These platforms are particularly useful when the underlying biological mechanisms are poorly understood, making material predictions virtually impossible.[89,92] High throughput screens have been used to identify materials capable of stem cell differentiation, modulating immune cell responses and resisting bacterial attachment.[129] Using screening platforms individual moieties, materials or

specific properties that cause the desired response can be identified.[130] With the large amounts of data available it can be developed into a predictive tool.[93]

High throughput screening techniques have been utilised in the Engineering and Physical Sciences (EPSRC)-funded Next Generation Biomaterials Discovery Programme Grant (EP/N006615/1) to Alexander and colleagues at the University of Nottingham to identify "hit" materials that: have low attachment to prevent biofilm formation, modulate immune responses – macrophage polarisation and fibroblast phenotype – and stem cell differentiation, for example towards osteogenesis.[91,92,130–135] Microarrays printed with hundreds of unique, UV polymerizable meth/acrylates have been studied with a wide range of cell types and extensively characterised using surface analysis techniques.[89,129] The challenge is in transferring these materials to 3D formats, specifically for applications where the dip-coating of a foundation material or product is not practical such as wound healing, injectable therapeutics or scaffolds for stem cell differentiation.[90]

Microparticles are an ideal candidate for these applications, however, as discussed, the effectiveness of particles made from a bio-instructive core material is screened by surfactants such as PVA. Studies were carried out to overcome this by forming the "hit" materials into surfactants.[90] The chosen monomers were copolymerised to form poly(ethylene glycol)-base, comb-graft surfactants, as in Figure 1-6 A. In this case the "hit" chemistries were a selection of those shown to modulate bacterial response in 2D. The development process is as follows: high throughput screen – specialised screen (for surfactant components)

– surfactant production – droplet-microfluidic optimisation – particle production and finally back to the microbiologists for attachment tests on the particles.

Tests were performed with a range of hydrophobic "hits" with poly(ethylene glycol) (PEG) and poly(ethylene glycol)methacrylate (mPEGMA) of different molecular weights in different ratios. The copolymer surfactants were compared in a 2D format, and it was found that the hydrophilic component could be added a up to 75:25 (hydrophobic: hydrophilic) without detriment to the biological response, though a 90:10 ratio was the optimum composition. The final particles showed the same behaviour at their 2D equivalents.[90]

These novel surfactants hold great potential for overcoming the limitations of traditional particle systems. Additionally, by using bio-instructive surfactants approximately only 2% of the particle is formed from the "hit" material and the bulk of the particle can be made from lower cost materials. However, these surfactants are not characterised as well as available commercial surfactants (e.g. PVA).[90] Several of these surfactants, combining a range of "hit" chemistries in a 90:10 ratio with mPEGMA were studied in this work to provide understanding of their behaviour and effectiveness in droplet stabilisation.

1.8 Project Overview and Aims

Microparticles have the capacity to greatly improve outcomes in healthcare and tissue engineering applications. However, to fully utilise the vast range of particle designs, deeper understanding of specific microparticle formation is required. In most cases, both simple and complex microparticles are formed through lengthy trial-and-error experiments to optimise materials and processing

parameters. Modifications to existing systems can reduce this somewhat, though may not provide an ideal solution.

Micropipette manipulation techniques have been proven for the assessment of fundamental measurements in immiscible systems. This is the same basis of understanding required to master microparticle formation and design. The aim of this work is to prove the hypothesis that micropipette manipulation methods can aid the understanding of microparticle formation systems, from individual material characterisations to controlling final morphology.

Within this, several smaller aims were set. The first was to develop the analysis techniques currently employed for micropipette manipulation studies to provide a more robust and efficient methodology. In turn, this would allow more detailed analysis of the systems and behaviour assessed.

The most common materials for microparticles are PLA (or a related polymer, e.g., PLGA) with PVA for emulsion stabilisation. However, while investigations into the effects of ESE processing parameters, such as stirring rate have been considered, the base characteristics of this system have been mostly neglected. To this end, the second aim of this work was to perform an extensive assessment of the effects of PLA (PDLLA) and PVA. The polymers were treated as additives to a pure water/organic solvent system to understand their effects individually and in combination. Following this the aim was to use these same techniques to characterise a series of novel surfactants in the context of droplet microfluidics, based on a solvent-free droplet system. Prior to this work, neither the core monomers nor the surfactants had been assessed in this role. Additionally, it

represents the first time such materials have been characterised using micropipette manipulation techniques. An additional aim of this part of the project was to apply these findings to demonstrate how micropipette manipulation techniques can be used to expedite the optimisation of droplet production.

The final aim was to bring together these components to study a specific, biologically relevant, microparticle system. This includes the optimisation of surfactant and understanding of solidification through solvent transfer for a flow-focusing microfluidic device. Droplet morphology was studied and manipulated in single particle studies by the selection of surfactant and solvent concentrations.

Chapter 2: General Methods and Materials

Chapter 2 - General Materials and Methods

2.1 Materials

2.1.1 Core materials

Two types of microparticle system were studied, grouped by type of material forming the core of the particle. Biodegradable particles were formed from poly($_{D,L}$-lactic acid) (PDLLA), Mn 47 000 gmol^{-1}, from Evoniknd, dissolved in solvent to a chosen w/v%.

For non-degradable, solvent-free systems, one of two monomers: 1,6-hexanediol diacrylate (HMDA, 80%) or ethylene glycol dicyclopentenyl ether acrylate (EGDPEA) from Sigma-Aldrich were used. Drops of these materials were polymerised on exit of the microfluidic chip to create particles. The molecular structures of the three core materials are shown in Figure 2-1.
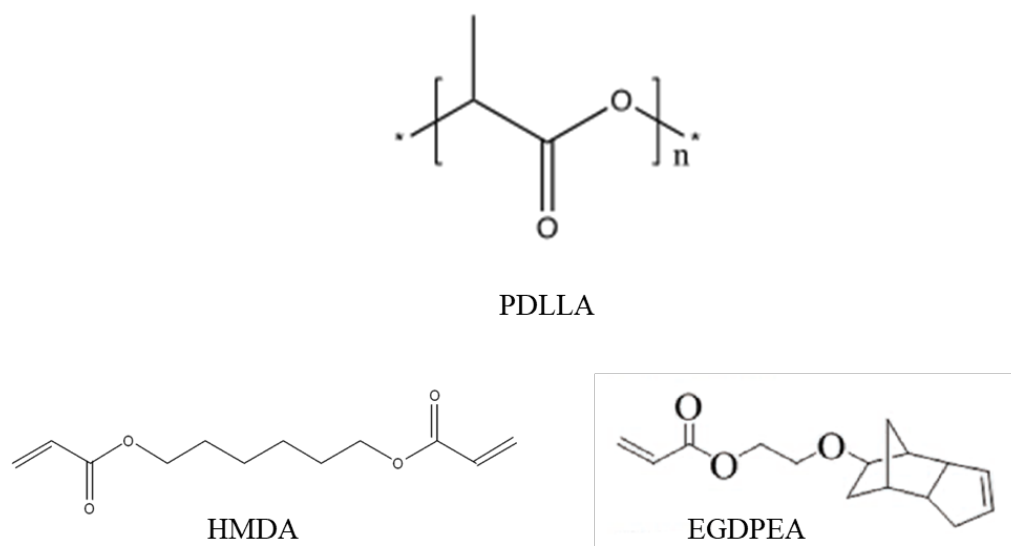
PDLLA

HMDA

EGDPEA

Figure 2-1 Microparticles were formed from either biodegradable poly($_{D,L}$-Lactic acid) (PDLLA), or non-degradable monomers, 1,6-hexanediol diacrylate (HMDA) or ethylene glycol dicyclopentenyl ether acrylate (EGDPEA) monomers.

2.1.2 Solvents

De-ionised water, used for the aqueous phase, was obtained through MilliQ (18.2 MΩ) purification, and used in both micropipette and microfluidic systems.

Dichloromethane (DCM) and ethyl acetate, used in the dispersed phase, were purchased from Sigma-Aldrich. Additional organic solvents: chloroform, decanol, hexane, octanol, pentanol, and toluene used in method development studies were purchased from Sigma-Aldrich and Fischer Scientific.

2.1.3 Surfactants

A range of surfactants were investigated, both individually and in combination. Commercial surfactant: poly(vinyl acetate-alcohol) (PVA) Mw 25 kDa, 88% hydrolysed, was obtained from Sigma-Aldrich.

Novel surfactants were produced by Dr Valentina Cuzzucoli Crucitti, Chemical Engineering, University of Nottingham, via catalytic chain transfer polymerisation. The hydrophilic components were poly(ethylene glycol) methyl ether methacrylate (mPEGMA), Mn = 300, or 2-(dimethyl amino)ethyl methacrylate (DMAEMA), both purchased from Sigma-Aldrich.

The hydrophobic components were a subset of "hit" materials identified by members of the Next Generation Biomaterials Discovery Programme Grant via microarray screening for their bio-instructive capabilities and are of particular interest for investigations and/or applications requiring microparticle formats. The selected monomers were ethylene glycol dicyclopentenyl ether acrylate (EGDPEA), 2-hydroxy-3-phenoxypropyl acrylate (HPhOPA), ethyl acrylate

(EA), ethylene glycol phenyl ether acrylate (EGPEA) and tetrahydrofurfuryl acrylate (THFuA) monomers, purchased from Sigma-Aldrich. The structures of these surfactants are shown in Figure 2-2.

2.1.3.1 Surfactant polymerisation

2, 2′-Azobis (2-methylpropionitrile) (AIBN, 98%), was used as the thermal initiator, and Bis[(difluoroboryl)diphenylglyoximato] cobalt (II) (PhCoBF) as the catalytic chain transfer agent. They were supplied by Sigma-Aldrich and DuPont, respectively. Cyclohexanone and heptane, used as solvents for the synthesis and precipitations, respectively, were supplied by Fisher Scientific. All materials were used without further purifications.

The hydrophilic and hydrophobic monomers were dissolved in cyclohexane in proportions needed to achieve the target ratio of 90:10 in the final polymer. The combined ratio of monomer in cyclohexane was 1:3. PhCoBF at 850 ppm and AIBN at 0.5 wt% with respect to the monomers were added to the cyclohexane mix. The reaction was held at 75 °C for 18 hours, following which the polymers were precipitated in excess heptane (5:1 v/v).

EGDPEA -mPEGMA
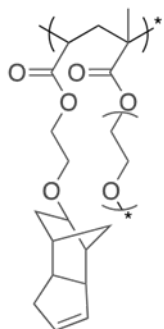
HPhOPA-mPEGMA
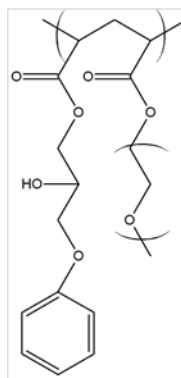
THFuA-mPEGMA
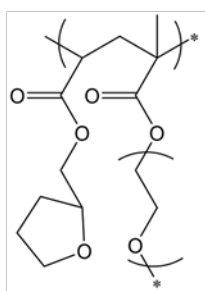
EGPEA-mPEGMA
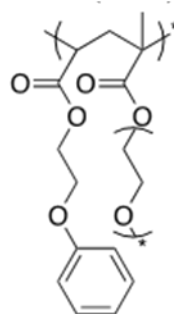
EA-DMAEMA
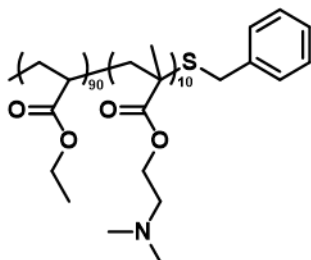
EA-*b*-DMAEMA
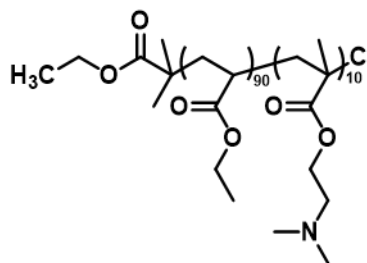
HPhOPA-DMAEMA
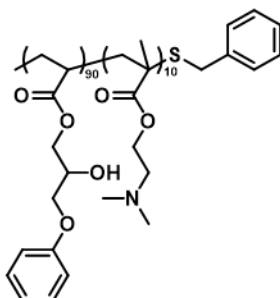
HPhOPA-*b*-DMAEMA
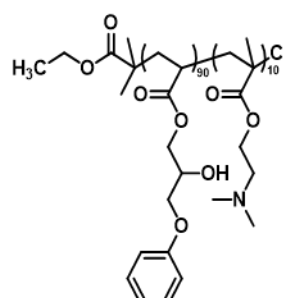
Figure 2-2 Structures of novel, bio-instructive surfactants assessed during this work. Surfactants were of a comb-graft type, except EA-b-DMAEMA and HPhOPA-b-DMAEMA which were block copolymers of A-B structure.

2.1.4 Micropipette Materials

Micropipettes were formed from borosilicate glass capillaries measuring 100 mm long with 0.7 mm outer diameter, and 0.4 mm inner diameter purchased from A-M Systems. These were used for all measurements. Glass chambers were made from long rectangular capillary glass (2 mm x 4 mm), CM Scientific, cut to lengths of approximately 2 cm. Hexamethyldisilazine (Sigma-Aldrich) was used to produce a hydrophobic coating on formed micropipettes.

2.2 Micropipette Techniques

2.2.1 Micropipette Formation

There are two key stages in forming micropipettes from capillary glass: pulling and forging. After this, micropipettes can be used as standard or given a hydrophobic coating, depending on the environment of the experiment.

2.2.1.1 Pulling

Sutter Instruments, Browning 97 was used to pull micropipettes, creating a pair of identically tapered pipettes from each capillary. Prior to pulling, a "ramp" test was performed to obtain the minimum temperature required to begin to stretch the glass. For this, a capillary was inserted through the heating filament and clamped in place. The filament was then heated until the glass first began to pull apart. This was performed for each batch of glass.

For interfacial tension measurements, pipettes require a distinct taper over a long distance and wide tip. A balance is needed between having a sufficient taper to provide clear equilibrium positions and having a long enough region to test over a range of pressures. A taper of between 2 and 4 degrees was used (example in Figure 2-3 A, i. For single droplet studies micropipettes need to be long, narrow, and almost parallel (example in Figure 2-3 A, ii). Varying the velocity, pull force, etc. allow the geometry to be tailored for the application. The pulling program settings for both micropipette types are shown in Table 1.

Table 1 Pulling parameters used for producing specific shaped micropipettes. Values are dimensionless values required for the Browning 97.

Micropipette Use	Heat	Pull	Velocity	Time
IFT	Ramp +15	30	30	250
Single Particle Studies	Ramp +15	100	100	200

To pull a micropipette, the capillary was passed through the heating element and clamped securely as for the ramp test, ensuring equal lengths on either side of the filament. Once secured, the program for the required pipette type was run. The filament heats while a pull is applied. The program cycles until the glass snaps.
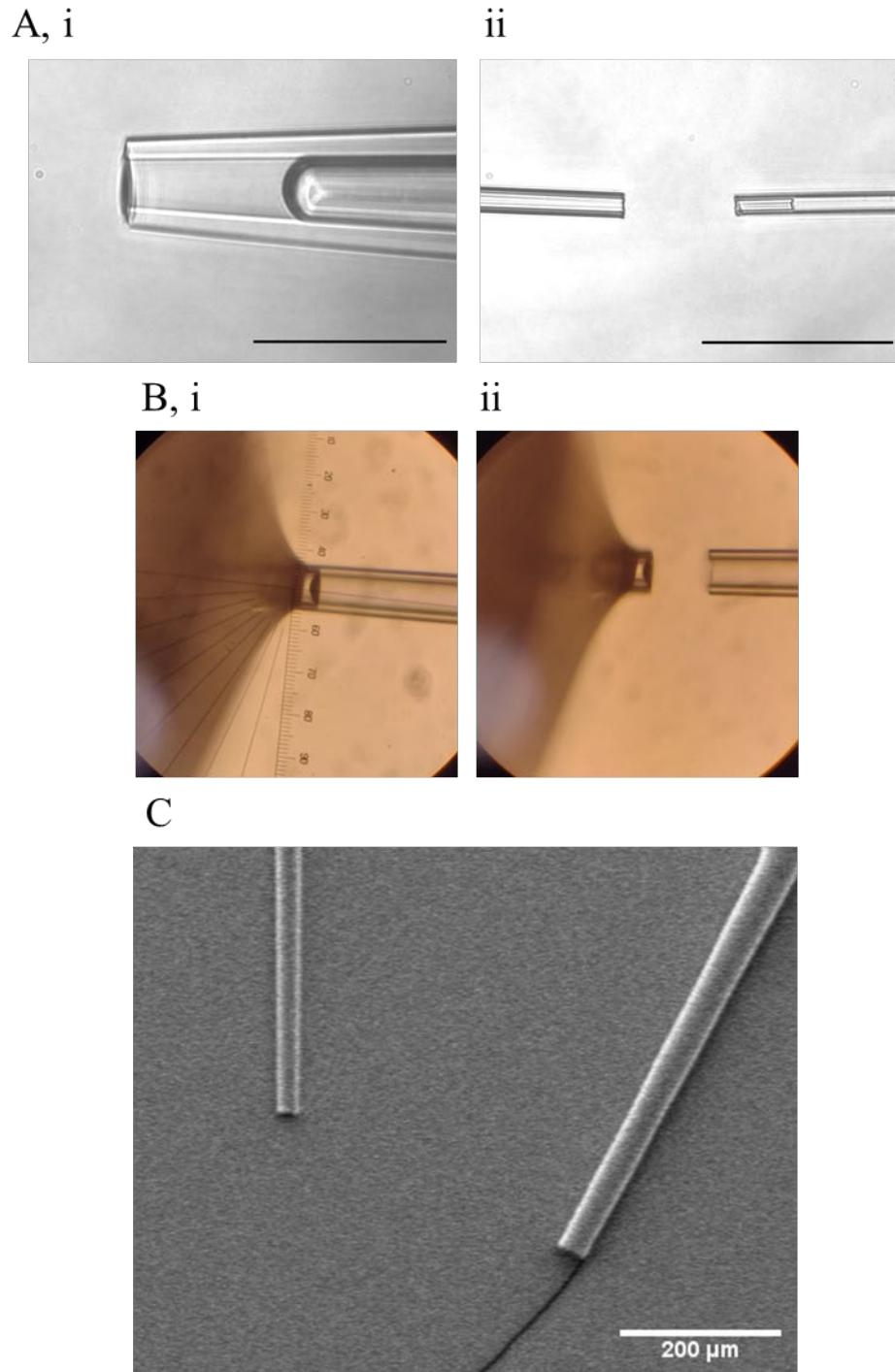
Figure 2-3 (A) Scale 100μm. The shape of a micropipette is specific to the application. (A, i) shows a micropipette tip for interfacial tension measurements, whilst (A, ii) shows a pipette designed for producing droplets for single particle studies. The forging process for micropipette tips requires inserting the tip into a molten glass ball (B, i) and allowing to cool until the tip snaps (B, ii) providing a neat tip. (C) an SEM image of two micropipettes for single particle studies is shown, scale 200μm.

2.2.1.2 Forging

Forging was done using a Narisige Forge, comprised of a lamp, a glass bead on a heating filament controlled by foot pedal and attached to a micromanipulator, a holder for the pipette and a magnifying eye piece. After pulling, one micropipette was mounted in the forge. The end of the micropipette was brought close to the glass ball, ensuring it was in line with the extreme of the drop. The bead was heated, and the very end of the pipette tip moved into the glass. The heat was removed, and the bead allowed to cool. As it did, the glass shrank taking with it the end of the micropipette that was inside. This initial break opened up the pipette.

The heating process was repeated, and the micropipette moved into the glass to the approximate position to give the final desired diameter. The molten glass travelled into the micropipette due to capillary forces. The heat was removed when the glass travelling into the micropipette was at the same position the glass travelling down the outside (Figure 2-3 B, i), this provided a neat break when the glass cooled. Figure 2-3 B, ii shows a clean break, obtained through this process.

Figure 2-3 C is an SEM image of two catching pipettes, showing their shape and final size. When forming micropipettes for single droplet studies, the tip of the catching pipette should be approximately twice the diameter of the delivery pipette to allow for smooth transfers.

2.2.1.3 Hydrophobic Coating

For single particle studies where the continuous phase was organic, a hydrophobic coating was required to ensure drops were produced rather than the dispersed phase simply wetting the outside of the pipette. For this, the pipettes were pulled and forged as above before treatment.

A drop (approx. 100 µl) of hexamethyldisilazine was added to a 2 mL vial with a silicone top. A small hole pierced in the lid allowed the micropipette to be held securely inside the vial without the fragile tip touching the sides or base. This was left overnight in a fume hood. As the hexamethyldisilazine evaporated it reacted with the oxygen on the surface of the glass, resulting in a thin, even coating.

2.2.2 Filling

2.2.2.1 Filling Micropipettes

Pipettes were front filled using a filling tower, Figure 2-4 A. The material of interest was contained in a 2 mL vial and placed in the holder. For volatile materials the pipette is first passed through a silicon lid, as for salinisation, which prevents excessive loss during filling, this can be seen in the inset in Figure 2-4 A. The back end of the pipette was secured in a "chuck", a small metal device in Figure 2-4 A which comprises a plastic screw containing a silicone O-ring to ensure a tight seal and connects to tubing at right-angles to the pipette to the syringe to control the applied pressure. In line with the pipette is a metal spur by which the chuck can be secured into the tower, or later to the micromanipulators.
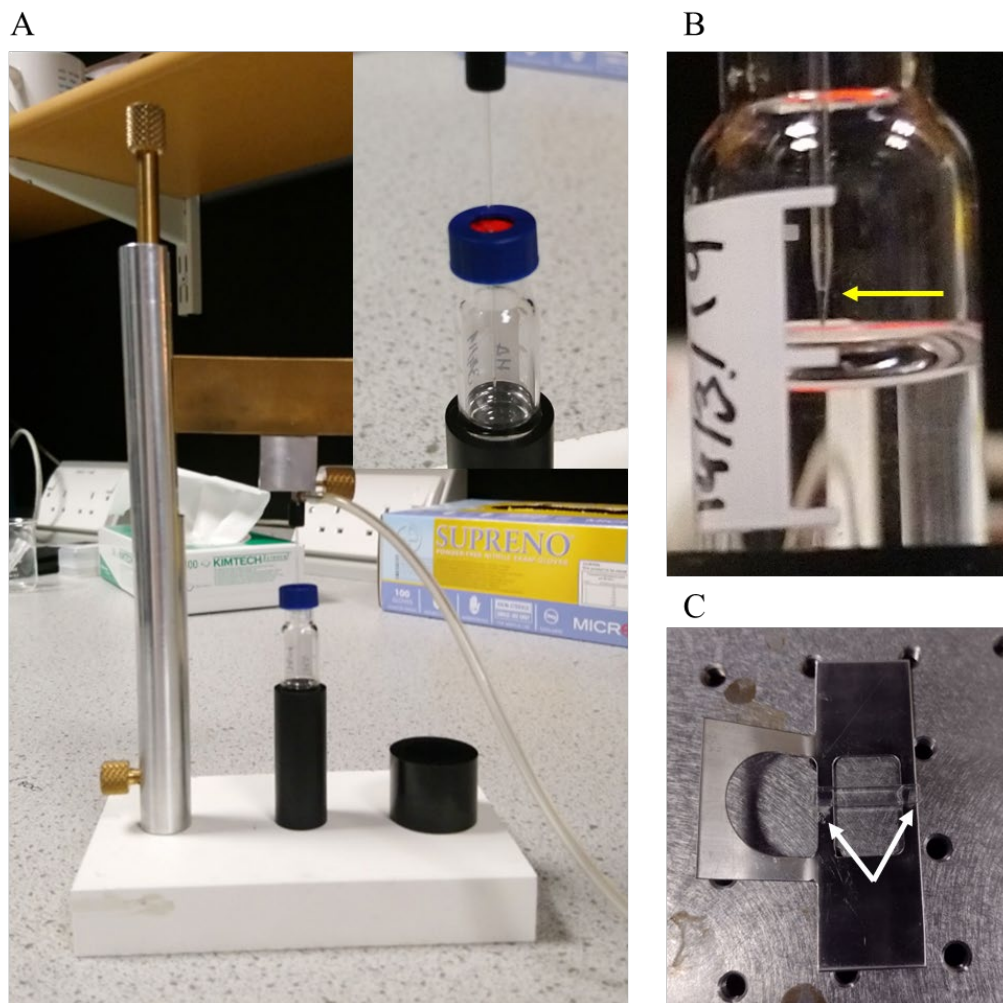
Figure 2-4 The filling tower allows for front filling of the micropipette with the sample material without damage. (A) The micropipette is clamped into the tower and connected to a syringe via a custom chuck. The pipette is passed through a silicone lid to prevent evaporation of volatile compounds during filling (inset top view). (B) the micropipette tip is lowered to the surface of the sample liquid, entering the liquid just enough to begin filling. The yellow arrow shows the liquid rising in the micropipette. (C) Glass chambers are mounted on a metal holder with grease (white arrows) and filled with the second test phase.

To avoid damage, it was important that the tip was only just in contact with the liquid. This was especially important for those with the hydrophobic coating as prolonged time in an aqueous material damages the coating and reduces its effectiveness. A small negative pressure was the applied to draw the test material into the pipette. Figure 2-4 B shows the depth to which the micropipette was inserted into the liquid and the sample filling the micropipette.

For volatile samples, a solvent plug was used to prevent material loss or solidification in the back of the pipette. For example, if the system of interest was PDLLA dissolved in DCM, measured against PVA in water, a solvent plug of water saturated with DCM was used to prevent DCM evaporation and so PDLLA solidification which would prevent stable pressure application. To form the plug a small amount of solvent-saturated water was drawn into the pipette before switching vial and continuing with front filling as described above. It is important in this step to avoid trapping air in between the phases.

2.2.2.2 Preparing and Filling the Chamber

The test chamber described above, was rinsed with the continuous phase to remove any residual cleaning solvent or dust. It was then mounted on the holder, held in place with grease, as shown in Figure 2-4 C. It was the filled with approximately 200 µL of continuous phase liquid.

2.2.3 Pressure Transducer

Pressure was measured using a Validyne DP15 variable reluctance pressure sensor connected to a LED readout (CD223 Validyne Engineering) and to a LABVIEW programme, with readout in cmH_2O (0.098 kPa).

2.2.3.1 Calibration

Regular calibration checks were carried out by connecting the sensor to a water manometer and syringe. The pressure applied through the syringe was increased and the relative positions of the water in the manometer measured, providing the pressure in cm H_2O. The process was repeated across the range of pressures of

interest (for liquid-liquid up to approximately 30 cm H$_2$O) to ensure a linear response throughout this region. The difference in the two water heights was compared to the pressure difference on the readout and the zero point and gain adjusted so the deviation between the readout and calculated pressure was never greater than +/- 0.1, the step size of measurement.

2.2.4 Acquisition Software

A LabVIEW program for recording the images (.JPEG) or video (.avi), pressure and time, was created by Dr Anders Utoft/Dr Koji Kinoshita, Department of Physics, Chemistry and Pharmacy, University of Southern Denmark. Figure 2-5 shows the display seen for an IFT measurement, with the time and pressure stamped onto the image (highlighted by red boxes.) The choice between images or video recordings could be made prior to acquisition. Frame rate was set to 15 fps for videos, which was cut down as required in the processing stages.
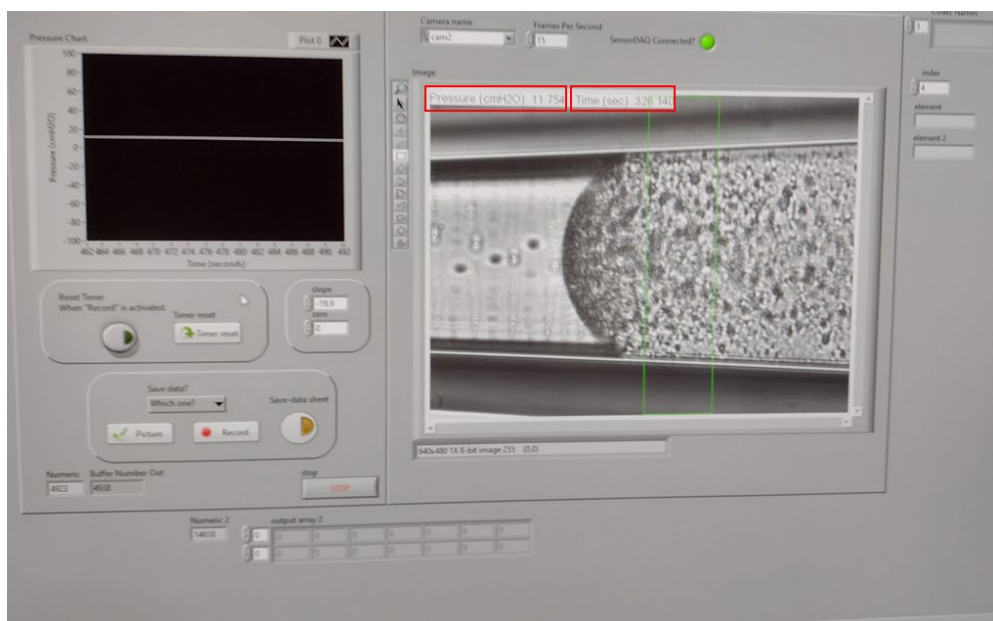
Figure 2-5 LabVIEW program for viewing and recording micropipette manipulation studies. The time and applied pressure are stamped on each image/frame, shown here in the red boxes.

2.2.5 Interfacial Tension Measurements

2.2.5.1 System Set-Up

The filled chamber and mount were placed on the stage above the microscope, and a tapered pipette secured in the chuck was mounted in a micro-manipulator before being fed into the chamber. The micro-manipulators allowed adjustment in x, y, and z directions. The chamber and pipette positions were adjusted such that they were centred above the microscope to avoid the influence of diffraction near the chamber walls.

Tubing connected the micropipette with the pressure sensor and a syringe to control the applied pressure. A valve allowed the isolation of the micropipette, pressure transducer and/or the syringe as necessary. Figure 2-6 A summaries this set-up.

On entry to the chamber, a micropipette fills with the continuous phase material, an interface forms between that and the material of interest in the micropipette (liquid throughout this work.)

To create a fresh interface for the measurement, the pressure was increased such that the interface was incident with the end of the micropipette. Then the pressure was released (0 cmH$_2$O applied pressure) and the interface rapidly receded into the pipette. This caused an interfacial area increase from approximately 630 μm^2 (at 20 μm tip diameter) to 250 000 μm^2 (in parallel region). As such, the old interface comprised only ~0.25% of the new interface; effectively producing an entirely new interface. The pressure was then increased to move the interface into the tapered region and was given time to reach its equilibrium position.
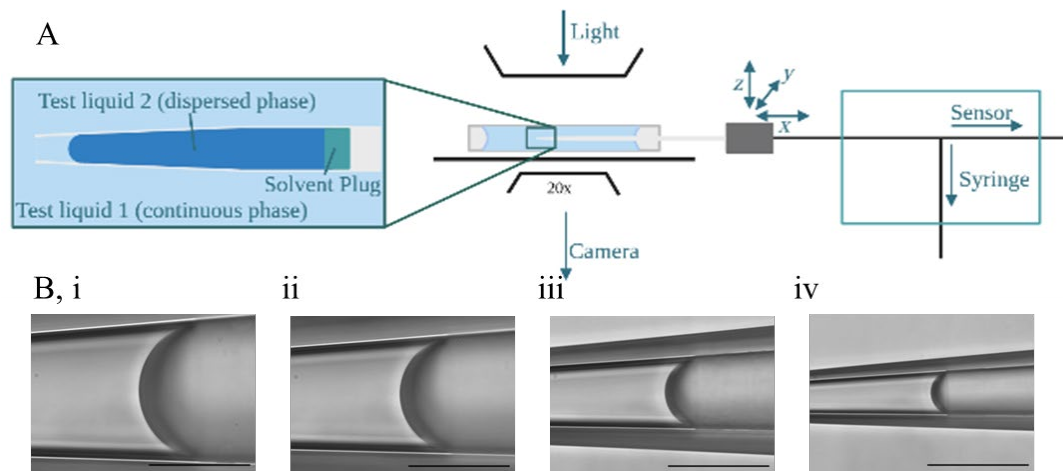
Figure 2-6 (A) diagram showing the experimental set-up for interfacial tension measurements using micropipette manipulation. (B) As the applied pressure is increased the interface is moved to a narrower portion of the micropipette. This is followed by adjusting the position of the micropipette within the chamber. Scale bar 100 μm.

2.2.5.2 Static Equilibrium Interfacial Tension Measurements

Equilibrium was confirmed by applying a small fluctuation to the pressure and ensuring the interface returned to its position. This was to ensure the interface was not only partially stable to due to pinning or wetting, as this fluctuation would free the interface to move to its true equilibrium.

An image was taken for the interface at its equilibrium position for the applied pressure. The pressure was then incremented a small amount and the process repeated. This process is shown in Figure 2-6 B. Once the interface was close to the micropipette tip, the receding measurement could be taken by reducing the applied pressure incrementally and allowing the interface to reach its new equilibrium positions. Measurements were taken along the full length of the tapered section. To take further repeats of this sample a fresh interface was formed as described above and the process then repeated. All interfacial tension data presented in Chapters 4-6 was obtained with this method.

2.2.5.3 Dynamic Interfacial Tensions

Dynamic interfacial tension methods were used here only for developing and testing the analysis methodology.

The initial set-up was carried out as for static equilibrium measurements up to the point of creating a fresh interface. The pressure was set to 0 cmH$_2$O, and the interface fully retreated. However, it was then almost instantaneously set to a positive pressure value between the value required to move the interface to the tapered section and to the end of the micropipette. Then, the movement of the interface as it travelled to reach the position associated with this new pressure was recorded as a video.

2.2.5.4 Analysis Overview

To obtain the systems interfacial tension, the radius of curvature of the interface in each image was measured. Full details on this analysis are given in Chapter 3, where the standard method is given, and the development of a new, automated version is discussed and compared.

2.2.6 Single Particle Studies

2.2.6.1 System Set-Up

The standard set-up for single particle studies required two, long thin, almost parallel pipettes. The micropipette with the smaller tip was filled with the material of the dispersed phase, becoming the "delivery" pipette. The second "catching pipette" remained empty, filling with the chamber liquid on entry.

The catching pipette was mounted in a chuck in the left micromanipulator. It was connected to a syringe for control, but it was not necessary to connect to the

transducer. The "delivery" pipette was secured in the manipulator on the other side. This is shown in Figure 2-7 A. The two micropipettes axially aligned in the centre of the chamber, in the centre of the field of view of the microscope.
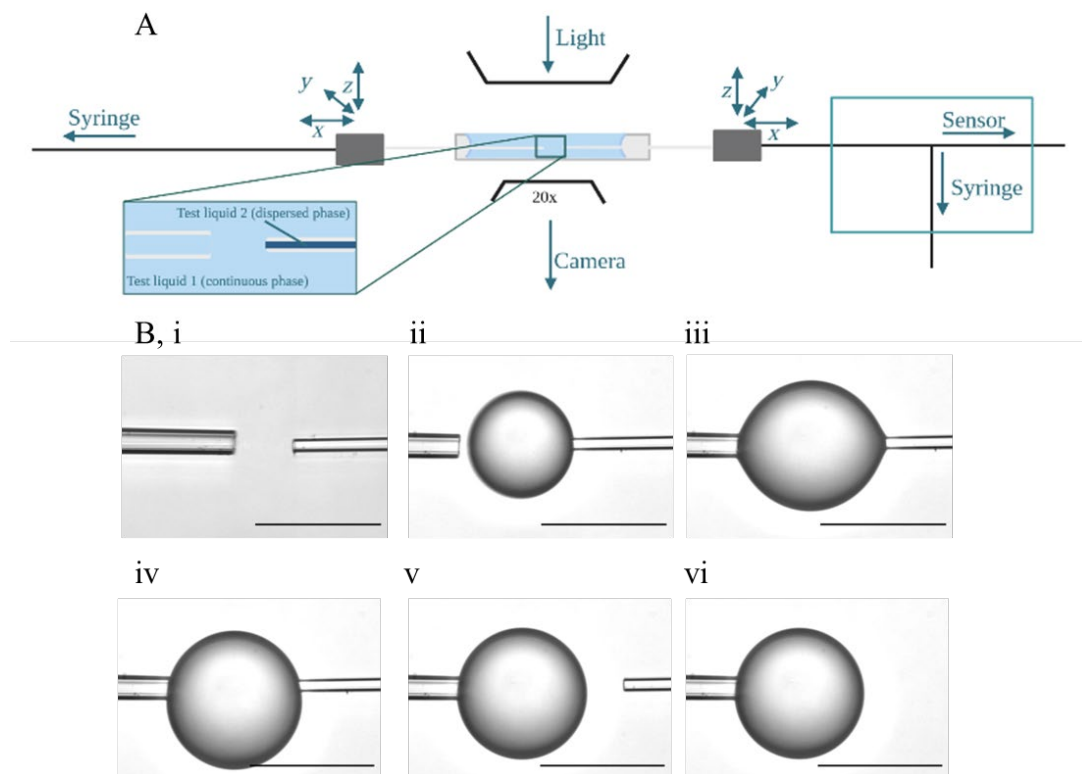
Figure 2-7 Single particle studies utilised the single drop catching method. (A) Diagram shows the relative positions of the micropipettes over the microscope. (B) The micropipettes are brought close together (i), before a drop is blown from the delivery pipette (ii). The catching pipette is moved so it is in contact with the drop surface, (iii). The two micropipettes are moved away from one another (iv) and the drop remains on the catching pipette (v). The delivery pipette is removed from the region while dissolution occurs. Scale bar 100μm.

2.2.6.2 Single Droplet Catching Method

Before forming a drop for measurement, the material at the end of the delivery pipette was blown out and disregarded. This was to avoid differing concentration in the test drops. A small drop was blown by increasing the pressure and then

knocked from the pipette, either by tapping or blowing it away using the catching pipette. The chamber was moved slightly so the surrounding continuous phase was fresh. The time was set to zero at the beginning of recording.

A drop was blown from the delivery pipette and the recording started as the material began to emerge. Once the drop reached the desired size the catching pipette was brought gently into contact, (Figure 2-7 B, iii). An ideally sized catching pipette (approximately twice the diameter of the delivery pipette) was able to attach and hold the drop without needing additional suction, however, a small (negative) pressure was applied as necessary to transfer the drop (Figure 2-7 B, iv). Care was taken to control the pressure such that transfer was managed without the drop being sucked in or caused to spin.

Once the drop was transferred, the delivery pipette was removed from the region of the chamber while dissolution was taking place. A small negative pressure was applied to the delivery pipette to prevent the further production of droplets which could interfere with the drop of interest.

The process was recorded for the duration of the dissolution. Then the drop was either discarded, by applying a positive pressure to the catching pipette, or removed to dry for SEM analysis.

2.2.6.3 Analysis Overview

The droplet videos were analysed to obtain the size of the drop as a function of time. This was carried out using a MATLAB script developed to improve the

reliability and number of frames that could be analysed. This is explained in detail in Chapter 3.

2.3 Microfluidics

2.3.1 Single Chip Set-Up for Droplet Microfluidics

Figure 2-8 shows the set-up of for microfluidic droplet production. Two syringe pumps (Harvard Apparatus PHD Ultra Syringe Pumps), fitted with glass syringes, controlled the flow of the continuous and dispersed phases. Tubing (Dolomite, FEP 250 µm internal diameter, 1.6 mm outer diameter) connected the pumps to the flow-focussing chip (Dolomite, 100 µm hydrophilic flow focusing), which was placed on a microscope with an accompanying high-speed camera to enable the observation and recording of droplet formation.
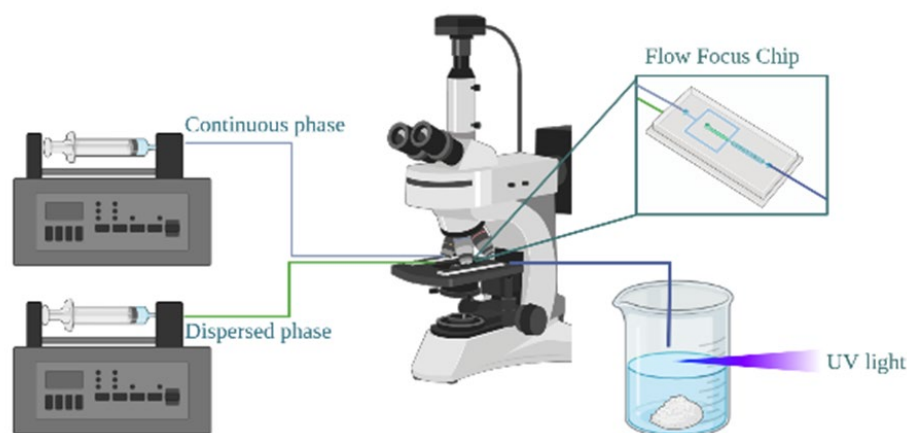
Figure 2-8 Droplet microfluidics set-up requires two syringe pumps, feeding the dispersed and continuous phases into the microfluidics chip. This is placed on a microscope. For the solvent free, monomer-based droplets, UV curing (365nm) of the drops occurred as they exited the tubing. For drops of dissolved polymer the collection vessel was stirred while the solvent evaporated.

In this work, this was the set-up used for studying particles with a monomer-based core. The droplets travelled down a second tube from the chip to a collection vessel filled with DI water. The droplet stream was irradiated with UV light (Omnicure LX180, 365 nm) as it exited the tubing.

2.3.2 Parallel Chip Set-Up for Droplet Microfluidics

The second set-up was designed for producing higher volumes of particles as there are multiple channels on each chip and many chips can be used in parallel. In this case a Telos® module, with a 2-reagent hydrophilic chip was used. The two fluids (dispersed and continuous) were controlled used two Mitos P-Pumps connected to a control PC (Dolomite Microfluidics). The pumps were connected to the chip module, and the chip to an outlet collection beaker with 250 μm FEP tubing with a 1.6 mm outer diameter (Dolomite Microfluidics). The particles formed using this system were those with a dispersed phase of PDLLA dissolved in organic solvent. The droplets were collected in DI water, where the solvent was removed from droplets to form particles.

2.3.3 Particle Collection

Particles were passed through a mesh of 40 μm, such that particles collected on the mesh while small polymer debris passed through. Particles were then collected in a vial and the remaining water allowed to evaporate, leaving a dry powder form.

2.4 Analysis Techniques

2.4.1 Microscopy

2.4.1.1 Overview

Optical microscopy, that which uses light to form the image, has been a core feature in scientific discovery since its inception in the 1600s.[136] Brightfield microscopy, used to observe the micropipette manipulation studies, is one of the simplest yet most versatile imaging techniques available.[137]

In brief, a light source produces light to illuminate the sample. It is passed through a condenser lens and a controlling aperture which focuses the light beam where the sample is placed. The light then passes through the sample, with more or less of the light being absorbed depending on the material and thickness of the sample. The transmitted light continues its path to the objective lens (or lenses) to magnify the image. The light then travels to a camera and/or eye piece, which may have additional magnifying lenses in place, so the user can observe the image produced.[138]

Optical microscopy has several limitations. Resolution is limited by the wavelength of light and the surrounding material which sits on a different focal plane. Additionally, light experiences diffraction by the sample, which can lead to constructive and destructive interference of the waves producing diffraction patterns in some areas.[137,138] While the wavelength is not a limiting factor in this work, it is worth noting that the other effects do impact on image quality in these studies. Diffraction at pipette walls limits the pipette size for interfacial tension

measurements as well as the amount of the interface that can be used for measurement. This is discussed in more detail in Chapter 3.

The spherical nature of the interfaces and drops studied means there is a compromise on focus for features that exist at multiple depths through the sample. To maintain consistency the focus is kept on the central plane of the drop or micropipette unless stated otherwise.

2.4.1.2 Experimental Set-Up

Throughout the micropipette manipulation studies an inverted microscope was used (Zeiss Axiovert 100). Here, the light source is at the top and the beam directed down through the condenser, sample, and objective before being reflected into the camera (Allied Instruments Pike) or eye piece. To avoid chromatic aberrations the light passed through a green filter before the condenser. A 20X objective lens was used throughout the studies. This lens was chosen to give the most detail whilst maintaining a wide field of view. Higher magnifications would have allowed greater detail for the droplet morphologies, but the accompanying reduction in field of view would have made formation difficult and limited other measurements.

2.4.1.3 Image Analysis Software

Image processing was carried out using ImageJ (Fiji), an open source, Java image processing program developed by the National Institutes for Health. Details of its usage are described in Chapter 3 and the macro scripts written in this application can be found in Appendix 1.

MATLAB R2017b, from MathWorks, was used for both image processing and analysis as well as further data analysis.

2.4.2 Scanning Electron Microscopy

2.4.2.1 Overview

Scanning Electron Microscopy (SEM) is a powerful imaging and analysis technique employed across the sciences to study samples on the nm and μm scale. The resolution limit imposed on light microscopy is overcome by using electrons, whose wavelength is much shorter than that of visible light. SEM was first developed nearly 100 years ago, but development lagged the forerunner, Transmitted Electron Microscopy (TEM), for many years.[139] SEM is utilised in this work to obtain images of the surfaces of the particles which, due to requiring transmitted light techniques for carrying out the particle production, could not be obtained during the studies.

SEM is carried out in vacuum and protected from vibrations. A beam of electrons is generated by an electron gun, which in the case of standard SEM set-ups is based on a thermal filament. The electrons are accelerated to energies of between 2 keV and 40 keV, depending on the sample and requirements of the analysis.[140] The beam produced by the electron gun is narrowed by condenser lenses to a spot size below 100 nm. Increasing electron energy or decreasing spot size causes the electron beam to penetrate deeper into the surface, resulting in a loss of topographical details and more pronounced damage to the surface and so should be chosen based on the goal of the analysis.[140,141]

Travelling down the SEM column, the beam passes through a series of apertures, scanning coils – responsible for directing the beam across the sample – and through an objective lens, before hitting the sample. Interaction with the sample then produces back-scattered electrons, secondary electrons, Auger electrons and characteristic X-rays.[140,141] Each can be utilised for different analysis techniques, however, it is the former two that are of interest for imaging. Back-scattered electrons, those which originated from the incident beam, are collected by a series of concentric detectors above the sample. Secondary electrons, which are emitted as a result of ionisation of the sample, are the most widely utilised signal. These are collected by a detector at an angle to the sample and as such not all emitted electrons are captured by the detector, making this particularly useful for visualising surface roughness and topographical features which appear as shadows.[141] Once collected, electrons are converted to light, the signal amplified and an image produced.

2.4.2.2 Sample Preparation for SEM Imaging

Suction was increased on the catching pipette as it was removed from the chamber. This helped to prevent particle loss as it crosses the liquid/air interface leaving the chamber. Once removed from the stage, the pipette back is pushed through the small hole in one of the silicone-lidded vials such that the tip and particle are pointing up, outside of the vial. Figure 2-9 A shows a series of pipettes in this manner. This configuration was then placed under a cover to prevent dust accumulating on the particle and to prevent disturbance. It was then

left for a minimum of 24 hrs to thoroughly dry out, finally transitioning to the glassy state.

An SEM stub was prepared with double-sided carbon tape, (Figure 2-9 B) Dried particles cannot easily be removed from the pipette and so were mounted on the stub as one. The pipette tip, including the particle, was laid on the tape and lightly pressed to ensure contact, (Figure 2-9 C). Tweezers were then used to hold the tip on the stub just before the transition to the parallel portion, and the body of the pipette lifted, causing it to break off at the point it was held, as in Figure 2-9 D.
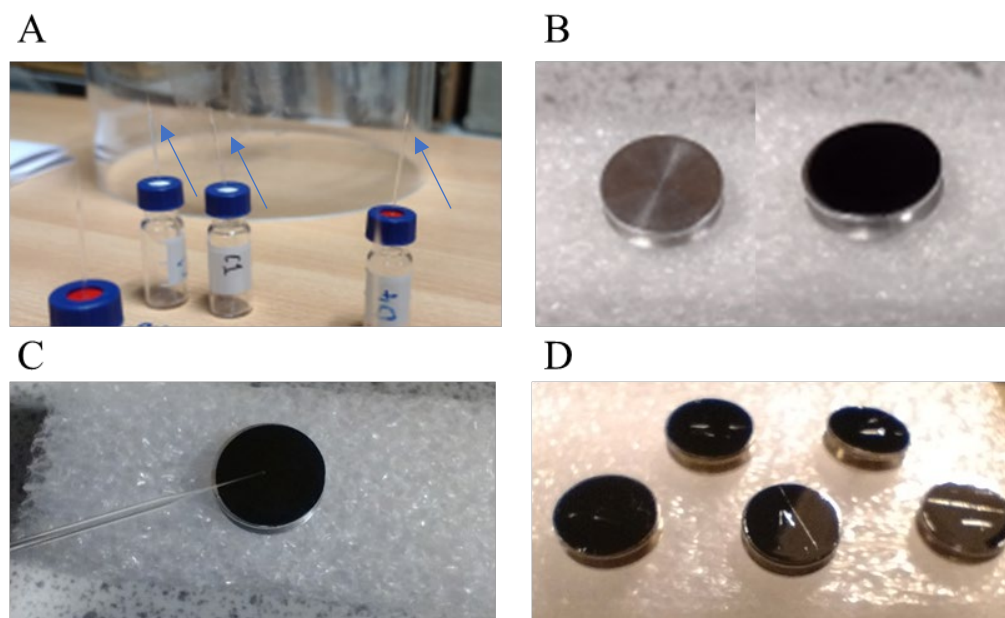
Figure 2-9 (A) Microparticles are kept on the end of the micropipette which is held vertically to dry for 24hrs. Arrows point to tips. (B) SEM stubs are prepared with double-sided carbon tabs before the dried micropipette and particle are placed on top (C). The glass of the micropipette is pressed gently onto the stub and the tip held in place whilst the rest is snapped, leaving behind the tip and particle on the stub. (D) Stubs with particles and tips attached ready for coating.

Bulk production microparticles, those produced in using a microfluidics system, were prepared for SEM analysis by depositing a small amount of particle powder

onto a stub prepared with double-sided carbon adhesive, and gently pressing to ensure a good contact to the tape. Loose or excess particles were removed with a jet of compressed air.

2.4.2.3 Sputter Coating

As the particles and pipettes are non-conducting, the samples had to be coated before imaging. This was done using a Polaron Platinum Sputter Coater. Using platinum ensures a very thin coating can be used. This allows better resolution of surface topographies. Additionally, platinum is better at preventing excess charge compared to alternatives such as carbon. This is particularly important for polymers and glass, both of which are used here which are prone to high charge build up.

Samples were loaded into the holder and the set-up pumped down to a vacuum below 6 Pa. Plasma was applied using a voltage of approximately 2.2 kV, adjusted to maintain a current of 15 mA, for 90 seconds, providing a covering of approximately 9 nm. Samples were then removed and secured for storage/transport prior to imaging.

2.4.2.4 SEM Imaging of Microparticle Surfaces

Particles produced in single particle studies and their micropipettes were analysed using the JEOL 6060LV SEM at University of Nottingham Nanoscale and Microscale Research Centre. Samples were mounted on the stage and the system brought under vacuum. Imaging was carried out at 5 keV with a spot size of 50 to avoid excessive charge and damage which would result from direct

charge on a single particle. Images were taken at magnifications between 27X and 3000X.

Imaging of particles produced using the microfluidics set-up were prepared as described above and imaged using a Hitachi TM3030 tabletop SEM with a beam voltage of 15 keV and with magnifications between 30X and 1200X. Imaging and analysis was carried out by Dr Adam Dundas, Department of Chemical and Environmental Engineering, University of Nottingham.

2.4.2.5 FIB SEM

Focused Ion Beam Scanning Electron Microscopy incorporates a second, ion beam - usually gallium ions - which can mill through a sample to create slices or even remove entire sections to analyse the internal structure of a sample in a highly controlled manner. A dual-beam set-up has the ion and electron beams arranged such that SEM imaging can take place whilst the ion beam mills the sample normal to the surface, allowing improved control.[142–144]

FIB-SEM was utilised here to image the insides of the particles produced in micropipette studies. This was chosen instead of the standard method for imaging the inside of particles, which is to freeze and break the particles, since this is not possible without a bulk sample.

The FEI Quanta200 3D DualBeam FIB/SEM was used for these studies, by Dr Chris Parmenter, Nanoscale and Microscale Research Centre, University of Nottingham. Analysis was carried out on particles already imaged in the JEOL 6060LV and as such followed the preparation set out above.

2.4.3 Time of Flight – Secondary Ion Mass Spectrometry

Time of Flight – Secondary Ion Mass Spectrometry is a highly sensitive technique for the chemical analysis of surfaces. As a technique it is capable of easily detecting parts per million or even per billion with a surface specificity on the scale of nanometres.[145] Unique ion fragments are identified which correspond to the material of interest, the intensity of which is proportional to the amount of that material present in the region being assessed.

Glass coverslips were manually dip-coated using 4% poly (hydroxyethyl methacrylate) in a 95:5 ethanol: water solution. The particles were dropped onto the coverslips before the coating completely dried, allowing the particles to adhere securely without the need for additional force or adhesives.

Samples were left at room temperature and pressure for 12 hours to allow for the complete removal of ethanol and water from the coating. Loose particles were removed with a jet of compressed air prior to analysis to prevent this occurring as a result of the vacuum in the ToF-SIMS chamber.[146]

An IONTOF GmbH ToF-SIMS IV instrument was used with a 25 keV Bi3+ primary ion source with a target current of ~0.3 pA. Low energy electron flood gun (20 eV) was used for charge compensation. A 500 μm × 500 μm scan area was analysed for positive and negative spectra. Other analysis parameters were a cycle time of 100 μs, one shot/frame/pixel, one frame/patch and 20 scans per analysis. The intensity is normalised by the total count. Images and spectra were acquired using SurfaceLab 6 software and analysed carried out using SurfaceLab 7.1 software. Measurement and analysis were carried out by Dr Adam Dundas,

Department of Chemical and Environmental Engineering, University of Nottingham.

2.5 Error, Error Propagation and Statistical Analysis

2.5.1 General

Unless stated otherwise, the data presented is a mean average of three repeats (minimum) and the error bars are ± 1 standard deviation (SD) of values around this mean.

2.5.2 Interfacial Tension Measurements

Error on individual measurements came from the sensitivity of the pressure transducer (±0.1 cm H_2O) and the error in radius of curvature measurement. This value depended on the method used, as discussed in Chapter 3. A single interfacial tension measurement is comprised of approximately 20 individual images and pressures. The interfacial tension is calculated from the gradient of a linear fit to the radius of curvature and pressure values. As such, error on the interfacial tension is derived from the 95% confidence bounds on the linear fit of the data. Unless stated otherwise, a minimum of three repeat measurements are made for each sample, n=3. The final value of interfacial tension presented is the average of these measurements and the accompanying error is the standard deviation of these measurements around the mean value.

2.5.3 Dissolution

Data concerning dissolution properties, e.g., diffusion coefficient, is the average of a minimum of four drops. The error associated with this value is then the standard deviation of the values around this mean. In situations where individual

droplet data is presented, the errors have been calculated by propagation from initial measurement or extracted from the 95% confidence bounds on linear fits as appropriate. Errors in these cases are often insignificant, being multiple orders of magnitude lower than the value. As such they may not be visible.

2.5.4 Particle size

For microparticles produced in large quantities, e.g., in using microfluidics, it is common to describe the level of polydispersity using the coefficient of variance, CV. The coefficient of variance is described by the standard deviation divided by the mean and is given by a percentage.

2.5.5 Statistical Analysis

To show significance between conditions and/or formulations, data was analysed using GraphPad Prism (9.5). An ordinary one-way ANOVA was used for comparison of single factors, e.g., effect of increasing the concentration of a single surfactant on the interfacial tension. This was used to access Tukey multiple comparison tests, assessing the significance between the data points. P-values below 0.05 confirmed significance of change.

For comparison between multiple factors, e.g., between different surfactants, the two-way ANOVA analysis was used to access Tukey's multiple comparisons between groups. Again, significant was determined by p-values below 0.05.

Chapter 3: Development of Analytical Routines and Tools

for Micropipette Manipulation Studies

Chapter 3 – Development of Analytical Routines and Tools for Micropipette Manipulation Studies

3.1 Introduction

As described in the preceding chapters, micropipette methodologies and their theoretical basis are well established. However, as part of this work, methods for improving the analysis techniques were identified. New analysis routines were developed for static and dynamic interfacial tension data and for measuring the size of droplets undergoing solvent dissolution. The aim was to provide reliable and accurate methodologies capable of handling increased volumes of data to improve usability of the technique. To achieve this aim software was developed to automate processing and analysis, with the objective of removing the error and bias associated with manual measurements.

In the following sections, current methodologies are evaluated and the basis for the new routines described. Details are given of the pre-processing, processing, and analysis steps developed, as well as validation of the results through comparison to alternate methodologies and, where appropriate, results obtained from literature. The methods shown in this chapter aim to reduce the variability and error in measurement down to the limit of detection (resolution/optical system limitations) as such the quality of image acquisition is vital and steps described in Chapter 2 are followed to achieve the best outcome.

Some droplets experience phase separation during dissolution which can be observed in real time. The development of internal microstructure in real-time is a unique opportunity afforded by using micropipette manipulation techniques. In

order to fully maximise this capability, new analysis routines were required. As part of the work investigating this behaviour the aim was to create analysis routines to extract usable information from the dissolution videos. Internal domains were too small and numerous to allow for manual analysis, necessitating the use of automated image manipulation and analysis.

The following chapter is divided based on the application of the new methodology: interfacial tension (static and dynamic), dissolution, and finally the assessment of internal microstructures.

3.2 Static Equilibrium Interfacial Tension Measurements

Interfacial tension measurements form the basis of many of the experiments described in the following chapters. The method for obtaining these measurements using micropipette manipulation, as described in detail in Chapter 2, Section 2.2.5.2, involves the manipulation of an interface formed within a tapered pipette. A small positive pressure is applied to the interface, causing it to move within the pipette until it reaches an equilibrium position. The radius of curvature at this position is unique for the pressure applied and relates to the interfacial tension as described by the Young-Laplace equation, Equation 1-4. To achieve a reliable measurement of interfacial tension a series of images are required, corresponding to a range of pressures and positions.

Both the pressure and radius of curvature measurements contribute to the final error on the tension value. As the error in the pressure measurement is fixed by the sensitivity of the sensor (± 0.1 cm H_2O), error minimisation must be achieved

by reducing inaccuracies in the measurement and calculation of radius of curvature as much as possible. This begins with image acquisition.

The front of the interface lies at the centre or the pipette. When taking an image, the microscope is focused on the front edge of the interface, as shown in Figure 3-1 A. The curvature here provides the most accurate picture of the interaction between the two phases. The portions of the interface closest to the internal walls of the micropipette, shown in red in Figure 3-1 A, are avoided when measurements of the radius are made for two reasons. Firstly, the shape of the interface here can be influenced by the contact with the glass and secondly, the diffraction caused by the walls blurs the interface.
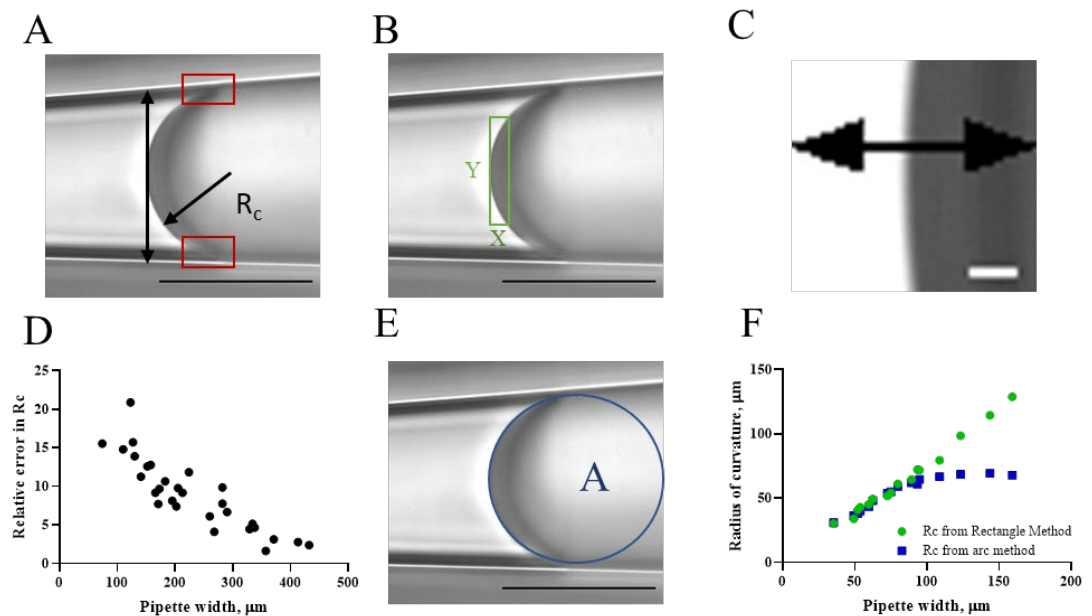
Figure 3-1 Evaluation of current methodologies for measuring the radius of curvature of an interface in a tapered pipette. (A) Reference image displaying the radius definition (single black arrow), the location for pipette width measurement (double black arrow, and the excluded regions of the interface (red boxes). (B) Depiction of the chord method. A rectangle is used for determining distances X and Y. (C) The width of the interface is determined by the pixel intensity changes. (D) The relative error (%) in radius of curvature that arises only from interface width, $\Delta R/R$. (E) The semi-automated arc method with a circle of area A fit to it. (F) Comparison of the chord method (green) and the arc method (blue). Scale bar 100 μm.

As the following discussion is based only on measuring geometries, and to allow for universality, the interfaces are referenced in respect to their position in the micropipette using the pipette width, rather than the applied pressure as for discussions on interfacial tension. Figure 3-1 A depicts the position the pipette width is measured in relation to the interface. Images used for demonstrating the analysis development are at pipette widths between 25 μm and 175 μm, a typical range for most systems.

3.2.1 Evaluation of Current Analysis Methodologies

The predominant method used to measure the radius of curvature of such interfaces is the chord method. First described in the inaugural paper on micropipette interfacial tension measurements,[11] this method involves manually drawing a rectangle over the interface, as given by the example in Figure 3-1 B. The top and bottom right-hand corners of the rectangle lie at points on the interface, while the centre point of the left-hand side sits on the horizontal limit of the interface. Taking the horizontal, X, and vertical, Y, measurements of this rectangle effectively provide the length position of a chord. From these values the radius of curvature, R_c, can be calculated:

$$R_c = \frac{\left(Y/2\right)^2 + X^2}{2X}$$

The chord method provides a reliable measure of radius in most instances. However, it has two major drawbacks, the first is that it is subject to bias and inconsistencies due to its manual nature. The accuracy of this measurement relies

on the careful positioning of the rectangle. The width of the interface averages 2.7 µm (or 8 pixels) across its length, (Figure 3-1 C.) Even with careful positioning of the rectangle, by using a manual selection there will be variation in the position of the interface for any given image. For large radii, this thickness has a negligible effect. However, as the radius of curvature decreases, the error arising from positioning the rectangle can lead to a relative error of as much as 25%. A demonstration of this for a representative dataset is shown in Figure 3-1 D. The second drawback of the chord method is that it is very time intensive, limiting the number of images that can be analysed. This is a particular issue for dynamic measurements where videos with higher frame rates are preferred to obtain as much detail about the approach to equilibrium as possible.

To improve reliability and processing times, a semi-automated method was trialled. A series of markers were placed along the interface using ImageJ, and a circle fit to the arc of points. An example of this is shown in Figure 3-1 E. The area of this circle was measured and used to obtain the radius. Whilst the circle fit has the advantage of being semi-automated, so should reduce analysis time, the method proved to be much less reliable. Several points are needed to produce a good fit, making the consistent choice of interface position both more important and harder to achieve, increasing the likelihood of error. Additionally, the fits failed at large radii, as the circles generated are limited by the size of the image – an applied circle can only be as large as the image it is on, whereas the radius of curvature describes a much larger circle.

Radius of curvature measurements obtained from both the chord and arc methods are shown in Figure 3-1 F for a representative data set. This shows the two methods have good agreement at low radii, but the arc method clearly reaches a limit and plateaus. The chord method performs much better, but the potential for variation and error remains.

The limitations of current methods necessitated the development of a robust and efficient processing method to measure the radius of curvature without manual bias. The analysis routine developed can be broken down into three distinct stages: pre-processing, automated analysis and extracting interfacial tension.

3.2.2 Pre-Processing Stages

Achieving robust and reliable analysis of the interfaces through an automated method relies on the quality of the image and of the pre-processing. This is performed using ImageJ, with all images from a single repeat processed as a batch. Pre-processing is performed in a separate routine to the analysis for several reasons. Most importantly, it allows the inspection of images before the analysis stage. From this, adjustments to the pre-processing routine can be made, for example, increased filtering was required for data sets with sub-optimal acquisition quality. It additionally allows the processed images to easily be saved separately to the raw files and images removed that are not for analysis, such as images of the pipette tip, without removing them from the original set of images.

Crop → Median Filter → Find Edges → Invert → Binarise → Skeletonise → Invert
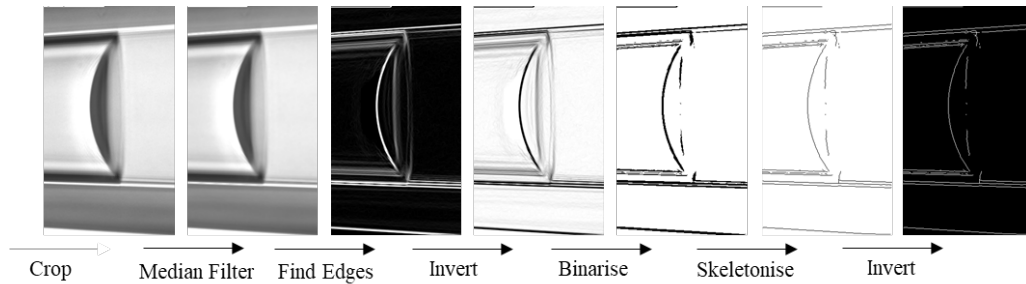
Figure 3-2 The pre-processing steps applied to an interface image to yield a thin (single pixel) line image of the interface and micropipette walls.

The pre-processing steps are shown in Figure 3-2 for an example image and proceed as follows. Firstly, the image is cropped based on a pre-set size. This not only removes the text bar but by removing unnecessary pixels, improves processing efficiency at later stages of the analysis. Guides on the LabVIEW screen during image acquisition ensure the interface is in the same position on each image so as not to be affected by this cropping. A median filter is then applied, with a default kernel size of 5x5 pixels. Edge detection is performed (*Find Edges* function, in-built in ImageJ.) This uses Sobel edge detection and returns a greyscale image where pixel intensity is representative of the intensity change in the original image. This is then inverted to carry out the next stages. Binarisation is achieved through the *Threshold* function where "Auto" and "white background" were selected. From this the image was eroded using the *Skeletonise* function which reduces all lines to the thickness of one pixel. The image was then inverted again as the stages involved in the automated analysis rely on identifying white pixels. The image was then saved, and the process repeated for all images in a batch. (See appendix 1A for ImageJ script.)
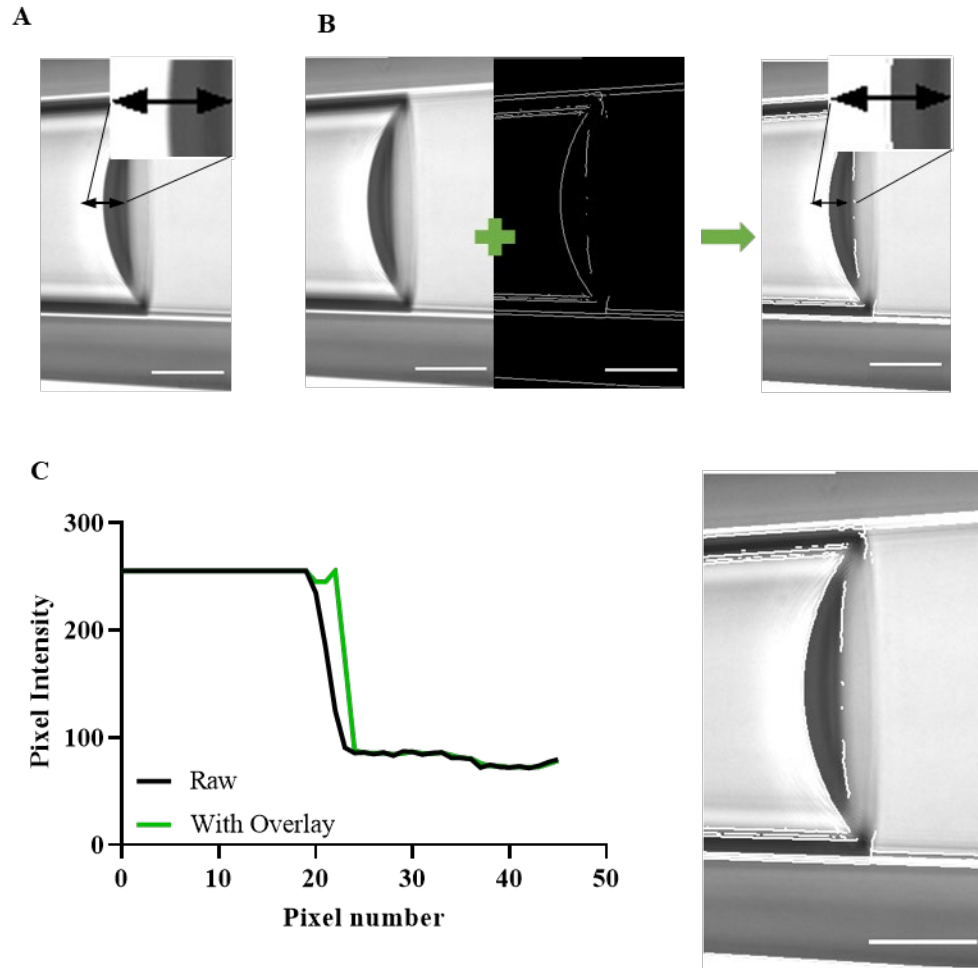
Figure 3-3 Comparison between the interface image before and after the pre-processing stages. (A) the pixel intensity is measured across the front of the interface for the raw image. (B) the final image is turned into a mask and combined with the raw image. The pixel intensity is measured over the same location. The pixel intensities are compared (C) to identify the interface position in the thin line image. Scale bar 100 pixels.

Figure 3-3 compares the final processed frame with its corresponding raw image. This was done by creating a mask of the processed image based on the white pixels and saving this as a region of interest. This was applied to the original image as an overlay and "*flattened*" to combine the images. The pixel intensity was measured across the front of the interface on the raw and combined images for comparison. For the raw image, the pixel intensity drops over approximately 8 pixels, corresponding to the width of the interface. The combined image shows

the pixel intensity reached a peak, denoting the overlaid white line, in the centre of the region associated with the interface. This confirmed that the processed interface lies in the centre of the imaged interface. The line of measurement consistently lies in the centre of the interface region across all systems tested, making the limit of detection the limiting factor.

3.2.3 Identifying Interface Pixels

In brief, an analysis routine, written in MATLAB, takes the processed images and associated pressure values, identifies, and fits a circle to, the interface to obtain the radius of curvature of the presented images then displays a plot of pressure vs. the inverse of R_c and the resulting interfacial tension of that data set.

The first stage in the image analysis is to identify the position of the micropipette walls to centre and crop it appropriately. Since interfaces appear at a range of pipette widths the wall position is not constant. Moreover, images have a different number of lines corresponding to the walls, depending on the pipette size and diffraction and shadows that form during image acquisition.

The positions of the micropipette walls are identified by assessing the pixel values in a single column close to the left side of the image (here $y=4$ column), represented by the green line in Figure 3-4 A, so chosen as it is far from the interface. The row index of each white pixel is saved, see all circled points in Figure 3-4 A, and this is compared to the midpoint row, as shown by circle on the black line of Figure 3-4. The first coordinates either side of the midpoint are determined to be the inner walls of the pipette and denote the region of interest.

The image is then cropped to this area and is taken forward into the next stage of analysis, as shown in Figure 3-4 B.
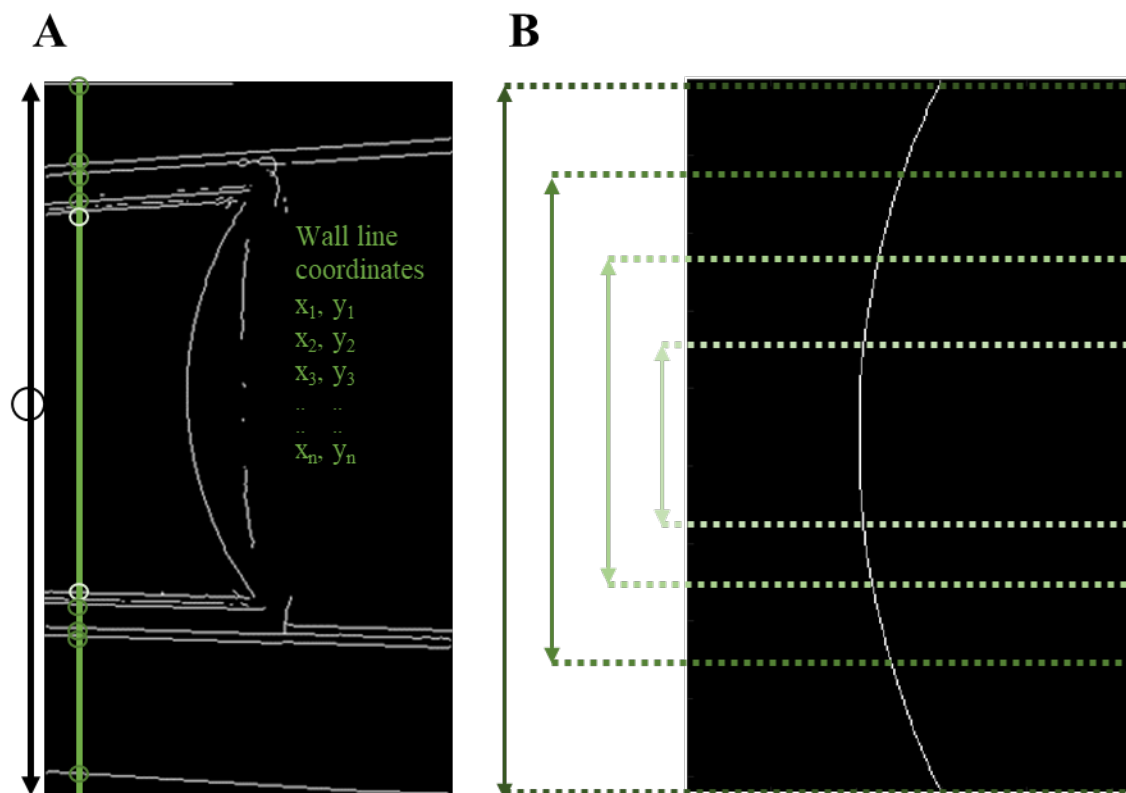
Figure 3-4 (A) the identification of walls and the selection of the inner walls by assessing the white pixels in a selected column marked in green. White pixels corresponding to pipette walls are highlighted by green circles. Each is compared to the mid-point of the image, shown by the black circle, to identify the inner walls (white circles). (B) The image is cut to the limit of these inner walls (dark green) and to a series of fractions centred on the midpoint (paler green dashes).

Images in the wider portions of the pipettes may show none, or only one, inner wall. In this case, the wall is set to default to the image boundary to avoid errors arising. By performing this crop, the measurable interface is maximised for all pipette widths which would not be possible with a fixed size crop. Additionally, by setting the region based on pipette width in a slightly narrower section, that a short distance to the left, the distorted parts of the interface found near the walls (Figure 3-1 A, red boxes), can be mostly avoided.

To obtain the most robust measurement of radius as possible, a series of measurements are taken on the image. This is done at a series of increasing area fractions, 0.2 to 1 in increments of 0.1, based on the original crop and midpoint. Representations of these are shown in darkening shades of green on Figure 3-4 B. This is to ensure the maximum coverage of the interface whilst avoiding influence from any non-ideal portions of the image. (See appendix 1B for examples of these images.)

For each fraction, k, the image is cropped to, the script cycles through each row saving the column index of the first white pixel in encounters, similar to the identification of the walls. These coordinates are fed into the *Pratt Fit* function which returns the determined radius.

As a regression-based method, the more points the fitting function is given, the more accurate the measurement. However, as discussed above, the edges are more likely to be where any artefacts are found. Figure 3-5 shows a typical set of R_c values for one image. Measurements at small area fractions are biased towards an overestimation, due to few pixels and the flat appearance of the small cap. To maximise the number of pixels used without including unnecessary error, the R_c values from each fraction are compared to the median R_c value for that image and values outside of one standard deviation from this median are removed from the set. Then, the R_c value from the largest remaining area fraction (highest k) is used.
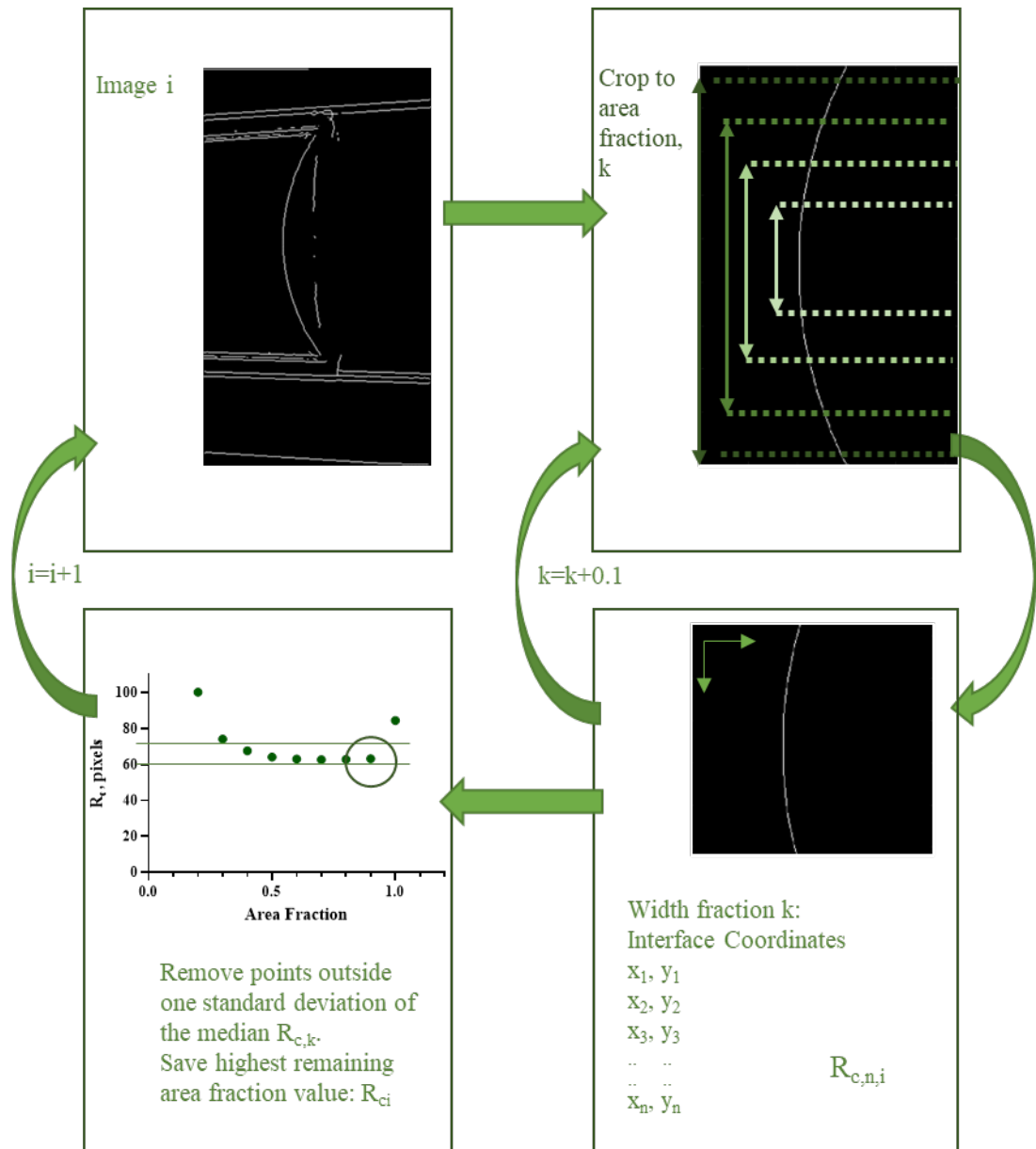
Figure 3-5 Graphic overview of analysis script as it cycles for each image. For each crop fraction, k, the coordinates of the interface are found, the R_c value calculated and compared to the median R_c for that image. The process then continues for the next image.

The R_c value is saved to an array with the accompanying pressure, and the script moves on to the next image in the set. Once all images have been analysed the reciprocal of R_c is taken and plotted against the pressure. The data is fitted to a linear equation and, from rearranging Equation 1-4, the gradient used to calculate the interfacial tension as it is for the manual methods. Figure 3-5 offers a

visualisation of the processes the script cycles through for each image and the MATLAB scripts itself can be found in Appendix 1 C.

3.2.4 Fitting Methods

Circle fitting algorithms fall into two categories: geometric and algebraic. Geometric fits act by minimising the distance between data points and the theoretical circle. These are generally the most accurate but are very computationally intensive and so impractical for use in this case. Algebraic fitting methods, are non-iterative processes and so are less intensive, thus are considered for this application.[147,148]

Four fits were considered, each minimises a function relating the data points to the circle. Kåsa fit is the simplest.[148] The Pratt fit, developed by and named after Vaughan Pratt (1987),[149] is based on the Kåsa method but with an additional function to improve performance. The Taubin fit the third method considered, uses a different base function.[148] Open-source MATLAB function scripts[150–152] of these three methods were used to test their effectiveness. A fourth fit, *Circfit*, was also tested. This is a MATLAB function designed to fit circles to data and is based on the Kåsa method. Kåsa, Pratt and Taubin have been shown to perform similarly, however, the Pratt and Taubin fits are more stable.[147,148]
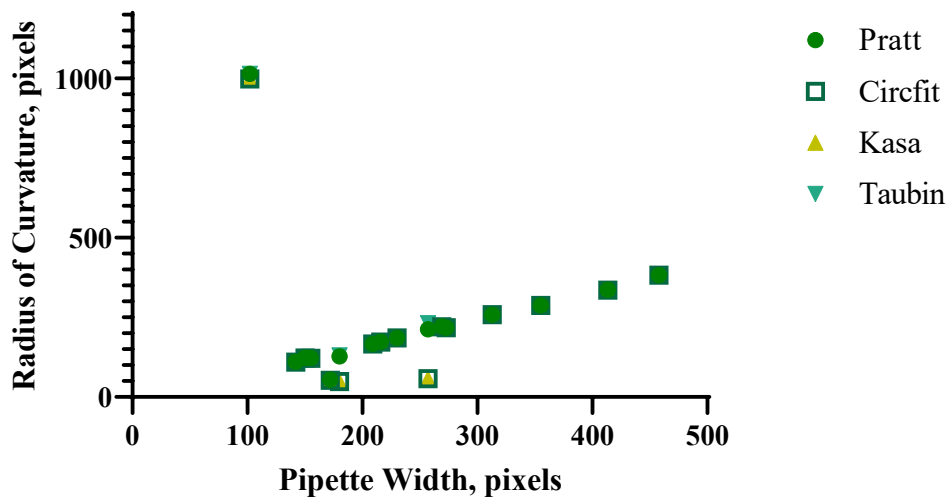
Figure 3-6 Comparison of four fitting methods considered for obtaining R_c values from the interface coordinates for a representative data set. (Pratt -circles, Circfit – open squares, Kåsa – pale green upward triangle and Taubin – teal inverted triangle)

Figure 3-6 shows the R_c values obtained for a representative data set using each of these fitting algorithms. All fits failed to fit an appropriate radius at the smallest pipette width. This was due to there being insufficient points, as discussed above for small cropping fractions. In all other instances the Pratt and Taubin methods performed equally. There were data points where the Kåsa and Circfit fits struggled whilst the other methods were able to produce reasonable measures of R_c, demonstrating their improved reliability over the other methods. Comparison between the Taubin and Pratt methods shows that in instances where the two differ the Taubin method gives a higher estimate than Pratt. The Pratt fit was chosen as neighbouring data suggests the estimation it provided is more accurate.

3.2.5 Validity Assessment

To assess the reliability of the new, automated analysis, a representative data set was analysed using both this and the chord method. Figure 3-7 shows the outcome of this assessment. The two methods agree, confirmed by a high an R^2 value of 0.9949. The automated method has less variation than the chord method, demonstrated in this case by the width of 95% confidence interval for the slope being 0.0612 for manual and 0.0533 for the automated process.

Since the chord method currently acts as the highest standard for measurement, agreement between measurements confirms the validity of the automated analysis. The error on each point is drastically reduced, from up to 25% to the limit of detection. Errors on the manual method values shown in Figure 3-7 A are the standard deviation of three separate chord measurements on this data. Careful consideration and triplicate measurement allow the small error seen here, nevertheless; it is still greater than that from the automated system.
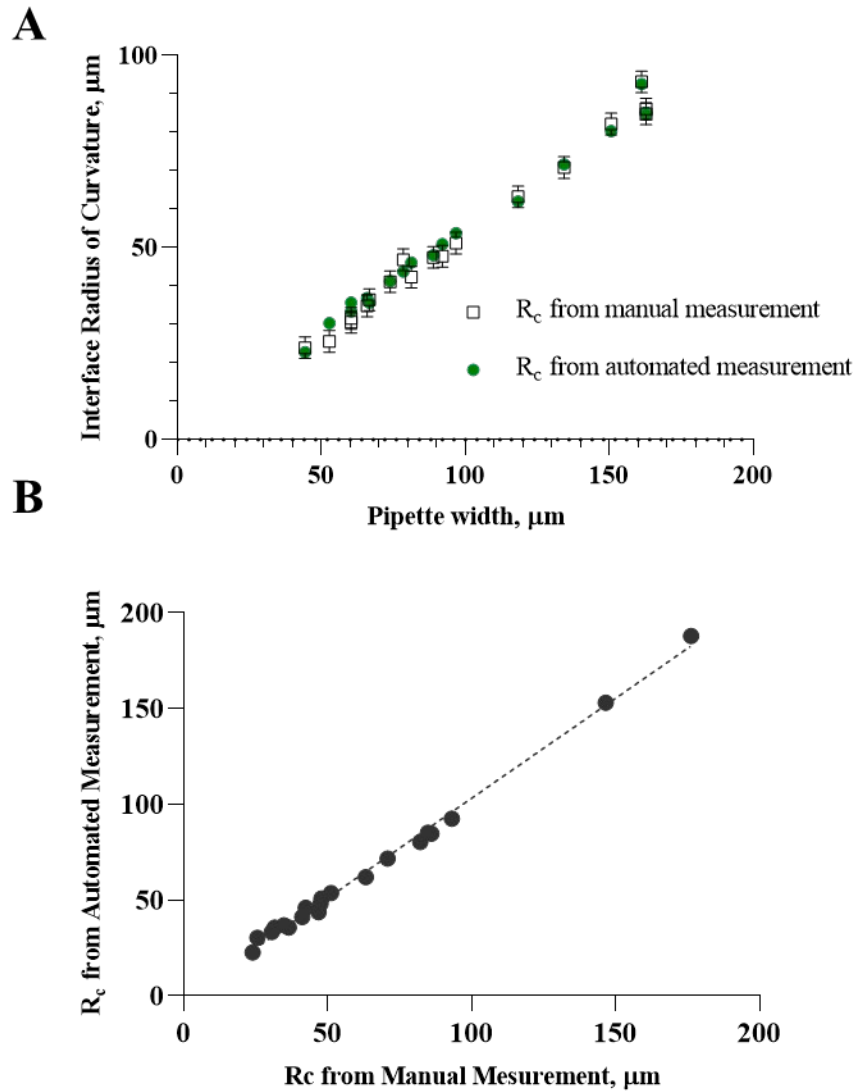
Figure 3-7 Comparison of manual (chord) and automated R_c measurement for a representative data set. (A) the two methods are plotted, R_c as a function of pipette width. The radius was measured three times for each image and the mean of these values taken. This was repeated for both methods. Error bars are ±1SD. (B) the R_c values are plotted against one another, giving an R^2 value of 0.9949.

To assess reproducibility, experiments were conducted on systems of known interfacial tension with the radius of curvature being measured using both the automated and chord methods to provide interfacial tension values. A

comparison is shown in Table 2, along with values obtained from literature using a range of other techniques. In each case the aqueous phase was MilliQ water.

Table 2 Comparison of interfacial tension measured by the automated and chord methods and a comparison to literature values. For both types of measurement, the presented value is the average of three repeats and the error is the standard error of these values.

Organic Phase	Literature Value, mNm^{-1}	Automated Method mNm^{-1}	Chord Method mNm^{-1}
Chloroform	30.8-32.8[153,154]	31 ± 1.2	32.8 ± 0.3
Dichloromethane	28.1-28.3[154]	28.3 ± 1.2	27.3 ± 2.4
Decanol	8.3-8.6[154]	8.4 ± 0.2	8.8 ± 0.2
Ethyl Acetate	6.4-7.73[154]	6.7 ± 0.1	6.4 ± 0.1
Hexane	51.1[154]	53 ± 0.3	54.3 ± 1.4
Octanol	8.5-9.1[154,155]	9.29 ± 0.05	8.3 ± 0.1
Pentanol	4.4-4.45[41,154]	4.5 ± 0.2	4.25 ± 0.1
Toluene	35.4-36.1[154,155]	35 ± 5	35.7 ± 1.0

3.2.6 Data Inflections from Interface Pinning

Since the uncertainty on individual measurements is reduced, it is possible to identify new behaviour in the systems during measurement. These appear as inflections or "kinks" in the plot of pressure versus $1/R_c$, as in Figure 3-8 A. They suggest temporary pinning of the interface which could result from impurities absorbing to/being cleared from the interface as the area changes. Inflections were characterised based on the pressure and pipette position where the deviation began and ended. However, comparison between data sets showed no correlation

based on material type or solute concentration. Additionally, there was no visible deformation in the images around this point.

After extensive comparison between images and data sets displaying these inflections, the most likely explanation is that they result from "pinning" due to incomplete wetting of the pipette walls during set up, this is supported by comparing the instances of inflection. Figure 3-8 B shows that they mostly occurred on the first repeat and were rare in the higher repeats. It was also noted that they were more prevalent in advancing measurements than receding ones. This observation led to a secondary improvement to the method: to avoid temporary pinning and jumping the interface should be passed up and down the pipette slowly before a fresh interface is formed and the measurements can begin.
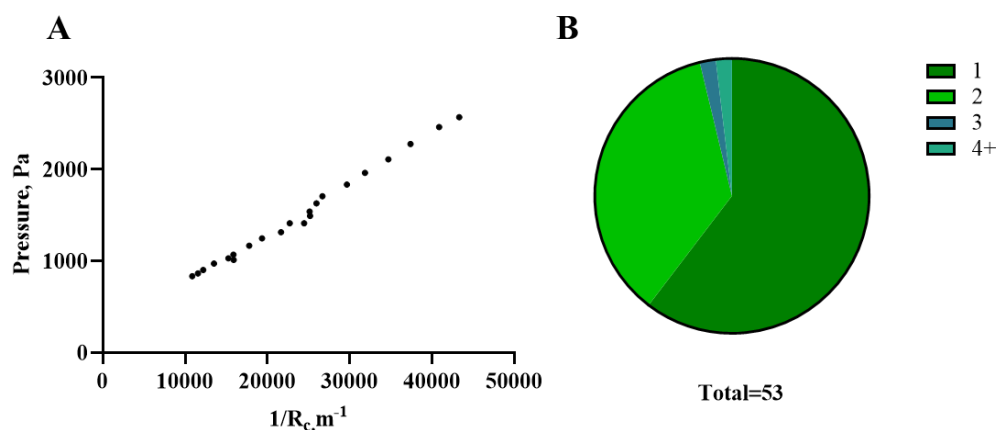
Figure 3-8 (A) Inflection can be seen in this data, caused by pinning of the interface. The overall measurement is unaffected as the points follow the same gradient on either side of the inflection. (B) Comparison of 53 data sets that showed inflections showed that 32 were the first repeat of the set, 19 were on the second repeat, 1 was the third and only 1 occurred at higher repeat runs

3.3 Dynamic Interfacial tension

Dynamic interfacial tension measurements are useful for understanding the behaviour of surface-active materials. For instance, how quickly surfactant molecules diffuse to the interface, enabling the diffusion in that medium to be measured, or to assess the behaviour of multi-surfactant systems.[12] Combining the system with a heated stage[10,11] would allow the effect of varied temperature to be observed over time, as offered by large scale methods – e.g. Wilhelmy Plate.

The process for obtaining these measurements is similar to that for the equilibrium interfacial tension. However, rather than incrementing pressure discretely and taking images of the interface at each equilibrium position, the excess pressure starts at zero, then almost instantaneously set to a chosen positive value and a video is taken of the interface moving to reach equilibrium.

Previous experiments have been limited by the number of frames it is reasonable to analyse. This can impact the ability to quantify interfacial tension change as changes are rapid in the early moments. Using automated analysis, the time limit is reduced to that of the frame rate, thereby increasing sensitivity and usability.

3.3.1 Specific Modifications in Data Processing

To utilise the automated analysis routine, both the ImageJ and MATLAB scripts are adjusted to process videos. For the pre-processing macro this necessitated changing the method used to threshold images; the Sauvola method within the local threshold function was chosen. The image analysis then proceeded as described above, treating each frame as the individual images were previously.

Interfacial tension values for static equilibrium were calculated using the Young-Laplace equation (Equation 1-4) and the gradient of *P vs 1/R*$_c$. However, since dynamic interfacial tension uses a single pressure rather than a series, *ΔP* needs to be calculated using the "zero-point" pressure. The 'zero-point' pressure can be defined as the pressure required to make the interface incident with the start of the tapered region of the micropipette. Since the transition between the two regions of the micropipette is not discrete, it is not possible to find this pressure visually. Instead, it is calculated from the intercept of the line of best fit of the *P vs 1/R* graph generated for an accompanying static equilibrium measurement. Following this, calculation of interfacial tension for each frame continues as for individual frames for equilibrium measurements.

3.3.2 Validation and Limitations

The result, shown for an example data set of decanol/water, is seen in Figure 3-9. The initial time delay related to the interface being in the parallel region. From then the interface decreases in radius as it moves along the micropipette. This is due to the decrease in interfacial tension as the decanol molecules rearrange at the interface.
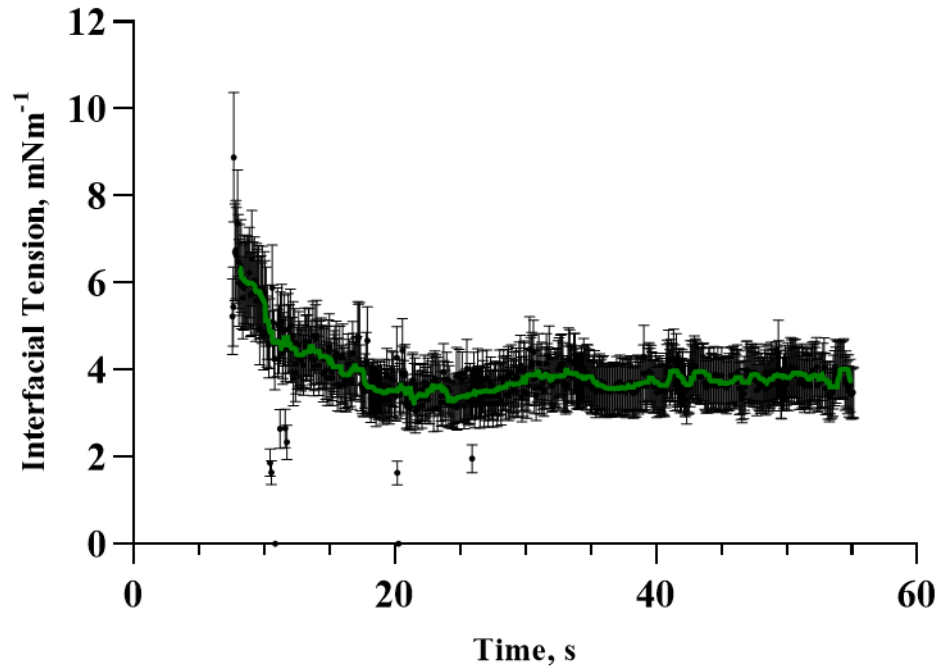
Figure 3-9 Dynamic interfacial tension measurement of the decanol/water interface as it approaches equilibrium. The interfacial tension calculated for individual frames is shown in black, with errors corresponding to the calculated error combining the limit of detection and pressure sensitivity. A rolling average, taken over one second is given in green.

The limiting factor in these measurements becomes the experimentalist: as the interface moves the micropipette itself must be moved and the focus adjusted manually. Slips where the interface becomes out of focus are responsible for the outlying points seen in Figure 3-9. To counteract the increased variation in measurement, a rolling average of the data is taken which better describes the behaviour. This is shown in green in Figure 3-9.
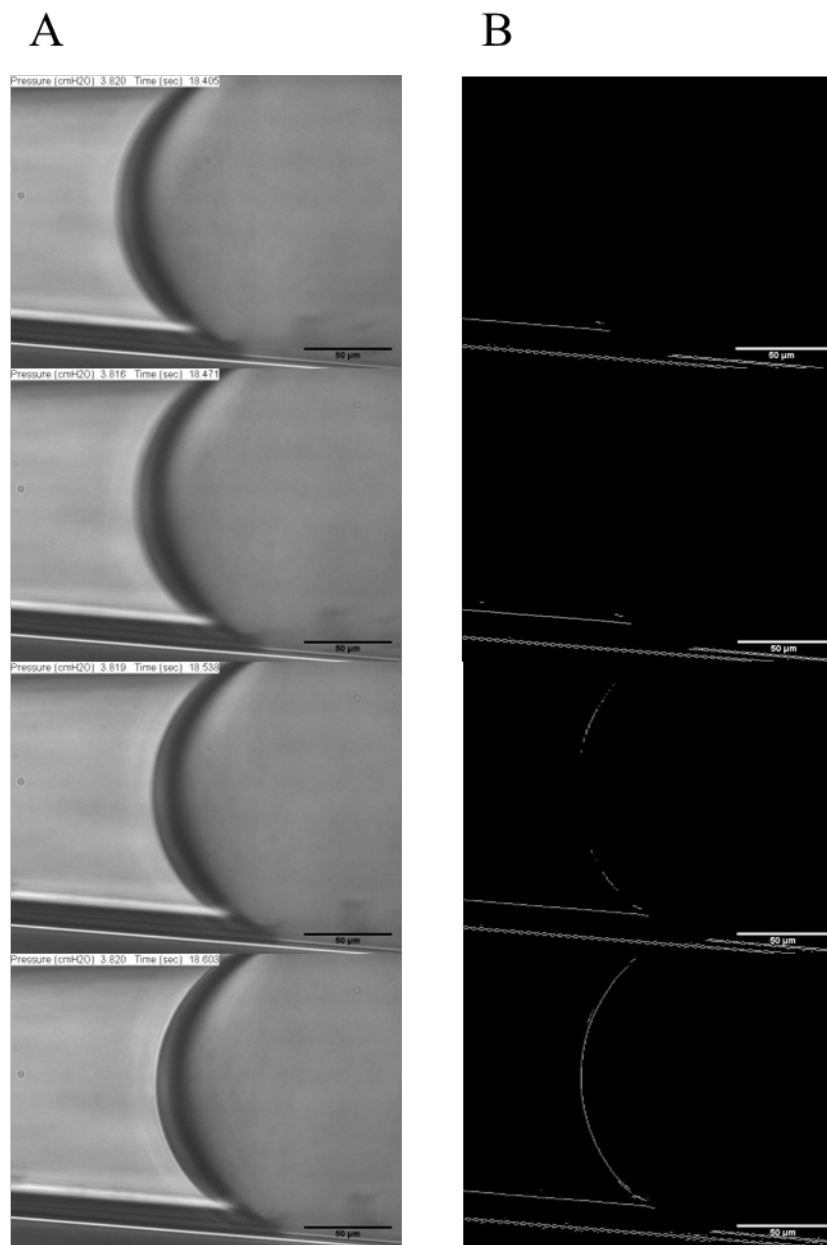
Figure 3-10 A series of frames of a dynamic interfacial tension comparing the raw image (A) to the processed image (B) when the interface is out of focus. Scale bars 50 µm.

Greater variation in R_c observed for the automated method than for the manually measured data. This is a result of the focus variation as the micropipette position is changed. Figure 3-10 shows how an out of focus interface often appears in both raw (A) and processed (B) images.

When an un-focused image is analysed manually, one can estimate the location of the interface. While this is not an accurate measurement it provides a close approximation. In comparison, the automated analysis of an un-focused image will give a false value. Using a high number of frames lowers the impact of this on the measurement and rolling average can be calculated to smooth out the anomalous points without losing detail, as seen in Figure 3-9.

3.4 Assessing Dissolution of Drops

3.4.1 Evaluation of Current Methodologies

Single particle studies obtain two parameters: drop radius and time. From this, the dissolution profile can be obtained, which in turn can be used to provide details about the system, such as the coefficient of diffusion, droplet lifetimes and the saturation of solute.[12,22] As was the case for interfacial tension measurements, available drop radius determination methods are all manual. The major disadvantage of this is the time required to analyse each frame. Even for a short dissolution there are more frames than can realistically be dealt with. For example, a three-minute dissolution video at 15 fps would yield 2700 frames to analyse.

The presently utilised methods available for determining the drop radius from a frame are shown in Figure 3-11, with Figure 3-11 A showing the raw frame as a reference. The first method, shown Figure 3-11 B is the circle overlay. This requires a circle be drawn over the droplet's circumference using image analysis software, for example, Image J. The properties of this circle are used to obtain the properties of the drop, e.g., diameter. While intuitive, there is great difficulty

in ensuring the drawn circle matches that of the drop at all points. Markers could be placed around the circumference and a circle fit with an appropriate tool; however, this would do little to overcome the limitations and would increase the time per measurement, reducing the number of frames that could be measured.
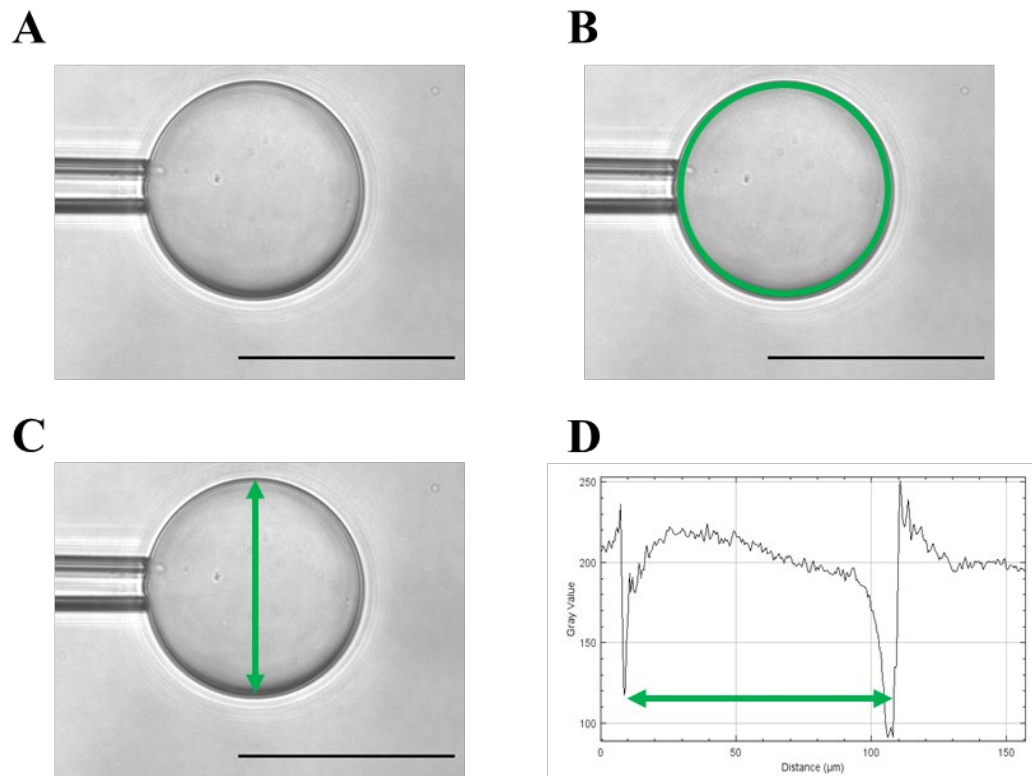
Figure 3-11 A comparison of current, manual methods for obtaining the radius of a drop. The raw frame (A) has (B) a circle drawn over the drop's circumference, in the circle overlay method or (C) the diameter across a drop directly measured. Alternatively (D) the pixel intensity of a line extended over the diameter of a drop is used to identify the edges of the drop. Scale bars 100 μm.

The simplest method, the drawn diameter, is shown in Figure 3-11 C, in which a line is drawn across the drop to give the diameter. In this case it is difficult to ensure the conditions of being on the edge of the drop and of passing through the centre. One way to eliminate the difficulty in marking the edge of the drop is to draw a line through the centre of the drop that extends past the drop edges and to

obtain the pixel intensities across that line, as in Figure 3-11. The sharp dips in intensity then identify the positions of the drop edge. This improves the accuracy of the measurement but increases the analysis time and still does not account for an off-centre error.

3.4.2 Development of Automated Analysis Routine

The routine developed to analyse droplet dissolution profiles utilises the clear contrast between the drop and the surrounding medium. The script, written in MATLAB, was developed to pre-process the image, determine the droplet radius, and then plot the dissolution profile. These measurements would then be exported and form the basis of additional characterisation.

On running the analysis script, a series of user interfaces prompt the user to enter the following information: number of frames, frame rate and the approximate minimum and maximum radii. The frame number and rate allow the time corresponding to each frame to be calculated. The minimum and maximum radii, in pixels, are used to aid the Hough Transform function in identifying the drop during the later stages. Each frame is treated as an individual image, with all processing and analysis steps carried out in a loop before moving onto the next frame.

To clear noise from the image, a median filter is applied with a 3x3 pixel kernel, giving the image in Figure 3-12 A. Following this, the image is binarized (using MATLAB function *imbinarize* from the Image Processing Toolbox with Otsu's threshold method based on variance minimisation) which produces the result shown in Figure 3-12. For the outer edge of the drop to be detected as the primary

circle, the drop must present as a solid object. To achieve this the image is inverted and the *imfill* function applied (Figure 3-12 C). This step also fills the pipette, further improving the robustness of the routine by removing any further artefacts that could lead to false positives.
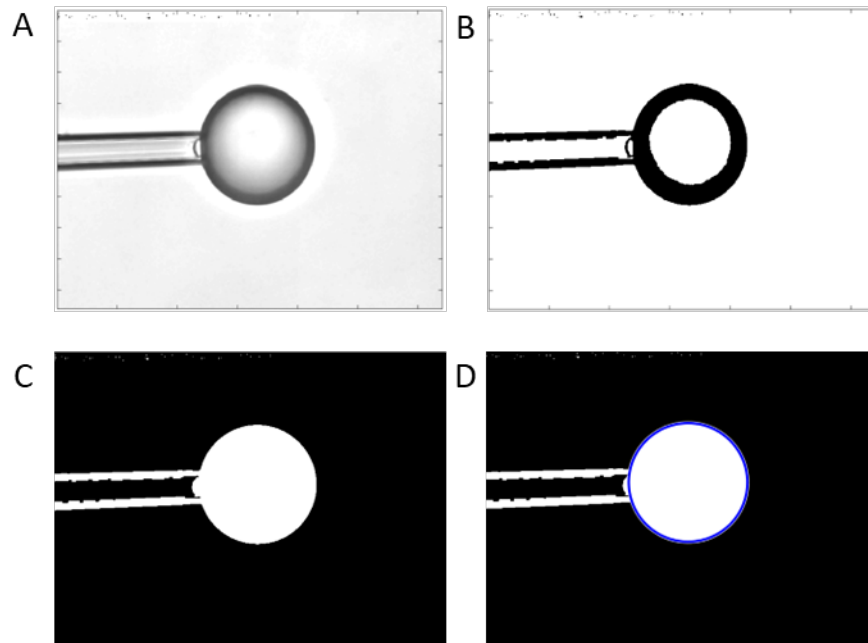
Figure 3-12 Image processing stages to measure the drop size. (A) the image is filtered and a threshold, (B) applied. The image is then inverted, and the drop filled (C) before the circle is identified (D) using Hough Transforms.

Detection of circles is carried out using an inbuilt function (*imfindcircles*, from the Image Processing Toolbox) which utilises the Hough Transform to identify circular objects, returning values corresponding to the objects' radii and centre coordinates. The sensitivity of this was set to 0.97 (function range 0 to 1) to ensure only the drop is identified. Setting the radius range to the minimum and maximum values estimated prior gives the function an approximate search range, further reducing the likelihood of false positives and improving processing speed. As a de-bugging precaution, if a radius is not found (as can occur in cases

where a drop falls or during formation where the drop is out of focus) the value is set to NaN (not a number) so as not to cause error in later processing steps. The option to display an overlay of the results of *imfindcircles* was used to produce the image in Figure 3-12 D. Radii were converted from pixels to micrometers using known calibration. The values were plotted against time, calculated from the frame rate.
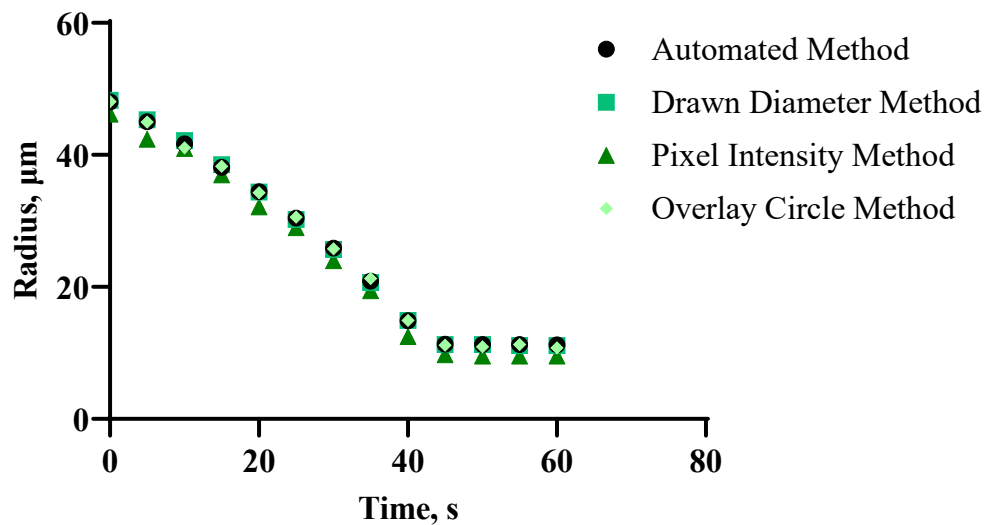
Figure 3-13 Comparison of drop radius obtained by the automated (black circle), drawn diameter (green square), pixel intensity (dark green triangle) and the overlay circle (light green diamond) methodologies.

A comparison of the four methods for finding drop radii is given in Figure 3-13. The two direct measurements (measuring a line drawn over the diameter and drawing a circle over the drop) agree with one another and with the results of the automated analysis. The radius value obtained from assessing the pixel intensity along a line across the drop is consistently lower than the alternative methods. A plot of the pixel intensity is shown in Figure 3-11 D for the example image considered. The diameter is calculated from this by identifying the positions of

the pixels with the lowest intensity. However, as seen in Figure 3-11, there is a range of pixels around the minimum at both sides of the drop. It is not appropriate to use the single lowest value, as this likely sits some distance from the edge of the drop. Instead, the first pixel (first valley) and last pixel (second valley) that are around the minimum value are assigned to the top and bottom edge of the drop respectively. Conversely, the alternative methods effectively take the first/last pixel not to be identified as background. This leads to the difference in estimation provided by the methods tested. The difference between results depends on the quality of the original image. The sharper the interface is, the higher the contrast, resulting in more accurate values.

Close agreement with alternative methods shows the automated analysis to be robust and reliable. Additionally, the comparison here was carried out on a small subset of frames due to the limitation introduced by manual measurement. In a general circumstance there is no limit to the number of frames that can be processed other than those set by the acquisition conditions.

3.5 Analysis of Internal Droplet Structure

It was observed that a series of smaller droplets, or sub-drops, appear inside the primary drop during dissolution for certain dispersed phase combinations. It was of interest to study this internal structure further. Internal structures can be split into two categories for analysis: those with clearly distinguished, relatively large droplets and those with densely packed small drops. The conditions producing these differing cases will be discussed in detail in Chapter 6; here the primary concern is developing methodologies for their analysis.

Currently there are no standard methods for this analysis. Most situations where drops of this size are present are concerned with bulk emulsions and not inside another drop, allowing alternative, analysis techniques for determining size to be employed; not based on microscopy (e.g., dynamic light scattering) Most cases of image-based analysis require clearly separated drops for analysis with processing techniques such as Hough Transforms or rely on manually measuring diameters.

Manually measuring the diameter by measuring a line drawn across a drop, as discussed in the previously (Section 3.4.1) and shown in Figure 3-12 C, is only practical in limited cases where the number and density of drops is low, and drops are large enough to get an accurate measurement. Additionally, the interest in the drops includes their change over time, requiring analysis to be carried out over many frames.

3.5.1 Low Density Internal Droplets

Processing frames using traditional image processing methods were mostly unsuccessful. This was due to the uneven background intensity across the drop, owing to its spherical nature, and droplet position depths resulting in some drops being brighter than the background and others being darker as can be seen in Figure 3-14 A and E. To overcome this, a more adaptive approach was needed. This led to the use of machine learning software, Ilastic. Ilastic is an open-source software designed for a range of object classification and segmentation approaches. This method uses *Pixel Classification*, a method of segmenting

images based on categorising pixels. Here the result is grayscale image with pixel intensities corresponding to the probability of that pixel being a part of a drop.

The first step in this process is to clear the background of the image so only the drop remains. This is carried out in ImageJ by drawing a circle over the drop (as in Figure 3-14 B) to create a selection and using the *clear outside* function. Frames from videos were saved as individual images

To process the images, Ilastic requires training on a small number of images to "learn" how droplet features are defined. Training was carried out on a small sample of images which covered the range of microstructures observed. Feature selection used *colour/intensity, edge,* and *texture*. Two categories were used: droplet and background. To train the program, lines were drawn around drops and across the background. An example training image is shown in Figure 3-14 B with yellow for drops and blue for background. Images are shaded in the corresponding colours as a live view of identified regions. The same selection is applied to the other training images and additional marks are added to improve the identification. The probability images are exported, such as Figure 3-14 C. Once optimised for the training images, batches of images can be assessed without further modification. Figure 3-14 E-G shows this for an example frame that was not part of the training set, note no training lines on Figure 3-14 F. Once probability images are obtained, they are further processed for analysis. ImageJ to enable identification and measurement of individual drops as in Figure 3-14 D and H.
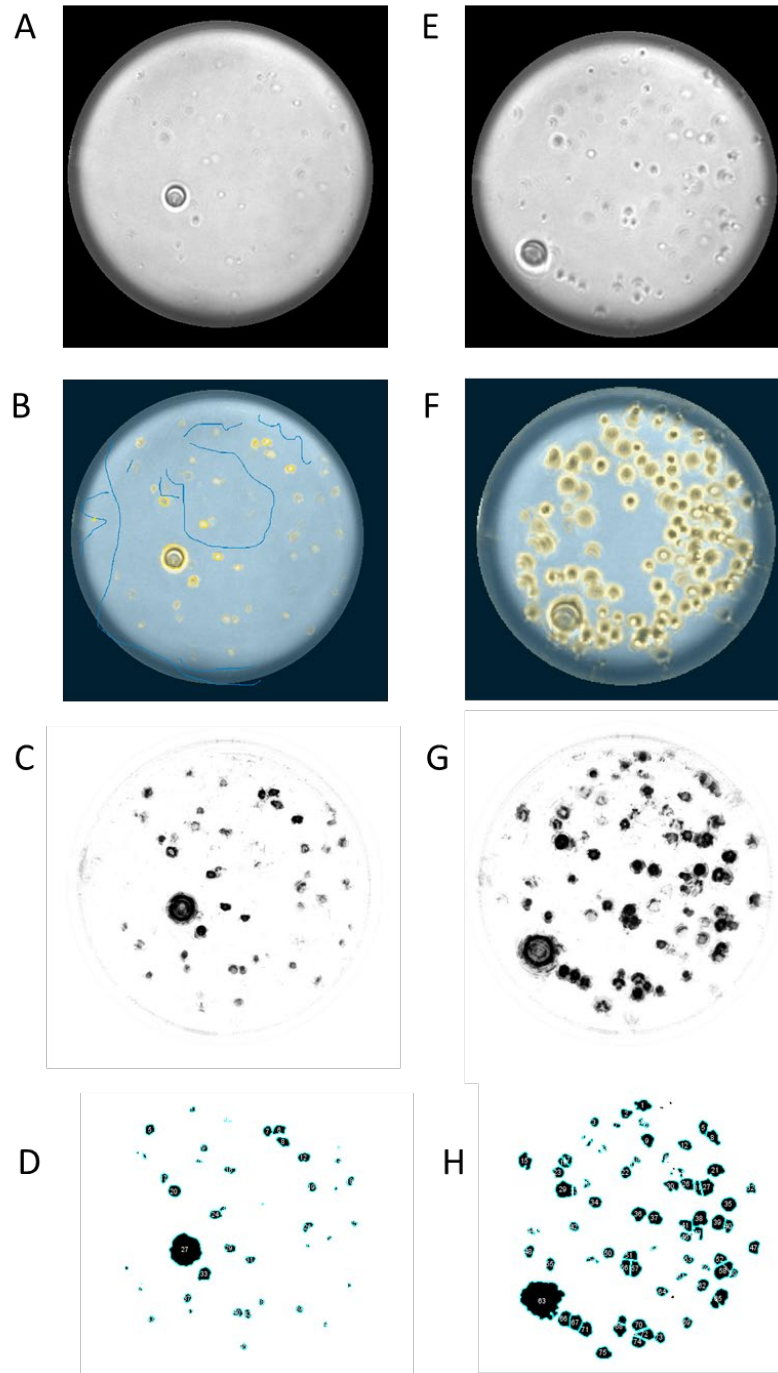
Figure 3-14 Droplet identification using Ilastic. (A-D) A training set is used to define how a drop is recognised. (A) Firstly, the background is cleared, leaving only the drop. (B) The regions (drop and background) are drawn to train the software which returns a greyscale image describing the probability of a pixel belonging to the drop region (C). (D) The image is taken for further processing to identify and analyse the drops. (E-H) The same stages are shown for a non-training set image. Identification is based on the learnt definitions.

Secondary processing stages are shown in detail in Figure 3-15 for raw drop image in A, and its generated probability image in B. Firstly, a median filter is applied with kernel size of 2x2 pixels to give the image seen in Figure 3-15 C before a threshold is applied to the image producing the image in Figure 3-15 D. Due to variations between images a constant value could not be applied, and the thresholding methods available were unable to produce consistent results across the different images. As such, thresholding was carried out manually for each image, setting a value which allowed the maximum information to be maintained whilst minimising saturation. Variation in intensity across the droplet added an additional degree of difficulty to achieving good thresholding. Drops in the centre of the original image were clearer than those at the edges, by nature of focusing across a spherical object, which translates into higher intensities in the probability images. The intensity of drops towards the edge is much lower and is often comparable to drop shadows and 'false-positives' in the centre of the image. As a result, a threshold that captured the edge droplets often caused saturation around central drops and conversely, attempts to retain defined centre droplets removed those with a lower intensity.

After thresholding the droplets needed to be separated for analysis. The *watershed* function was applied as in Figure 3-15 E. However, this was not sufficient in many cases to separate droplet clusters. Separation had to be completed manually by drawing lines between drops, using the original and probability images as guidance, resulting in the image seen in Figure 3-15 F. There was a trade-off between separating and eroding drops so changing size and

shape. A compromise was required at each stage of the processing and as such the drop numbers and their associated area are an approximation.

To identify and measure the drops, the *analyse particles* function was utilised. A minimum pixel area is set, and a circularity limit applied to avoid measuring noise. The function returns the number and cross-sectional area of the drops. An overlay of the identified objects was reviewed to check reliability and if necessary, processing steps were repeated, e.g., if clearer separation was required or detection criteria adjusted. Finally, this produced the results displayed in Figure 3-14 D and H. *Analyse particles* reports the area of each object, which was used to calculate the droplets' radii and in turn the size distribution of the droplets.
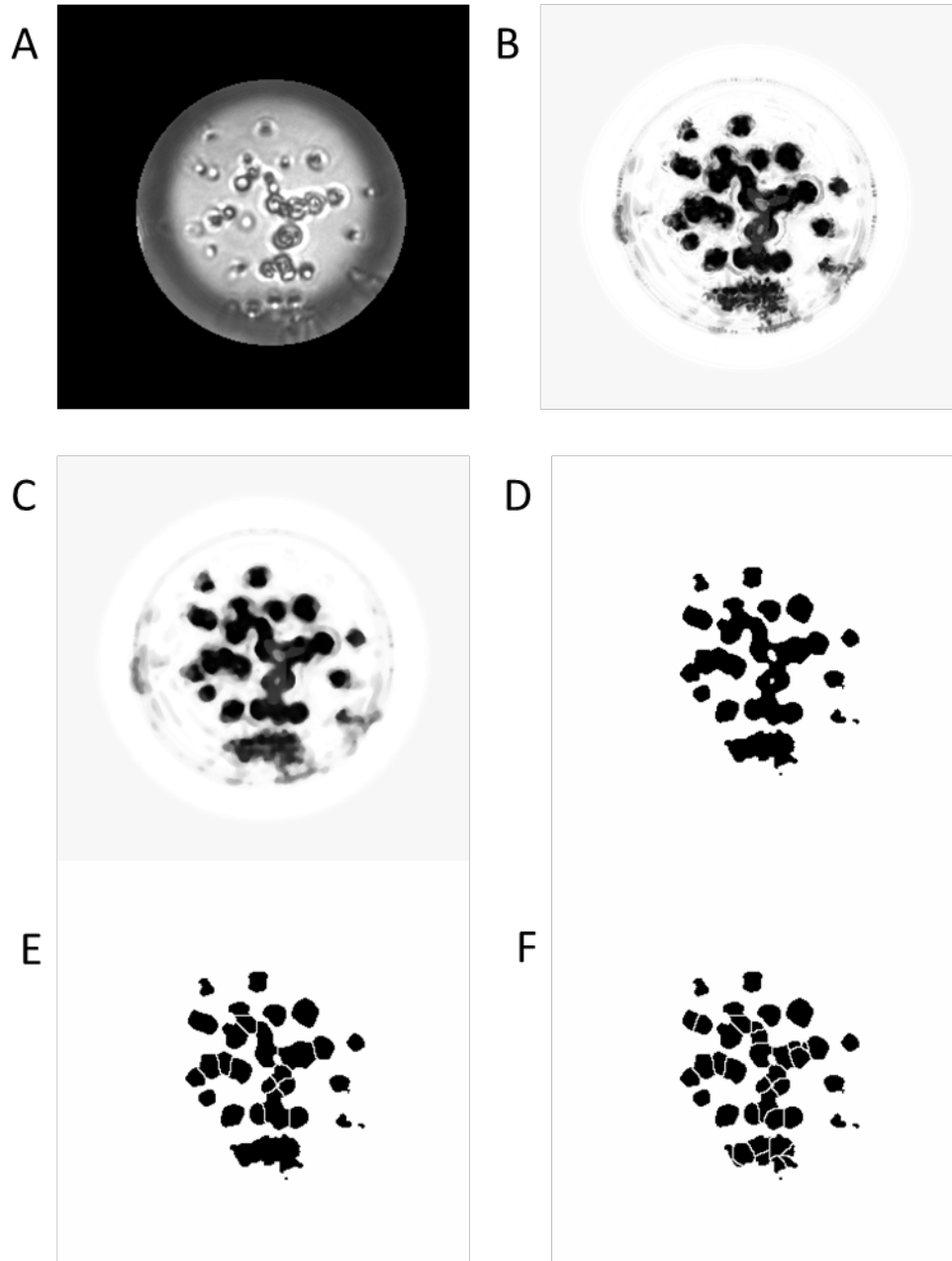
Figure 3-15 Stages of secondary processing. After the original image (A) is assessed to give the probability image (B) this image is filtered (C) and a threshold set (D). Watershed is applied to the image to separate droplets (E), and this is manually enhanced giving the image in (F) ready for droplet sizing.

3.5.2 High Density Surface Droplets

 The second classification of droplet structure is that in which drops are both too small and too densely packed to be able to individually distinguish. For this a quantitative measure of drop volume, etc. was not possible as it was for the previous class.

Experiments showed that these smaller drops, forming on the surface, are approximately of equal size and effectively block the view of any droplets of the type seen in Figure 3-14. Since the size is approximately constant, within the detectable limit, the change in their average pixel intensity across the drop can be related to the concentration of the drops – as their number/density increases the drop darkens.

Attempts were made to correlate the intensity change to the total volume; however, this was unsuccessful. This is because larger drops have dark edges and bright centres as in Figure 3-14, which produces an average intensity across the drop which is lighter than that for a very small drop, where no light centre can be seen. Therefore, the pixel intensity of a single large drop will be different to that of a series of small drops totalling the same volume.

Additionally, these drops cover the whole surface but only the effect of those on the front side can be observed. As a result, the quantitative information that can be gained from these images is limited. However, it is possible to use this information to compare formation of the structures over time and between similar drops.
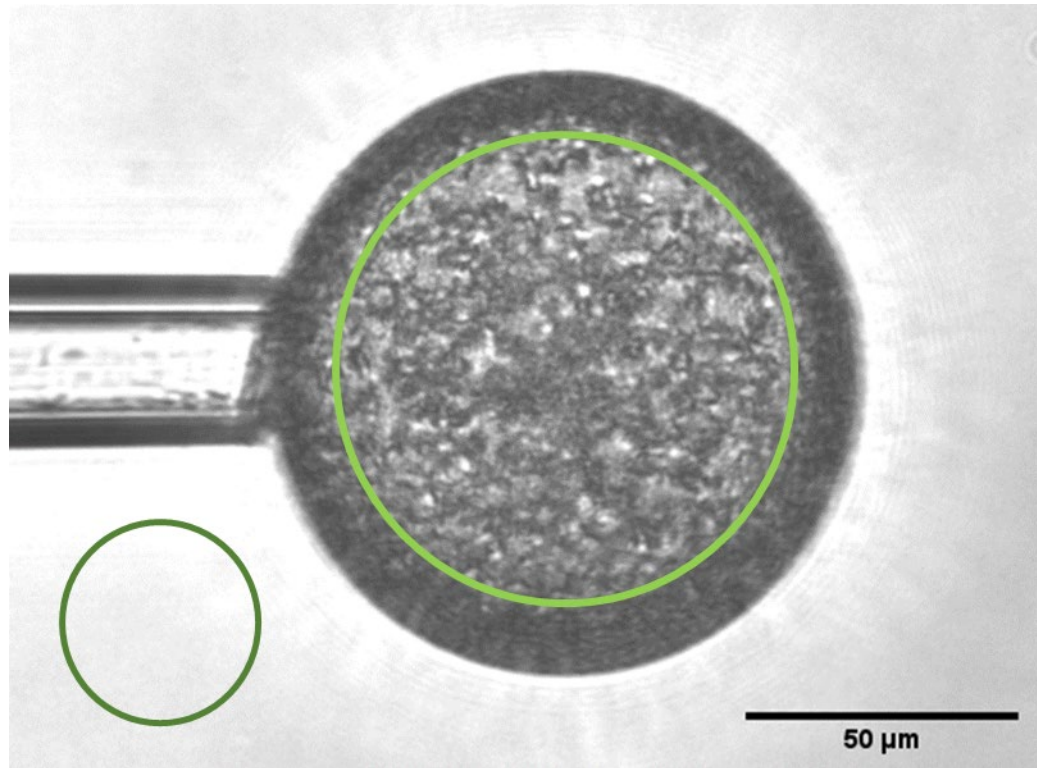
Figure 3-16 Method developed to assess the density of small drops using pixel intensity. The intensity of pixels on the drop surface (light green circle) is measured and normalised using background pixel intensity (dark green circle). Scale bar 50µm,

Each measurement requires two circles to be drawn on the image. The first is drawn over the drop itself as the pale green circle in Figure 3-16 shows. This should cover as much of the drop as possible whilst avoiding the dark edges. These would bias the average value as they are caused by the spherical nature of the drop and are not representative of the effects of the small droplets. The second is drawn over the background. The average pixel intensity of the regions defined by the circles is measured and the background intensity used to normalise the droplet intensity for comparison between drops and image sets.

3.6 Conclusion

This chapter describes the development of an alternative, fully automated method to analyse interfacial tension. It has been shown to improve reliability in radius measurements while maintaining the validity of the overall interfacial tension measurement. This in turn has enabled improvements to acquisition methods for both static equilibrium and dynamic interfacial tension measurements. The time taken to process a static equilibrium interfacial tension data set is reduced from greater than 30 minutes to as low as 5 minutes, increasing the practicality and usability of the method while maintaining or improving reliability. In such, the aim of developing the interfacial tension analysis routines has been met.

Automation of the radius measurements for single particle studies allows measurements of increased volumes of data, enabling more detailed analysis of droplet behaviour. In turn, new methods developed to analyse the internal microstructures of the drops successfully allow the estimation of drop numbers and sizes. However, these estimations are limited by the size and density of the drops. Additionally, an alternative method utilised the relationship between drop density and pixel intensity to provide a qualitative comparison for systems where separation of drops was not possible. The developed methods met the required aims for this work but would need improvement to be more widely used.

Chapter 4: Micropipette Manipulation Studies to Understand the Properties Governing the Formation of PDLLA Microparticles

Chapter 4 – Micropipette Manipulation Studies to Understand the Properties Governing the Formation of PDLLA Microparticles

4.1 Introduction

Biodegradable microparticles, whether for drug delivery or tissue engineering applications, are most commonly made from PLA or its derivatives.[63,65,105,156] Whilst there have been numerous studies concerning the behaviour and use of this material in microparticles, such as the impact of molecular weight[66,128] and ratio of D and L components,[157] these studies have been concerned with the final particle properties, not directly with particle formation. Furthermore, these studies were based on bulk particle production, usually via emulsion solvent evaporation, in which additional factors are active in determining particle formation and final properties, e.g., stirring rate, phase ratios.[158]

Similarly, PVA is the default stabiliser for microparticle systems, owing to its strong emulsifying properties, biocompatibility and improved media wetting capabilities compared to the core polymers.[75] However, as is often the case with surfactant studies, the impact of PVA on interfacial tension has mostly been assessed for the water/air interface, rather than mimicking emulsions for particle production.[36]

The two stages of particle production through emulsion solvent evaporation, and related methods, are the successful emulsification of the dispersed phase in the continuous, followed by the removal of solvent from the drops.[104] Since the first

stage generates a large surface area between two immiscible fluids, it is clear that there is a need for assessing the interfacial tension for the material combinations in use. Additionally, since the interfacial tension on microscale droplets is known to differ from that of the macroscale interface, it is imperative that this assessment is conducted on the appropriate scale.[44,47] Surfactant concentration should be optimised such that the maximum reduction in interfacial tension is achieved, using the minimum amount of material. This requires identifying the effective CMC.[32] Determining this concentration and mapping out the interfacial tension/PVA relationship for PDLLA in DCM and ethyl acetate is the first aim of this section of work.

When the interfacial tension is very low, the appearance of drops around an interface can result due to spontaneous emulsification. On a larger scale, this can often be seen as a small layer at the interface. The drops may appear in one or both phases depending on the surfactant and relative miscibility of the different phases, and only occurs as the interfacial tension reaches a critical level.[35]

The formation of spontaneous emulsions is defined by a lack of mixing which would otherwise be used to form the dispersion of one phase in another. In the micropipette, minimal mixing occurs. Therefore, drops that appear around the interface are most likely a form of spontaneous emulsion. By observing the presence of such drops, insights into critical concentrations of the system can be gained.

The second stage of particle formation is the solvent removal. Understanding the removal of solvent from the drops to form particles is important for both simple

and complex particles, as the solvent removal determines not only phase separation and encapsulation, but fundamentally the transition into solid particles without aggregation and deformation.[103]

Studies conducted in bulk particle systems require constant agitation to prevent aggregation during this phase.[104] As such, material effects cannot be separated from processing effects. Developing an understanding of the processes and transitions individual drops go through whilst held stationary allows the separation of properties, which in turn permits a better understanding of processing parameters when returning to bulk particle investigations.

Solvent removal is a diffusion controlled process, as such the key parameter in quantifying the dissolution of solvent from the drop to the continuous phase is the diffusion coefficient.[19] If the saturation concentration of the solvent in the continuous phase is known, along with the starting concentration, then single particle studies using micropipette manipulation methods allow almost direct measurement of the diffusion coefficient, D. By employing the EP model, as described in Chapter 1, Section 1.3.3, the aim is to find the diffusion coefficient of DCM and ethyl acetate in the presence of the core polymer and/or surfactant.

For a solvent molecule to be removed from the droplet to the surface of the system for evaporation, it must move through the droplet, across the interface and through the continuous phase. The first part of this is assumed to be rapid enough that the drop is always homogenously mixed. The measurement of diffusion considered is that from the interface and through the continuous phase. If the solvent molecule meets extra resistance, for example due to high viscosity

continuous phase or resistance at the interface, diffusion will differ from that of a pure solvent system.[35]

In this chapter, a series of studies to understand the impact of both PDLLA and PVA on interfacial properties and solvent removal are presented. The polymers are treated as additives to pure solvent/water systems in order to identify and isolate their effects. Both DCM and ethyl acetate are used as solvents, as the two most commonly used organic solvents for microparticles of this composition.

Static equilibrium interfacial tension measurements were performed to assess the impact of PVA in conjunction with different solvents and PDLLA concentrations. Part of this aim included obtaining an empirical relationship that could be used to aid future particle formulations.

Furthermore, dissolution behaviour was assessed using single particles studies with the aim of comparing the resulting profiles to the EP model for pure solvent systems, and to the modified, activity-based EP model, Equation 1-16, to identify the impact of additives.

4.2 Methods and Materials

The methods used in this chapter were as discussed in Chapters 2 and 3, Sections 2.2.1 to 2.2.6 and 3.2 and 3.4 for acquisition and analysis, respectively. Additional methods used are described below.

Poly($_{D,L}$-lactic acid), (PDLLA), poly(vinyl acetate-alcohol), (PVA), dichloromethane, (DCM) and ethyl acetate were used as obtained from the sources given in Chapter 2, Section 2.1.

4.2.1 Measuring the Formation of Spontaneous Emulsions

To utilise the appearance of spontaneous emulsion drops in defining and understanding a critical interfacial tension for the system, an analysis routine was developed as follows:

• The drops, seen in Figure 4-1, are present at the interface, therefore images acquired for interfacial tension measurements could be used to obtain the information required.

• A region of interest (ROI) around the interface was defined by the distance between the centre front of interface and the perpendicular line marking the point where the interface meets the glass wall – blue dashed line in Figure 4-1. The same distance (blue arrows) was extended in front of the interface giving the area outlined in dark blue in Figure 4-1. This ROI was chosen since the drops concentrate at the interface for both phases. Drops are characteristic of the phase they are in so are easily distinguished. In Figure 4-1, the drops are all in the continuous phase, those appearing to be past the interface are actually on the back of the spherical cap.

• Using ImageJ, drops in the ROI were manually counted, and the diameter measured – this was approximate as not all drops were in focus by nature of their positions – focus was generally maintained on the central plane with the front of the interface.
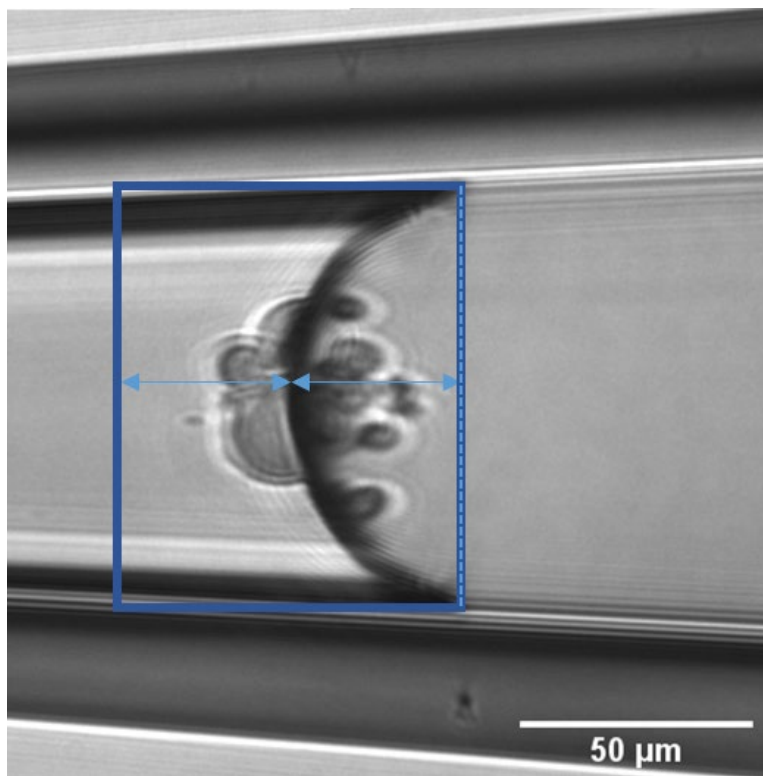
Figure 4-1 Assessment of spontaneous emulsion formation at the interface within the micropipette. Drops are counted within the region that extends the same distance forward as back. Scale bar 50μm.

4.2.2 Stability Assessment

A bench top assessment of stability was carried out by pipetting 0.5 mL DCM into 2 mL vials containing 0.5 mL of PVA solution. The vials were then agitated for 30 seconds and left to settle. Separation of the phases was timed from the end of the agitation to when the two phases had clearly separated, as assessed by eye.

4.2.3 Determining Diffusion Coefficients

The Epstein Plesset (EP) model, defined in Equation 1-15, can be used to calculate the diffusion coefficient for solvents undergoing transfer. Since drops

reach steady state within the first moments of creation, the transient term,

$\frac{1}{\sqrt{\pi D t}}$, can be ignored. This reduces Equation 1-15 to

$$\frac{dR}{dt} = \frac{Dc_s(1-f)}{\rho}\frac{1}{R}$$

where all terms are as defined previously, with $f = {c_0}/{c_s}$. This can now easily

be solved for R, such that

$$R = \sqrt{R_0{}^2 - \frac{2D(1-f)c_s}{\rho}t}$$

Where R_0 is the drop radius at time, $t = 0$. R, R_0 and t can be obtained from

measurements of the drop dissolution, as described in Chapter 3, Section 3.4.2,

while the density, ρ, saturation concentration, c_s, and initial saturation, c_0, are

known.

By squaring Equation 4-2, a linear relationship with time is created.

$$R_0{}^2 - R^2 = \frac{2Dc_s}{\rho}t$$

In turn this allows the coefficient of diffusion, D, to be calculated from the

gradient of a $R_0{}^2 - R^2$ vs t plot.

4.2.4 Fitting of Dissolution Profiles

To compare the measured dissolution profile to the EP model, the radius at each given time point was calculated using the known values of density and saturation concentration, the measured time and initial radius and the calculated diffusion coefficient.

In order to employ the activity-based model (Equation 1-16) to the data, $f_i(t)$, describing how the saturation fraction of solvent at the interface (in the continuous phase) changes with time, needed to be calculated.[22] This was done by performing dissolutions into a water filled chamber partially pre-saturated with the solvent of interest (DCM or ethyl acetate).

Dissolution was carried out as usual until the drops reached a steady size. Figure 4-2 A shows the profiles for a series of drops in a water chamber with DCM at 0.6 of the saturation concentration. The concentration of the drop was calculated using the final size and the initial, "stock" concentration, as shown in Figure 4-2 B. The final concentration of each drop was obtained by taking an average of the corresponding plateau region.

The equilibrium drop concentration for that saturation condition was found from averaging the final drop concentrations, and the error obtained from the standard deviation on this average. These values were plotted against the saturation fraction, Figure 4-2 C. This equilibrium concentration equals the concentration at which the saturation at the interface is equal to that in the surrounding medium; so there is no driving force for further dissolution.

Using this knowledge – that drops reach an equilibrium concentration when the saturation is matched – the inverse situation can be described: the saturation can be found for any given drop concentration. The *Curvefit* tool (MATLAB) was used to fit saturation fraction vs. equilibrium concentration to a polynomial. In this case the equations found were:

$$f_i(t) = -0.0134c(t) + 1.296$$

<div align="right">*Equation 4-4*</div>

for DCM, and

$$f_i(t) = -0.01144c(t) + 1.237$$

<div align="right">*Equation 4-5*</div>

for ethyl acetate.

where $c(t)$ is the PDLLA concentration in the drop and any given time, t. These equations were then used in the activity-based model to describe the dissolution of the respective solvents. The scripts used for dissolution analysis, including calculation of the diffusion coefficient, EP model, radius calculations from the activity based model and simplex fitting can be found in Appendix 2.
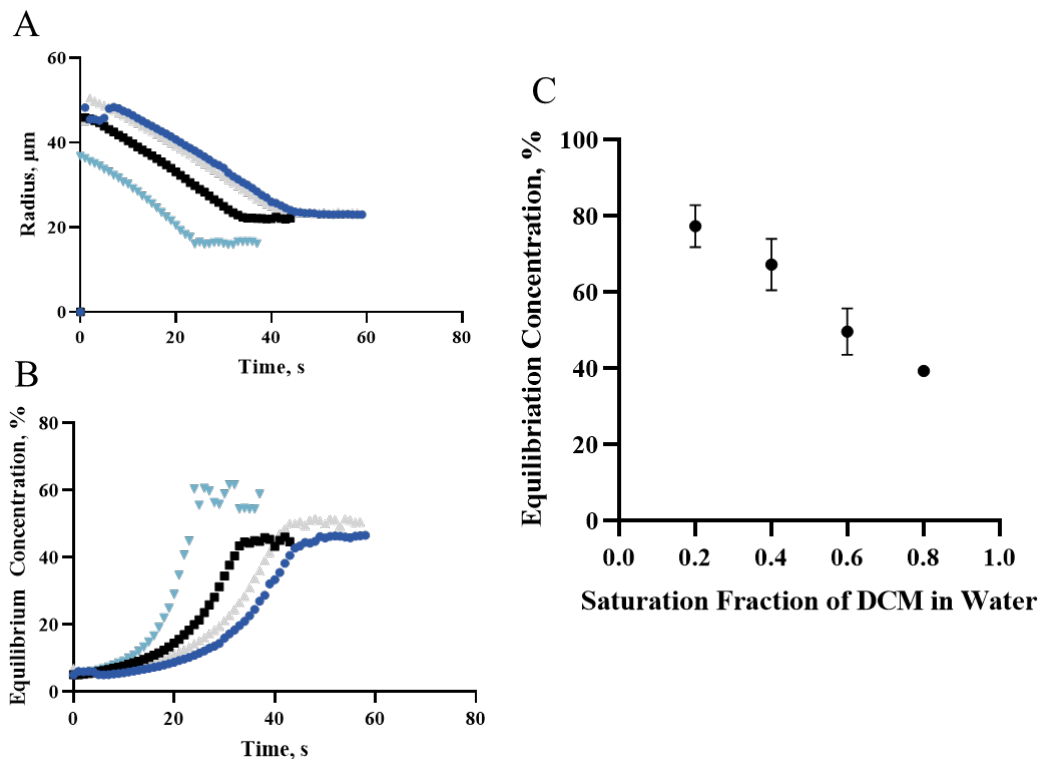
Figure 4-2 (A) Dissolution profile for a series of 5% (w/v) PDLLA (DCM) drops into water at 0.6 saturation of DCM. (B) PDLLA concentration when equilibrium with the surrounding is reached. (C) Drop equilibrium concentrations as a function of DCM saturation fraction in the continuous phase. For 0.2, 0.4 and 0.6 saturation fractions, n-4 drops. A single drop was used for 0.8. Error bars ±1SD.

4.3 Results and Discussion

4.3.1 Interface Characterisation

4.3.1.1 Minimising Interfacial Tension

Minimisation of IFT is crucial for the formation of stable emulsions – the precursor stage to particle formation. Here, PDLLA and PVA were treated as additives to a base system of water/DCM and water/ethyl acetate. The base systems were found to have interfacial tensions of 26.7 ± 0.9 mN m^{-1} and 6.4 ± 0.15 mN m^{-1}, respectively, as confirmed by literature.[154] Treating the systems in

this manner allowed the effects of the polymer and surfactant to be understood individually and as a combination.

The results of increasing the concentration of PDLLA in the solvents in shown in Figure 4-3 A. The was no significant change in interfacial tension with increased polymer concentration in either solvent system, p>0.9999 for ethyl acetate and 0.2236 to >0.9999 for DCM.

Conversely, the addition of PVA to the water phase showed a decrease in interfacial tension with increasing concentration for both solvent systems. This is shown for comparison in Figure 4-3 B, where an organic phase of 5% PDLLA in DCM and ethyl acetate, respectively, were used. For the ethyl acetate system comparison to the surfactant free system showed all concentrations above 0.75% had p-values below 0.007. In DCM, comparison between 0% PVA and any concentration of PVA gave a p-value below 0.0001. This decrease in tension was expected for both systems, as PVA is a known to be an efficient surfactant.[36]

The DCM/water system has a higher interfacial tension than ethyl acetate/water throughout the addition of either PDLLA or PVA, which is a result of the higher IFT of the base system. By utilising a base system with a lower IFT, improved stability is achieved without the need for high concentrations of surfactant. This is useful for some systems, for example when the surface chemistry of the particle is key to its application the amount of PVA presenting at the surface will need to be minimised.[89]
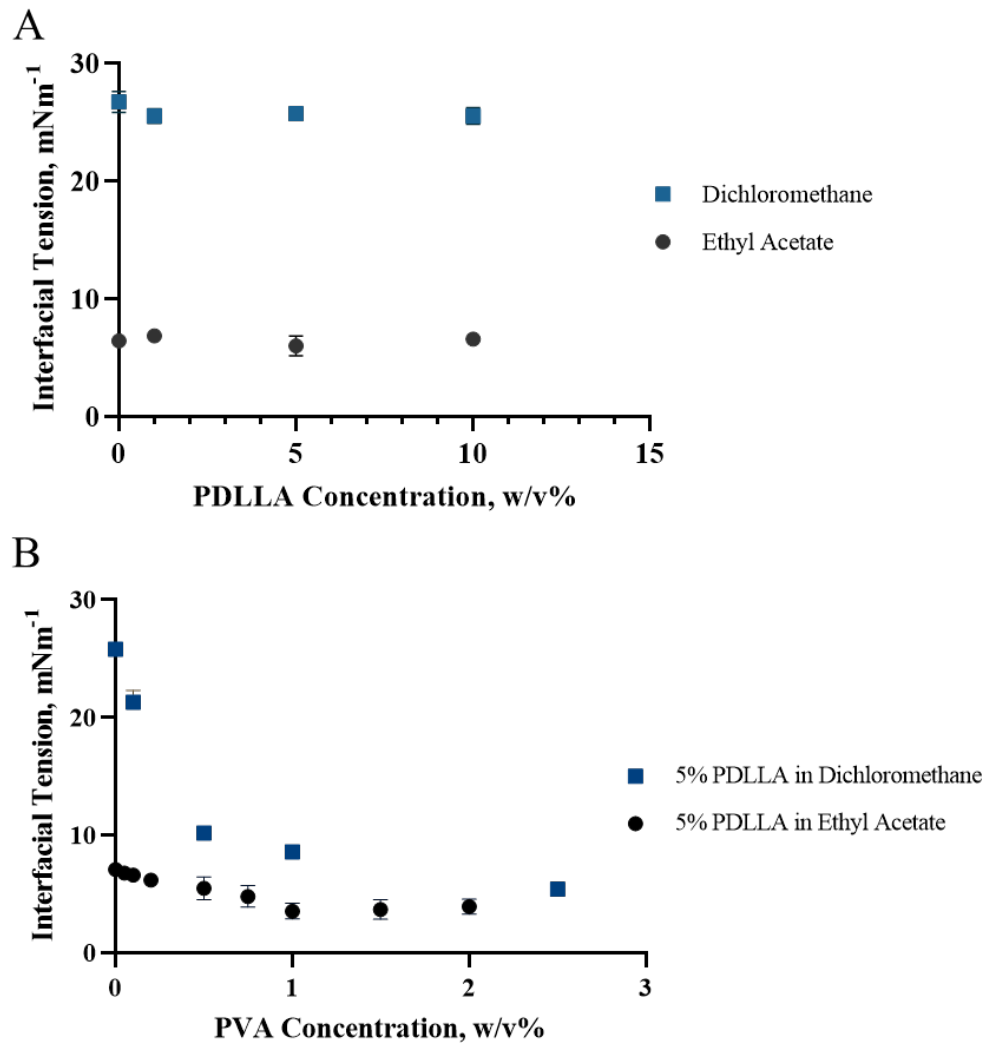
Figure 4-3 Interfacial tension for (A) increasing PDLLA concentration in DCM and ethyl acetate and (B) Increasing PVA concentration in the aqueous phase for dispersed phases of 5% PDLLA in DCM and ethyl acetate. In all cases each point is the average of 3 repeat measurements formed of 10-20 pressure points/images. Error bars are ±1SD.

In both systems the IFT tends towards a plateau. This suggests a point where the concentration is sufficient to saturate the interface and would be synonymous with approaching the CMC. Similar behaviour of surface tension for increasing PVA has been shown, with the plateau also being around 1% (w/v).[36]

At concentrations around 2% (w/v) PVA, the IFT of the two systems is comparable. At this point the PVA has minimised IFT as much as possible, covering the interface and screening the effect of the solvent.

A detailed investigation into the combined effects of PDLLA and PVA in a DCM/water system are shown in Figure 4-4. Figure 4-4 A presents the effect of increasing the PVA concentration for fixed PDLLA concentrations, whilst Figure 4-4 B shows the IFT of increased PDLLA for each PVA concentration assessed. Considering Figure 4-4 A, there is negligible effect from the addition of PDLLA, with all datasets following the same trend; the same as seen in Figure 4-3 B previously. All exhibit a sharp decrease in IFT with the addition of a small (<1% w/v) amount of PVA, and then tend to approximately 5 mN m^{-1} above 2% (w/v) PVA.

A

B
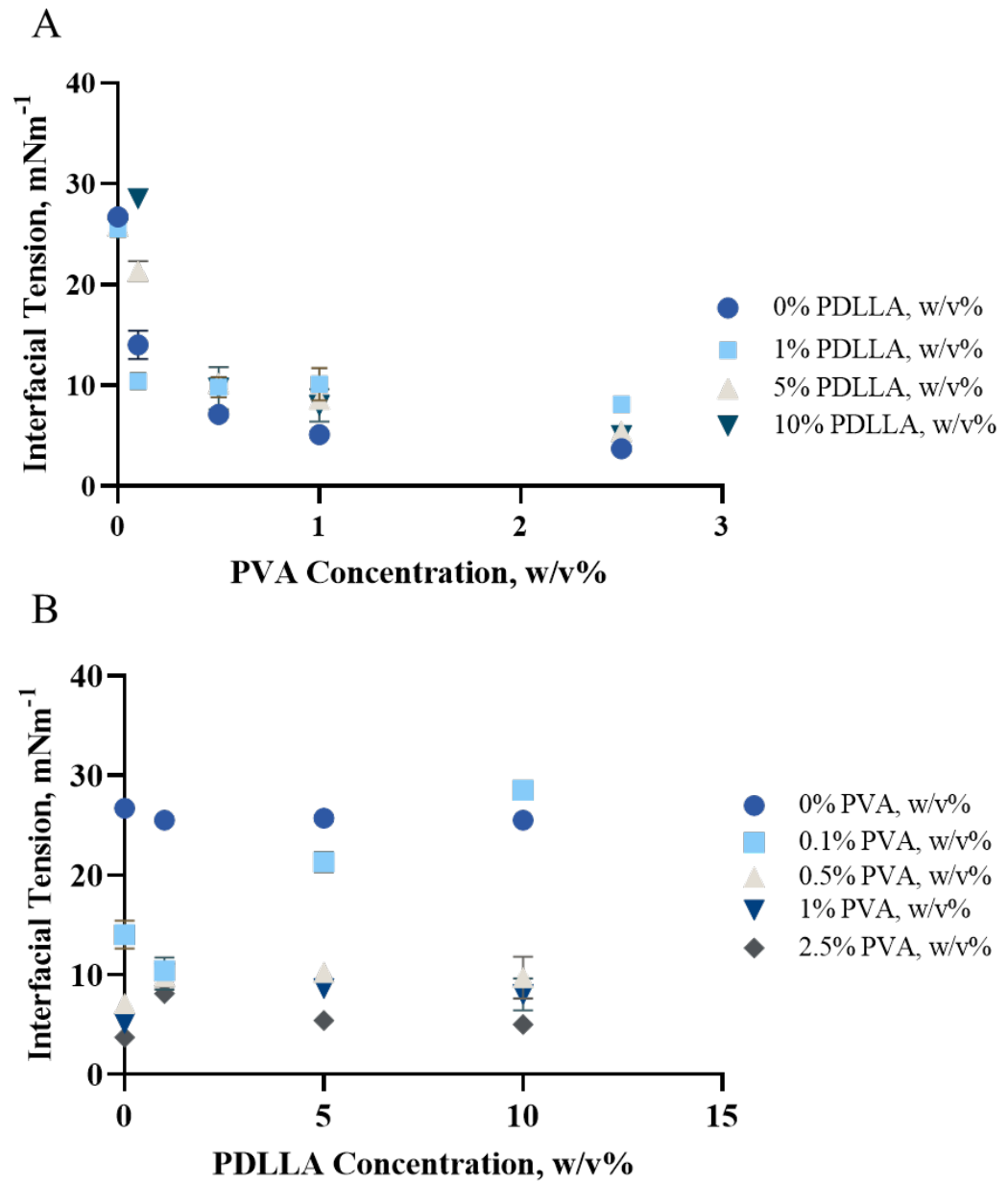
Figure 4-4 Interfacial Tension for combined PVA and PDLLA concentrations. Displayed for (A) constant PDLLA concentration and (B) constant PVA concentration. In all cases each point is the average of 3 repeat measurements formed of 10-20 pressure points/images. Error bars are ±1SD.

The lack of effect of PDLLA concentrations on the IFT of the system is most clearly demonstrated in Figure 4-4 B for 0% PVA, as IFT is approximately constant. For concentrations of 0.5% and 1% (w/v) PVA there is a small increase in IFT with the addition of PDLLA, but it remains constant as the concentration increases further. 2.5% (w/v) PVA in the continuous phase shares this increased IFT for 1% (w/v) PDLLA, however it proceeds to return to the value seen for 0% as further PDLLA is added. 0.1% (w/v) PVA shows a clear and significant increase in IFT as PDLLA concentration is increased. This does not match the profile expected based on the other concentrations.

A possible explanation for this deviation is that the increased PDLLA does slightly increase IFT, but it is only noticeable at low PVA concentrations. Higher levels of PVA are counteract the effects of PDLLA. However, since it is not seen in PDLLA only systems (0% PVA), it is more likely to be an anomaly. Another potential explanation is the presence of a surface-active contaminant whose effect is lessened as diluted – as the preparation method is to start at 5% (w/v) and dilute. However, if this were the case, this increase in apparent IFT would be expected to be seen in all cases as the same stock solution was used throughout. Looking from the point of view shown by Figure 4-4 A, 0.1% (w/v) PVA has a lot of spread. Further repeats, using new samples, would be needed to confirm if the behaviour is authentic or an alternate effect. Systems with low concentrations of surfactants are often more susceptible to variation as impurities compete at similar concentrations.

Interfacial tension falls smoothly with increased concentration of a non-ionic surfactant. A fit of such data, produced empirically, can be used to predict interfacial tension or for surface excess concentrations. The requirement for that application is a readily differentiable equation, however, beyond that there are few constraints. Exponential decay is a common starting point for describing such tension-concentration relationships.[32] The response to PVA concentration is an exponential decay, whilst the effect of PDLLA is approximately linear. As such an equation is formed of exponential dependence of PVA concentration, linear PDLLA concentration and a coupled parameter:

$$\gamma = Ae^{-Bc_{PVA}} + c_{PDLLA}e^{-Cc_{PVA}} + Dc_{PDLLA} + F$$

<div align="right">Equation 4-6</div>

where A to F are numerical constants defined by the fit. The fitting of an individual concentration of PDLLA for increasing PVA concentrations showed the best fit for IFT response to PVA concentration, c, is a double exponential decay. The fit acquired was

$$\gamma = 16.67e^{-3819c} + 9.447e^{-0.215c}$$

<div align="right">Equation 4-7</div>

The result of this fit, shown in Figure 4-5, has an R^2 value of $R^2 = 0.9951$, giving confidence in this form.
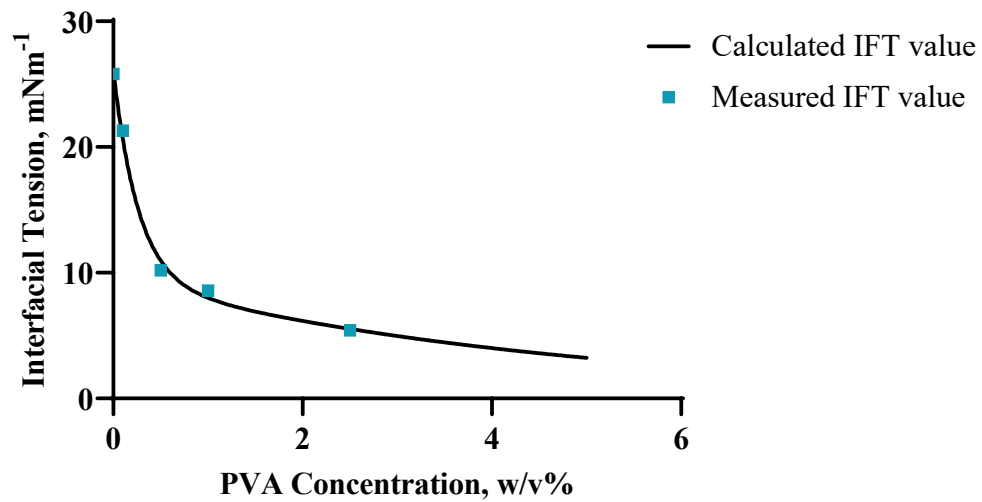
Figure 4-5 Interfacial tension values for 5% (w/v) PDLLA (DCM) with increased concentrations of PVA in water. Data (blue squares) were fitted with a double exponential, yielding Equation 4-6 (black line) with $R^2=0.9951$

By fitting the IFT values, it was possible to create an empirical equation describing the relationship between IFT and the concentrations of both PDLLA and PVA.

Applying this to the data shown in Figure 4-4 gives an empirical relationship of to both components:

$$\gamma = 19.23e^{-3.552c_{PVA}} + c_{PDLLA}e^{-0.2507c_{PVA}} - 0.4324c_{PDLLA} + 4.328$$

with an R^2 value of $R^2 = 0.93$. The fitting was carried out without 1% (w/v) PDLLA due to its anomalous response to PVA addition.

This empirical equation allows the identification of the concentrations needed to fulfil specific system requirements. For example, if a particle system required an

untested concentration of PDLLA, the amount of PVA required to achieve stable particles, could be calculated without extensive experimental procedures. This is especially beneficial when using scaled-up particle production methods which are material and time intensive. This approach could be applied to less well characterised surfactants, where it could have great impact on understanding.

4.3.1.2 Spontaneous Emulsification and the Indication of a Stability Limit

Images across the full range of PDLLA and PVA concentrations, in DCM and water, respectively, were analysed to identify those with drops present at the interface. The number of drops present in the area surrounding the interface, as defined in Section 4.2.1, was compared to different system properties. Figure 4-6 A shows that when plotted against the interfacial tension of the system they appeared in, a clear cut-off point was observed. Drops were unlikely to form in systems with interfacial tensions above approximately 11.1 mN m^{-1}. The number of drops per μm^2 does not increase with decreasing interfacial tension, rather drops are either present or are not.

By comparing the "cut-off" IFT value to the concentration of PVA, as in Figure 4-6 B, the assessment of spontaneous emulsion drops translates into a useful tool for dictating surfactant levels to be used in particle systems. IFT values below the "cut-off" would be expected to stabilise a system, whilst those above it would not thus giving a minimum required PVA concentration.
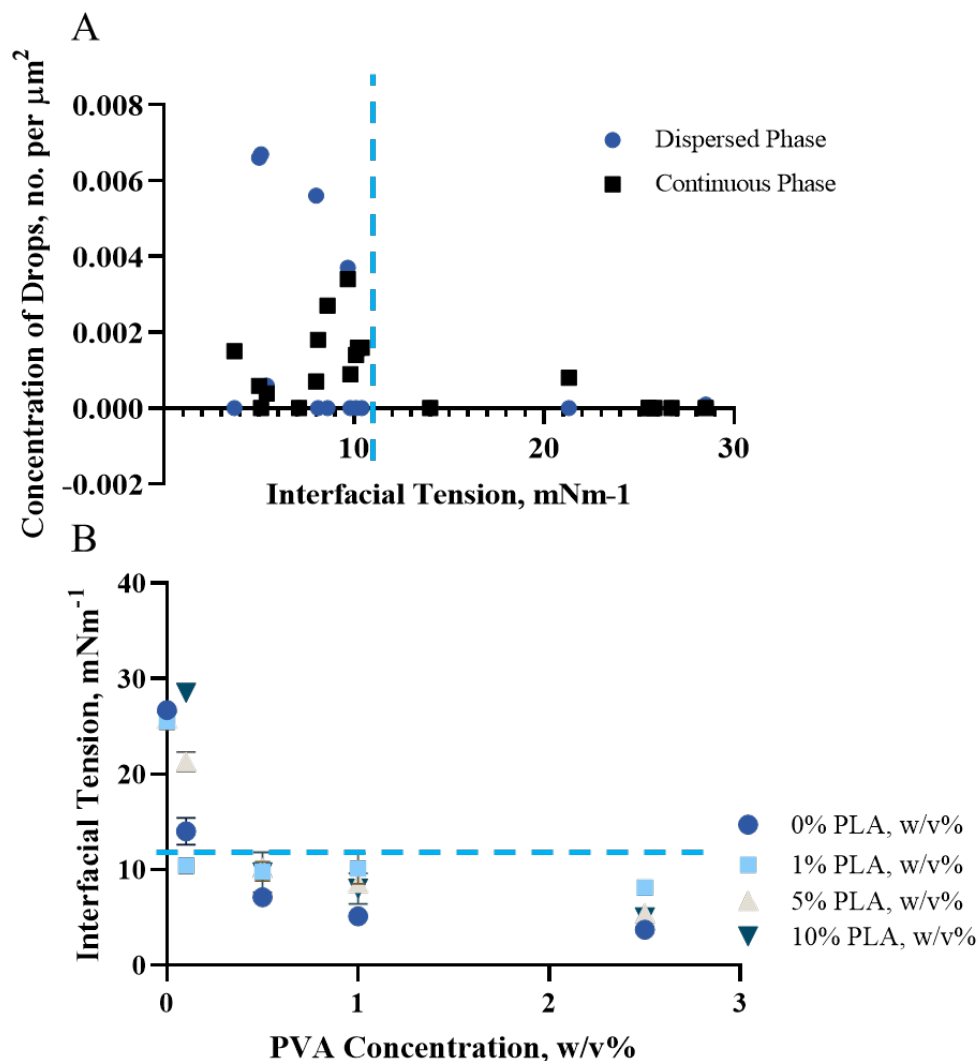
Figure 4-6 Appearance of spontaneous emulsion drops in the micropipette can be used to identify a cut-off tension value for stability. (A) concentration of droplets around the interface for systems of increasing IFT. (B) the IFT limit defined was compared to the PVA concentrations required to achieve IFT reduction. (B) is a replication of figure 4.4 A, with the limit included here each point is the average of 3 repeat measurements formed of 10-20 pressure points/images. Error bars are ±1SD.

A bench top stability test was performed to confirm the stability limit indicated by the presence of spontaneous emulsions, the method for which is described in Section 4.2.2. Figure 4-7 A shows the time taken for DCM/Water (PVA) to separate after mixing, back into two distinct bulk phases. PVA concentrations 0, 0.05% and 0.1% (w/v) separated completely within a few seconds. These are

systems whose IFT value is higher than the stability limit identified. The mixes containing 0.5% and 1% (w/v) took over two minutes for the bulk phases to separate. The interfaces were observed again at 72 hours, a close view of which are shown in Figure 4-7 B. At PVA concentrations below 0.5% the interface is clear. However, for samples with 0.5% and 1% PVA droplets of the opposite phase remained at the interface.
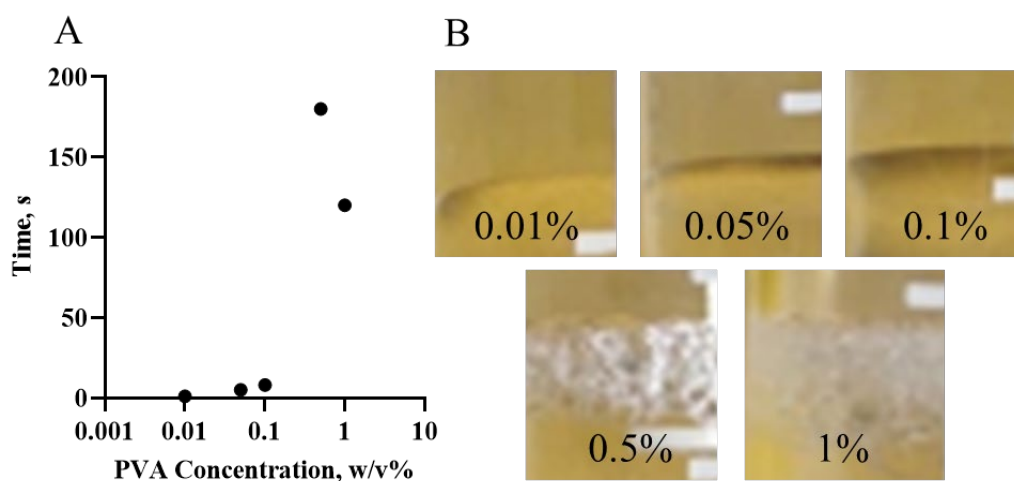
Figure 4-7 Stability was assessed by (A) comparing the time taken for DCM/Water mixes containing different PVA concentrations to separate and (B) comparing the interfaces 72 hours after initial agitation. A single repeat was conducted for this.

Using Equation 4-8 for 0% PDLLA, the PVA concentration required to achieve an IFT value of 11.1 mN^{-1} or below must be equal to or greater than 0.284% (w/v). This agrees with the concentration limit observed in bench-top tests, thus confirming the stability limit.

By adding PDLLA, it was possible to produce crude particles in this method. For all PVA concentrations, the particles remained intact as enough DCM had been removed to prevent aggregation. However, upon analysis it was found that the effect of irregular agitation dominated the particle size. In a controlled process it

would be expected that the change in interfacial tension would directly impact the size of particles formed.[109] Therefore, to correlate the effect of IFT on particle size in this system emulsion solvent evaporation experiments with controlled and constant shear should be carried out.

4.3.2 Solvent Removal Studies

Solvent removal was investigated using the methods described in Chapter 2, Section 2.2.6, for increasing concentrations of PDLLA and PVA in DCM/ethyl acetate and water, respectively. Again, the polymers were treated as additives to the base system. Figure 4-8 shows the dissolution profile of representative droplet as an example. The radius has been extracted using the method described in Chapter 3 Section 3.4.2. Micrographs A-F show the drop throughout the removal of DCM. Their corresponding radius measurements are marked on the graph (blue dots).
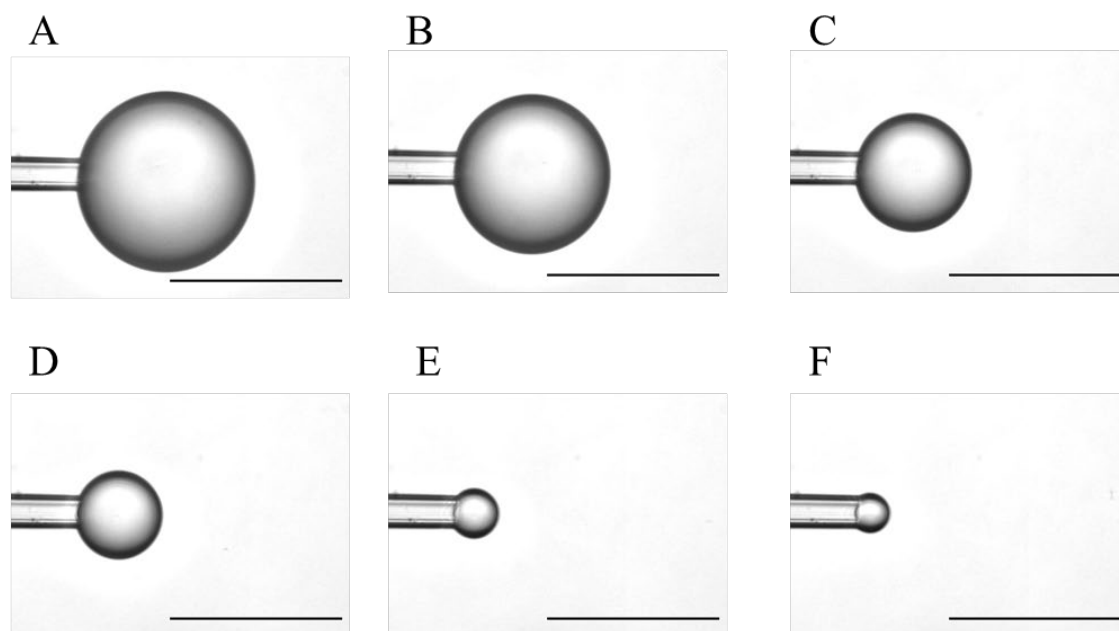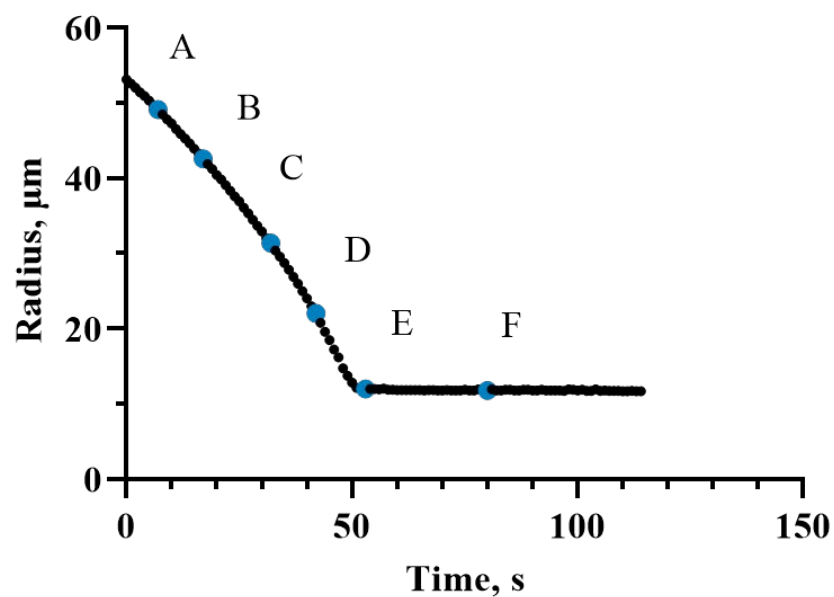
Figure 4-8 Droplet dissolution profile for a PDLLA(DCM) example drop. Micrographs A-F correspond to the drop at the times marked in blue. Scale bars 100µm.

4.3.2.1 Effects of Varying PDLLA Concentrations

Dissolution profiles for drops formed at a similar initial size for a range of PDLLA concentrations in DCM and ethyl acetate are shown in Figure 4-9 A and B, respectively. The dissolution profiles for each concentration follow the same

curve. Curves begin to deviate when they approach the viscous boundary, VB. The VB occurs in Figure 4-8, around point E.

Those with a higher initial concentration reach the VB first and a steady size at a larger radius. This is as expected, as drops starting with a higher initial concentration have less solvent to be removed. Ethyl acetate-based drops began at a larger size but reached the VB quicker than their DCM counterparts. This is explained by examining the parameters governing dissolution rate.
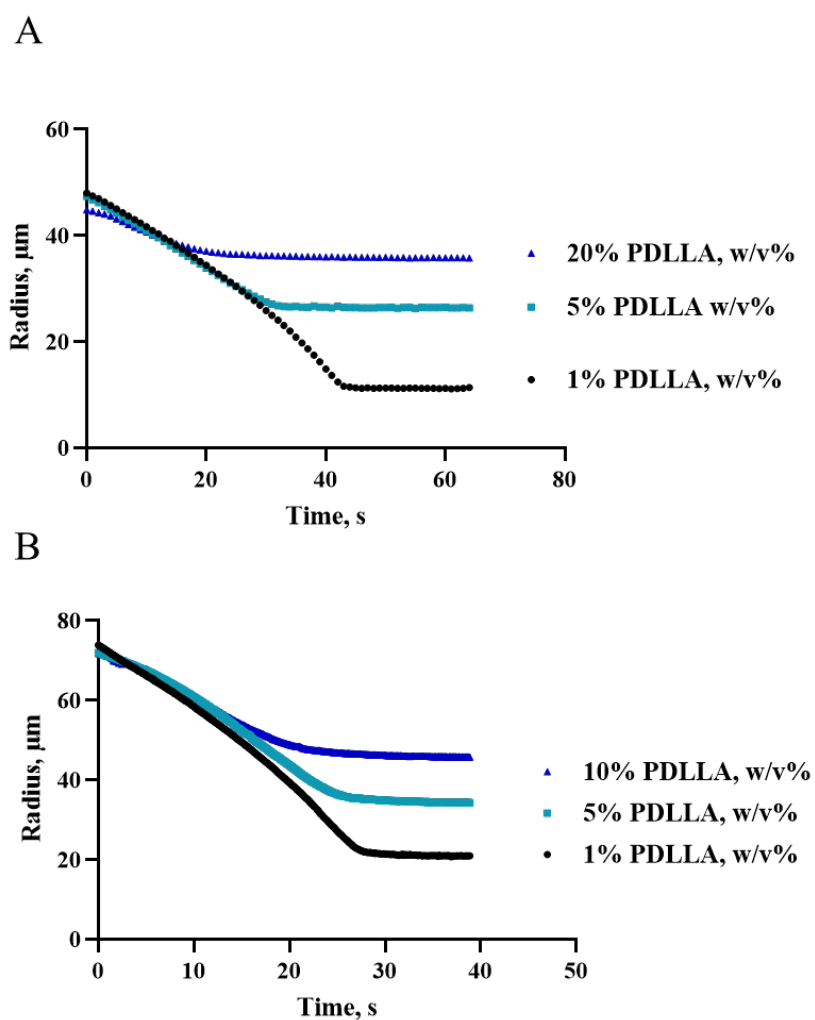
Figure 4-9 Profiles of individual drops of different PDLLA concentrations in (A) DCM and (B) ethyl acetate for similar starting size undergoing dissolution into water.

4.3.2.2 Diffusion Coefficient Calculation

A representative DCM-water dissolution profile is shown in Figure 4-10. The data has been linearised (Figure 4-10 A) following Equation 4-3, and a linear fit applied to obtain the gradient. The diffusion coefficient, D, for DCM was obtained through rearrangement of this equation, giving $D = 2.19 \times 10^{-5} \pm 7 \times 10^{-8}$ $cm^2\,s^{-1}$. The error in diffusion coefficient is calculated from the fit of the gradient. This value was then reinserted into the full Epstein-Plesset equation, EP, (Equation 1-15) and the result plotted with the measured points in Figure 4-10 B for comparison. The EP model follows until complete dissolution has occurred. In practice, the ability to measure complete dissolution is limited by the pipette size, as drops are drawn into the pipette when they reach the same radius as the inner walls due to capillary pressure.
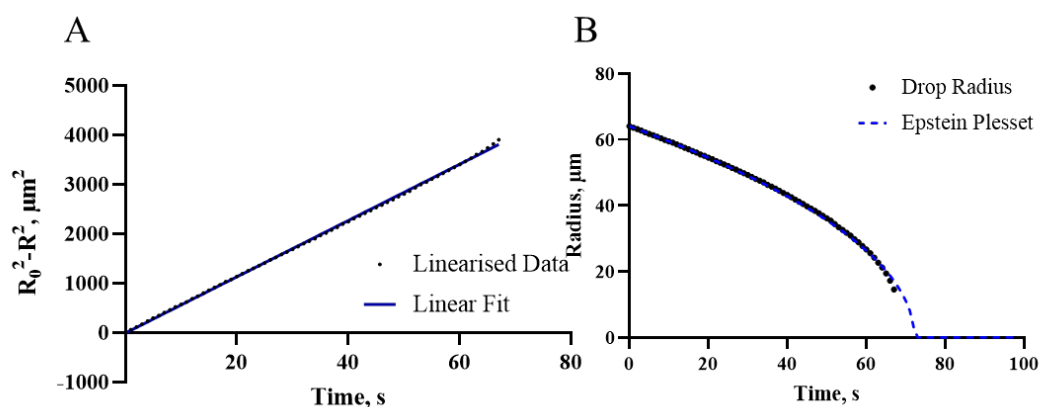
Figure 4-10 (A) Linearised dissolution profile of a representative DCM drop into water to find the diffusion coefficient. (B) Comparison of the EP model to the measured profile.

The same analysis was also carried out for polymer containing drops as in Figure 4-11 A, which shows an example of 5% (w/v) PDLLA in DCM. The gradient of the linear portion of the data was used to give a diffusion coefficient of $D = 2.1419 \times 10^{-5} \pm 1.2 \times 10^{-7}$ cm^2 s^{-1}. Again, in part B of this figure, the EP model has been plotted alongside the measured radii. Here, the drop reaches a constant radius due to the polymer it contains, whilst the EP model shows what would be followed if the drop were pure DCM. The deviation from EP begins as the VB is approached. This could be used to help understand the changes in dynamics occurring as this point is reached. It also gives the time when all solvent appears to be removed and so what may be left after the VB has been reached.
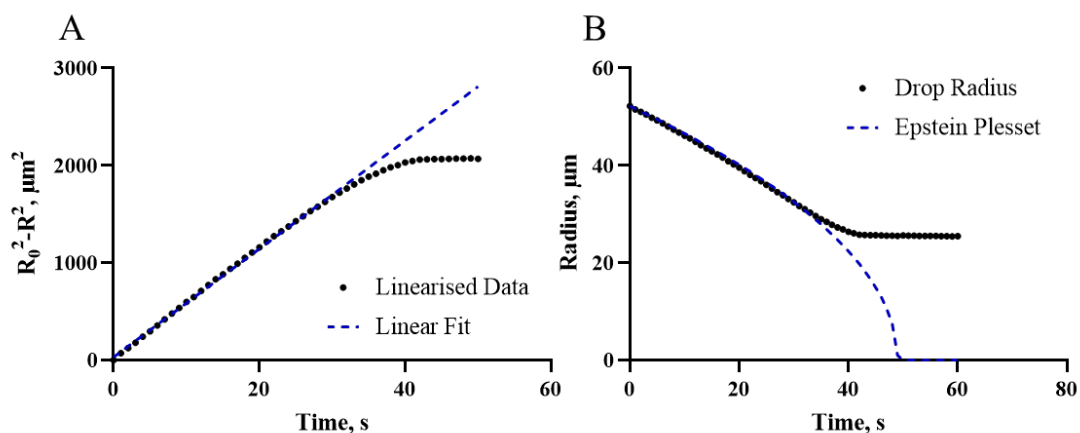
Figure 4-11 (A) Linearised dissolution profile of a 5% (w/v) PDLLA (DCM) drop into water to find the diffusion coefficient. (B) Comparison of the EP model to the measured profile.

The diffusion coefficient for DCM and ethyl acetate with increasing concentrations of PDLLA and PVA are shown in Figure 4-12 A and B, respectively.
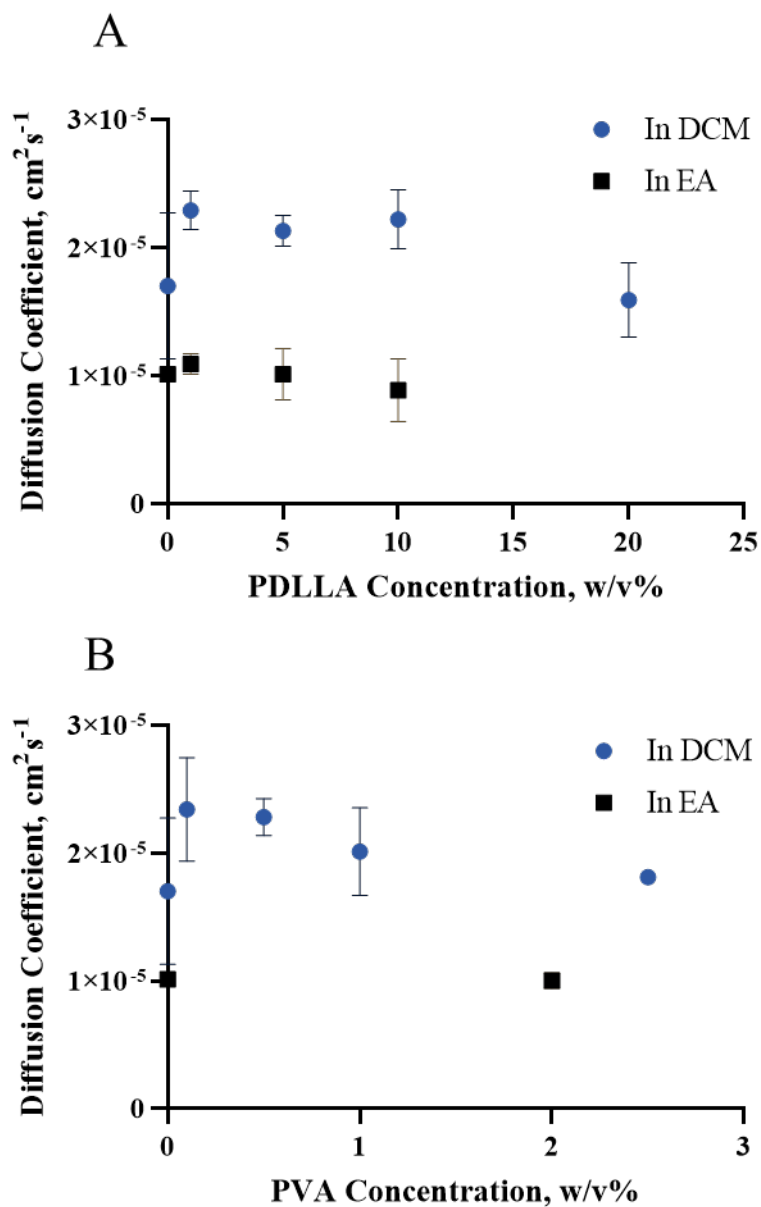
Figure 4-12 Diffusion coefficient of DCM and ethyl acetate in systems with (A) different concentration of PDLLA in the drop and (B) PVA in the continuous phase. Values are obtained from the average of diffusion coefficients of 4-7 drops, and error bars are ±1SD of the values around this mean.

The value of diffusion coefficient for DCM to water, with no additives, is within an acceptable range of published values, ($1.8 \times 10^{-5} \pm 1 \times 10^{-6}$ cm^2 s^{-1} and $2 \times 10^{-5} \pm 2 \times 10^{-6}$ cm^2 s^{-1} from K. Kinoshita[8] and A. Utoft)[37], respectively, found using

micropipette manipulation, and of 1.3×10^{-5} cm^2 s^{-1} from predictive models by Hayduk and Laudie, 1974.[159]

The value obtained for ethyl acetate is higher than the reported value 8.65×10^{-6} $\pm\ 9 \times 10^{-7}$ cm^2 s^{-1} using the same method.[20] However, considering variation in reported saturation concentrations and possible differences in temperature this is an acceptable deviation. Additionally, it still provides a useful baseline for comparing the effects of additives.

Variation in both 0% PDLLA measurements is likely due to incomplete dissolution profiles when droplets shrink below a critical size and so the later stages of dissolution cannot be observed.

In all cases, there is a small increase in the measured diffusion value with the initial addition of either polymer (1% (w/v) PDLLA or 0.1% (w/v) PVA) as summarised in Table 3. Following this initial increase, higher concentrations of polymer cause the diffusion to lower to approximately the value obtained for the base solvent systems.

Table 3 Comparison of diffusion coefficients of DCM and ethyl acetate in water when low concentrations of polymer are added. Values are obtained from the average of diffusion coefficients of 4-7 drops and errors are ±1SD of the values around this mean.

Solvent	Base system, x10^{-6} cm^2 s^{-1}	1% (w/v) PDLLA, x10^{-6} cm^2 s^{-1}	0.1% (w/v) PVA, x10^{-6} cm^2 s^{-1}
DCM	17 ± 3.8	22.9 ± 1.5	23.4 ± 4
Ethyl acetate	10.1 ± 0.28	11 ± 0.81	

The initial increase in measured diffusion was surprising. For increased polymer in the organic phase any change would be expected to be a reduction in the rate of diffusion, as the increase in viscosity would hamper diffusion of solvent molecules within the drop to the surface, and therefore out of the drop. The decrease in diffusion rate as the concentration increases further is likely due to this reason. In the case of PVA, the increased concentration of large molecules at the interface could be expected to impede diffusion of molecules from the drop surface, especially as CMC is reached.

A further investigation that could prove insightful would be to assess diffusion when surfactants (and core polymers) of different molecular weights are used. Understanding the impact of weight on solvent removal would help in the selection process for optimising particle production, though other factors are important in choosing the M_w, such as degradability. The impact on the diffusion coefficient may not be high, especially early removal of solvent close to the surface, but the amount of trapped solvent may vary which would impact the final viscosity/elasticity of the drop/particle. The presence of trapped solvent hampers, or even prevents the use in biomedical applications.[104,106] Alternatively, trapped solvent has to be removed in later stages (e.g., washing, freeze drying) which is an unhelpful extra step and can change the morphology of particles.

Pervious works from K. Kinoshita[8] and A. Utoft[37] found that additions to the continuous phase did not cause a change in the diffusion rate of DCM. Additionally, these works noted the variability in diffusion values arising from the choice of saturation concentration value used.

The changes in diffusion discussed are small, and due to the spread in results, barely significant. No concentration of PDLLA added to ethyl acetate gave a p-value lower than 0.9 compared to the base solvent, whilst for DCM two populations with large spreads were seen and no significance was found within these populations. Possible reasons for the observed spread on each result are variations in initial drop concentration caused by solvent at the end of the delivery pipette moving into the chamber prior to drop formation, and saturation changes in the continuous phase – though care is taken to minimise these as much as possible.

Another possible reason for the variation in measurements could be the initial droplet size. Larger drops can create more convection around them during initial formation.[160] In this case, diffusion is not the sole mechanism for material loss as the EP model assumes. Therefore, the overall material transfer is faster and leads to an over estimation of diffusion. A comparison of the diffusion coefficient calculated for different size drops was conducted and the results are shown in Figure 4-13. It was observed that for DCM containing 1%, 5% and 10% (w/v) PDLLA the calculated diffusion rate increased with droplet size. However, it was constant across drop sizes for droplets containing no solute and those formed with ethyl acetate. This does suggest that initial size is at least partially responsible. However, since this is only observed in certain cases, the factors discussed above must also be partially responsible.
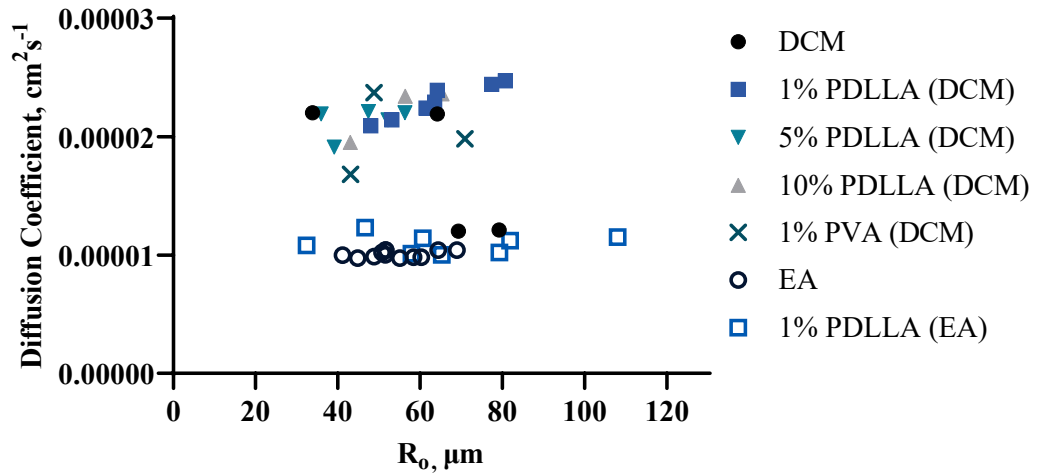
Figure 4-13 Diffusion coefficient calculated from droplet dissolution profiles as a function of initial droplet radius for pure DCM drops (black circles), drops of 1% (w/v) PDLLA (dark blue squares), 5% (w/v) PDLLA (blue inverted triangles) and 10% (w/v) PDLLA (grey triangles), DCM into water with 1% (w/v) PVA (blue cross) and ethyl acetate drops (open dark circle) and ethyl acetate drops containing 1% (w/v) PDLLA (open blue square).These are values for individual drop, errors are 1+ orders of magnitude smaller and so not visible.

4.3.2.3 Evaluating Dissolution Profiles

The activity-based dissolution model accounts for the volume lost during the droplet formation. However, in the systems studied here this term was found to be negligible. A correction for the area of droplet not experiencing ideal dissolution due to the pipette was included, as this change persists over the whole dissolution time. For the following assessment, the radius is calculated from the drop radius at the previous time interval.

The resulting equation for R at time t is therefore:

$$R_t = R_{t-\Delta t} - \Delta t \frac{R_0 + \sqrt{R_0^2 + R_{pip}^2}}{2R_0} \frac{Dc_s(f_{i(t)} - f)}{\rho} \left[\frac{1}{R_{t-\Delta t}} + \frac{1}{\sqrt{\pi D(t_{off} + t)}} \right]$$

Equation 4-9

where Δt is the time interval, R_{pip} is the internal radius of the micropipette tip, and t_{off} is the offset time between formation and the beginning of dissolution. All other terms are as defined previously.

For each solvent investigated the saturation function, $f_i(t)$ was calculated as described above in Section 4.2.4, to give Equation 4-4 and Equation 4-5 for DCM and ethyl acetate respectively.

For each dissolution profile the same value of diffusion coefficient and initial concentration were used for both the EP and activity-based models. Examples of the models compared to the measured radii are shown in Figure 4-14. A-C show the results for DCM drops containing 1%, 5% and 10% (w/v) PDLLA, respectively, and which plots D-F show the same concentrations in ethyl acetate.

In each case the EP model mostly agrees with the measured values, while the activity-based model gives a much quicker dissolution rate. The data for 1% (w/v) PDLLA (Figure 4-14 A for DCM and Figure 4-14 D for ethyl acetate) follows the curve of the EP model – showing ideal dissolution is maintained. As seen Figure 4-9, comparing the dissolution profiles of drops of different initial polymer concentration, those with higher polymer concentration reach the VB earlier and so will deviate from the EP sooner. This is confirmed by the deviations seen in the rising PDLLA concentrations in Figure 4-14.
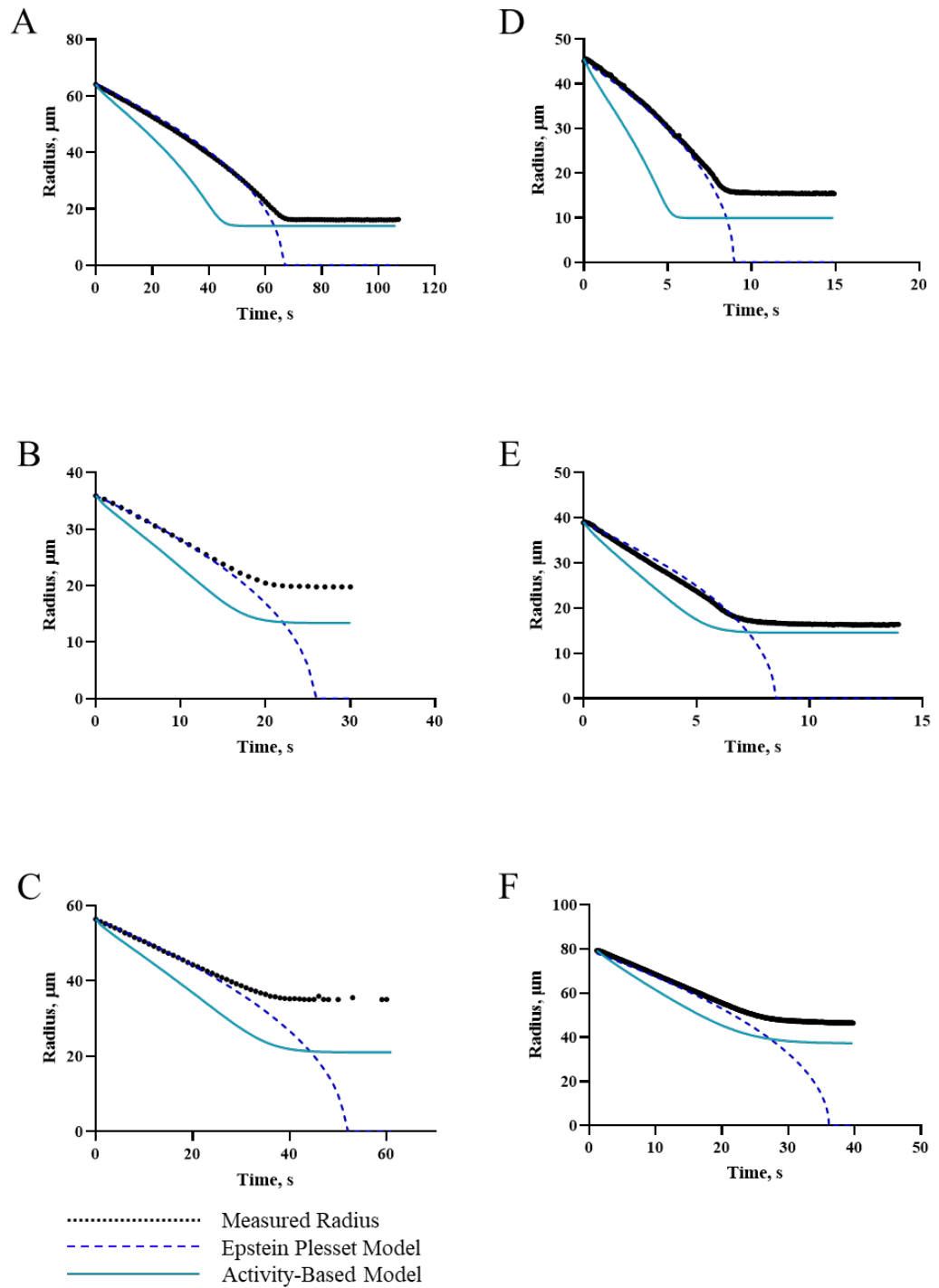
Figure 4-14 Comparisons between measured radii (black circles), radii predicted by the EP model (dashed blue line) and radii predicted by the activity-based dissolution model (blue line) for the same starting concentrations and diffusion coefficients for drops of (A) 1% (w/v) PDLLA in DCM, (B) 5% (w/v) PDLLA in DCM (C) 10% (w/v) PDLLA in DCM (D) 1% (w/v) PDLLA in ethyl acetate (E) 5% (w/v) PDLLA in ethyl acetate and (F) 10% (w/v) PDLLA in ethyl acetate. Each is for an individual drop.

Profiles belonging to drops of a higher initial concentration have a shape more like the activity-based model. The discrepancy in shape between the models, as can be seen from the equations (Equation 1-15 and Equation 1-16) is the $f_i(t)$ function. This suggests the $f_i(t)$ calculated is giving an overcorrection in the low solute drops but is necessary when higher polymer concentrations are present. However, in all cases the activity-based model gives a higher rate of dissolution than is observed. This suggests that the $f_i(t)$ function calculated also gives an over-estimate of the concentration change. This function could be improved by additional repeats of drops into partially saturated chambers, as drops showed a wide range of equilibrium concentrations (Figure 4-2).

Perhaps most crucially, the $f_i(t)$ function relies on having an accurate starting concentration which, while assumed to be the same as stock concentration, could have significant variations as discussed above and noted in other works.[20] The activity-based model gives the radius that is expected, providing that the initial concentration is as intended. This should hold true even though the curve is different from the EP as the final size is based on the input concentration and the initial radius, not the behaviour in between. Considering the examples shown in Figure 4-14, the difference in final radii between the measured data and that predicted by the activity-based model vary by between 14% (1% (w/v) PDLLA in DCM) and 40% (10% (w/v) PDLLA in DCM). There are two possibilities here, either the initial concentration is different to that assumed, or there are

substantial volumes of solvent remaining in the drop after a steady size is reached.

The deviation between the final volumes and the time taken to reach the VB were considered for ethyl acetate dissolution. As shown in Figure 4-15 A the difference in volume for 1% (w/v) PDLLA is approximately constant, no matter the initial size, this suggests a systemic error. However, for 5% (w/v) PDLLA the deviation increases with initial size, as would be expected for an alternate starting concentration but with too much variation to draw a relationship from.

From Figure 4-15 B, the VB is predicted to be reached sooner than measured in all cases. The difference between the measured and predicted times increases with initial size, as would be expected if caused by a difference in concentration. Both predicted and measured values have the time to VB increase linearly with initial surface area, as is expected for systems with diffusion dominated dissolution.
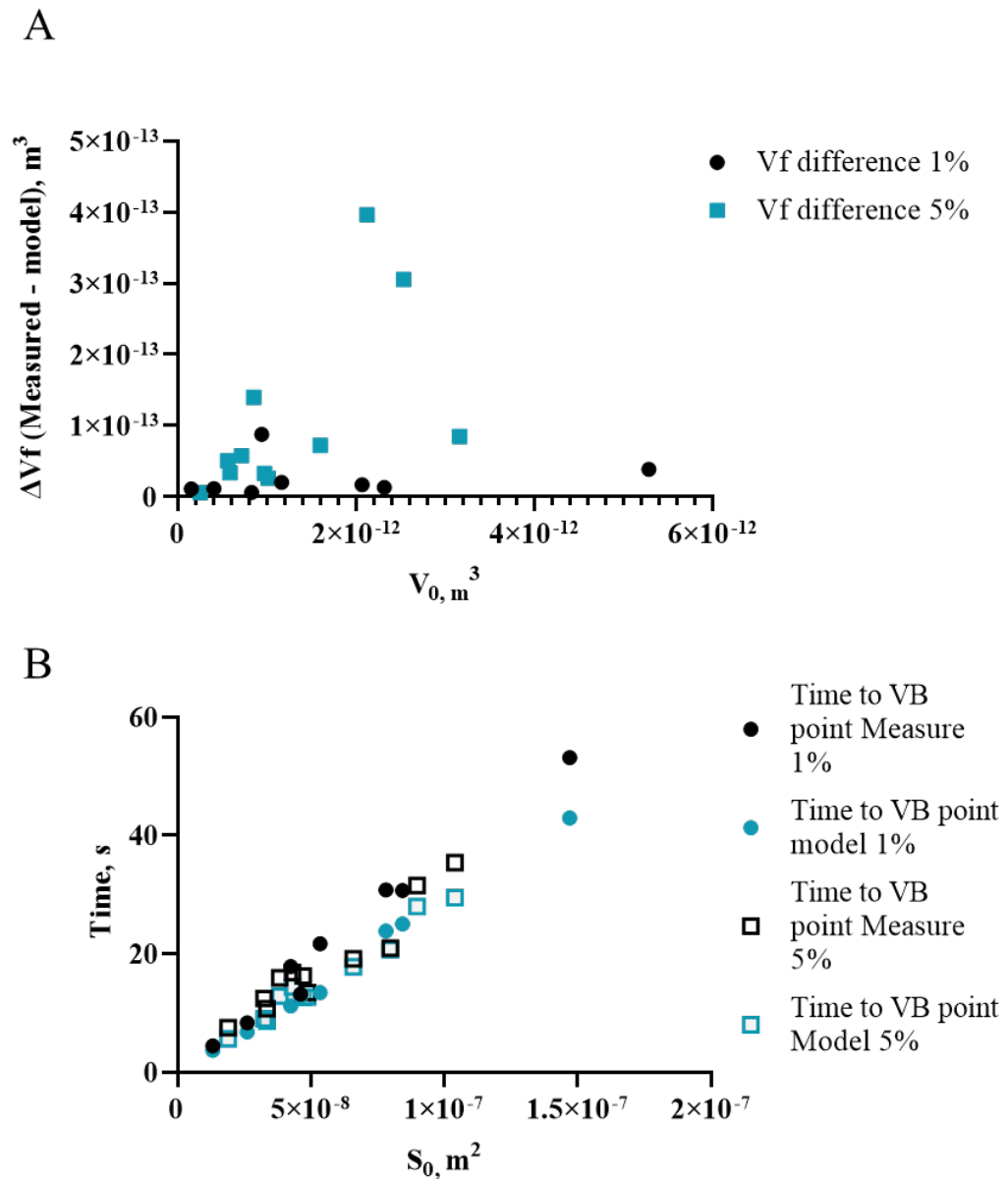
Figure 4-15 Comparison between measured behaviour and that given by the activity-based model for dissolution for PDLLA in ethyl acetate droplets. Points are shown for individual droplets. (A) Comparison between measured final volumes and expected final volumes for 1% (black circles) and 5% (w/v) PDLLA (blue squares). (B) The time taken for drops to reach the viscous boundary according to measurement (black) and model (blue) times for 1% (circle) and 5% (w/v) PDLLA (squares).

The disagreement between predicted and measured final drop sizes could be the

result of trapped solvent. When the VB is reached the particle is in its gel state

rather than the glassy state, and small amounts of solvents do remain. However,

given the discrepancy here, it is likely to be a greater volume than would ordinarily be present.[28] This is supported by the easy deformation of the drops despite being well below the melting temperature of the polymer.[128]

Nevertheless, this deformation also shows the drops are semi-solid. Pipettes easily slide through drops with high levels of solvent – such as the drops that are initially formed and are known to be liquid. The drops at the end are not as solid as expected but their surfaces remain intact, the pipette is unable to penetrate the drop and can be seen in the example micrographs in Figure 4-16.

The drop in Figure 4-16 A is deformed easily, following which it recovered some of the indentation caused by the pipette, but not entirely. The droplet in Figure 4-16 B had a large force applied which only left a small deformation. Conversely, the Figure 4-16 C drop was not able to be deformed, instead the pipette was deflected, and the drop rolled – suggesting this is much more solid. There was, however, no correlation between the deformability or recovery and the initial concentration or the deviation from final concentration.

The fact that ideal dissolution is followed during most of the solidification suggests there is not a fixed 'skin' on the drop, rather, that a concentration gradient exists, with higher polymer concentrations towards the surface, as hypothesised previously by Su and Needham.[20] This would account for the retardation of diffusion as time progresses, as is seen by the approach to the VB being extended for higher initial polymer concentrations as indicated by the more linear profile of drops of 5% (w/v) and 10% (w/v) PDLLA in Figure 4-14, whilst the corresponding diffusion coefficients appear to be unaltered (Figure 4-12) as

they are found using the linear relationship in Equation 4-3 using the earlier stages of dissolution, when solvent diffusion inside the drop is freer. This in turn would explain why the solvent fraction equilibrium curves, and so f_i, are not adequately describing the behaviour as well as would be expected and is shown for non-polymeric solutes.[22]
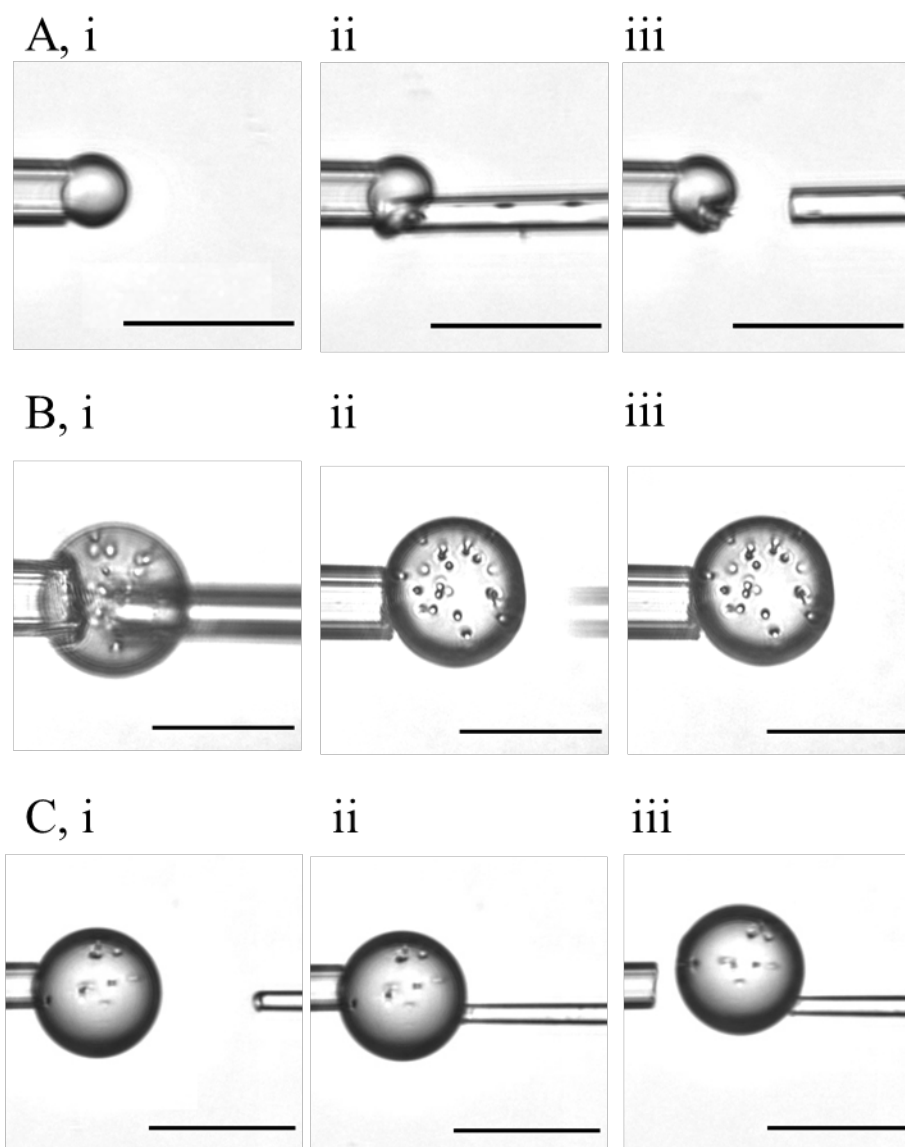
Figure 4-16 Micrographs showing the deformation of three drops after reaching a steady radius. (A) 1% (w/v) PDLLA (DCM) (B)5% (w/v) PDLLA (ethyl acetate) (C) 5% (w/v) PDLLA (DCM). (Labels i, ii and iii denote the order in time). Scale bars 50μm

This hypothesis could be tested by either carrying out the dissolution with PDLLA of different molecular weights, as discussed in Section 4.3.2.2, which could impede internal diffusion of the solvent further, or by increasing the temperature to increase polymer movement. In the latter case diffusion would be expected to increase in all systems, but a polymer gradient would be harder to form at higher temperatures as it could re-equilibrate quicker.

An alternative approach to assessing the data was to use a Simplex fitting algorithm, scripted in MATLAB (Prof. P.M. Williams). By setting the known values for pipette size, density, and saturation concentration, the values of diffusion coefficient, initial concentration of solute and initial saturation fraction of the solvent in the continuous phase could be found. The more parameters known and fixed the more reliable the generated fit.

The fit was generated using the activity-based model as before (Equation 4-9), with the relevant $f_i(t)$ included. The initial saturation fraction, f_0, was assumed to be zero since no solvent was added to the continuous phase initially, and sink conditions were maintained for repeat droplets.

Two examples of this fit as applied to data are shown in Figure 4-17. Figure 4-17 A shows the profile of a 1% (w/v) PDLLA in DCM drop and the corresponding fit which has an RMS of 0.1988. From this the values of the diffusion coefficient and initial concentration were found to be 1.585×10^{-5} cm^2 s^{-1} and 1.44% (w/v), respectively.

A

B
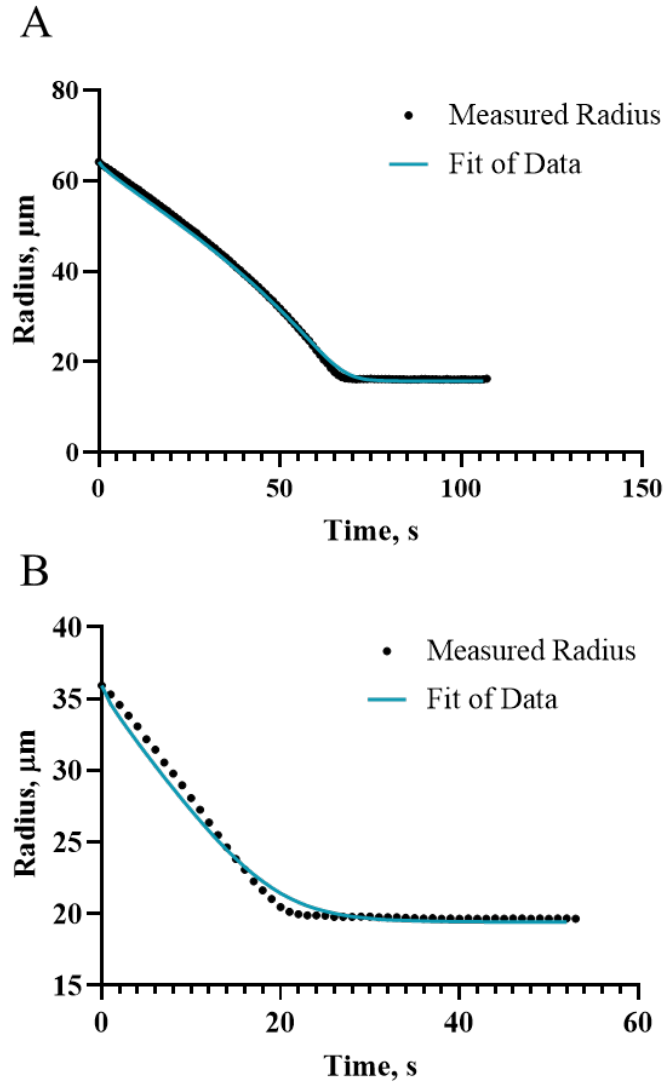
Figure 4-17 Drop dissolution profile for (A) "1% (w/v") PDLLA in DCM and (B) "5% (w/v)" PDLLA drops. A simplex fit (blue line) was applied to the data (black circles) to calculate actual starting concentration and diffusion coefficient: (A) 1.585×10^{-5} cm^2 s^{-1}, 1.44% (w/v) and (B) 1.65×1^{-5} cm^2 s^{-1}, 15.29% (w/v)

In Figure 4-17 B the data is from a 5% (w/v) PDLLA in DCM drop and the fit has an RMS of 0.134. In this case the diffusion coefficient and initial concentration were found to be 1.65×10^{-5} cm^2 s^{-1} and 15.29% (w/v), respectively. The concentration obtained from the fit is close to the expected concentration for the 1% (w/v) PDLLA drop. However, there is a three-fold difference for the "5%

(w/v)" drop. Though a small shift in drop concentration is could be expected, given the care taken to avoid producing drops from pre-depreciated materials, this difference is too large to be accounted for solely by experimental variation.

For proteins and select other solutes[22,24,25] the initial concentration can be calculated exactly, working backwards from the time when the refractive index of the drop matches that of the surrounding medium: this occurs at a specific concentration in each case. This is not available for polymers. This fitting method offers an alternative approach for determining concentrations when traditional methods are not available. This could prove useful for assessing bulk solutions prior to particle production, allowing the confirmation of the stock concentration by forming a small number of drops.

In this fit, the initial concentration is determined based on the assumption that all solvent is removed. It has been demonstrated that this is most likely not the case. However, it provides a useful estimation for comparing systems and drops. Further work will be needed to account for residual solvent.

4.4 Conclusion

Micropipette manipulation techniques were employed to assess the impact of PDLLA and PVA on DCM/water and ethyl acetate/water systems as a precursor to microparticle fabrication. Static equilibrium interfacial tension measurements were used to find the effective CMC of PVA, yielding a value of approximately 1% (w/v). The appearance of spontaneous emulsions was utilised to identify a limiting value of interfacial tension, approximately, 11.1 mN m^{-1}, for forming stable emulsions. Empirical equations were generated to describe the interfacial

behaviour in response to these additives. In turn these were used to identify the critical concentration of 0.24% (w/v) PVA to stabilise DCM/water system long enough to produce long-life droplets. These results satisfy the aims of understanding the interfacial tension response to PVA concentration for both solvent base systems and identifying the optimum concentration of surfactant for this system.

The diffusion of DCM and ethyl acetate from drops to the surrounding aqueous phase was assessed and the diffusion coefficients calculated, as required. There was no significant change in diffusion coefficient with increased additive concentration, suggesting neither added material acted as an additional barrier to solvent transport, at least in the initial stages. However, in comparing the behaviour to established models of dissolution it was concluded that excess solvent remained trapped in the droplets. This was likely due to rearrangement inside the drops slowing earlier and more so than seen in drops containing non-polymeric solutes. Through this assessment the objective of studying the impact of additives on solvent transfer has been achieved. It has also identified potential areas to consider in future productions and investigations.

Chapter 5: Informing Droplet Microfluidic Processes for the Formation of Microparticles with Novel Bio-instructive Surfactants

Chapter 5 – Informing Droplet Microfluidic Processes for the Formation of Microparticles with Novel Bio-instructive Surfactants

5.1 Introduction

Microparticle materials must be carefully selected based on the required biological response. PLA and PLGA are often chosen for their inert properties.[65] Whilst ideal for some applications, such as drug delivery, the lack of ability to influence cell behaviour can hamper their use in tissue engineering applications. This is often overcome by the addition of growth factors or other deliverable cues, though this adds additional levels of complexity to the system.[79]

Using materials with bio-instructive capabilities to directly influence cellular response negates this and removes the difficulties associated with tailoring release profiles. Natural and synthetic polymers can be used in microparticles for this role. Synthetic polymers are usually easier to control the properties of.[65]

The use of synthetic bio-instructive polymers can be expensive. Furthermore, the effectiveness of the material is lessened once surfactants become bound to the surface.[89] Since cells can only sense the chemistry of the surface and a few nanometres below, the bio-instructive component must to be presented at the surface.[93] While this can be obtained through post-production surface modification,[30,76] it would be more convenient, in terms of time and financial concerns, if this were achieved within the particle production steps. Additionally, this would likely improve uniformity. The use of surfactants incorporating the

desired chemistry could achieve this. Commercially available surfactants are not able to achieve this, requiring synthesis of bespoke surfactants.

As part of the work of the Engineering and Physical Sciences (EPSRC)-funded Next Generation Biomaterials Discovery Programme Grant (EP/N006615/1), University of Nottingham, high throughput screens have been used to identify methacrylate-based polymers capable of modulating fibroblast phenotype, influencing macrophage polarisation and stem cell differentiation and preventing bacterial attachment.[91,94,134,161] Whilst applications for some of these materials, for example reducing bacterial attachment on urinary catheters, require dip-coating of the material on pre-existing surfaces, others require a more alternative translations into 3D.[90,91,162] Microparticles and microparticle constructs, such as scaffolds, are ideal for the translation of materials in these cases. By producing surfactants from bio-instructive materials, particles can be produced with specific, instructive surface chemistries.

Surfactants were developed within the above programme by combining the hydrophobic target chemistry (determined from biological microarray screens) with either poly(ethylene glycol) methacrylate (PEGMA) or poly(ethylene glycol) methyl ether methacrylate (mPEGMA) of different molecular weights (Dr Valentina Cuzzucoli Crucitti, Chemical Engineering, University of Nottingham). A range of ratios of the hydrophobic and hydrophilic components were trialled and comparative studies to the homopolymers conducted in a 2D screen. From this, it was determined that hydrophilic components could be added it up to rations of 85:15 (hydrophobic: hydrophilic) without compromising on

the biological effectiveness. Surfactants were then produced by copolymerising the "hit" hydrophobic component in this ratio with mPEGMA (M_N=300) using catalytic chain transfer polymerisation.[90] Comb-graft and block copolymers have been utilised. It is a selection of surfactants from this study that are presented in this chapter. EGDPEA-mPEGMA and HPhOPA-mPEGMA were chosen, as detailed in the A. Dundas, *et al*. paper, for their contrasting behaviour supporting (HPhOPA) or preventing (EGDPEA) biofilm formation. EA was assessed in 2D as part of that study and is assessed here as a material of interest for related works.

Since the applications relating to the bio-instructive chemistries of interest benefit from using monodisperse particles, droplet microfluidics was identified as the best platform for producing particles using these surfactants. Interfacial stability is key for any emulsion formation, but with the confined flow of a microfluidic device interfacial forces become more influential and the need to understand interfacial tension is critical.[123] Typically, optimising formulations in particle production is done through trial-and-error experimentation. This is inefficient and costly. The surfactant concentration needs to be sufficient to provide stabilisation, but material volume should also be minimised. Microfluidic systems are very sensitive to changes in both interfacial tension and viscosity, and the use of polymeric surfactants has a large impact on both of these properties.

The use of novel surfactants provides another layer of difficulty to this challenge. Most commercially available surfactants are well characterised, and whilst

concentrations often need fine tuning, knowledge from previous studies can offer a good starting point for formulation. The surfactants of interest here have minimal information available about their behaviours in real systems. In this section of work the aim was to use micropipette manipulation studies to provide invaluable information about the impact these materials have on the interfacial tension of microparticle producing systems, and thus determine optimum surfactant concentration.

As with formulation, the optimisation of flow rates for droplet microfluidics is also usually achieved through trial and error. Given the scope of flow rates possible and the range of flow regimes that can be achieved, identifying the ideal flow rates can be a long and difficult process. Not only is this time intensive but also wastes material. Flow maps, discussed in Chapter 1 Section 1.6.6, can be used to describe the flow patterns for different flow rate combinations and then allow for the prediction of stable flows. Flow maps can be produced by varying the continuous and dispersed phases in turn and observing the flow regimes produced. Alternatively, given certain parameters of the system, they can be calculated.

The capillary number, Ca, defined in Equation 1-17, describes the competition between interfacial and viscous forces. It is commonly used for flow maps as its dimensionless quality allows comparison between different systems. Stable dripping is often observed for capillary numbers between 10^{-3} and 10. In some cases its use can be extended to aid in the prediction of droplet size.[118]

Alternatively, for flow-focussing devices, a set of equations based on Ohnesorge numbers (Equation 1-18 to Equation 1-20) can be used to directly calculate the flow rates of the continuous phase, Q_c, and dispersed phase, Q_d, that will produce monodisperse, spherical drops. For both methods, the interfacial tension, phase viscosity and exit channel dimensions are required. Using these, the range of stable flow rates for a given combination of phase materials and surfactant concentration can be identified.[8,126] creating and testing such a predictive map for a selected system constitutes the second aim for this part of the investigation.

A detailed study of the interfacial tension for a selection of novel surfactants, using micropipette manipulation techniques is presented below. This represents the first time such materials have been characterised using these methods. In addition to identifying the optimum concentrations, a study is presented on the effects of chemistry and structure of these surfactants on relevant interfaces. To demonstrate the potential for flow optimisation, flow maps derived through calculation and experiment are compared for an example system.

The base system used for these studies centres around a solvent free, monomer based dispersed phase. The surfactants tested were solubilised directly by the monomer, (though an exception was made for surfactants with block architectures, which required small amounts of DCM for solubilisation.) For particle production the dispersed phase comprised the core monomer (hexanediol diacrylate (HMDA)), the chosen surfactant and a photoinitiator. The use of HMDA as the core material presents an extra challenge as there is limited documentation of use in this role, and then only with PVA as the surfactant.[163]

HMDA was chosen as the core material as it is relatively low cost, compatible with the surfactants and in biological tests presented by A. Dundas, *et al.*[90], was shown to be inert or cause behaviour in-between the surfactant chemistries. This was a necessary feature for biological testing, to identify whether the surface or internal chemistry was dominating. Once formed the drops were then polymerised as they entered the collection vial via UV radiation.

Material transfer tests were carried out between HMDA and water to discover what occurs to the drops between formation and polymerisation. As a solvent-free system minimal transfer was expected, however, the material demonstrated unusual behaviour. This work aims to assess this behaviour and propose a mechanism for it.

5.2 Methods and Materials

Static equilibrium interfacial tension measurements, used throughout this chapter, were performed as described in Chapter 2, Section 2.2.5. Mass transfer studies were performed on drops formed as described in Chapter 2, Section 2.2.6.

Micropipettes for these studies were produced following the process in Chapter 2 Section 2.2.1 and for the inverted system of water drops in HMDA, were salinized following the process in Section 2.21.3. IFT measurements were made using the static equilibrium method. All analysis of micropipette experiments was carried out using the methods developed in Chapter 3.

5.2.1 Materials

The materials, used as obtained without additional processes, were: 1,6-hexanediol diacrylate (HMDA) and ethylene glycol dicyclopentenyl ether acrylate (EGDPEA). MiliQ water (18.2MΩ) was used as the continuous phase throughout, in both micropipette and microfluidic experiments. Additionally, in microfluidics processing 1% (w/v) photoinitiator (2,2-dimethoxy-2-phenylace-topenone (DMPA)) was used. This was not included in micropipette experiments to avoid any polymerisation from non-specific UV whilst under the microscope.

Novel surfactants: ethylene glycol dicyclopentenyl ether acrylate co poly(ethylene glycol) methacrylate, EGDPEA-mPEGMA (random copolymer), 2-hydroxy-3-phenyoxypropyl acrylate co poly(ethylene glycol) methacrylate HPhOPA-mPEGMA (random and block copolymers), ethyl acrylate co 2-(dimethyl amino)ethyl methacrylate, EA-DMAEMA (random and block copolymers) and 2-hydroxy-3-phenyoxypropyl acrylate co 2-(dimethyl amino)ethyl methacrylate, HPhOPA-DMAEMA (random and block copolymers) were produced by Dr Valentina Cuzzucoli Crucitti, Chemical Engineering, University of Nottingham, following the methods described in Chapter 2, Section 2.1.3.1.

5.2.2 Pendant drop Interfacial Tension Measurements

Interfacial tension analysis using the pendant drop method was carried out for comparison and confirmation. A KSV Cam200 goniometer was used with the pendant drop functionality. Drops of the organic phase of interest were formed

in air. Drops were analysed using the inbuilt software of the instrument to obtain the interfacial tension. The average was taken over n=5-12 drops.

5.2.3 Microfluidic Flow Rate Calibration

Harvard Apparatus PHD Ultra syringe pumps used for microfluidic particle production were set to a value in mL/hr, however, the input values needed to be calibrated to allow comparison to theory-based calculations. To do this, droplet formation videos were analysed. Images were calibrated using the known dimensions of the channel (red in Figure 5-1 A, 100 μm is the inner diameter). Droplet diameters (blue in Figure 5-1 A) were used to calculate the drop volumes and, combined with the frequency of drop production, were used to calculate the flow rate of the dispersed phase. The continuous flow rate was calculated by using the flow of the drops and the volume of between them (yellow in Figure 5-1 A).

Videos of a several flow rate combinations were assessed. The measured rates were compared to the input rates, Figure 5-1 B and C for continuous and dispersed phase respectively, and a linear fit applied to allow conversion between the two. The bounds in Figure 5-1 B and C are the 95% confidence bounds obtained from the fit and were used to provide error on the flow rate value.

The calibration is good but not perfect, as seen by the offset from zero. For the measurements to be made, the system had to be in the dripping regime. In order to observe dripping over a range of flow rates multiple systems had to be used. While the continuous phase was kept as water, the materials for the dispersed phase were changed, thus changing viscosity and compressibility slightly which

could be responsible for the variation observed in the measured rates. By nature of using a single regime only a small range of rates were assessed.

A
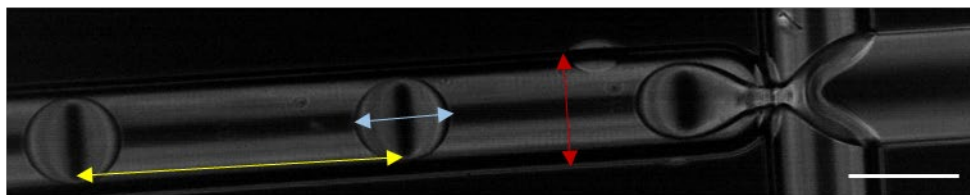
B
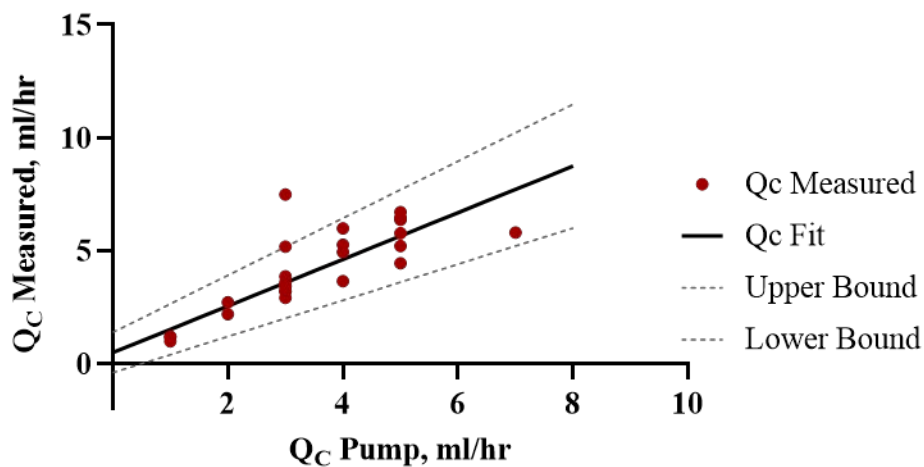
C
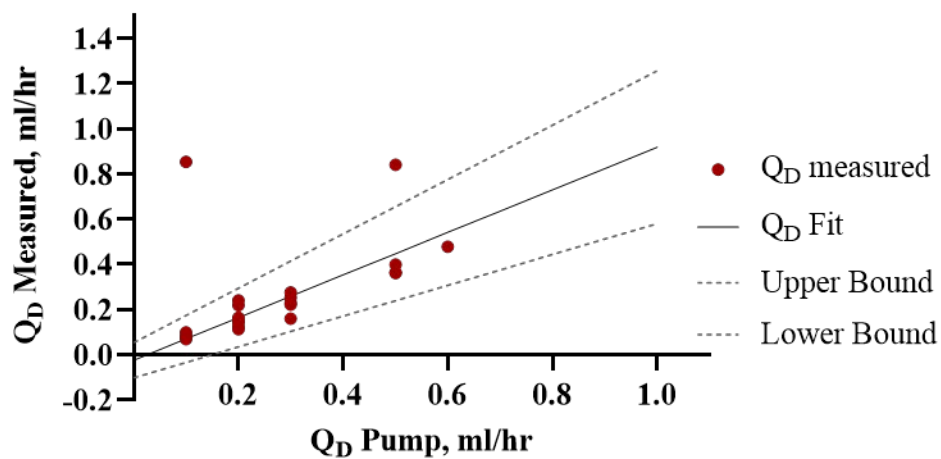
Figure 5-1 (A) Calibration of flow rates were performed using the geometry of the channel (red arrow) and the size (blue arrows) and spacing of the drops (yellow arrows). Scale bar 100 μm. Correlations between the measured flow rate and the input rate for the continuous flow rate, Q_C, (B) and dispersed flow rate Q_D, (C) were generated to calibrate the experimental flow rates.

5.2.4 Viscosity Measurements

Viscosity measurements of the dispersed phase were made using a liquid handling system developed for high-throughput characterisation of potential 3D printing formulations.[164] This methodology was selected due to its ability to obtain measurements with minimal amounts of materials, in keeping with the benefits of using micropipette manipulation experiments.

In brief this technique, depicted in Figure 5-2 A, aspirates a volume of the test sample into a pipette at a set speed. The pressure required to maintain this speed varies due to the shape of the pipette. The pressure as a function of time, Figure 5-2 B, in conjunction with information about the pipette geometry, was used to calculate the dynamic viscosity of the material by balancing the pressures acting against the handler to draw in the liquid.

The procedure and analysis were carried out by Dr Zouxin Zhou, Centre for Additive Manufacturing, University of Nottingham. The viscosity measurements for HMDA with different concentrations of HPhOPA-mPEGMA are shown in Figure 5-2 C. A clear increase was seen for increased surfactant concentration; however, this appears to be approaching the limit of sensitivity for this methodology.
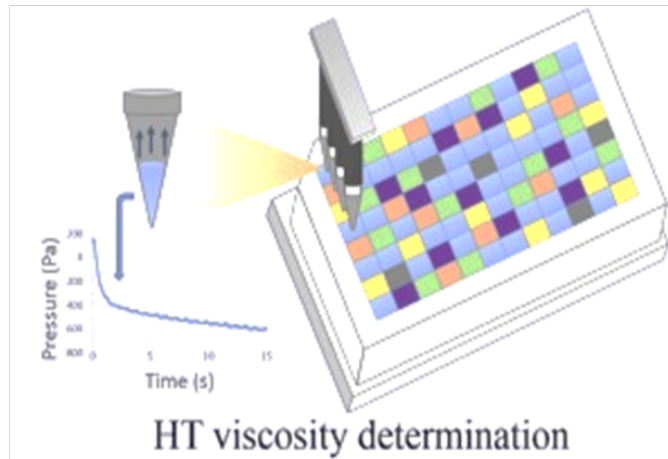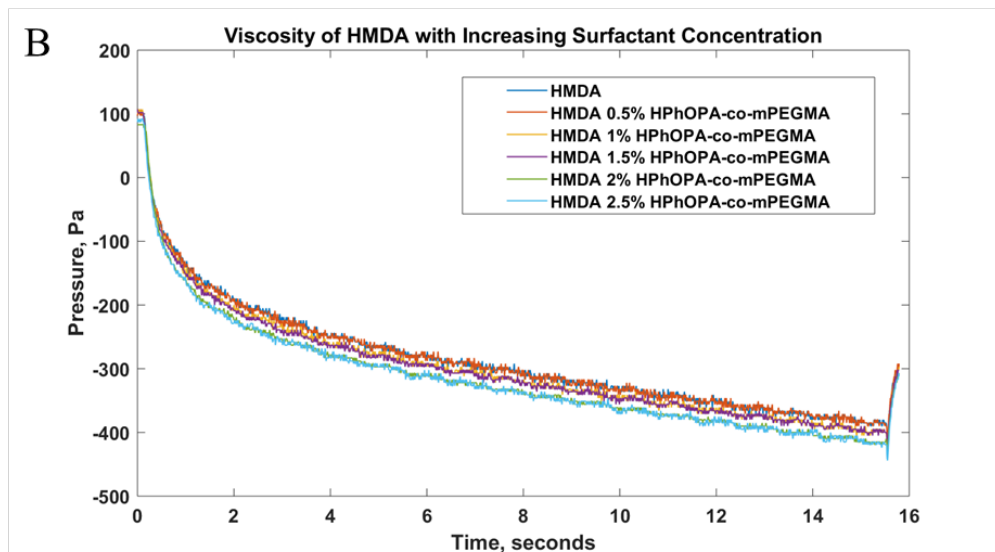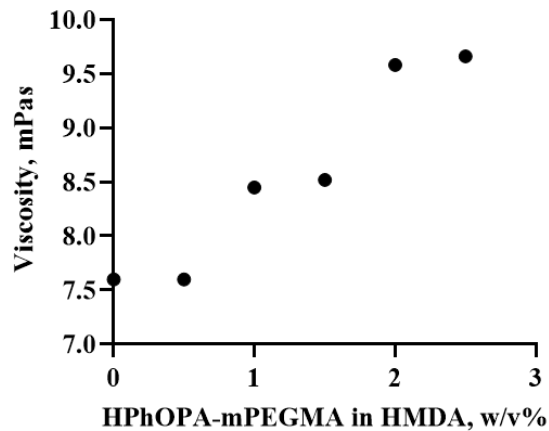
Figure 5-2 Dispersed phase viscosity measurements using a liquid handler system. (A) The handler can assess several samples in parallel. The liquid is drawn into a pipette tip at a set speed. (B) The pressure required to draw in the sample is plotted against time for each sample. (C) The viscosity of HMDA with increasing HPhOPA-mPEGMA concentration was then calculated.

5.3 Results and Discussion

5.3.1 Study of Novel Surfactants

5.3.1.1 Pendant Drop Comparison

As new surfactants, the materials used in this work are not yet well characterised. Furthermore, none of the available characterisations carried out combine the surfactant with the other materials comprising the dispersed phase.[90] Previously, the validity of the IFT measurements using micropipette have been confirmed by comparison to literature values for base systems. As this was not possible in this case, a secondary method was used to provide validation. This was important, since although the methodology has been proven, this is the first time that micropipette manipulation methods have been applied to study monomer systems and it was not known what the behaviour of the novel, comb-graph surfactants in the pipette would be.
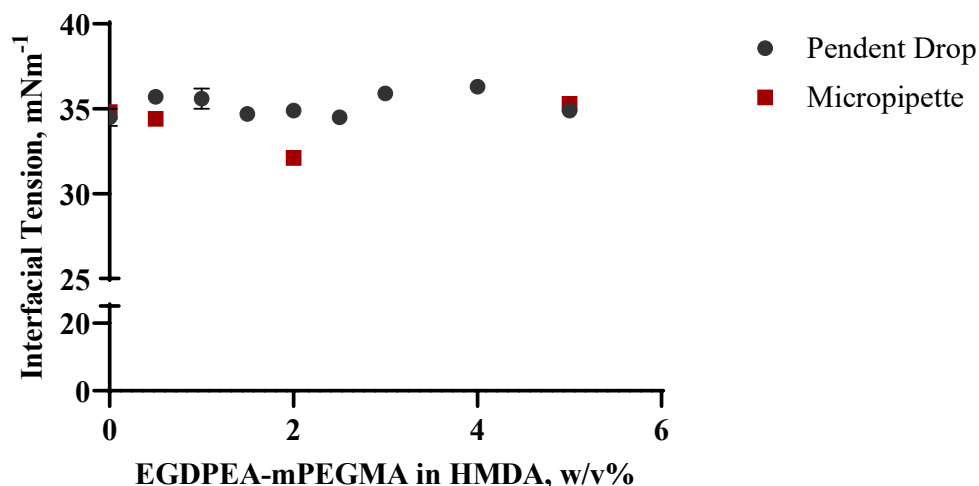
Figure 5-3 Comparison of measurements obtained from the static equilibrium interfacial tension method using micropipette manipulation (red squares) and from the pendant drop method (black circles) Pendent drop values are the mean of between 4 and 10 drops, the micropipette values are the mean of seven repeats taken across two samples, (n=3 and 4). Error bars on both sets are ±1SD.

Surface tension values obtained from micropipette manipulation and the pendant drop method for EGDPEA-mPEGMA surfactant in HMDA are shown in Figure 5-3. The two methods agree for the surfactant free system, with values of 34.5 ± 0.5 mN m^{-1} obtained from the pendant drop and 34.8 ± 0.3 mN m^{-1} from micropipette manipulation (p = 0.4189).

The micropipette data shows a decrease in surface tension for 0.5 and 2% (w/v), while the pendant drop showed an initial increase for 0.5% (w/v) to 35.7 ± 0.6 mN m^{-1} before decreasing, to reach the same value as the base system as more surfactant is added. The value increases again for 3 and 4% (w/v) EGDPEA-mPEGMA but is lower again at 5% (w/v), at which point the pendant and micropipette methods agree (within error) with values of 34.9 ± 0.3 mN m^{-1} and 35.3 ± 0.2 mN m^{-1}, respectively (p =0.1046).

Both the micropipette and pendent drop results showed a similar amount of variation. Neither had a distinct trend, as would have been expected for increasing surfactant addition – for example that seen for PVA in Chapter 4.

From this experiment, it was concluded that the measurements from micropipette manipulation for these systems is as reliable as traditional methods. However, it also points to EGPDPEA-mPEGMA as a poor surfactant.

5.3.1.2 Optimising the Concentration of Surfactants

The values of the interfacial tension between water and four surfactants, EGDPEA-mPEGMA, HPhOPA-mPEGMA, EA-DMAEMA and HPhOPA-DMAEMA in one of two monomers, EGDPEA or HMDA are given in Figure 5-4. A wide range of behaviour was observed.

EGPEPEA-mPEGMA showed small IFT decrease in EGDPEA (Figure 5-4 A) and no significant decrease in HMDA (Figure 5-4 C) ($p > 0.1$ except between samples). This is most surprising in the EGDPEA monomer, as since the hydrophobic part of the surfactant is the same as the core material, the presence of the hydrophilic portion should make the surfactant much more preferable to the interface and so result in an IFT reduction. Instead, it makes only a small difference, reducing IFT from 18.7 ± 0.2 mN m^{-1} to 16.5 ± 0.4 mN m^{-1} with 2% (w/v) surfactant ($p = 0.0047$).
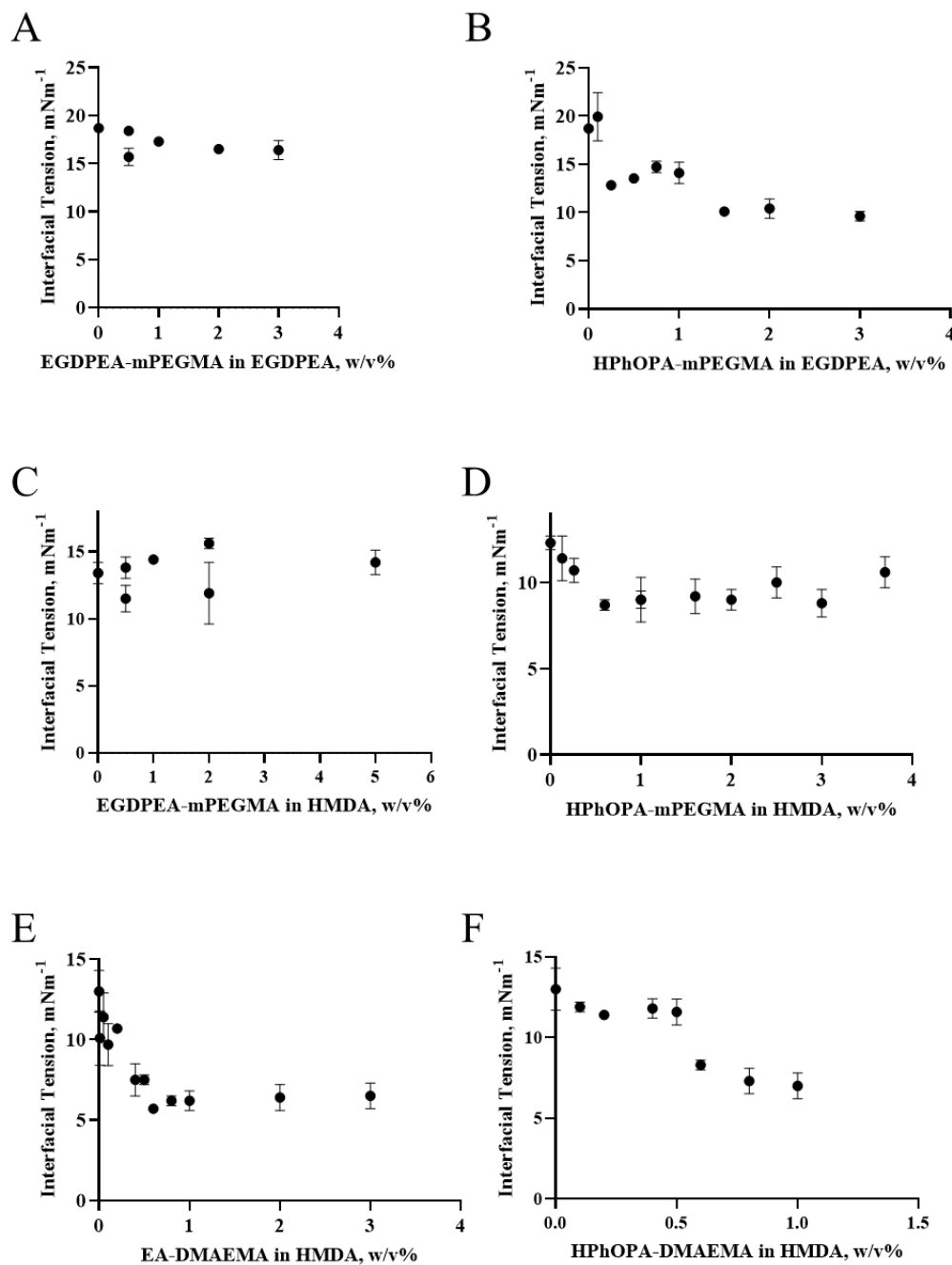
Figure 5-4 Interfacial tension between the water and different concentrations of surfactant. (A) EGDPEA-mPEGMA in EGDPEA monomer, (B) HPhOPA0mPEGMA in EGDPEA monomer, (C) EGDPEA-mPEGMA in HMDA, (D) HPhOPA-mPEGMA in HMDA, (E) EA-DMAEMA in HMDA and (F) HPhOPA-DMAEMA in HMDA. All data points are the mean of 3-4 repeat measurements for one sample. Separate points at the same concentration are obtained from a separate sample. Error bars are ±1SD on the mean.

When added to HMDA instead, there is no significant difference. HMDA/water has a much lower IFT than EGDPEA/water has, indeed a much lower value than EGPEA/water reached even with the addition of EGDPEA-mPEGMA. This suggests that HMDA is more favourable at the interace than the surfactant. This is supported by HMDA's ability to form particles in microfluidics without the presence of any surfactant (A. Dundas et $al.$).[90] However, in the same study, ToF-SIMS of HMDA/EGDPEA-mEPGMA particles showed that EGDPEA-mPEGMA was at the surface rather than HMDA.[90] This suggests it is a slow moving surfactant, with only slightly higher surface affinity than the base monomer. EGDPEA-mPEGMA that is at the surface will still provide physical stabilisation.

HPhOPA-mPEGMA was able to lower the IFT of the EGDPEA base system from 18.7 ± 0.2 mN m^{-1} to 10.1 ± 0.3 mN m^{-1} with 1.5% (w/v), beyond which no significant change occurred (Figure 5-4 B) ($p \geq 0.9871$). This confirmed that the EGDPEA-mPEGMA surfactant is weak, rather than the EGDPEA monomer base system being the cause of the negligible changes seen in Figure 5-4 A.

HPhOPA-mPEGMA was shown to be a good surfactant, reducing IFT in both EGDPEA and HMDA base systems from 18.7 ± 0.2 mN m^{-1} to 10.1 ± 0.3 mN m^{-1} and 12.3 ± 0.4 mN m^{-1} to 8.7 ± 0.3 mN m^{-1}, respectively. In HMDA a plateau around this minimum value was recached at a concentration of 0.6% (w/v), whilst EGDPEA required a higher concentration of approximately 1.5% (w/v). The tendency of the HMDA systems to reach the minimum IFT with lower surfactant concentration than EGDPEA systems is possibly a combination of the

lower initial IFT and a complementary effect between the monomer and surfactant. The other surfactants tested with HMDA, EA-DMAEMA (Figure 5-4 E) and HPhOPA-DMAEMA (Figure 5-4 F) reach their minimum at similar concentrations: approximately 0.6% (w/v) and 0.8% (w/v) respectively.

Comparing all surfactants in HMDA, EA-DMAEMA was the most effective. The IFT reaches a value of 5.7 ± 0.2 mN m^{-1} at 0.6% (w/v) and remains at this value for higher surfactant concentrations. Additionally, it behaves the most like a traditional surfactant; the IFT for increased concentrations follows a smooth curve tending to a minimum, with low variation in the measurement for higher concentrations.

This is useful to feedback into the microfluidics optimisation, providing the minimum concentration required to achieve stable particle production for efficient use of materials. However, it should be noted that the IFT in the microfluidic junction is not necessarily the same as equilibrium IFT.[165] As the timescale for formation is comparable to the timescale for diffusion, larger molecule surfactants/slower diffusing surfactants may not perform as well in processing as would be expected from their equilibrium IFT measurements. As such, the concentration of surfactant required for stabilisation is often greater than the concentration that would be needed to saturate an interface at equilibrium.[124]

5.3.1.3 Investigating the Effect of Surfactant Structure

Whilst most surfactants were soluble in the base monomer, some block copolymers were either not soluble or were only soluble at very low

concentrations. As such, an organic solvent needed to be added to these systems. However, such additions can change the system properties dramatically. To ensure the level of solvent needed would have minimal impact, IFT measurements were conducted using a surfactant that could be solubilised without additional solvent. EA-DMAEMA was soluble in HMDA in its random form but not as a block copolymer. A comparison between HMDA/EA-DMAEMA (random) with and without DCM is shown in Figure 5-5.

At DCM concentrations required for the solubilisation of block copolymers, no significant difference was seen. This allowed for direct comparison between block and random copolymer surfactant systems. In a separate study, the DCM fraction was increased to equal parts with HMDA, in this case the IFT was drastically altered, (Appendix 3 A.)
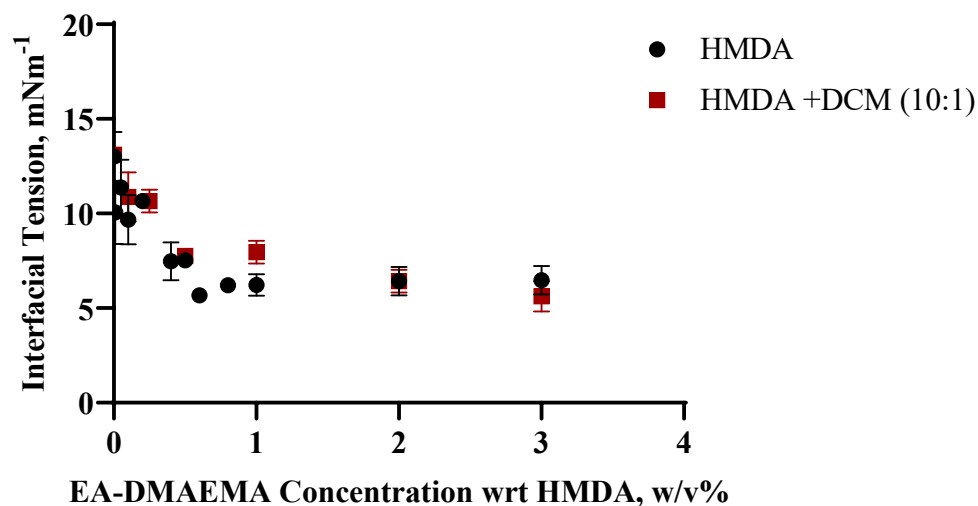
Figure 5-5 Interfacial Tension of EA-DMAEMA (random, comb-graft) in HMDA with (red squares) and without (black circles) DCM. All data points are the mean of 3 repeat measurements for one sample. Error bars are ±1SD on the mean.

It should be noted however, that whilst the IFT remains unchanged at this volume fraction, the impact on viscosity will be non-negligible, impacting the stability in a microfluidics system. DCM must be removed before the HMDA is polymerised to avoid trapped solvent, consequently, a longer residence time will be required prior to UV exposure.

An investigation was conducted into the different IFT impacts of block and random copolymer surfactants formed from the hit chemistry HPhOPA with either mPEGMA or DMAEMA as the hydrophilic component. DCM has been included with the block copolymers to allow for complete solubilisation, however, as shown above it has negligible effect on the IFT of the system so block and random can be directly compared. The results are shown in Figure 5-6.
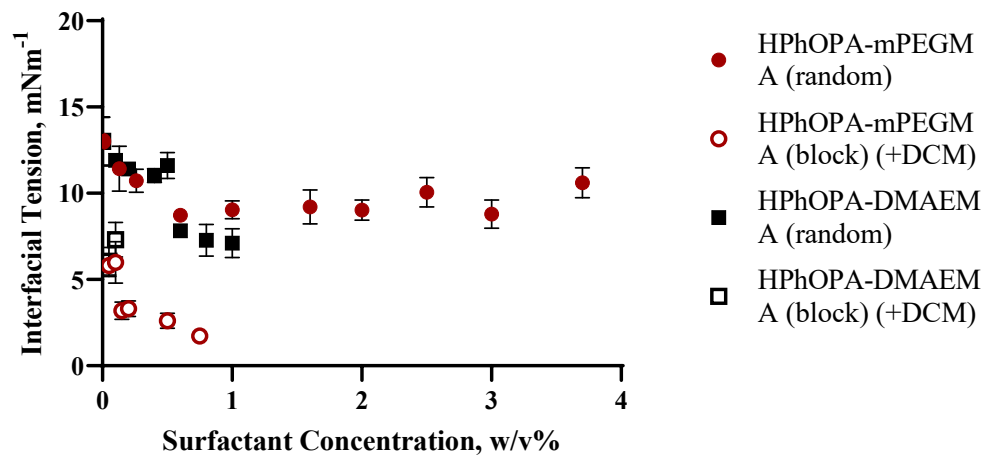
Figure 5-6 Comparison of surfactant structures and hydrophilic groups for the hydrophobic component: HPhOPA. Interfacial tension is shown for a range of concentrations of HPhOPA-mPEGMA as a random (red circle) and block (open red circle) copolymer and for HPhOPA-DMAEMA in random (black square) and block (open black square) archticures. All data points for HPhOPA-mPEGMA (random and block) and HPhOPA0DMAEMA (random) are the mean of 3 repeat measurements for one sample. HPhOPA-DMAEMA (block) uses 3 repeats, however these consisted of less than 10 individual points each. Error bars are ±1SD on the mean.

It is clear from the data in Figure 5-6 that the surfactant structure is having a much greater effect than the chemistry. At low concentrations the random copolymer surfactants - both mPEGMA and DMAEMA – show approximately the same IFT values (~11.4 mN m^{-1}). The same is seen for the block copolymers. Using 0.05% of each surfactant, the p-values comparing the two random architectures is >0.9999 and that for the two block architectures is 0.9741, whilst comparing within the chemistries the p-values for both mPEGMA and DMAEMA are <0.0001

As the concentrations of the random copolymer surfactants increase above 0.5% (w/v) the chemistries begin to give different tension values, with HPhOPA-DMAEMA continuing to lower IFT to 7.1 ± 0.9 mN m^{-1}, whilst HPhOPA-mPEGMA remained approximately constant at 9 ± 0.6mNm^{-1}, with even a slight increase overall.

The block co-polymers gave a significantly lower IFT than their random copolymer counterparts even at the lowest concentrations assessed (p < 0.0001). Measurements of these surfactants were limited to concentrations below 1% (w/v) for HPhOPA-mPEGMA and 0.2% (w/v) for HPhOPA-DMAEMA because above these concentrations there were high levels of mixing at the interface, sticking, and wetting of the walls which led to pockets and/or interfaces that were unable to reach an equilibrium position and "floated" or were non-responsive to pressure change.

The extreme behaviour seen with the block-copolymer surfactants in Figure 5-7 show:

- A: deformed interfaces

- B: excesses of drops forming around the interface

- C: extreme wetting and pocketing
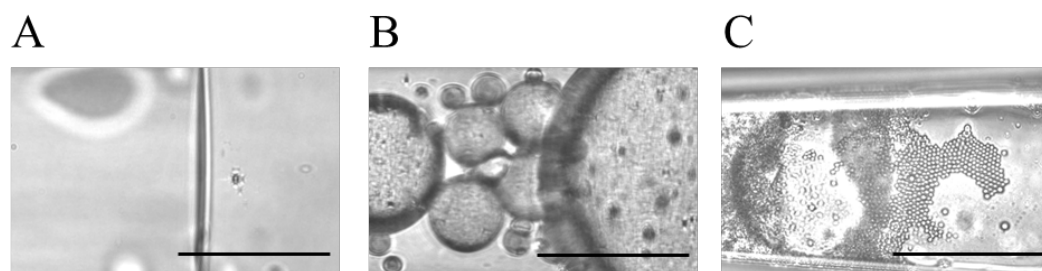
Figure 5-7 Behaviour displayed by water/HMDA systems with block copolymer surfactants. (A) Deformed and non-responsive interfaces. (B) Formation of many large drops of the dispersed phase at the interface which interrupt movement. (C) Wall-wetting of the dispersed phase leading to pockets of one phase within the other. Scale bar 100μm.

In the case shown in Figure 5-7 C, the organic phase has wet the wall to an extent that when pressure is changed the organic phase remains on the walls, and the aqueous phase passes through the centre (or the organic phase moves down the walls, depending on pressure and directions) leading to pockets of organic phase within the aqueous phase and vice versa. These break into small droplets on the micropipette wall, as seen in Figure 5-7 C, in approximately 1 minute. These form rafts, demonstrating they are of similar sizes. Additionally, these small droplets remained in the phase when a large drop was formed as for single particle studies. The persistence of the small droplets within the organic phase over time suggests using these block copolymer surfactants could be a way of creating specific internal microstructures for drops and in turn, particles.

Surfactants that strongly wet the glass cannot be entirely removed and will lead to continual wall-wetting.[120] Since the surfactant is in the dispersed phase in this case, it will prevent any stable droplet formation in microfluidics. Thus, though capable of easily lowering IFT, this surfactant would not be recommended for use in O/W droplet microfluidics. This knowledge is a useful outcome of the optimisation tests.

Receding measurements were often not possible with the monomer/novel surfactant systems due to pinning and jumping. This suggests a higher affinity for glass than the systems in Chapter 4 and previous works.[12,37] Additionally, inclusions formed in the dispersed phases easily.

5.3.2 Prediction of Stable Flow Regions

Flow rates determined using the equations laid out by de Bruijn (Equation 1-18 to Equation 1-20)[126] were calculated using the viscosity obtained as in Section 5.2.4 and the IFT values calculated using micropipette manipulation. These flow rates were compared to the experimentally determined dripping regime flow rates, which were calculated from the input values using the method described in Section 5.2.3. Additionally, the comparison was carried out using the dimensionless capillary numbers (Equation 1-17.)

A comparison between experimental and predicted flow rates for 2% (w/v) HPhOPA-mPEGMA in HMDA as the dispersed phase and DI water as the continuous phase is shown in Figure 5-8 A. The region bounded by a black line depicts the ideal region from the de Bruijn equations. Errors from the measurements of IFT, viscosity and channel size were used to calculate the error

on these bounds and are marked for the points used to calculate the limits. The dark red region depicts the stable flow rates observed in experiments, with the paler region around this showing the error in flow rate as per the calculations in Section 5.2.3. Experimental microfluidic data is courtesy of Dr Adam Dundas, Department of Chemical and Environmental Engineering, University of Nottingham.

The experimental and theoretical stable regions agree reasonably well: 52% of the predicted region was confirmed to give spherical stable drops whilst 63% of the experimentally stable values lay in the bounds of the predicted limits. Stable flow is observed for lower flow rates than indicated by the de Bruijn limit. For low flow rates, drops that appear stable at the junction can often coalesce downstream due to collisions.[57] This may explain the discrepancy observed in that region. Likewise, drop formation outside the expected region has documented previously.[122]
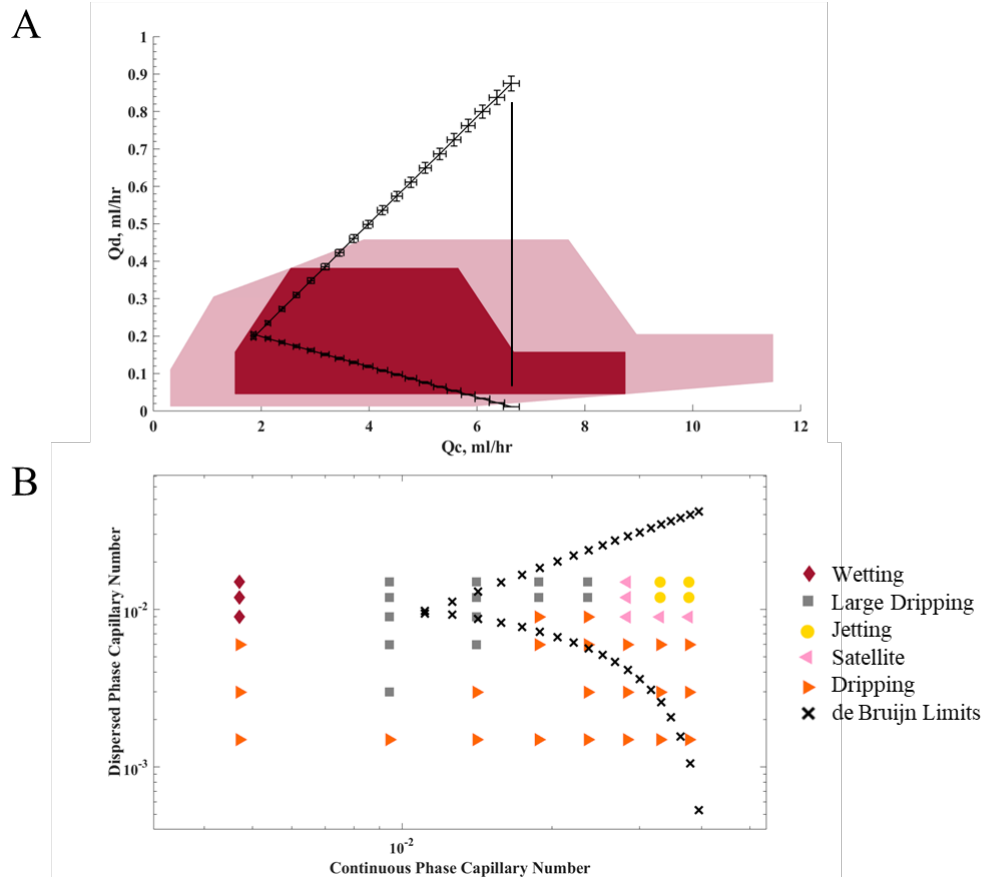
Figure 5-8 Comparison of stable flow rates found experimentally to predicted values from the de Bruijn equations. (A) Dispersed and continuous flow rates are used to create the flow map. Experimentally identifyied dripping regime is in dark red whilst lighter red shows possible variation due to flow error. Stable flows from de Bruijn equations are bound by black lines. (B) The same flow map given in terms of capillary numbers of each phase. Here de Bruijn limits are marked by black crosses. All regimes found experimentally are given: wetting (red diamond), large dripping (grey square), dripping (orange right triangle), satelite drops (pink left circle) and jetting (yellow circle).

An alternative visualisation, given in Figure 5-8 B, compares the data in the form of capillary number. Capillary number is often most useful because it describes the balance between the determining viscous and capillary forces.[123] While this is most commonly used in discussions around stability conditions and processing parameters, it is less intuitive for adjusting flow rates.

The data in Figure 5-8 B follows a similar pattern for the stable regions as the diagram published by Cubaud and Mason[118] (see Figure 1-5 A). Note, in that

work jetting was considered a stable regime as drops were formed, just further from the junction. In this work it is not considered a stable flow.

Capillary numbers for stable dripping in comparable systems (flow-focusing with similar viscosity, flow rates and aspect ratio) is between Ca=10^{-3} to 10^{-2}.[117,166] Here the stable dripping regime is between 10^{-3} and 10^{-2} for the dispersed phase but 10^{-1} to 10^{-2} for the continuous phase. This fits with the argument that flow focussing systems are usually stable for moderate to high flow rates.[167] The limit to switch between the jetting and the dripping regime is minimal, shown by the direct transitions in Cubaud and Mason's work.[118] Here, satellite dripping signals the transition between regimes, allowing corrections to be made.

In addition to dripping, the capillary numbers of the other regimes observed – wetting, jetting, satellite, and large dripping – are plotted in Figure 5-8 B. The limits from the de Bruijn equations are plotted in capillary number form for comparison. Large dripping is a semi-stable region. Drops are too large to remain perfectly spherical and are deformed by the channel, however their appearance is generally regular and controllable, hence its inclusion as a stable region in most literature. Low viscosity drops would be able to recover their shape quickly once in a wider channel/collection beaker. As such, the de Bruijn model includes these regions as stable. This in turn explains the extension of the stable de Bruijn region into high Q_D. Providing the flow remains low enough to be pinched by the continuous phase, larger drops will continue to form. High Q_D was not assessed experimentally. Satellite dripping, where drops form irregularly, sits close to the

stable region, and as such covers much of the rest of the region predicted by the de Bruijn equations, though not strictly a stable region itself.

The prediction and experimental findings do not align exactly, however, it is still a useful tool. All the non-stable regimes are outside predicted region. Therefore, even though it does not predict exactly what will give ideal drops, it successfully identifies the conditions that will not allow stable drop production, thus guiding the user on their choice of processing parameters.

A study forming HMDA droplets by Nisisako, *et al.* found stability required capillary numbers of 0.01 and below, corresponding to the lower end the range found here. However, this was for a T-junction geometry and based on a slightly different viscosity value (6.71 mPas compared to 9.5 mPas).[163]

The de Bruijn equations are analogous to the capillary number equations, with the variable empirical factor *f*, replacing *Ca.* It is supposed to account for all variations, however, as discussed by Cubaud and Mason, universal flow maps cannot be produced– capillary number boundaries are not fixed when the system changes. The deviation between the prediction and measured stable flows suggests that ratio limit (0.000272) is not sufficiently describing the system. A lower ratio value would be needed to reach the region of stability seen for high Q_C, low Q_D, and match to the limit of large dripping. A fixed number does not appear adequate to describe the system,

From the IFT versus HPhOPA-mPEGMA concentration studies, Figure 5-4 D, the IFT values were approximately constant for concentrations of 0.6% (w/v) and

above. Therefore, in terms of reducing interfacial tension, there was no benefit to using higher concentrations. Instead, due to the lower viscosity of the dispersed phase with lower concentrations of surfactant, the range of flow rates for stable particle production should increase, as shown in Figure 5-9. This would allow greater flexibility in size adjustments to the particles, more robust processing, and improved material efficiency.
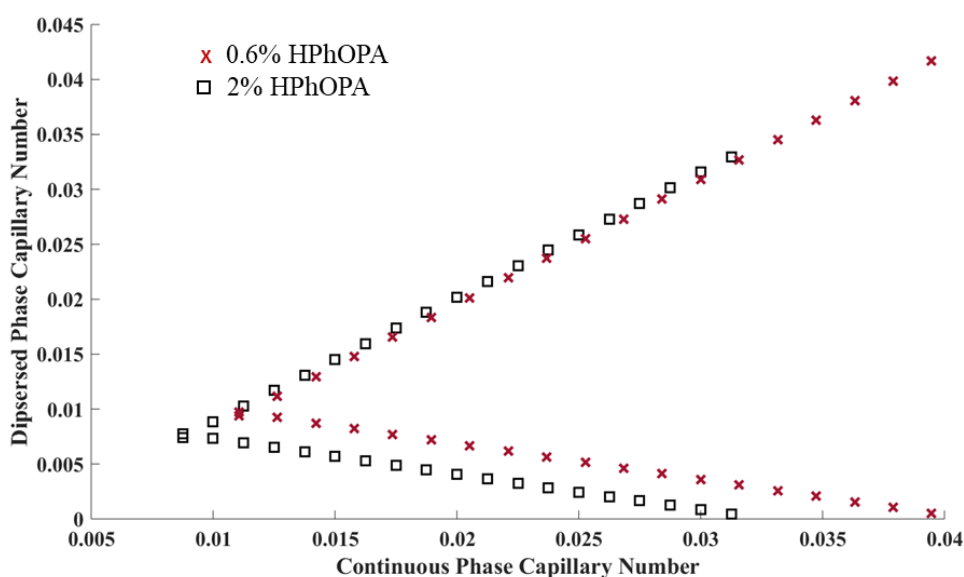
Figure 5-9 Bounds of flow stability predicted by de Bruijn equations for continuous phase of water and dispsersed phase of HMDA with 0.6% (w/v) HPhOPA-mPEMGA (red crosses) and 2% (w/v) HPhoPA-mPEGMA (black squares).

5.3.3 Material Transfer Between Phases

Single particle studies were carried out using the particles' core material HMDA to assess if, and how much, material transfer would occur between the dispersed and continuous phases during particle production. HMDA is partially soluble in water – 0.36 g/L,[168] no data is available for the inverse solubility. Drops

underwent slow dissolution, as shown in Figure 5-10. On the timescale of interest, i.e., the time taken for a drop to travel from its formation at the junction to where it is UV cured (30 seconds or below), the material loss is negligible. However, carrying out these studies led to interesting findings about the material transfer properties.

Ideal dissolution follows the EP equation, as seen in Chapter 4, by which the change in surface area is linear with time. Here instead the drops showed a linear relationship between radius and time. The second point to note is that a steady radius is reached, as shown in Figure 5-10 A, despite there being no solute added to the drop and the surrounding medium presenting sink conditions. Thirdly, comparing the rate of material loss for different initial size drops as seen in Figure 5-10 B, there is a marked decrease in rate with initial drop size. Initial surface area was used to compare drops rather than the initial radius as that would usually be the key parameter. The largest drop had an initial surface area of 7362 μm^2 (corresponding to an initial radius, $R_0 = 48.4$ μm) had a *dR/dt* of 5.8×10^{-3} μm s^{-1} $\pm 2 \times 10^{-5}$ μm s^{-1}, whilst the material loss for a drop beginning at 1521 μm^2 ($R_0 = 22$ μm) was 1.25×10^{-3} μm s^{-1} $\pm 3 \times 10^{-5}$ μm s^{-1}. Additionally, drops remained deformable, though they could not be merged. To confirm that drops were not polymerising the experiments were repeated in darkness, with the microscope lamp being turned on only for images to be taken at regular time points and immediately turned off again. The same behaviour was observed.
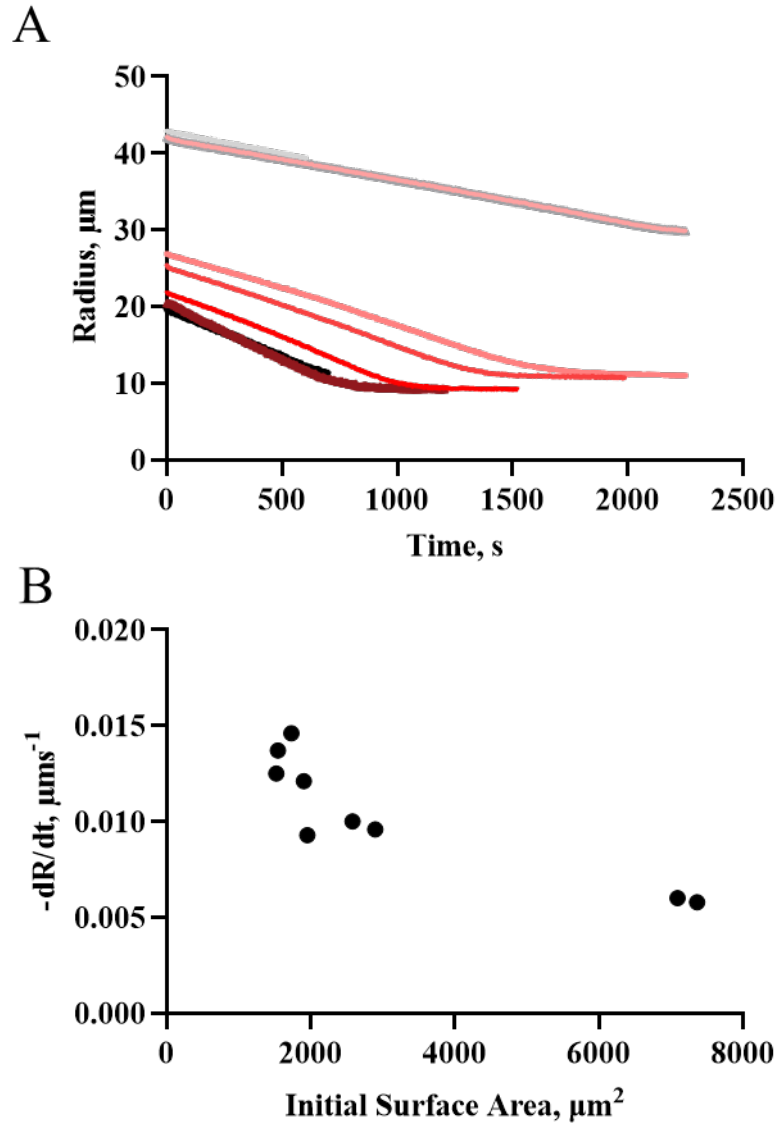
Figure 5-10 Mass transfer of HMDA to water. (A) Dissolution profiles for a series of HMDA drops in water. (B) The rate of change of the drop size as a function of initial drop surface area.

The inverse system of water into HMDA was studied, as material transfer occurs between both phases. Figure 5-11 A shows a water drop and a similarly sized HMDA drop undergoing dissolution into the opposite phase. Water into HMDA behaved much more like an ideal system. In comparison to HMDA, the water

drop's dissolution was very quick, showing a significant difference on the time scale of interest. Therefore, it would be expected that some water would be present in the drops at the time of polymerisation and so be locked in.
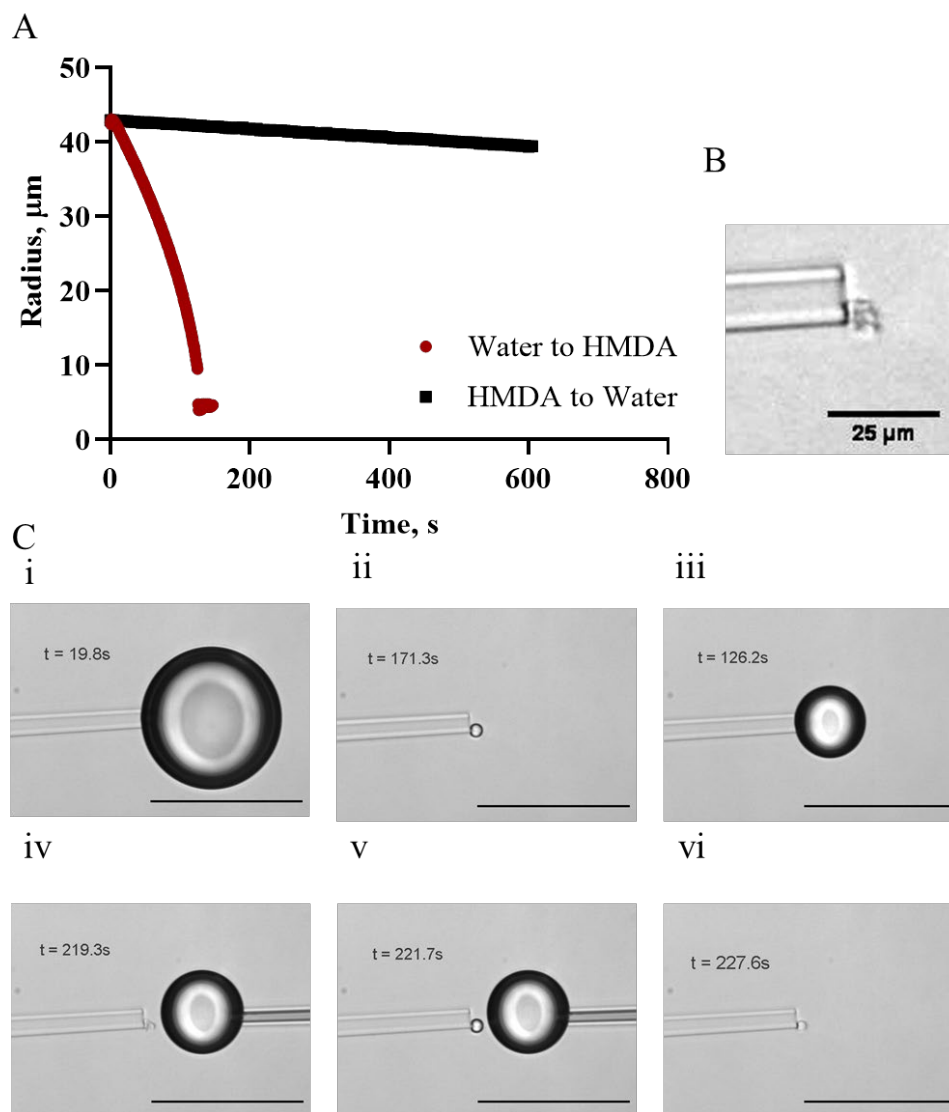
Figure 5-11 Dissolution of water into HMDA. (A) Comparison of drop profiles of a water drop in HMDA (red circle) and HMDA drop in water (black circle). (B) Film like debris remaining after the water dissolution. Scale bar 25μm (C) Dissolution of water into HMDA shown for several key timepoints, the material left behind filled with water from a fresh drop. Scale bars 100μm.

At the end of the study, the water had all transferred to the surroundings. However, a thin, film-like debris remained, shown in Figure 5-11 B. This material must have come from the continuous phase (HMDA) as the water was purified – 18.2 MΩ MilliQ water. Yeung, *et al.* (2000) saw similar behaviour in their micropipette study of single water droplets in a continuous phase of heptanol containing 0.1% bitumen.[9] They determined a layer had adsorbed from the continuous phase onto the drop. Similarly, they also observed that two drops brought together would not merge and concluded the adsorbed layer provided steric stabilisation.

The micrographs in Figure 5-11 C show the dissolution of the water drop and the result of bringing a second, fresh, water drop near the remnant. Diffusing water from the new drop replenished the water that had been removed from the original drop. This water filled the film-like remnant, which only grew to a set size. The cycle of diffusion and replenishment could be repeated many times. Similar results have been demonstration for crystal rehydration (A. Utoft, *et al.,* 2018)[17].

There are a number of insights that can be gained from the data shown in Figure 5-10 and Figure 5-11. The readiness of water to transfer into HMDA, in comparison to HMDA to water explains why, during IFT measurements, drops are observed in the HMDA phase much more frequently and in much higher numbers than in the water phase, and why these drops, unlike those discussed in Chapter 4 Section 4.3.1.2, are not related to the IFT of the system nor are they or as distinct as the drops associated with spontaneous emulsions. This speaks to HMDA having a hygroscopic nature.

As mentioned above, when single HMDA drops are held and studied for their material loss, water is also able to enter the drop. The rate of droplet growth is also dependent on the surface area and so proportional to R^2. Thus, there are two competing factors, one increasing the drop size and one decreasing it. This partially explains the shape of the dissolution profile seen for HMDA drops.

Assuming the lifetime of a drop, between formation and polymerisation, is approximately 20 seconds, the water transferred into a HMDA particle could be over a third of an average drop's volume. Therefore, it is expected that by the time the drops are polymerised there is a significant amount of water contained in the volume. Drops have a radius of approximately 40 μm when formed. The corresponding particles analysed by SEM, dried and in a vacuum, have a radius of 30 μm ± 0.5 μm. This equates to a volume change of 57%. If 33% of this can be attributed to water the rest is likely due to structural changes.

While water transfer partially explains the modified dissolution profile, the oligomeric outer shell cannot be ignored. The HMDA used here has a purity of 80%, one or more of the other compounds present are likely responsible for forming this skin.

A proposed process for the mechanism acting to change the dissolution profile is given in Figure 5-12. In the case of HMDA drops into water, the "skin"-forming material would move from the drop's interior to the interface rather than adsorbing from the continuous phase as in the reversed system. Figure 5-12 A illustrates the proposed motion of molecules that form this layer. Initially, surface HMDA is free to diffuse away from the drop into the surrounding water. As the

secondary component reaches the surface it begins to inhibit the HMDA motion. As this layer thickens over time and eventually becomes more solid – likely as result of oligomers forming – it completely prevents the HMDA from crossing the interface, leading to the radius plateau observed.

This would also explain why the rate is dependent on initial size of the drop. As shown in Figure 5-12 B and C, a drop contains a set volume of the arresting component as it exists at a fixed concentration the HMDA sample. As such, a drop with a greater initial size will always have a thicker boundary than a drop of a smaller initial size when the same radius is reached, and therefore a slower rate of radius change. From the results of the rehydration experiment, it is known that water can pass through this "skin", so it is therefore likely that both this mechanism and influx of water are occurring.
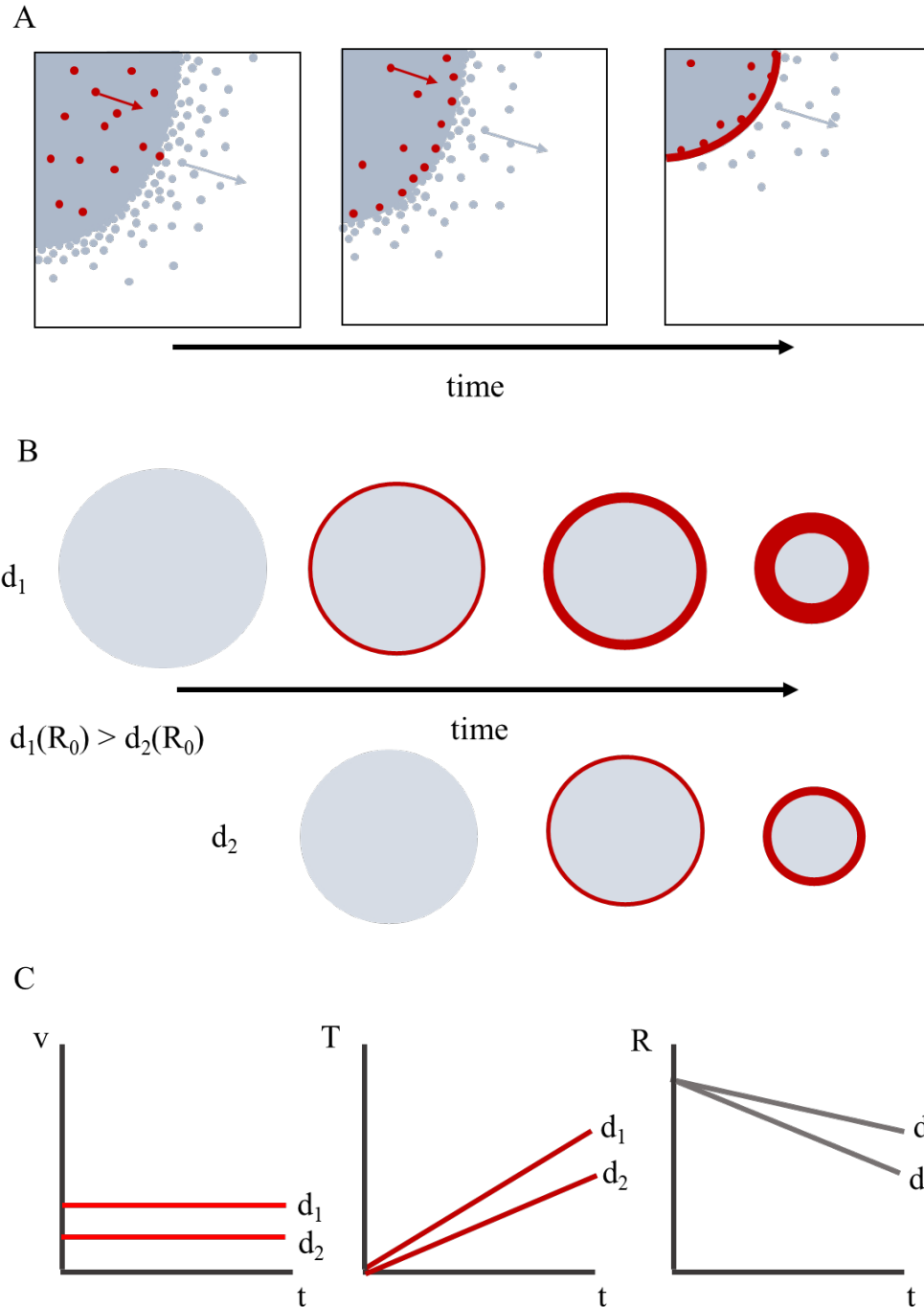
Figure 5-12 Proposed explaination for observed material transfer behaviour of HMDA into water. (A) Movement of a skin forming component to the drop interface, preventing movement of HMDA from the drop. (B) Drops of different sizes contain different volume of the skin-forming material, such that the larger drop will have a thicker skin and slower mass transfer when the two drops reach an equal radius. (C) The effect of the skin-forming material, volume, v, of skin material is constant over time. The thickness, T, of the skin increases over time, leading to a slower change in radius, R, for larger drops.

Finally, the effect of the surfactant on material transfer was assessed for EGDPEA-mPEGMA in HMDA. The rate of radius change was measured for 0.5% (w/v) and 2% (w/v) surfactant. A decrease in the average rate was seen for 0.5% (w/v) EGDPEA-mPEGMA, 0.011 μm s^{-1} ± 0.002 μm s^{-1} to 0.009 μm s^{-1} ± 0.002 μm s^{-1}. For 0.5% (w/v) to 2% (w/v) the averaged rate was approximately constant. Variation between drops meant the changes were not consistent. This variation is caused by the small differences in initial size. Future work of interest would be to look at the different surfactant structures but with a more reliable diffusing material.
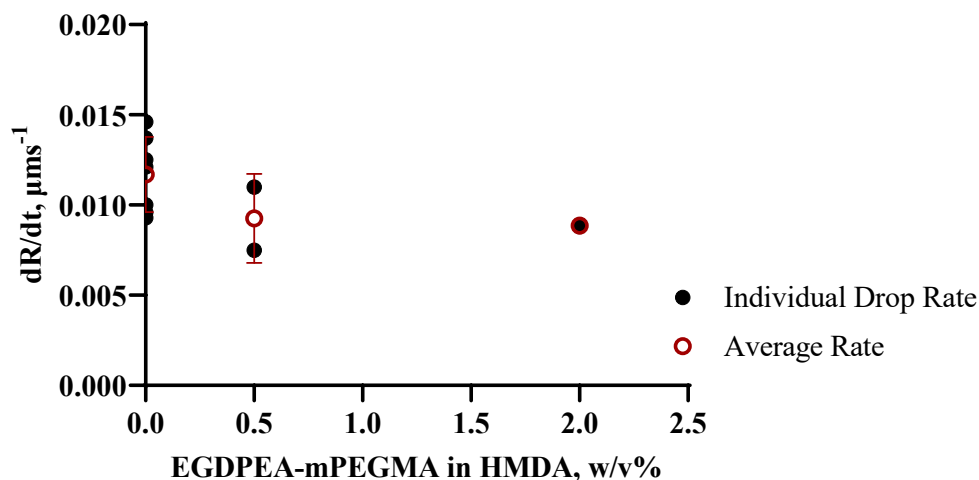
Figure 5-13 Rate of drop size change for HMDA drops containing different concentrations of EGDPEA-mPEGMA. Dissolution rates are presented for individual drop (black) of a similar initial size, and the average of these values is shown in red crucles, error bars are ±1SD of these points around the mean. For 2% (w/v) only one drop was available of a comparable size and so error here is taken directly from the gradient fit.

5.4 Conclusion

Several novel surfactants with bio-instructive chemistries were assessed using the micropipette manipulation technique, static equilibrium interfacial tension measurement. From this the effectiveness of the different surfactant chemistries and structures were compared and optimum concentrations for use in microfluidics for select surfactants identified, meeting the aims set out relating to surfactant characterisation. EGPEA-mEPGMA was shown to be a poor surfactant, unable to reduce interfacial tension. HPhOPA-mPEGMA was able to minimise IFT in HMDA and EGPEA monomers to 8.7 ± 0.3 mNm^{-1} and 10.1 ± 0.3 mNm^{-1} at concentrations of 0.6% (w/v) and 1.5% (w/v) respectively. Both EA-DMAEMA and HPhOPA-DMAMEA were able to lower IFT of HMDA/water with the optimum concentrations found to be 0.6% (w/v) and 0.8% (w/v) respectively. In addition, this work showed that the architecture of these surfactants had a much greater impact on their ability to reduce IFT than the hydrophilic component used. This is the first time micropipette manipulation techniques have been used to assess the interfacial behaviour of methacrylate monomers and polymer surfactants. It is also the most complete assessment of the surfactants in context.

Stable flow rate ranges were calculated using de Bruijn's equations and compared to experimentally defined regions, as was the goal. Reasonable agreement was seen between the two. Combining with the surfactant optimisation data, these calculations were able to offer a suggested flow space for different HPhOPA-mPEGMA concentrations. Between this and the

investigations into surfactant concentration, this work has demonstrated that micropipette manipulation studies can notably improve formulation and processing optimisation for microparticle production using microfluidics.

Material transfer was found to be insignificant from HMDA to water but considerable from water to HMDA. Unusual behaviour was observed for the HMDA drops, with their rate of radius change depending on the initial size and being linear with time. A mechanism has been proposed to explain this behaviour, by which impurities which cannot move into the aqueous phase build up at the interface and prevent further dissolution.

Chapter 6: Informing Droplet Microfluidic Processes Using

Novel Bio-instructive Surfactants

Chapter 6 – Optimisation and Structural Investigation of Biodegradable Microparticles in Droplet Microfluidics

6.1 Introduction

Wound healing is a complex process, involving numerous cell types and non-cellular components.[169] One of the key cell types is fibroblasts. These are found in all connective tissues and are important throughout all stages of wound healing.[170] Given specific cues from the microenvironment, such as stiffness and growth factors, they differentiate into myofibroblasts.[171] Persistent myofibroblast presence at the wound site has been linked to adverse wound healing, such as fibrosis. A fibrotic response is more likely if the wound is severe, repeatedly opened, there is an inflammatory disease, or the foreign body response is triggered.[172] Accelerated wound healing is preferred in order to minimise this risk. Methods to accelerate wound healing, and avoid fibrosis include the use of deliverables, such as chitosan to improve healing, and anti-inflammatory drugs via dressings, microparticles and nanoparticles.[78] An alternative approach of using microparticles as cell instructive scaffolds has been successfully utilised for cartilage, bone, heart and skin healing *in vivo*.[78,79,169]

As part of the Engineering and Physical Sciences (EPSRC)-funded Next Generation Biomaterials Discovery Programme Grant (EP/N006615/1), University of Nottingham, high throughput screens were performed to identify materials that increased and decreased fibrosis, with the aims being able to avoid the foreign body response and to dictate wound healing. After screening and

scale-up studies, two materials were identified for translation into microparticles. These were ethylene glycol phenyl ether acrylate (EGPEA) (pro-fibrotic) and tetrahydrofurfuryl acrylate (THFuA) (anti-fibrotic).[173] These were formed into surfactants as detailed in Chapter 2, Section 2.1.3, by Dr Valentina Cuzzucoli Crucitti, Department for Chemical and Environmental Engineering, University of Nottingham, by copolymerisation with mPEGMA, to give EGPEA-mPEGMA and THFuA-mPEGMA.

Many wound healing applications rely on the particles' ability to degrade and so the core material chosen in this study was PDLLA.[66] The strategy adopted was to create the dispersed phase by dissolving PDLLA and one of the two bespoke surfactants (i.e., EGPEA-mPEGMA or THFuA-mPEGMA). Ethyl acetate was chosen as the organic solvent for the dispersed phase due to its lower toxicity than DCM.[106]

In choosing ethyl acetate for the organic solvent, a secondary avenue of investigation was opened. It has been reported previously that the use of ethyl acetate in microparticle production has led to uneven surfaces, pinholes in particles and visible droplets inside the particle.[75,107,174] However, most studies have noted these features without additional investigation. Proposed mechanisms for these effects differ, as do explanations as to what the internal domains are formed of.

Internal structures are a useful characteristic for biodegradable particles as they can help determine degradability rate of the particles[65] as well as providing specific features throughout the breakdown of the particles. However, previous

work has only been concerned with their removal or prevention, rather than how this internal microstructure can be manipulated.[112,175,176] Creating pores through double emulsions often requires several stages and does not offer a fine level of control.[64,71,177] Although using droplet microfluidics helps to overcome these obstacles, capitalising on pre-existing material effects would be more efficient.

Modified topographies have been shown to impact cell interaction.[30,31,73,78,79,85,86,178] In addition to internal structure, the combination of materials used here were able to generate fine surface structures, seen in both single particle studies and particles from droplet microfluidics. Current approaches for creating topographies require the removal of the phase separating material postproduction. This is critical since the chosen material is often toxic to cells (e.g., fusidic acid). By utilising separation behaviour of materials integral to the final particle application, not only is the toxicity concern removed, but it is more efficient.

It was proposed that a two-surfactant system could be used to modulate the interfacial properties of the oil-in-water microfluidic system whilst retaining the important chemical surface moieties that modulate fibroblast behaviour. As interfacial tension is one of the main driving forces for successful droplet production in microfluidics, it was vital to assess how the bespoke surfactants influenced this property. As for the surfactants in Chapter 5, they had not been previously assessed in emulsions. The first aim of the work presented in this chapter is to assess these surfactants within the context of the chosen microparticle system.

To this end, increasing amounts of the bio-instructive surfactants and PVA were added to 5% (w/v) PDLLA in ethyl acetate and water respectively. All polymeric components, including the core polymer PDLLA, were treated as additives to a pure ethyl acetate/water system. The investigations were conducted using static equilibrium interfacial tension measurements. These enabled the optimal concentrations of the different surfactants to be determined. Whilst the general effects of PVA on interfacial tensions have been discussed previously (Chapter 4) it was necessary to quantitatively understand how it interacted with the other surfactants.

Particles were formulated using droplet microfluidics with the optimised concentrations and the resulting particles were characterised using SEM and time of flight-secondary ion mass spectrometry (ToF-SIMS) to evaluate the success of this approach in developing unique biodegradable particles with cell-instructive surfaces.

Single particle studies were used to understand the effects of surfactant, core polymer concentration and solvent saturation. The objective was to be able to understand the relationship between formulation and microstructure. The effects of these parameters individually and in combination are presented. Particles formed in these studies were also assessed using SEM to provide detail about the particle surfaces.

6.2 Methods and Materials

6.2.1 Materials

PDLLA, PVA and ethyl acetate were used as obtained from the sources given in Chapter 2, Section 2.1. Two bespoke surfactants were formed from ethylene glycol phenyl ether acrylate (EGPEA) and tetrahydrofurfuryl acrylate (THFuA) copolymerisation with mPEGMA to give EGPEA-mPEGMA and THFuA-mPEGMA. These were formed as detailed in Chapter 2, Section 2.1.3, by Dr Valentina Cuzzucoli Crucitti, Department for Chemical and Environmental Engineering, University of Nottingham.

6.2.2 Micropipette Manipulation Studies

Interfacial tension values were obtained through static equilibrium measurements, as described in Chapter 2, Section 2.2.5. Each value presented is the average of a minimum of three repeats and the accompanying error is the standard deviation of those repeats. Single droplets were formed as described in Chapter 2 Section 2.2.6 and recorded until the end of their dissolutions and morphology changes. Analysis was carried out as in Chapter 3.

6.2.3 Microfluidic Particle Production

Particles were required at a higher volume than those in Chapter 5 as they were of interest for further biological studies.[135] To accommodate this need, whilst validating the optimization information gained from the micropipette studies, particles were produced using a Telos® High-Throughput System manufactured by Dolomite Microfluidics. A single Telos® module was used with a 2-reagent hydrophilic chip.

Particles were produced with one of two concentrations of PVA in the continuous phase. 0.1% (w/v) PVA solution in water was used in systems containing one of the novel surfactants (EGPEA-mPEGMA or THFuA-mPEGMA) in the dispersed phase and a 2% (w/v) PVA solution was used for comparison particles. The dispersed phase comprised 5% (w/v) PDLLA solution in ethyl acetate with 0.1% (w/v) of THFuA-mPEGMA or EGPEA-mPEGMA relative to ethyl acetate for the particles with the novel surfactant included.

Emulsions were collected into DI water, and the solvent allowed to be removed from the particles fully before collection and drying. Fluids were controlled using two Mitos P-Pumps connected to a control PC, by Dolomite Microfluidics. 250 µm FEP tubing with a 1.6 mm outer diameter (Dolomite Microfluidics) was used to connected pressure pumps to the Telos module and to connect the outlet to the collection vessel. Bulk particle production, along with the accompanying analysis, was conducted by Dr Adam Dundas, Department of Chemical and Environmental Engineering, University of Nottingham.

6.2.4 Analysis Methods

6.2.4.1 TOF-SIMS

Samples were prepared and analysed by Dr Adam Dundas, Department of Chemical and Environmental Engineering, University of Nottingham, as described in section 2.3.3. Ion fragments unique to EGPEA, THFuA, mPEGMA and PVA were identified. As the fragments form, free hydrogens attach, giving the final composition detected.

6.2.4.2 Scanning Electron Microscopy

Two scanning electron microscopes were used to capture the for images shown below. For imaging the bulk particles produced with the microfluidic system, a Hitachi TM3030 table-top scanning electron microscope was used. Images were taken using a 15 keV beam with magnifications between 30X and 1200X. Size analysis was performed on three regions of interest taken at 250X magnification using ImageJ software. Single particle imaging was carried out on a JEOL 6060LV SEM at 5 KeV to reduce the damage caused by direct charge on single particles. Particles were prepared and mounted as described in Chapter 2 Section 2.3.2.2.

FIB-SEM was employed to inspect the internal structure of particles using the FEI Quanta200 3D DualBeam FIB/SEM by Dr Chris Parmenter of the Nanoscale and Microscale Research Centre, University of Nottingham.

6.3 Results and Discussion

6.3.1 Optimising Surfactant Concentrations

Through the studies shown in this section, the optimum concentration of each surfactant was determined. The effect of the novel surfactants on the water/PDLLA (ethyl acetate) interface is shown in Figure 6-1 A. EGPEA-mPEGMA did not significantly reduce the interfacial tension, rather, it fluctuated around the value exhibited by the surfactant-free system (lowest p-value in comparison of points to 0% surfactant is 0.2399). In contrast, THFuA-mPEGMA produced a slight, but gradual, decrease in the interfacial tension from a value of 6.00 ± 0.80 mN m^{-1} (no surfactant) to 4.89 ± 0.04 mN m^{-1} (2% surfactant)

(p=0.0287). This suggests that these are mild surfactants, agreeing with the findings of the Chapter 5 investigations into related surfacts. This behaviour is comparable to that of EGDPEA-mPEGMA (Chapter 5, Section 5.3.1.2, Figure 5-4.)
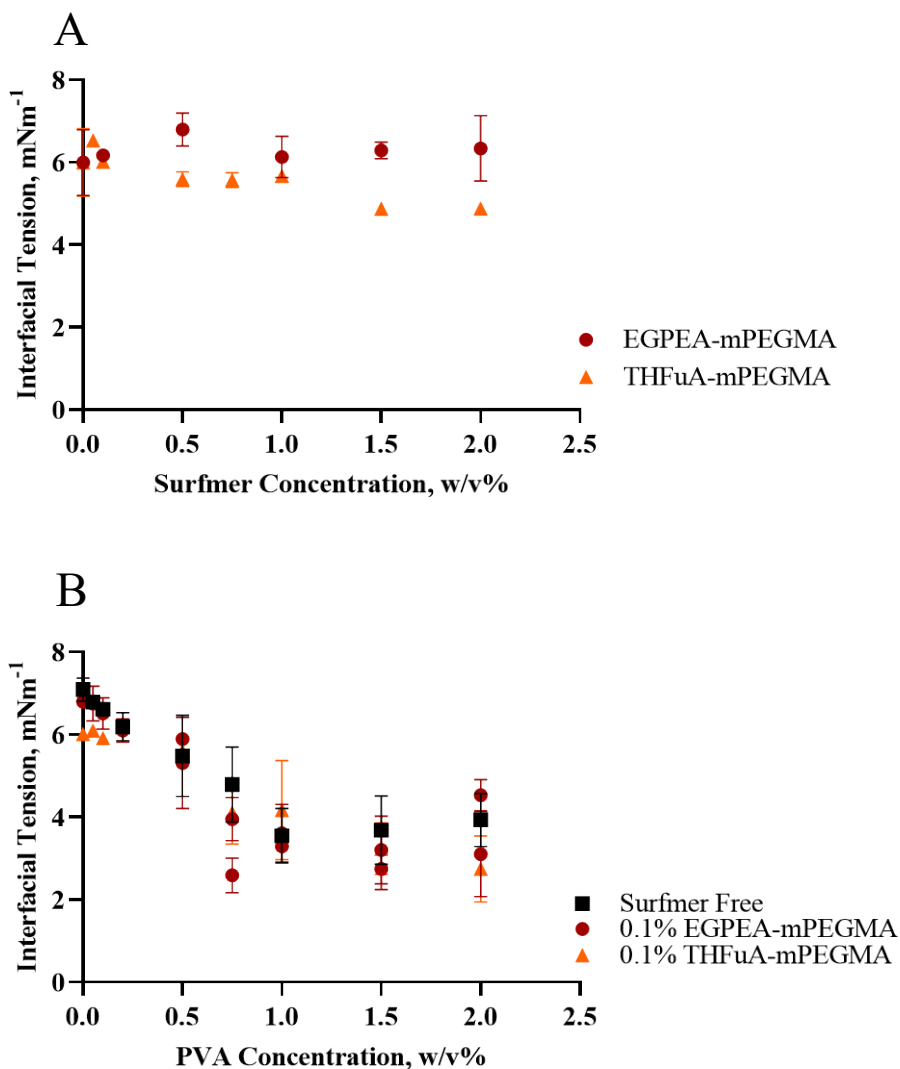
Figure 6-1 Interfacial tension of (A) 5% (w/v) PDLLA(ethyl aceate)/water for concentrations of EGPEA-mPEGMA (circles) and THFuA-mPEGMA (triangles) and (B) range of PVA concentrations in the water phase with no surfactant (squares), 0.1% EGPEA-mPEGMA (circles) or 0.1% THFuA-mPEGMA (triangles) in the dispersed phase. Each point represents the mean of 304 repeats for one sample. Repeated points show data from separate samples. The error bars are ±1SD.

Whilst the decrease in tension achieved with 2% (w/v) THFuA-mPEGMA would improve stability in the microfluidics system, the concentration needed was so high in relation to the core polymer concentration (5% (w/v) PDLLA) it would represent a considerable proportion of the final particle, much greater than a unimolecular coating. Furthermore, as this material is non-degradable a relatively thick coating may restrict the decomposition of the final particles.

Previously, as in Chapter 5 and in A. Dundas, *et al*, (2020)[90] the use of up to 2% (w/v) of surfactant in the solvent-free systems would only result in a thin layer over the surface of the particles. However, in those cases the dispersed phase was comprised of only hexanediol diacrylate monomer, which formed the core of the particle, the surfactant and a photo-initiator. The lack of solvent meant that the ratio of surfactant to core stayed constant throughout the whole process. In this study, the dispersed phase contained the surfactant, PDLLA and ethyl acetate.

If an initial surfactant concentration of 2% (w/v) had been used, as in the comparative study, with 5% (w/v) PDLLA and solvent, then the final particle composition would be approximately 30% surfactant, leading to a thickness of 1.1 μm on a 10 μm radius particle. To maintain biodegradability of the particles, the target is to have a uni-molecular coverage on the particles. This, therefore, necessitated the reduction of surfactant concentration to an initial value of between 0.1% and 0.2% (w/v). This way particles possessed a final composition of approximately 98% and 2% PDLLA and surfactant respectively. However, using surfactant concentrations in this range produced insufficient stabilisation.

The addition of PVA to the aqueous phase to create a dual surfactant system allowed a much greater decrease in interfacial tension. The two novel surfactants, EGPEA-mPEGMA and THFuA-mPEGMA were kept at 0.1% (w/v) to meet the requirement of maintaining a thin coating. PVA was used in concentrations up to 2% (w/v). Comparing the single and dual surfactant systems in Figure 6-1, it is clear PVA is more effective in the high concentration range than either of the novel surfactants are. However, in the low concentration range (<0.5% (w/v)) they behave very similarly. Common concentrations of PVA in the water phase used in microparticle formation are between 0.5% and 2% (w/v).[30,76,96,110,112,163] though some are as high as 5% (w/v) of the aqueous phase.[103,121]   From the trend in Figure 6-1 B, the optimum concentration to minimise the interfacial tension was between 1% and 1.5% (w/v) PVA (Chapter 4). However, to preserve the desired surface chemistry, the PVA concentration also needed to be minimised. Thus, a weak (0.1% (w/v)) PVA solution was used as the continuous phase to improve the stability of emulsions in a high throughput droplet microfluidics set-up.

When small amounts of the novel surfactants were used with relatively high PVA concentrations the interfacial tension values match those of PVA on its own (Figure 6-1). This was expected as the concentration of PVA far exceeds that of the other surfactant. However, for low PVA concentrations the combination of PVA and novel surfactant showed a greater reduction in interfacial tension than either did alone. For 0.1% (w/v) THFuA-mPEGMA with ≤0.1% (w/v) PVA the

interfacial tension was lower than either THFuA-mPEGMA or PVA produced as single surfactant systems, as confirmed by 2-way ANOVA.

The difference in interfacial tension at the required levels was small. For EGPEA-mPEGMA there is no significant change, however, the surfactants are required for their key role in providing the surface coverage of the bio-instructive chemistry. Though the performance of PVA at the chosen concentration is relatively weak, it satisfied the needs of the system – as shown by sustained, monodisperse particle production, seen in Figure 6-2.

At these low concentrations it cannot be said whether the novel surfactant or the PVA dominates. Comparing the effect of PVA with that of the novel surfactants over the same concentration range (comparing between Figure 6-1 A and B) shows that they are much weaker surfactants than PVA. Despite this, they are amphiphilic enough to achieve the desired coating on the particle surfaces, as demonstrated in the surface chemistry analysis in Figure 6-3, thus satisfying their purpose.

The two surfactants showed very different behaviour in terms of spread of the results: in most cases the standard deviation on the THFuA-mPEGMA measurements is an order of magnitude lower than EGPEA-mPEGMA. The difference observed arises from "pinning" of the interface which results in a slight deformation of the interface or a small deviation from the expected position. This affected the individual radius of curvature, R_c, measurements which in turn impacted each interfacial tension measurement. The effects of pinning are increased for materials with a strong affinity for glass and high

viscosity. Both THFuA-mPEGMA and EGPEA-mPEGMA have the same amphiphilic component, which could suggest the difference in behaviour is a result of the bio-instructive chemistry component.

Particles in Figure 6-2 were produced using the microfluidics set-up described in Section 6.2.3, from 5% (w/v) PDLLA in ethyl acetate with either 0.1% (w/v) THFUA-mPEGMA or 0.1% (w/v) EGPEA-mPEGMA in the dispersed phase with 0.1% PVA in the continuous phase or, as a comparison, with PVA at 2% (w/v) as the only surfactant. They were collected in a collection vessel containing DI water and then centrifuged to separate from the water. The SEM images in Figure 6-2 allow a comparison between the two novel surfactants and the PVA systems which acts as a control. The diameters of the particles produced with the two novel surfactants were similar, and the particles were monodisperse, as confirmed by the coefficients of variance being 5.2% and 5.3% for THFuA-mPEGMA and EGPEA-mPEGMA particles, respectively. These results confirm that the addition of 0.1% (w/v) PVA to the continuous phase was sufficient to produce stable particles if used alongside the bespoke surfactant in the dispersed phase. The PVA-only particles were the smallest, 19.9 ± 1.1 µm compared to 23.1 ± 1.2 µm and 23.7 ± 1.3 µm for particles with THFuA-mPEMGA and EGPEA-mPEGMA, respectively, despite the same flow rates. This could be due to the lower interfacial tension delivered by 2% PVA, as lower interfacial tension values produce smaller particles when all other conditions are the same.[109]

A
2% PVA

B
0.1 % THFuA-co-mPEGMA
0.1 % PVA

C
0.1 % EGPEA-co-mPEGMA
0.1% PVA

19.9 ± 1.1 µm
(CV 5.7 %)

23.1 ± 1.2 µm
(CV 5.2 %)

23.7 ± 1.3 µm
(CV 5.3 %)
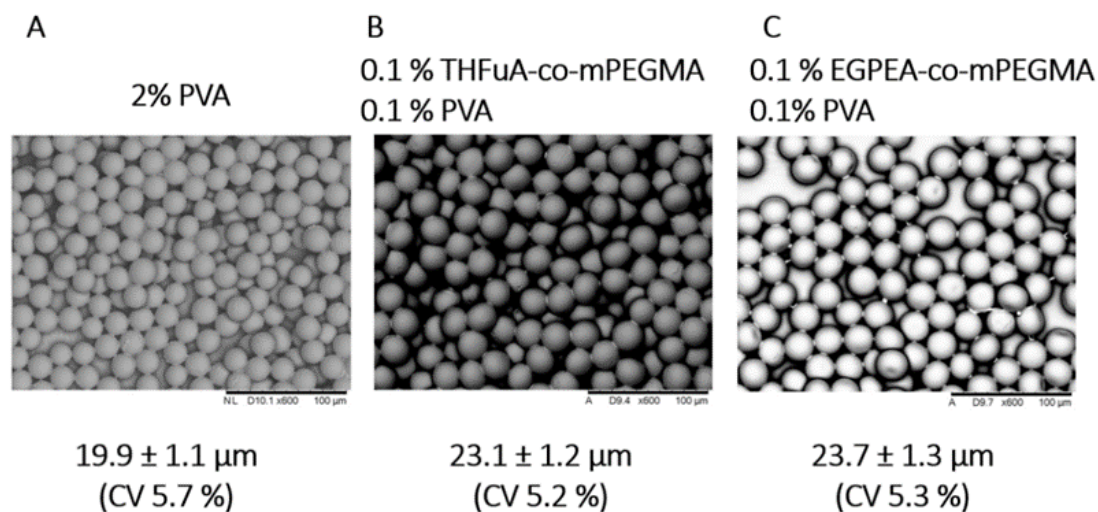
Figure 6-2 SEM analysis of particles produced with droplet microfluidics. Particles were produced from 5% (w/v) PDLLA in ethyl acetate with (A) 2% PVA in the continuous phase, (B) 0.1% THFuA-mPEGMA in the dispersed phase and 0.1% PVA in the continuous phase or (C) 0.1% EGPEA-mPEGMA in the dispersed phase and 0.1% PVA in the continuous phase. Scale bar 100µm.

Unique ions were identified using ToF-SIMS allowing the different surfactant structures used in the microfluidic particle preparation to be confirmed. $C_6H_5^+$ and $C_5H_9O^+$ were identified as unique ions for EGPEA-mPEGMA and THFuA-mPEGMA, respectively. $C_4H_9O^+$ was shown to represent PVA. The result of the ToF-SIMS analysis on these particles is shown in Figure 6-3.
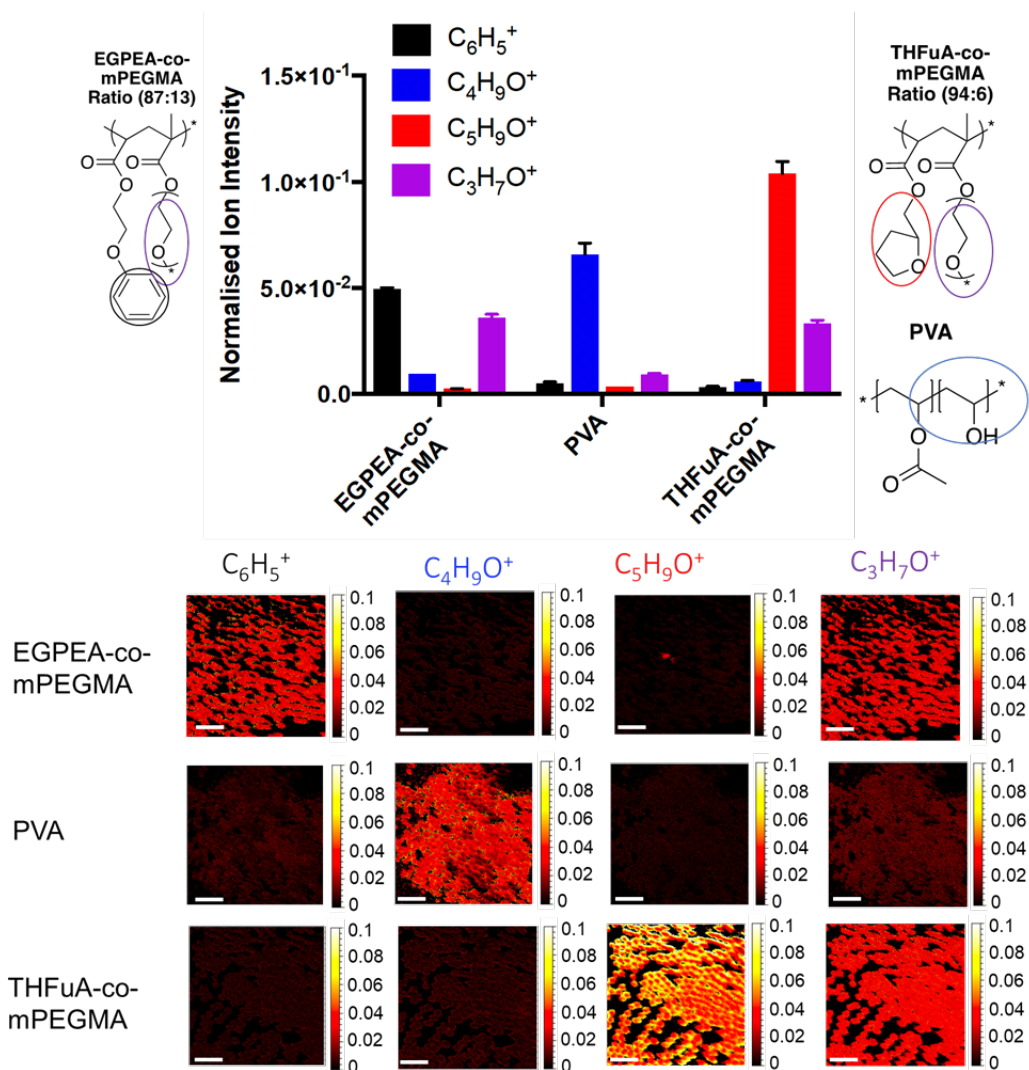
Figure 6-3 ToF-SIMS analysis of microparticles, showing the intensities and chemical map images of 3 unique ions associated with the 3 surfactants: $C_5H_5^+$(EGPEA-mPEGMA), $C_5H_9O^+$ (THFuA-mPEGMA) and $C_4H_9O^+$(PVA). Error bars are the standard deviation of repeat measurements (n=3) Scale bars are 100μm.

The unique ions representing each chemistry are clear on the surface of the particles which are based on that surfactant, and only those particles. Additionally, PVA could be seen on both particles with THFuA-mPEGMA and EGPEA-mPEGMA at low levels, 4% and 10% respectively, demonstrating that the surface functionality is dominated by the target chemistry introduced into the dispersed phase despite there being the same concentration of each surfactant.

The dominance of the bio-instructive surfactants may be due to them being in the dispersed phase and so concentrating on the initial droplet interface or that PVA, by being in the continuous phase, is diluted and so, even though they all have a similar driving force, the result is a lower coverage of PVA on the final particle. An alternative explanation may be that PVA contributes to the initial stability, as evidenced by unsuccessful emulsion production in its absence and the surfactants migrate to the surface over longer timescales to provide lasting stabilisation, with their structure providing steric hindrance to prevent aggregation during the later stages of production, as was experienced by the HMDA droplets in Chapter 5. The competing effects could be investigated through their dynamic interfacial tensions.

The viscosity changes in the dispersed phase, due to the addition of the surfactants at this concentration, can be considered negligible compared to the contributions of the core polymer and solvent, whose proportions were initially selected to satisfy this limit. However, it is possible the improved stability observed was due to the viscosity ratio of the two phases changing due to the addition of PVA producing a small change in the continuous phase viscosity. This is a potential avenue for future investigation but was beyond the scope of this work.

6.3.2 Solvent Removal from Droplets

Solvent removal studies were carried out as for the dissolution studies in Chapter 4. The focus here was the comparing the time taken for drops of increasing size and initial concentration to complete their solvent removal. This information is useful to microfluidics processing as the solvent needs to be removed before the particles are collected otherwise they can coalesce on collection.[112] The time taken for drops of varying size to reach a steady diameter in micropipette studies for 1% and 5% (w/v) PDLLA in ethyl acetate is shown in Figure 6-4. The relationship (Equation 4-2) to describe the radius as a function of time can be rearranged to estimate the time taken for a drop to become a solid particle:

$$t = \frac{\rho\left(R_0{}^2 - R_f{}^2\right)}{2D(1 - f)}$$

Equation 6-1

where the final radius, R_f, is given by $R_f = c_{PDLLA}R_0$. The diffusion coefficient used was that found in Chapter 4.

The assumptions here are that the dissolution is complete, and the initial concentration is exactly known. From the findings shown in Chapter 4, this is not always the case but provides a good estimation, especially in low concentration droplets.
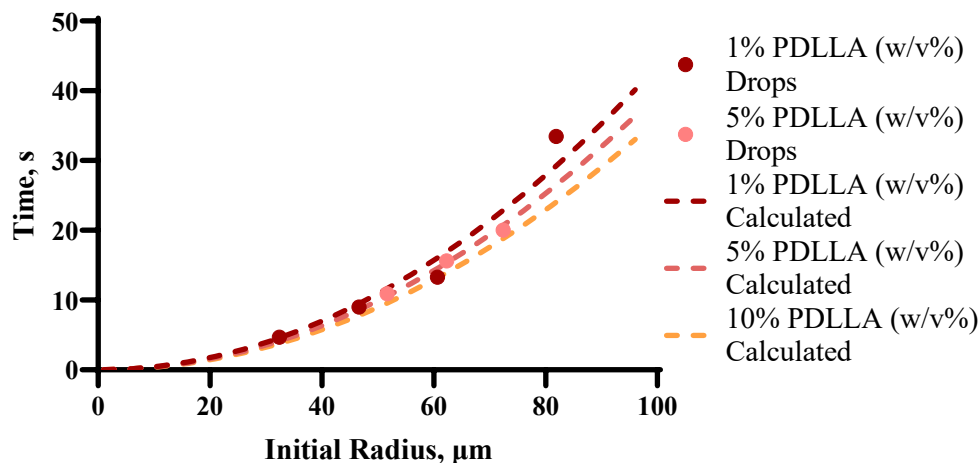
Figure 6-4 Solvent removal studies were used to inform on the collection vessel properties to reduce aggregation. The estimated time for solvent removal for drops of 1%, 5% and 10% are shown for different starting radii (dashed lines), calculated using the Epstein-Plesset model. Circles in corresponding shades give the time taken for example droplets.

From the information in Figure 6-4, 5% (w/v) PDLLA droplets starting at an initial radius of 80 μm should be given 25 seconds of flow in as close to sink conditions as possible to ensure full solvent removal. Diffusion will be limited during production as, unlike in the micropipette studies, many drops are present at the same time.

There are additional conditions that are present in microfluidic processes that cannot be replicated in micropipette studies. These include the effects of flow and saturation. Sink conditions provide a constant saturation of the continuous phase (generally zero) which is the driving force for dissolution and so allows faster solvent removal than in the chip or tubing of the microfluidics system where there are many drops in a small volume and so saturation of the continuous phase will be expected.

Conversely, the effects of flow in microfluidics could speed up removal. To an extent these effects will counter one another. However, as a precaution, advised times should start when droplets leave the tubing and entre the collection vessel where conditions are closer to those in the micropipette. In this case the flow particle speed will depend on the gravitational and drag forces acting on the particle. The presence of aggregation, should the particles be collected too quicky, suggests there is residual solvent still being removed. Alternatively, it may be that solvent present in the continuous phase is sufficient to dissolve the outer layer of the particle enough to encourage sticking. In either case this presents an opportunity for further improvements to be investigated.

6.3.3 Controlling Particle Topography and Internal Structure

6.3.3.1 Formation of Internal Structure within PDLLA Drops

When ethyl acetate was used as the solvent for the dispersed phase, additional structures appeared inside the main drop. During this discussion the term "sub-drops" will be used to refer to these due to their drop like appearance. Figure 6-5 and Figure 6-6 show the formation of these sub-drops in drops of 1% and 10% (w/v) PDLLA, respectively. In each figure micrographs of key moments in the sub-drop formation are shown in relation to the drop dissolution. The first appearance of sub drops in each case is shown in micrograph "A". This can occur very early in the dissolution or even during the formation of the droplet, though only a few are present at this point. Significant numbers of sub-drops appeared later, shown in "B". The increase in sub-drop number was rapid at this point and

the sub-drops quickly became well defined and reached a maximum number, as in micrograph "C".
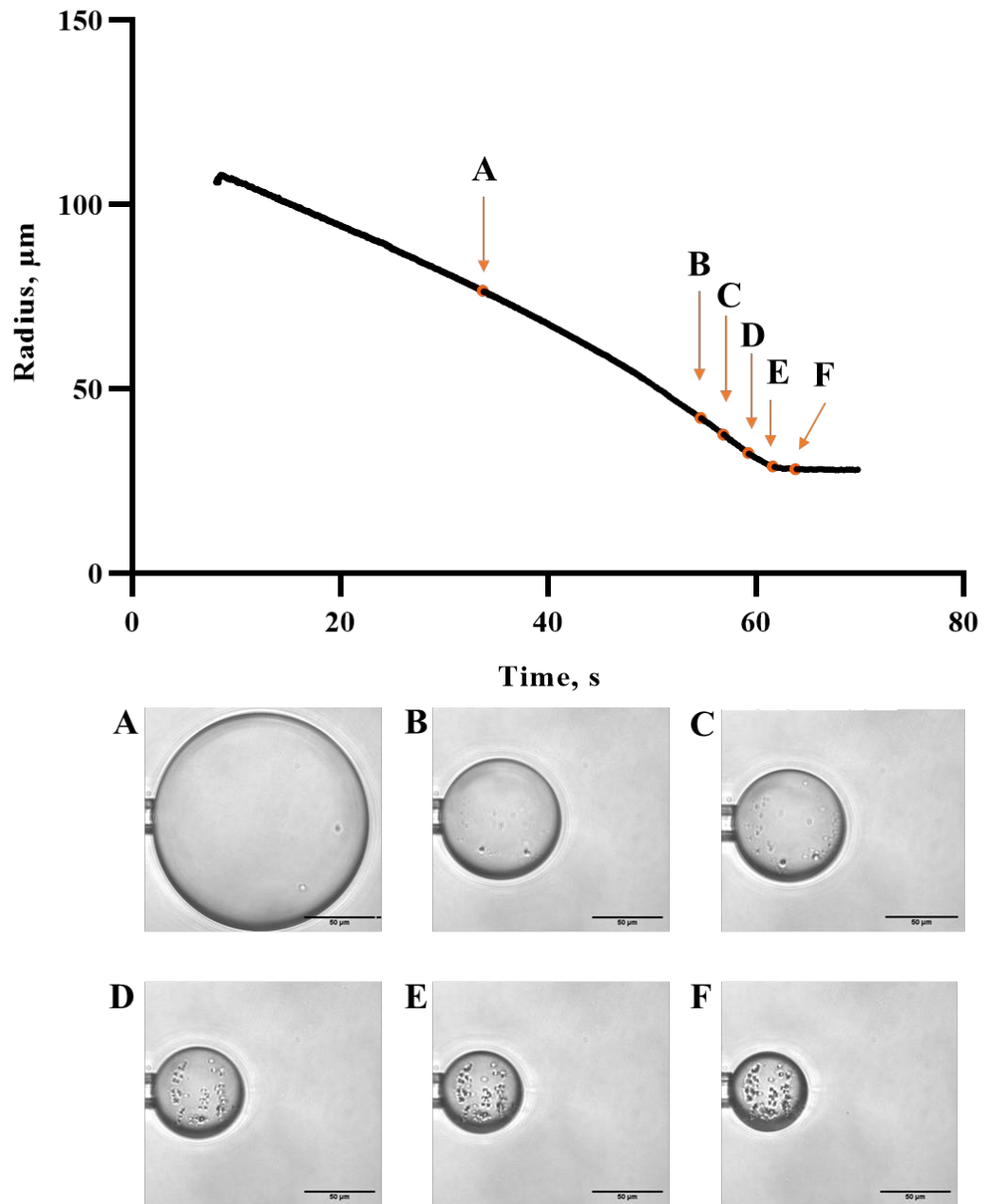
Figure 6-5 1% (w/v) PDLLA (ethyl acetate) dissolution profile. Micrographs show key points in the internal droplet formation. (A) first sub-drops appear, (B) more sub-drops appear, (C) sub-drops are clear, (D) sub-drops stop moving, (E) viscous boundary and (F) steady size drop. Scale bars 50μm.

Comparing positions between frames indicated the sub-drops moved freely inside the drop up until shortly before the VB was reached, when their position froze, and their only movement was radially inwards as the drops shrank further. This free movement suggests that the viscosity of the polymer phase is not what prevents the sub-drops merging. "D" shows the point at which the motion stopped, whereas the VB implied by the dissolution curve is shown a short time later in "E". The location of the sub-drops remained the same from "D" onwards as the drops continued to slowly shrink after the VB was passed, as can be seen by comparing "D", "E" and "F" in the figures. In small drops the movement is limited whereas, in larger drops this movement allowed convection currents inside the drops to be visualised, confirming earlier suspicions that such currents were present.

The occurrence of such structures has been observed previously when microspheres are formed using ethyl acetate as the dispersing solvent.[112,175] A number of these studies were considering W/O/W double emulsions and as such did not distinguish between the structure caused by the first aqueous phase and any additional sub-drops in the polymer.[110,174] Other studies have noted the appearance but have not been concerned with exploring their nature. It appears that, to an extent, this is an accepted property of such systems and frequently ignored.[75,111] There are multiple hypotheses as to what the sub-drops are formed of: water, ethyl acetate, precipitated polymer, and isolated domains of the dispersed phase.
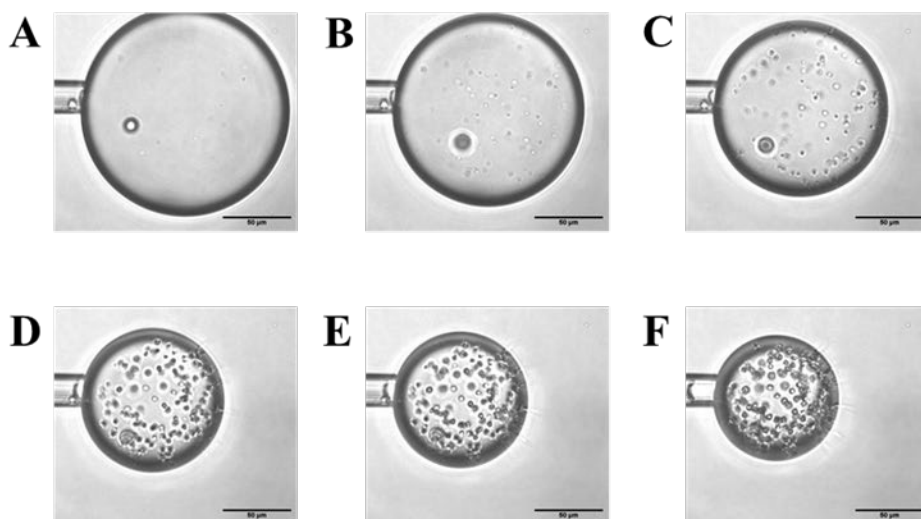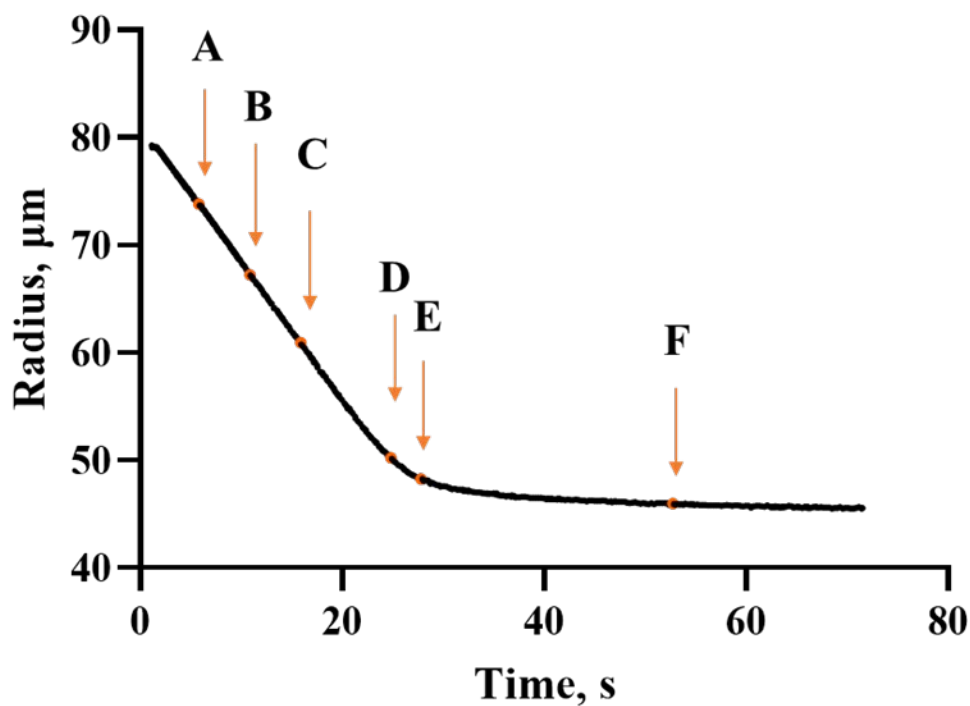
Figure 6-6 10% (w/v) PDLLA (ethyl acetate) dissolution profile. Micrographs show key points in the internal droplet formation. (A) first sub-drops appear, (B) more sub-drops appear, (C) sub-drops are clear, (D) sub-drops stop moving, (E) viscous boundary and (F) steady size drop. Scale bars 50 μm.

It is known that PDLLA, and indeed all forms of PLA are hygroscopic and so could be capable of drawing in water from the continuous phase.[156] However, given that no such behaviour was seen when DCM was used instead of ethyl

acetate, it is unlikely that this would be the cause. The much more likely path of water inclusion comes from the ethyl acetate itself. Water is much more soluble in ethyl acetate than it is in DCM (water solubility in ethyl acetate is 3.3% (w/w), whereas in DCM it is only 0.2% (w/w)).[179] As discussed previously, mass-transfer between the drops and the surrounding medium is a two-way process. Water can be drawn into the ethyl acetate present in the drop up to the saturation limit. However, as ethyl acetate is more soluble in water than the reverse system, and the amount of water in the continuous phase far exceeds the content of the drop, the ethyl acetate will continue to move from the drop to the surroundings. As ethyl acetate concentration in the drop decreases, the water and polymer can no longer exist in the same phase and sub-drops of water appear. Polymer viscosity continues to increase, and the water is trapped. Hydration measurements of PLGA microspheres conducted in studies elsewhere have shown they contain high amounts of water, far exceeding the hydration of similar spheres prepared with DCM.[112]

Many of the difficulties experienced with ethyl acetate as the dispersed solvent arise from its fast diffusion into water, even preventing droplet formation through solidifying before shear can be applied.[180] If ethyl acetate became trapped inside the drops due to the outer edges solidifying too quickly it could form into small drops, unable to solubilise the surrounding polymer to an extent to allow for its transport to the interface. Alternatively, the fast removal of ethyl acetate could result in the precipitation of polymer, as has been seen at the surface of some microspheres.[75,174]

An additional explanation revolves around the use of PDLLA specifically. It is likely that this would be an additional effect rather than the leading cause, as presence of sub-drops was limited to the use of EA. When both forms of PLA (PDLA and PLLA) are used the chains can crystalise in different manners. Stereocomplex crystallites, involve both components and have a lower critical solubility than their homocrystallite counterparts. As such the crystallites form early in the dissolution process and as solvent continues to be removed, they are brought closer together and unable to accommodate the change in structure leading to gaps between them which eventually become pores as the solvent is fully removed. This leads to interesting and complex internal and surface structures throughout the microspheres, on the scale observed here.[157] Those studies considered a mix of PDLA and PLLA rather than a copolymer and so the effect would be lessened here.

In both examples shown in Figure 6-5 and Figure 6-6 sub-drops began to appear close to the start of the dissolution. However, for the low concentration drop, it was a while before the sub-drop presence became clear. Comparing the concentration of the polymer in the drops at this point showed no agreement between the drops of different initial starting concentrations. Whilst early drop formation concurs with the hypothesis of polymer precipitation due to rapid solvent extraction, the delay between the initial drops and the later formation would not be present. If only the initial drops formation resulted from precipitation of surface polymer, the secondary formation could be explained by the polymer concentration reaching a critical limit and the polymer precipitating

out. However, the concentration of the two drops at this point differs by almost a factor of two, whereas, if the sub-drops were a result of reaching a concentration limit, they would be expected to do so at the same concentration. Additionally, sub-drops are clearly spherical which indicates that they come from a liquid state. Polymer precipitates are irregularly shaped.[174]

A study into the formation and characteristics of the sub-drops was carried out across a range of initial drop concentrations and sizes. An example set of results, corresponding to the 1% (w/v) PDLLA drop shown in Figure 6-5, is shown in Figure 6-7. The number of sub-drops, Figure 6-7 A, experiences a sharp increase around 50 seconds after dissolution starts, as seen in micrograph B in Figure 6-5. Despite the increase in drop number, the radius of sub-drops remains constant throughout, Figure 6-7 B. Therefore, there was no aggregation, flocculation or Otswald Ripening occurring between sub-drops. Once a sub-drop formed it maintained its size. Growth could be expected if precipitated polymer acted as a nucleation site.
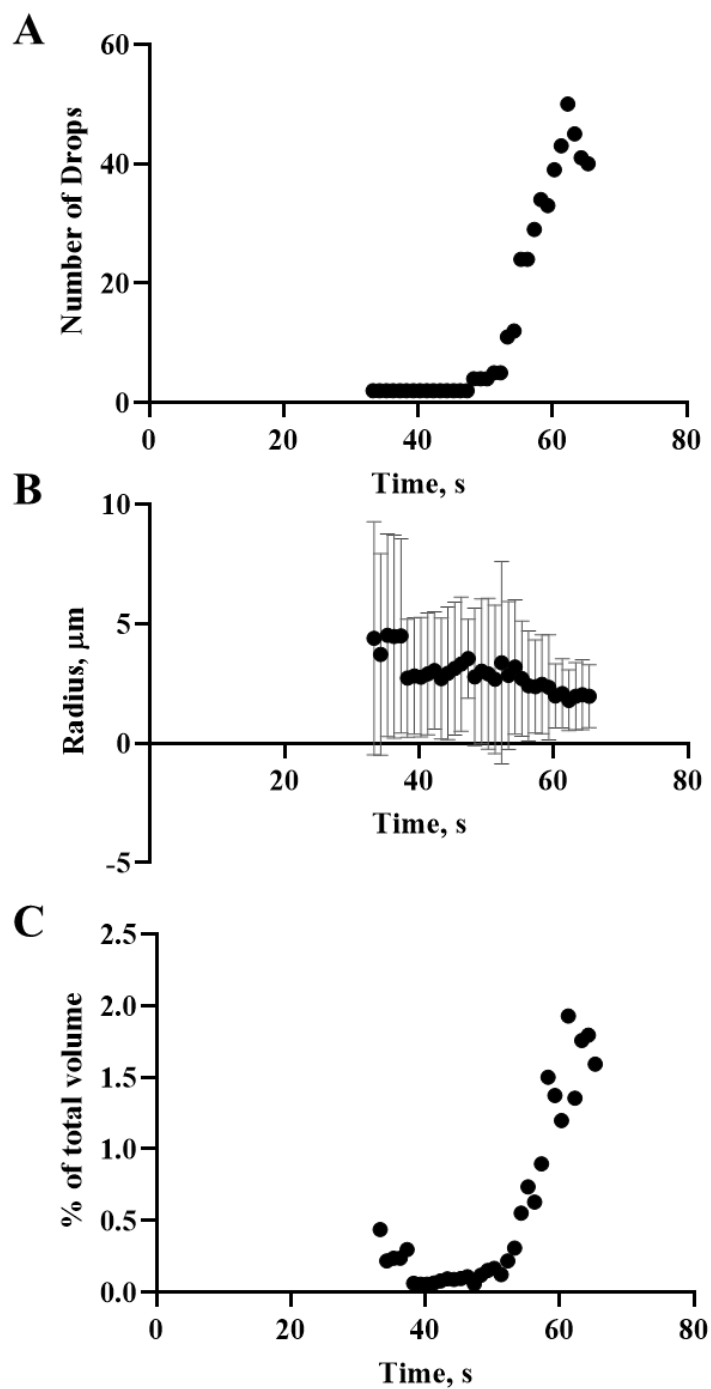
Figure 6-7 Analysis of sub-drop formation in a 1% (w/v) PDLLA (ethyl acetate) drop undergoing dissolution into water. (A) Number of sub-drops as a function of time after the main drop formed, (B) average radius of the sub-drops present and (C) the total volume of the main drop occupied by the sub-drops. For the radius calculations in (B) all drops visible at that timepoint were included and the average mean radius given here. The error bars represent one standard deviation of radii values around this mean.

The total volume occupied by the sub-drops is directly proportional to the number of drops. The initially higher radius seen in Figure 6-7 B and correspondingly the higher volume percentage in Figure 6-7 C is a result of the image analysis limitations: sub-drops not in the focal plane can appear larger than they are. Additionally, the total volume of the sub-drops at the end of dissolution was not high enough to account for the deviation from expected size and/or concentration discussed in Chapter 4. Therefore, no matter what the sub-drops are formed of there was still additional solvent and/or water present in the drop.

While sub-drop size remained approximately constant across all drop systems, the number of drops present increased with initial drop concentration, as seen in Figure 6-8. This supports the idea of polymer precipitate. Trapped solvent could also be increased in this case. If the outer layer solidified too quickly to permit its removal, the result would become more extreme the higher the initial polymer content as that corresponds to a higher initial polymer content near the surface and less solvent needing to be removed to cause the surface to solidify. However, trapped water cannot be supported as simply this way because there is less time and availability for the water to be drawn in.
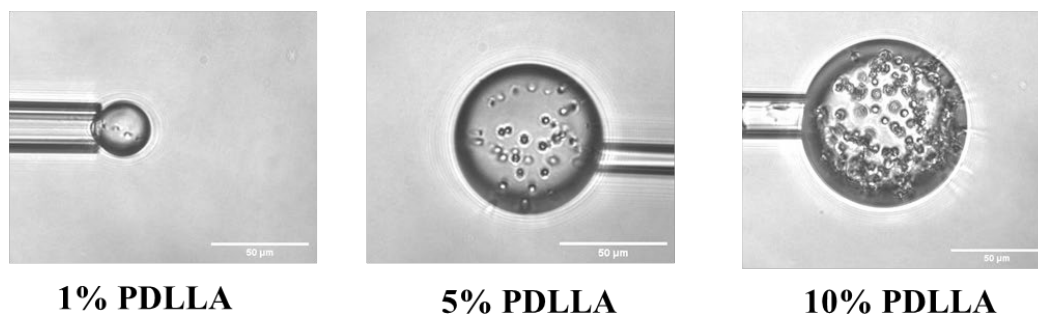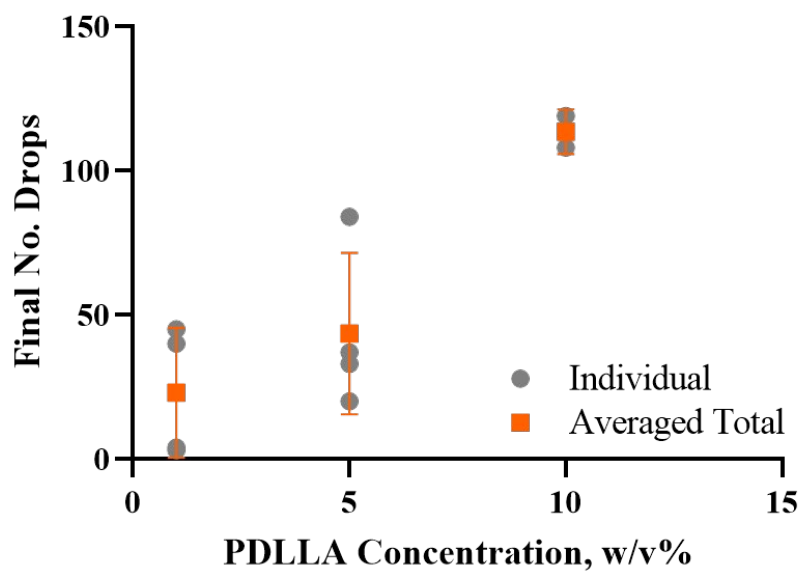
Figure 6-8 Number of sub-drops present in drops beginning as 1%, 5% and 10% (w/v) PDLLA. The number of -sub-drops for individual drops is given as well as the average. Error bars are the standard deviation on the average using these points. Scale bars are 50 μm.

Despite passing the VB and reaching a steady size, drops have generally not reached the final phase of dissolution at the times recorded – they are not in a glassy state. Figure 6-9 A shows a drop removed from the chamber shortly after dissolution appeared to be finished. The internal structure of the drop was completely lost within a few seconds of having been exposed to air. This would not be the case for polymer precipitate, instead suggests a highly volatile composition, such as trapped ethyl acetate.

A

B

i

ii
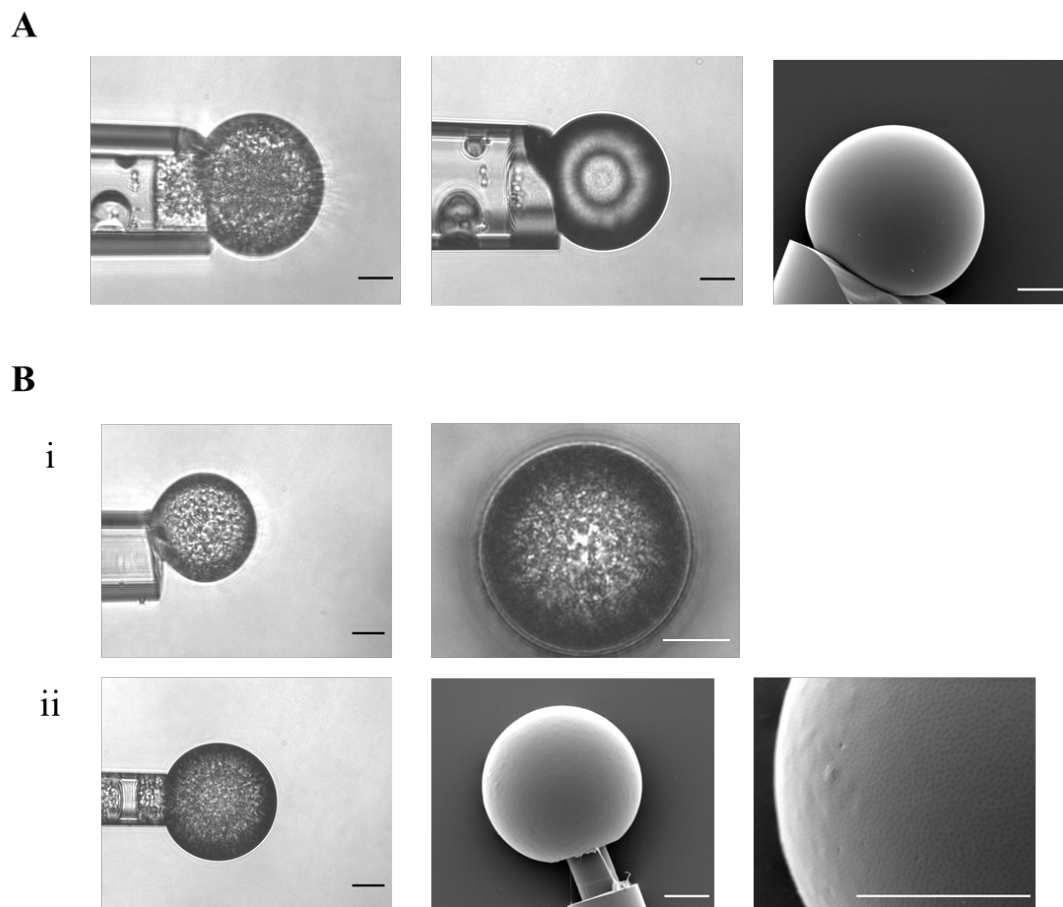
Figure 6-9 Effect of time in the chamber post-dissolution on internal microstructures. (A) drop was removed soon after a steady radius was observed. (B) Drop of the same composition was left in the chamber for 30 minutes before (i) evaporation on a slide or (ii) removal and preparation for SEM. Scale bars all represent 20 µm

Figure 6-9 B shows two drops of the same composition. In the case of Figure 6-9

B, i the drop was removed from the pipette after dissolution but left in the

chamber. The contents of the chamber were emptied onto a glass slide and left

overnight for the water to evaporate. The remaining drop was imaged, and the

internal structure remained. However, the drying process prevented its removal

for SEM. The drop shown in Figure 6-9 B, ii was left for 30 minutes in the water

chamber before its removal. When it was imaged in air the internal structure of

sub-drops remained. This was taken for SEM imaging, and unlike the drop in

Figure 6-9 A, presented a dimpled surface morphology. Providing adequate drying time the dimpled appearance reproduceable.

Though identifying the underlying route of sub-drop formation was not possible during this study, ways of manipulating the number/density and size of sub-drops and their location was. Initial assessment focussed on the simplest particle system: PDLLA in ethyl acetate into water. This is only possible in micropipette studies where single droplets are manually created, as bulk particle formation cannot occur without the aid of surfactants.

Drops of increasing initial PDLLA concentration shown in Figure 6-8 showed an increasing number of sub-drops. The number of drops was higher for higher initial concentrations of PDLLA in ethyl acetate. Varying concentration could be used to help manipulate the internal structure. However, by changing the amount of polymer present, the final particle size will be greatly altered. Substantial changes in processing would have to be made to offset this.

6.3.3.2 Impact of the Addition of Surfactants on Droplet Morphology

As discussed throughout this chapter, the surfactants used were key to the particles' final application. The addition of surfactants caused a change in the formation and location of drops. In the surfactant-free systems sub-drops formed on the inside of drops. Their motion (Figure 6-5 and Figure 6-6) showed they were close to the surface when initially forming but did not sit at the surface, rather they were trapped throughout the bulk. However, the addition of surfactant to either phase caused sub-drops with different characteristics to form.

In Figure 6-10 a surfactant containing drop is shown at three time points. In the first image, Figure 6-10 A, only the internal sub-drops seen and discussed above are present. Very small structures then appeared on the surface of the drop. These can be seen in Figure 6-10 B as slight shadowing. As time progressed and the drop shrank, these secondary sub-drops flocculated into a denser covering over the surface. In the example shown, the internal sub-drops can still be seen and their development and motion is clearly distinct from the secondary structures. Varying focus through the drop confirmed that the secondary sub-drops were at the surface, whilst the larger sub-drops remained dispersed throughout the bulk of the drop.

Due to their size and density the analysis methodology shifted to that in Chapter 3 Section 3.5.2, using average pixel intensity to compare the relative density of sub-drop coverage since individual drops were indistinguishable. Their presence on the surface and the fact they only appear when surfactants are present suggest that these drops are from the surfactant trapping material.
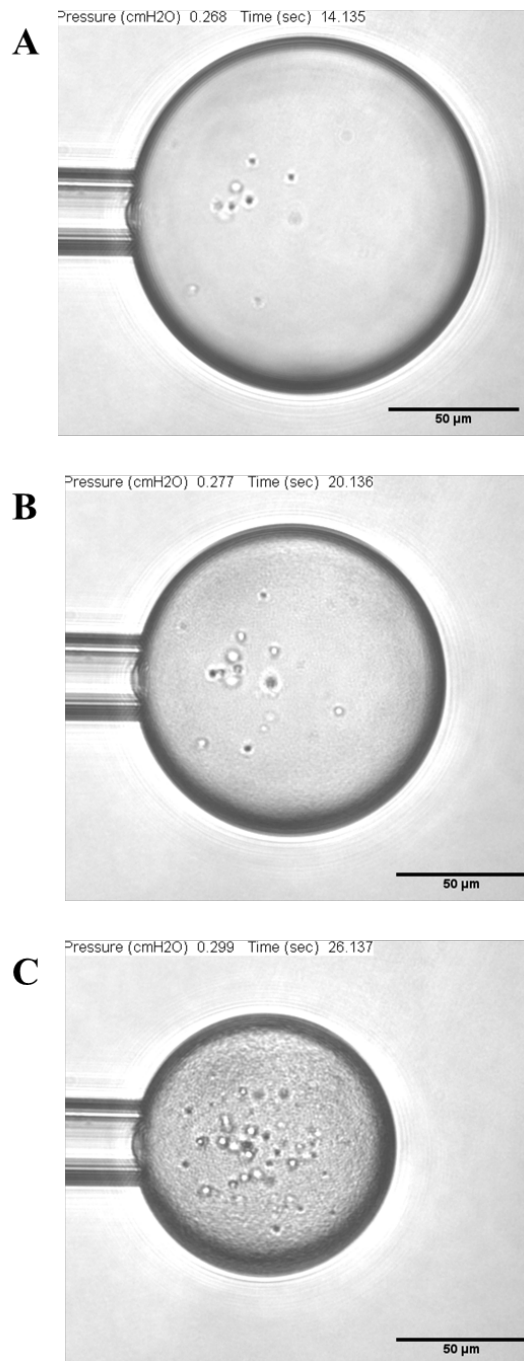
Figure 6-10 Surfactant containing drop over approximately 10 seconds. (A) only sub-drops inside the drop can be seen, as time progresses (B) shadowing across the surface hints to the formation of smaller sub-drops there which become clearly visible. (C) Scale bars 50 μm.

Figure 6-11 shows the effect of adding increased amounts of THFuA-mPEGMA to the dispersed phase containing 5% (w/v) PDDLA. The normalised pixel intensity decreased with increasing THFuA-mPEGMA concentration, which

corresponded to an increased density of surface based sub-drops. The coverage became considerable from 0.5% (w/v) THFuA-mPEGMA and above, masking the internal drops. The drop shown with 1% (w/v) surfactant has a lower coverage, however, these drops were also much smaller and so the difference in sub-drop concentration could be linked to this instead. All other concentrations tend towards complete coverage at 2% (w/v).
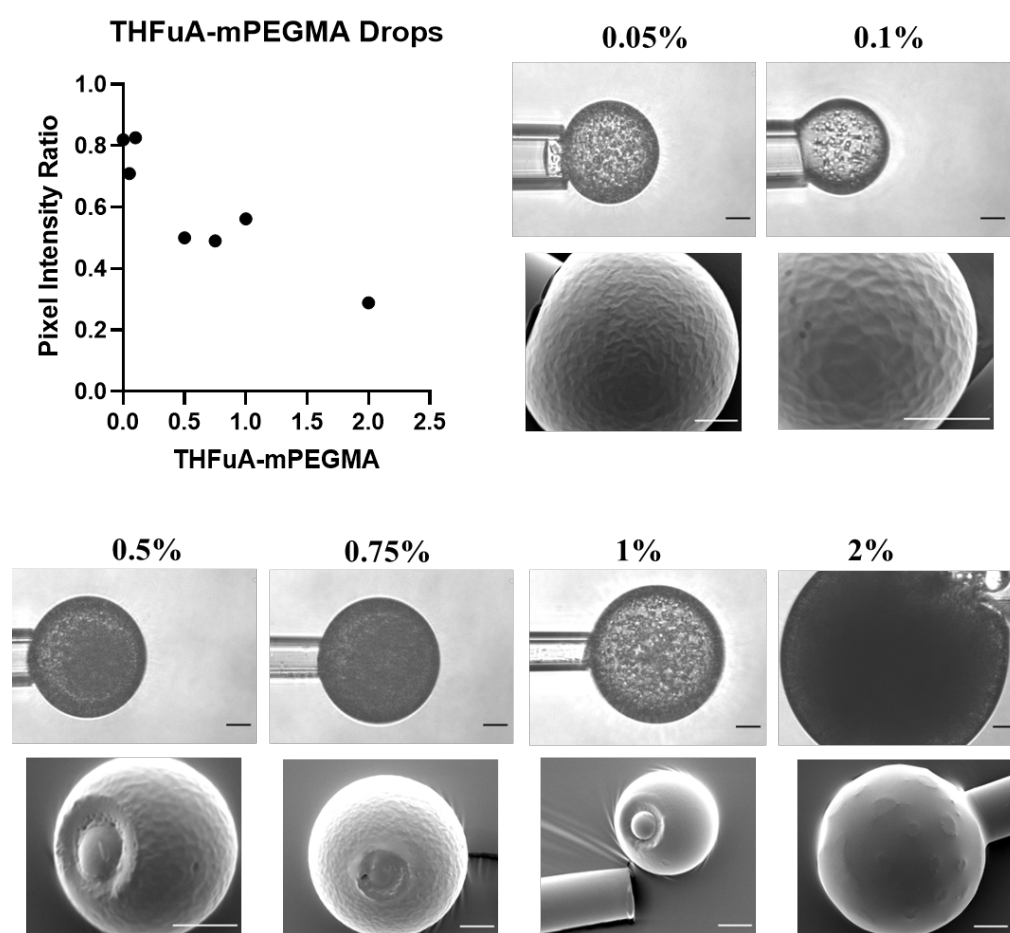
Figure 6-11 Change in sub-drop coverage with THFuA-mPEGMA addition to 5% (w/v) PDLLA drops. Brightfield and SEM images accompany analysis via pixel intensity, all scale bars show 20 μm.

SEM images of example drops are shown with the drop micrographs in Figure 6-11. Images of 0.05% and 0.1% (w/v) show a crinkled morphology. This could suggest shrinkage of the drop after the outer polymer has solidified and would correspond to the final removal of water or ethyl acetate inside the drops. This could have occurred when the particles were dried prior to mounting. Dark spots visible on SEM images of 0.5% (w/v) THFuA-mPEGMA particles are similar to pinholes commonly seen when fast evaporation of trapped solvent occurs, such as when placed into a vacuum.[107]

The morphology for 0.5% and 1% (w/v) surfactant (Figure 6-11) moved from a crinkled surface to bumps, though for 0.5% it is hard to determine whether the features protrude or intrude. Similar morphology was seen in studies by Bowen Yu, *et al*. investigating the effect of PDLA and PLLA mixtures, where the combination of the different chains caused protruding crystallites and pores to form close to the surface.[157] The size of the features on the 1% (w/v) particle appears to be large compared to the appearance of the surface based sub-drops from the micrographs. During the dissolution process the surface sub-drops appeared, to an extent, to aggregate. It could be that during post-dissolution stages these merged to form larger surface features.

The surface of the 2% (w/v) particle, seen in the SEM image in Figure 6-11) has a completely different topography than the other particles, and from what was expected given the images obtained when the particle was still on the micropipette. The surface is smooth with a series of rings made of small spheres. These spheres appear to be just below the surface rather than sitting on the

surface itself. Given the density of sub-drops on the micrograph, the expected topography would be an even covering of features or for them to be so small the surface appears smooth. The appearance of rings was unexpected.

Since the ideal concentration of THFuA-mPEGA given by the optimisation work in 6.3.1 was 0.1% (w/v), a study was conducted during which this concentration was maintained whilst various PVA concentrations were assessed, Figure 6-12. The resulting surfaces were uneven without distinct features. Small holes were seen, which as discussed above can be attributed to rapid solvent removal, most likely caused by from placing in a vacuum.
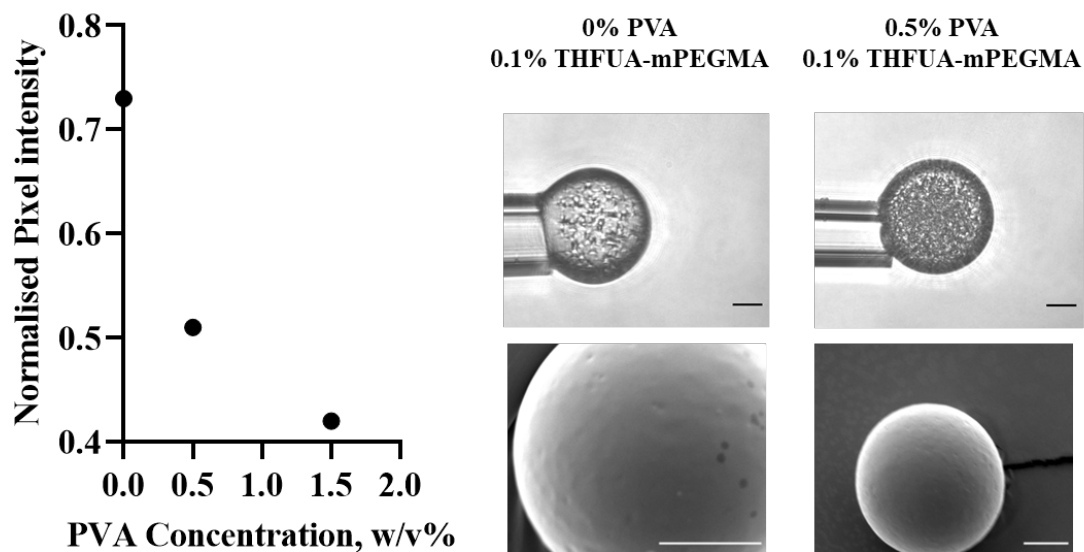
Figure 6-12 Change in sub-drop coverage with PVA addition to the aqueous phase with 5% (w/v) PDLLA, 0.1% (w/v) THFuA-mPEGMA drops. Brightfield and SEM images accompany analysis via pixel intensity. All scale bars show 20 μm.

The studies were repeated for EGDPEA-mPEGMA surfactant added to the dispersed phase of 5% (w/v) PDLLA in ethyl acetate. The pixel intensity shows a clear and significant decrease as EGPEA-mPEGMA concentration was increased, tending towards a limit, Figure 6-13. The corresponding SEM images show a transition from a smooth particle to particles with clear and separated protruding features. For intermediary concentrations, the resulting surface was densely covered with smaller features, suggesting merging occurred between dissolution and imaging on the higher concentration particles. The low variation seen in the pixel intensity and clear features suggest good control and reproducibility for these particles.
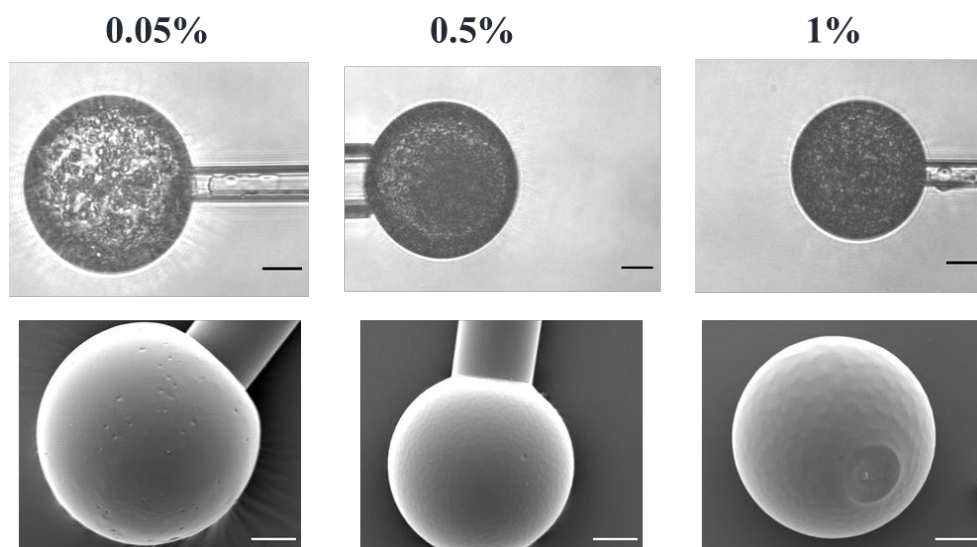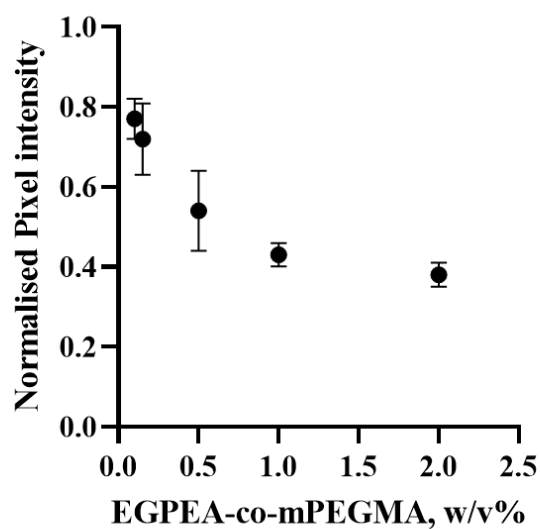
Figure 6-13 Change in sub-drop coverage with EGPEA-mPEGMA addition to 5% (w/v) PDLLA drops. The average normalised pixel intensity is obtained by taking the mean normalised intensity over the last 6-12 frames of the dissolution video. The error bars represent ±1SD around this mean. Brightfield and SEM images accompany analysis via pixel intensity. All scale bars are 20μm.

When 2% (w/v) EGPEA-mPEGMA was used, a different morphology was seen.

Figure 6-14 A shows the surface of one of these particles (with a higher magnification image in Figure 6-14 B.) Large indentations were seen with small protrusions covering the surface in between. Analysis of the features shows the average size of the indents and protrusions were 8 μm ± 3 μm and 0.9 μm ±

0.4 μm respectively. However, the number of protrusions greatly exceeds the indents such that the two occupy the same area on the surface – approximately a third each. Figure 6-14 C was acquired via FIB-SEM on the same particle. Darker regions in the lower part of the particle suggest the presence of the internal sub-drops is maintained. The bright areas could be crystallised polymer. Some of these bright regions are small whilst others appear to be the shell of larger pores. Unfortunately, the topography of this particle was less reproducible.
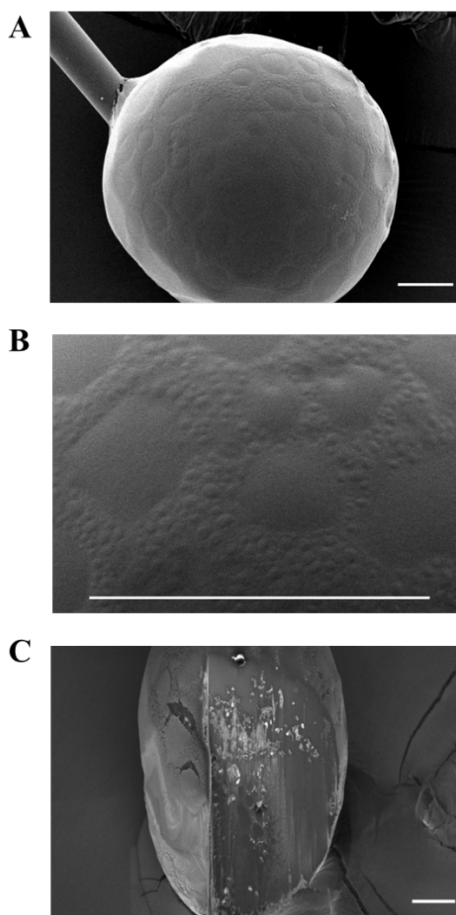
Figure 6-14 SEM of a particle formed from 2% (w/v) EGPEA-mPEGMA, 5% (w/v) PDLLA in ethyl acetate. Distinct topographical features were seen on SEM images at (A) 800X and (B) 3000X magnification. The internal structure was assessed using FIB-SEM (C). All scale bars are 20 μm.

The study was repeated with EGDPEA-mEPGMA maintained at 0.1% (w/v) and PVA concentration varied to replicate the formulation used for bulk particle production. These tests yielded similar results to that seen for THFuA-mPEGMA with PVA. Particles with 0.1% (w/v) of both EGPEA-mPEGMA and PVA for 5% (w/v) PDLLA were produced in bulk as well as using micropipette manipulation. Figure 6-15 shows analysis of particles from microfluidic processing (A and B) and micropipette manipulation (C and D).

AFM analysis of surface roughness of the three particle types made in microfluidics, conducted by Dr Francesco Pappalardo, School of Pharmacy, University of Nottingham is shown in Figure 6-15 A. Particles with EGPEA-mEPMGA were significantly rougher than those with the other surfactant combinations, with protrusions of over 0.1 μm (variation between each particle formulation had p-values <0.0001). This was confirmed by ToF-SIMS analysis of the surfaces (Dr Adam Dundas, Department of Chemical and Environmental Engineering, University of Nottingham) which showed small circular features approximately the same distance from the bulk surface. The height and approximate diameter of the features suggests they are hemispheres on the surface, concurrent with being small microspheres of surfactant-trapped material as suggested above.
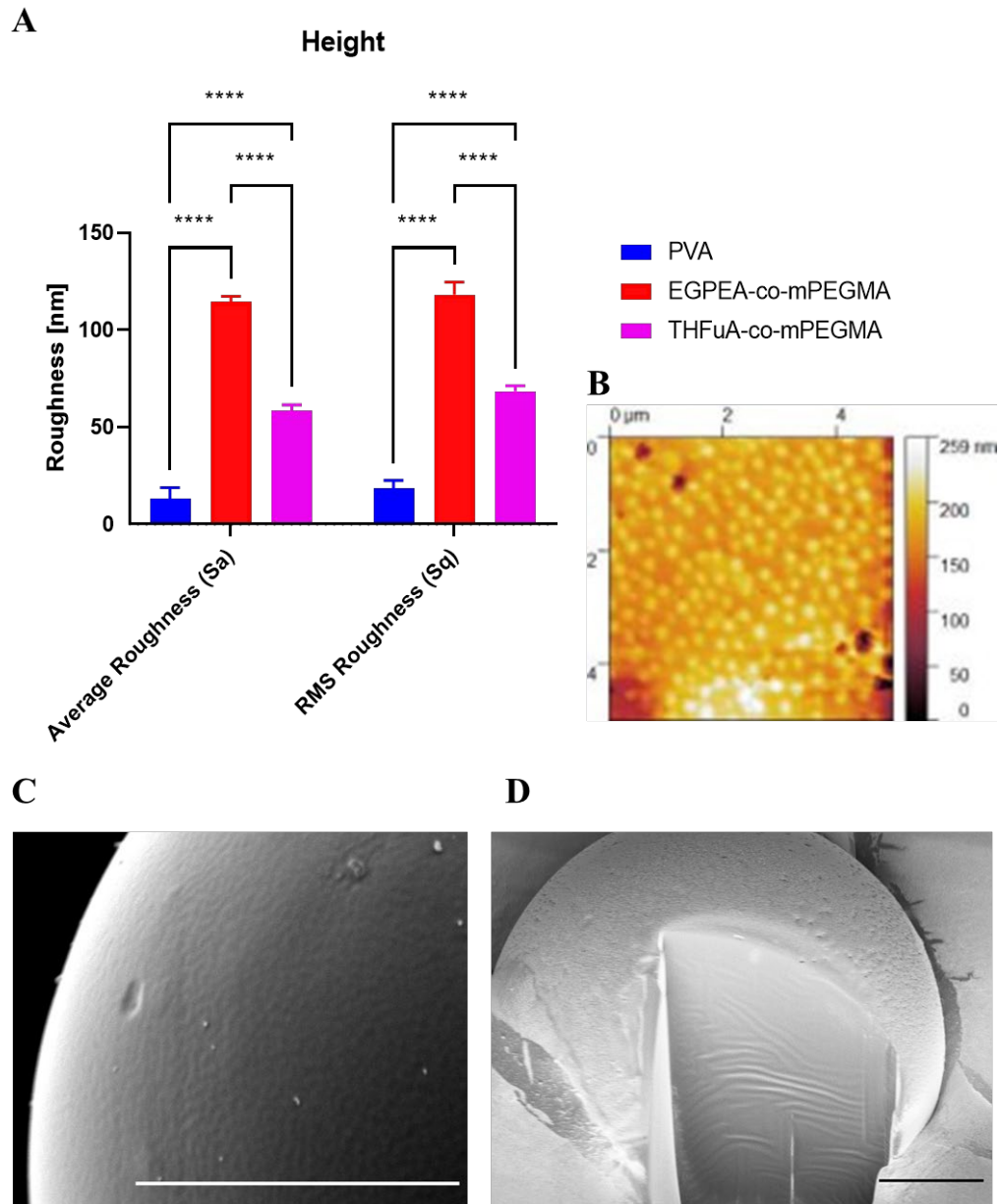
Figure 6-15 Analysis of 0.1% (w/v) EGPEA-mPEGMA, 0.1% 9w/v) PVA, 5% (w/v) PDLLA (ethyl acetate) particles produced in bulk (A, B) and as single particles (C, D). (A) surface roughness for all three microparticle formulations produced using droplet microfluidics, (**** show p<0.0001) AFM conducted by Dr Francesco Pappalardo. (B) ToF-SIMS analysis of particle surface texture, heat map correlates to hight of feature. (C) SEM of particle produced in single particle studies as 3500X magnification. Scale bar 20 μm (D) FIB-SEM of same particle formulation, from single particle studies. Scale bar 20μm.

A particle of the same composition produced via micropipette manipulation is shown in Figure 6-15 C. Though the spatial resolution here is not as high as the TOF-SIMS analysis, there appears to be approximately the same size and shaped features. The agreement between bulk and single particle studies suggests this is a reproduceable effect and bulk effects can indeed be controlled simply through surfactant concentration as in micropipette studies. FIB-SEM carried out on the micropipette-produced particle (Figure 6-15) showed no pores existed within the particle as had been expected. Instead, ripples were seen, though this could be an effect from the slicing, it remains unclear as to why the internal structure disappeared while the surface remained unchanged.

6.3.3.3 Partial Saturation of the Continuous Phase to Reduce Internal Drop Density

In order to reduce the presence of undesired internal structures related to the use of ethyl acetate the solvent removal process is commonly modified to reduce the rate of dissolution. This is done either by carrying out a two-step process whereby the drops are first made in a relatively small amount of aqueous material that quickly saturates before being quenched in a larger bath or by partially pre-saturating the continuous phase with ethyl acetate prior to dispersing the organic phase.[106,112,175] The second path was replicated here by partially saturating the chamber with ethyl acetate and forming drops using 5% (w/v) PDLLA in ethyl acetate (no surfactants present in either phase). A comparison was carried out on drops of similar radii which showed an approximately linear decrease in the number of sub-drops present with increasing saturation fraction.
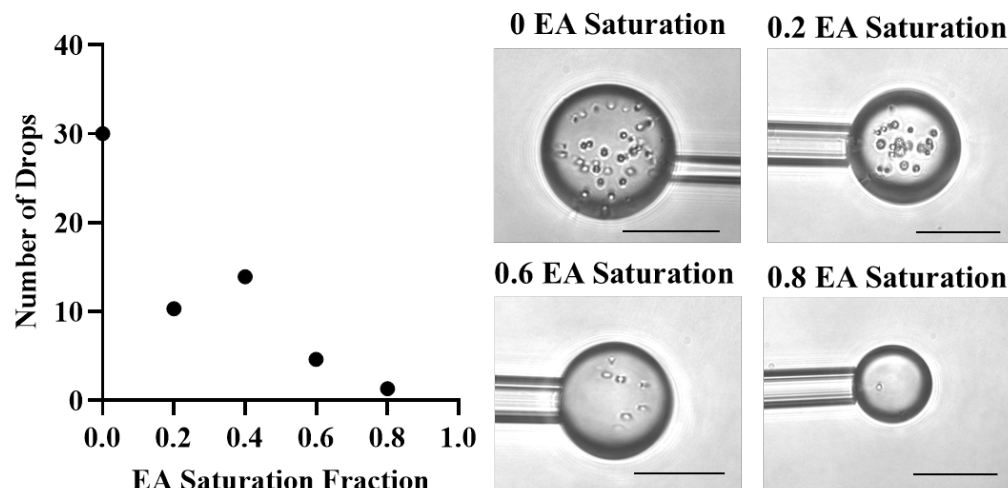
Figure 6-16 Addition of ethyl acetate to the continuous phase prior to droplet formation to control the formation of internal sub-drops. Scale bars 100 μm.

6.4 Conclusion

A dual-surfactant system was optimised using micropipette characterisation to identify the required concentration of PVA to allow the stable production of droplets for bio-degradable microparticles with bio-instructive surface chemistries. To minimise surface coverage whilst maintaining stability, 0.1% (w/v) PVA in conjunction with 0.1% (w/v) EGPEA-mPEGMA or THFuA-mPEGMA required for particle production. Surface analysis using ToF-SIMS demonstrated that the unique surfactant chemistry was visible at the surface with minimal PVA coverage. Changes to particle collection were advised based on the calculation of solvent removal time to allow a minimum of 25 seconds in sink conditions.

Internal microstructure formed in the drops as a result of using ethyl acetate as the dispersed phase solvent. Whilst drop size remained unchanged, the density

of sub-drops could be increased through increasing the concentration of PDLLA in the drop or decreasing the pre-saturation of the continuous phase with ethyl acetate. The addition of surfactants, namely EGPEA-mPEGMA and THFuA-mPEGMA, generated small drops on the droplet surfaces which resulted in different particle topographies depending on the concentration and surfactant used.

The work presented here accomplished the aims set for this system, demonstrating the successful employment of micropipette manipulation techniques to understand and optimise microparticle formulation and production. The assessment of internal microstructure satisfied the initial aims here. Using the analysis routines developed as part of this project, videos of individual microparticles forming were used to identify correlations between formulation and internal microstructure. This investigation was extended further to assess the impact on the microparticle topographies. By relating this to the topographies of particles produced using microfluidics, it strengthened the hypotheses that micropipette manipulation studies directly inform microparticle formation using microfluidics.

Chapter 7: General Discussion

Chapter 7 – General Discussion

This work has been successful in proving the hypothesis that micropipette manipulation techniques can aid the understanding of microparticle formation systems; from individual material characterisations to controlling the final morphology of bio-instructive, bio-degradable polymeric microparticles. It has built upon the micropipette manipulation work from the University of Southern Denmark's Centre for Single Particle Science and Engineering. An improved understanding of one of the most common microparticle base systems has been attained in addition to characterising novel polymeric surfactants. New methodologies have been developed to improve performance and usability of micropipette manipulation experiments, whilst also extending its use in informing droplet microfluidic production in both formulation and processing.[8]

During this work, several areas have been noted for additional exploration. The deviation from model behaviour for microparticles containing polymeric solutes (Chapter 4, Section 4.3.2) should be investigated. Concentration was found to be the biggest discrepancy, and it is unclear how much of this due to inconsistency in the initial concentration. Therefore, materials should be identified that behave similarly to PDLLA but that will undergo refraction index matches as for proteins. This will remove the uncertainty in solute concentration, allowing the solvent trapping to be thoroughly assessed.

As it was found to be difficult to quantify the solvent left in the current formulation, SEM assessment of dried particles should be conducted to compare size changes pre- and post-drying. This would help ascertain the material change. In conjunction to this, different drying stages could be trialled, including mimicking solvent extraction or slow evaporation.

The empirical equations developed for stable formulations require confirmation using bulk particle production (Chapter 4, Section 4.3.1). Included in this is the use of un-tested concentrations to confirm the reliability of the equations. Emulsion solvent evaporation methods should be used with fixed processing parameters across the different formulations to correlate particle size to interfacial tension and core polymer content. This would enable a set of empirical equations to calculate the optimal composition to achieve the desired final particle. In turn this could be combined with processing parameter investigations, e.g., shear speed, to generate particle "recipes".

Characterisation of several novel -mPEGMA and -DMAEMA based surfactants was achieved using static equilibrium interfacial tension measurements (Chapter 5, Section 5.3.1). As a number of these materials were poor at reducing the interfacial tension, whilst successful in covering microparticle surfaces, it is suggested that they are slow-diffusing materials with mild surface affinity, providing only steric stabilisation. To investigate this, dynamic interfacial tension measurements should be performed with the surfactants of interest. For these studies a non-amphiphilic core material, preferably a well understood solvent based system should be used. For completeness, the surfactants should

also be tested in static equilibrium with a non-amphiphilic core material. Dual surfactant systems, e.g., PVA with THFuA-mPEGMA (Chapter 6), would also benefit from dynamic interfacial tension investigations. Information regarding the competition between surfactants would be attained, which in turn would help understand the individual and combined roles each material plays.

The optimised surfactant concentrations determined using static equilibrium interfacial tension measurements were useful in obtaining stable droplet production in flow-focusing microfluidics, for both solvent-free systems and biodegradable particle production (Chapter 5, Section 5.3.1 and Chapter 6, Section 6.3.1). Additionally, the prediction of stable flow rates matched approximately the experimentally derived flow maps (Chapter 5). Solvent removal and mass transfer studies were able to determine the length of time required between droplet generation and collection/polymerisation. In combination these micropipette manipulation studies were able to drastically reduce the time and material usually required for optimising droplet-microfluidics system through trial-and-error. Future particle productions could benefit greatly from utilising these techniques, especially for complex formulation or the use of novel materials.

Though the viscosity measurement method used in this work requires only a few millilitres of material, a more ideal situation would be if viscosity measurements could be made using micropipette manipulation. Since the basis for these techniques is routed in assessing the mechanical properties of cells, and was tested on lipid membrane particles, it should be possible to develop a method to

measure the droplet viscosities. In a similar vein, compression tests of single particles and microspheres, conducted using parallel plates (Zhibing Zhang, Centre for Formulation Engineering, University of Birmingham)[181,182] have been proven valuable for assessing the mechanical properties (breaking and deformation) of pharmaceutical powders and microspheres. Adaptations to the current micropipette manipulation set-up could allow these investigations *in situ* during and post particle production. This would be a unique and useful tool.

Chemical analysis on the particles produced in micropipette studies would allow confirmation of the mechanism behind the topography and allow full comparison to those produced via droplet microfluidics. ToF-SIMS has the capability to assess the particles, as demonstrated for bulk particles, however, the mounting of single particles for this application may be difficult. Alternatively chemical analysis could be combined with SEM, such as energy dispersive X-Ray spectroscopy (EDX). However, this is generally limited to elemental analysis and so not effective at differentiating between polymers. 3D OrbiSIMS would overcome the limitations of both these techniques.

Determining the cause and composition of internal sub-drops would be greatly aided by chemical analysis capabilities. *In situ* Raman spectroscopy would provide valuable insights, not only in this endeavour but also to more complex phase separating behaviours. This has previously been demonstrated for the phase separation of fusidic acid.[28] Furthermore, the capacity to perform release profile exams on single microparticles would be provided by this set up. This would be invaluable to drug-delivery platform development.

Given the effect of in-chamber drying time on the preservation of internal structure, additional investigation should be performed. Particles formed and left in different conditions for different lengths of time would then be assessed using FIB-SEM to observe the resulting structures. This would enable a more quantitative approach to continuous phase quenching for preventing microstructure formation, or equally for controlling this property through simple processing adjustments and improve the protocol for micropipette manipulation studies.

Microparticles of increasing complex internal and surface microstructures are being required and used in tissue engineering and drug delivery applications. Generating these morphologies through phase separation followed by the removal of the separated material is a lengthy process and risks the exposure of cells to toxic material. Utilising phase separation behaviour of materials whose presence is required in the final particle overcomes these limitations.

This has recently been demonstrated with PLGA-b-PEG/PLGA blend particles. By varying the polymer blend particles were formed with topographies varying from smooth, to wrinkled to "sheet-like textures" across the surface. The particles generated with up to 20% PLGA-b-PEG were similar in appearance to those generated in this work with low concentrations of THFuA-mPEGMA.[97] Microparticles featuring extreme spikes or dense strands were also generated using PLGA-b-PEG separation.[86,98] Finally, polymerisation of macromolecular, methacrylate-based monomer drops has been used to produce particles with

topographies ranging from smooth surfaces, to similar surfaces to the particles in Chapter 6 all the way to deep waves across the surface.[59]

Given the relation to morphology and materials used in this work, it is reasonable to propose similar particles could be created utilising the novel surfactants and known biodegradable polymers in various combinations. Through utilisation of micropipette manipulation, the individual and combined effects of materials could be quantified such that a library of particles could be generated with formulations optimised for various morphologies, chemistries, and processes.

In conclusion, the findings presented in this thesis demonstrate the ability of micropipette manipulation techniques to inform the formulation and processing of microparticles. Based on the information obtained, improvements and optimisations to several biologically relevant microparticle systems have been described and implemented. Developments to the analysis methodologies and demonstrations of the relation between micropipette and bulk scale studies, along with the suggested areas of future study, provide a solid basis for continued and enhanced use of micropipette methods in microparticle research.

Chapter 8 – References

(1)   Mitchison, B. Y. J. M.; Swann, M. M. THE MECHANICAL PROPERTIES OF THE CELL. **1954**.

(2)   Evans, E. A. New Membrane Concept Applied to the Analysis of Fluid Shear- and Micropipette-Deformed Red Blood Cells. *Biophys. J.* **1973**, *13* (9), 941–954. https://doi.org/10.1016/S0006-3495(73)86036-9.

(3)   Artmann, G. M.; Sung, K. L. P.; Horn, T.; Whittemore, D.; Norwich, G.; Chien, S. Micropipette Aspiration of Human Erythrocytes Induces Echinocytes via Membrane Phospholipid Translocation. *Biophys. J.* **1997**, *72* (3), 1434–1441. https://doi.org/10.1016/S0006-3495(97)78790-3.

(4)   Zhelev, D. V.; Needham, D.; Hochmuth, R. M. A Novel Micropipet Method for Measuring the Bending Modulus of Vesicle Membranes. *Biophys. J.* **1994**, *67* (2), 720–727. https://doi.org/10.1016/S0006-3495(94)80530-2.

(5)   Hochmuth, R. M. Micropipette Aspiration of Living Cells. *J. Biomech.* **2000**, *33* (1), 15–22. https://doi.org/10.1016/S0021-9290(99)00175-X.

(6)   Tözeren, H.; Chien, S.; Tözeren, A. Estimation of Viscous Dissipation inside an Erythrocyte during Aspirational Entry into a Micropipette. *Biophys. J.* **1984**, *45* (6), 1179–1184. https://doi.org/10.1016/S0006-3495(84)84266-6.

(7)   Chien, S.; Sung, K. L.; Skalak, R.; Usami, S.; Tözeren, A. Theoretical and Experimental Studies on Viscoelastic Properties of Erythrocyte

Membrane. *Biophys. J.* **1978**, *24* (2), 463–487. https://doi.org/10.1016/S0006-3495(78)85395-8.

(8)   Kinoshita, K.; Parra, E.; Hussein, A.; Utoft, A.; Walke, P.; de Bruijn, R.; Needham, D. From Single Microparticles to Microfluidic Emulsification: Fundamental Properties (Solubility, Density, Phase Separation) from Micropipette Manipulation of Solvent, Drug and Polymer Microspheres. *Processes* **2016**, *4* (4), 49. https://doi.org/10.3390/pr4040049.

(9)   Yeung, A.; Dabros, T.; Masliyah, J.; Czarnecki, J. Micropipette: A New Technique in Emulsion Research. *Colloids Surfaces A Physicochem. Eng. Asp.* **2000**, *174* (1–2), 169–181. https://doi.org/10.1016/S0927-7757(00)00509-4.

(10)   Lee, S.; Kim, D. H.; Needham, D. Equilibrium and Dynamic Interfacial Tension Measurements at Microscopic Interfaces Using a Micropipet Technique. 1. A New Method for Determination of Interfacial Tension. *Langmuir* **2001**, *17* (18), 5537–5543. https://doi.org/10.1021/la0103259.

(11)   Lee, S.; Kim, D. H.; Needham, D. Equilibrium and Dynamic Interfacial Tension Measurements at Microscopic Interfaces Using a Micropipet Technique. 1. A New Method for Determination of Interfacial Tension. *Langmuir* **2001**, *17* (18), 5537–5543. https://doi.org/10.1021/la0103259.

(12)   Kinoshita, K.; Parra, E.; Needham, D. New Sensitive Micro-Measurements of Dynamic Surface Tension and Diffusion Coefficients: Validated and Tested for the Adsorption of 1-Octanol at a Microscopic

Air-Water Interface and Its Dissolution into Water. *J. Colloid Interface Sci.* **2017**, *488*, 166–179. https://doi.org/10.1016/j.jcis.2016.10.052.

(13)   Kinoshita, K.; Parra, E.; Needham, D. Adsorption of Ionic Surfactants at Microscopic Air-Water Interfaces Using the Micropipette Interfacial Area-Expansion Method: Measurement of the Diffusion Coefficient and Renormalization of the Mean Ionic Activity for SDS. *J. Colloid Interface Sci.* **2017**, *504*, 765–779. https://doi.org/10.1016/j.jcis.2017.05.077.

(14)   Needham, D.; Kinoshita, K.; Utoft, A. Micro-Surface and -Interfacial Tensions Measured Using the Micropipette Technique: Applications in Ultrasound-Microbubbles, Oil-Recovery, Lung- Surfactants, Nanoprecipitation, and Microfluidics. *Micromachines* **2019**, *10* (2). https://doi.org/10.3390/mi10020105.

(15)   Parra, E.; Kinoshita, K.; Needham, D. Micropipette Technique Study of Natural and Synthetic Lung Surfactants at the Air-Water Interface: Presence of a SP-B Analog Peptide Promotes Membrane Aggregation, Formation of Tightly Stacked Lamellae, and Growth of Myelin Figures. *Langmuir* **2016**, *32* (41), 10570–10581. https://doi.org/10.1021/acs.langmuir.6b01420.

(16)   Duncan, P. B.; Needham, D. Test of the Epstein - Plesset Model for Gas Microparticle Dissolution in Aqueous Media : Effect of Surface Tension and Gas Undersaturation in Solution. *Langmuir* **2004**, *20* (7), 2567–2578.

(17)   Utoft, A.; Kinoshita, K.; Bitterfield, D. L.; Needham, D. Manipulating

Single Microdroplets of NaCl Solutions: Solvent Dissolution, Microcrystallization, and Crystal Morphology. *Langmuir* **2018**, *34* (12), 3626–3641. https://doi.org/10.1021/acs.langmuir.7b03977.

(18) Liu, S.; Li, X.; Hu, L.; Deng, S.; Zhang, W.; Liu, P.; Zhang, Y. Interfacial Instability of Emulsion Droplets Containing a Polymer and a Fatty Alcohol. *Langmuir* **2020**, *36* (14), 3821–3825. https://doi.org/10.1021/acs.langmuir.0c00463.

(19) Duncan, P. B.; Needham, D. Microdroplet Dissolution into a Second-Phase Solvent Using a Micropipet Technique: Test of the Epstein-Plesset Model for an Aniline-Water System. *Langmuir* **2006**, *22* (9), 4190–4197. https://doi.org/10.1021/la053314e.

(20) Su, J. T.; Needham, D. Mass Transfer in the Dissolution of a Multicomponent Liquid Droplet in an Immiscible Liquid Environment. *Langmuir* **2013**, *29* (44), 13339–13345. https://doi.org/10.1021/la402533j.

(21) Su, J. T.; Duncan, P. B.; Momaya, A.; Jutila, A.; Needham, D. The Effect of Hydrogen Bonding on the Diffusion of Water in n -Alkanes and n -Alcohols Measured with a Novel Single Microdroplet Method. *J. Chem. Phys.* **2010**, *132* (4). https://doi.org/10.1063/1.3298857.

(22) Bitterfield, D. L.; Utoft, A.; Needham, D. An Activity-Based Dissolution Model for Solute-Containing Microdroplets. *Langmuir* **2016**, *32* (48), 12749–12759. https://doi.org/10.1021/acs.langmuir.6b03126.

(23) Rickard, D. L.; Duncan, P. B.; Needham, D. Hydration Potential of Lysozyme: Protein Dehydration Using a Single Microparticle Technique. *Biophys. J.* **2010**, *98* (6), 1075–1084. https://doi.org/10.1016/j.bpj.2009.11.043.

(24) Aniket; Gaul, D. A.; Rickard, D. L.; Needham, D. MicroglassificationTM: A Novel Technique for Protein Dehydration. *J. Pharm. Sci.* **2014**, *103* (3), 810–820. https://doi.org/10.1002/jps.23847.

(25) Aniket; Gaul, D. A.; Bitterfield, D. L.; Su, J. T.; Li, V. M.; Singh, I.; Morton, J.; Needham, D. Enzyme Dehydration Using Microglassification[TM] Preserves the Protein's Structure and Function. *J. Pharm. Sci.* **2015**, *104* (2), 640–651. https://doi.org/10.1002/jps.24279.

(26) Kim, D. H.; Costello, M. J.; Duncan, P. B.; Needham, D. Mechanical Properties and Microstructure of Polycrystalline Phospholipid Monolayer Shells: Novel Solid Microparticles. *Langmuir* **2003**, *19* (20), 8455–8466. https://doi.org/10.1021/la034779c.

(27) Yang, C.; Plackett, D.; Needham, D.; Burt, H. M. PLGA and PHBV Microsphere Formulations and Solid-State Characterization: Possible Implications for Local Delivery of Fusidic Acid for the Treatment and Prevention of Orthopaedic Infections. *Pharm. Res.* **2009**, *26* (7), 1644–1656. https://doi.org/10.1007/s11095-009-9875-5.

(28) Gilchrist, S. E.; Rickard, D. L.; Letchford, K.; Needham, D.; Burt, H. M. Phase Separation Behavior of Fusidic Acid and Rifampicin in PLGA

Microspheres. *Mol. Pharm.* **2012**, *9* (5), 1489–1501. https://doi.org/10.1021/mp300099f.

(29) Parra, E.; Hervella, P.; Needham, D. Real-Time Visualization of the Precipitation and Phase Behavior of Octaethylporphyrin in Lipid Microparticles. *J. Pharm. Sci.* **2017**, *106* (4). https://doi.org/10.1016/j.xphs.2016.11.019.

(30) Alvarez-Paino, M.; Amer, M. H.; Nasir, A.; Cuzzucoli Crucitti, V.; Thorpe, J.; Burroughs, L.; Needham, D.; Denning, C.; Alexander, M. R.; Alexander, C.; Rose, F. R. A. J. Polymer Microparticles with Defined Surface Chemistry and Topography Mediate the Formation of Stem Cell Aggregates and Cardiomyocyte Function. *ACS Appl. Mater. Interfaces* **2019**, *11* (38), 34560–34574. https://doi.org/10.1021/acsami.9b04769.

(31) Amer, M. H.; Alvarez-Paino, M.; McLaren, J.; Pappalardo, F.; Trujillo, S.; Wong, J. Q.; Shrestha, S.; Abdelrazig, S.; Stevens, L. A.; Lee, J. B.; Kim, D. H.; González-García, C.; Needham, D.; Salmerón-Sánchez, M.; Shakesheff, K. M.; Alexander, M. R.; Alexander, C.; Rose, F. R. Designing Topographically Textured Microparticles for Induction and Modulation of Osteogenesis in Mesenchymal Stem Cell Engineering. *Biomaterials* **2021**, *266* (June 2020). https://doi.org/10.1016/j.biomaterials.2020.120450.

(32) Barnes, G. .; Gentle, I. R. *Interfacial Science: An Introduction*, Second.; Barnes, G. ., Gentle, I. R., Eds.; Oxford University Press: Oxford, 2011.

(33)   Myres, D. *Surfaces Interfaces and Colloids: Principles and Applications*,
Second.; WILEY-VCH Verlag: New York, 2002.
https://doi.org/10.1002/0471234990.

(34)   Jones, R. A. . *Soft Condensed Matter*, Illustrate.; Oxford University Press:
Oxford, 2002.

(35)   DAVIES, J. T. *Interfacial Phenomena*, Second.; Academic Press, 1963.

(36)   Bhattacharya, A.; Ray, P. Studies on Surface Tension of Poly (Vinyl
Alcohol): Effect of Concentration, Temperature, and Addition of
Chaotropic Agents. *J. Appl. Polym. Sci.* **2004**, *93* (1), 122–130.
https://doi.org/10.1002/app.20436.

(37)   Utoft, A. Micropipette Manipulation Studies: Material Characterization of
Multiphase, Multicomponent Systems, 2017.

(38)   Arashiro, E. Y.; Demarquette, N. R. Use of the Pendant Drop Method to
Measure Interfacial Tension between Molten Polymers. **1999**, *2* (1), 23–
32.

(39)   Saad, S. M. I.; Policova, Z.; Neumann, A. W. Design and Accuracy of
Pendant Drop Methods for Surface Tension Measurement. *Colloids
Surfaces A Physicochem. Eng. Asp.* **2011**, *384* (1–3), 442–452.
https://doi.org/10.1016/j.colsurfa.2011.05.002.

(40)   Kakiuchi, T.; Nakanishi, M.; Senda, M. The Electrocapillary Curves of
the Phosphatidylcholine Monolayer at the Polarized Oil–Water Interface.
I. Measurement of Interfacial Tension Using a Computer-Aided Pendant-

Drop Method. *Bulletin of the Chemical Society of Japan*. 1988, pp 1845–1851. https://doi.org/10.1246/bcsj.61.1845.

(41)   Kwok, D. Y.; Hui, W.; Lin, R.; Neumann, A. W. Liquid-Fluid Interfacial Tensions Measured by Axisymmetric Drop Shape Analysis: Comparison between the Pattern of Interfacial Tensions of Liquid-Liquid and Solid-Liquid Systems. *Langmuir* **1995**, *11* (7), 2669–2673. https://doi.org/10.1021/la00007a055.

(42)   Eastoe, J.; Dalton, J. S. Dynamic Surface Tension and Adsorption Mechanisms of Surfactants at the Air-Water Interface. *Adv. Colloid Interface Sci.* **2000**, *85* (2), 103–144. https://doi.org/10.1016/S0001-8686(99)00017-2.

(43)   Miles, R. E. H.; Glerum, M. W. J.; Boyer, H. C.; Walker, J. S.; Dutcher, C. S.; Bzdek, B. R. Surface Tensions of Picoliter Droplets with Sub-Millisecond Surface Age. *J. Phys. Chem. A* **2019**, *123* (13), 3021–3029. https://doi.org/10.1021/acs.jpca.9b00903.

(44)   Yeung, A.; Dabros, T.; Masliyah, J. Does Equilibrium Interfacial Tension Depend on Method of Measurement? *J. Colloid Interface Sci.* **1998**, *208* (1), 241–247. https://doi.org/10.1006/jcis.1998.5807.

(45)   Hommelen, J. R. The Elimination of Errors Due to Evaporation of the Solute in the Determination of Surface Tensions. *J. Colloid Sci.* **1959**, *14* (4), 385–400. https://doi.org/10.1016/0095-8522(59)90003-0.

(46)   Bzdek, B. R.; Reid, J. P.; Malila, J.; Prisle, N. L. The Surface Tension of

Surfactant-Containing, Finite Volume Droplets. *Proc. Natl. Acad. Sci. U. S. A.* **2020**, *117* (15), 8335–8343. https://doi.org/10.1073/pnas.1915660117.

(47)   Bianco, H.; Marmur, A. The Dependence of the Surface Tension of Surfactant Solutions on Drop Size. *J. Colloid Interface Sci.* **1992**, *151* (2), 517–522. https://doi.org/10.1016/0021-9797(92)90499-C.

(48)   Zhou, H.; Yao, Y.; Chen, Q.; Li, G.; Yao, S. A Facile Microfluidic Strategy for Measuring Interfacial Tension. *Appl. Phys. Lett.* **2013**, *103* (23). https://doi.org/10.1063/1.4838616.

(49)   Renvoisé, P.; Bush, J. W. M.; Prakash, M.; Quéré, D. Drop Propulsion in Tapered Tubes. *Epl* **2009**, *86* (6). https://doi.org/10.1209/0295-5075/86/64003.

(50)   Metz, T.; Paust, N.; Zengerle, R.; Koltay, P. Capillary Driven Movement of Gas Bubbles in Tapered Structures. *Microfluid. Nanofluidics* **2010**, *9* (2–3), 341–355. https://doi.org/10.1007/s10404-009-0551-1.

(51)   Honaker, L. W.; Lagerwall, J. P. F.; Jampani, V. S. R. Microfluidic Tensiometry Technique for the Characterization of the Interfacial Tension between Immiscible Liquids. *Langmuir* **2018**, *34* (7), 2403–2409. https://doi.org/10.1021/acs.langmuir.7b03494.

(52)   Needham, D.; Kinoshita, K.; Utoft, A. Micro-Surface and -Interfacial Tensions Measured Using the Micropipette Technique: Applications in Ultrasound-Microbubbles, Oil-Recovery, Lung- Surfactants,

Nanoprecipitation, and Microfluidics. *Micromachines* **2019**, *10* (2), 1–58. https://doi.org/10.3390/mi10020105.

(53) Carrier, O.; Bonn, D. *Contact Angles and the Surface Free Energy of Solids*; Elsevier Inc., 2015. https://doi.org/10.1016/B978-0-12-800722-8.00002-3.

(54) Murakami, D.; Jinnai, H.; Takahara, A. Wetting Transition from the Cassie-Baxter State to the Wenzel State on Textured Polymer Surfaces. *Langmuir* **2014**, *30* (8), 2061–2067. https://doi.org/10.1021/la4049067.

(55) Epstein, P. S.; Plesset, M. S. Erratum: On the Stability of Gas Bubbles in Liquid†ï¿½Gas Solutions. *J. Chem. Phys.* **1951**, *19* (2), 256. https://doi.org/10.1063/1.1748182.

(56) Chu, S.; Prosperetti, A. Dissolution and Growth of a Multicomponent Drop in an Immiscible Liquid. *J. Fluid Mech.* **2016**, *798*, 787–811. https://doi.org/10.1017/jfm.2016.310.

(57) Anna, S. L.; Bontoux, N.; Stone, H. A. Formation of Dispersions Using "Flow Focusing" in Microchannels. *Appl. Phys. Lett.* **2003**, *82* (3), 364–366. https://doi.org/10.1063/1.1537519.

(58) Watanabe, T.; Kimura, Y.; Ono, T. Microfluidic Fabrication of Monodisperse Polylactide Microcapsules with Tunable Structures through Rapid Precipitation. *Langmuir* **2013**, *29* (46), 14082–14088. https://doi.org/10.1021/la403883a.

(59) Liu, J.; Liu, Y.; Xue, Y.; Ren, Y.; Fan, X.; Wang, R.; Zhang, H.; Zhang,

B.; Zhang, Q. Fabrication and Characterization of Controllable Wrinkled-Surface Polymer Microparticles. *J. Mater. Sci.* **2019**, *54* (7), 5852–5864. https://doi.org/10.1007/s10853-018-2421-2.

(60)   Song, S. H.; Lee, J. H.; Yoon, J.; Park, W. Functional Microparticle R&D for IVD and Cell Therapeutic Technology: Large-Scale Commercialized Products. *Biochip J.* **2019**, *13* (1), 95–104. https://doi.org/10.1007/s13206-019-3107-9.

(61)   Herrero-Vanrell, R.; Bravo-Osuna, I.; Andrés-Guerrero, V.; Vicario-de-la-Torre, M.; Molina-Martínez, I. T. The Potential of Using Biodegradable Microspheres in Retinal Diseases and Other Intraocular Pathologies. *Prog. Retin. Eye Res.* **2014**, *42*, 27–43. https://doi.org/10.1016/j.preteyeres.2014.04.002.

(62)   Tan, M. L.; Choong, P. F. M.; Dass, C. R. Recent Developments in Liposomes, Microparticles and Nanoparticles for Protein and Peptide Drug Delivery. *Peptides* **2010**, *31* (1), 184–193. https://doi.org/10.1016/j.peptides.2009.10.002.

(63)   Makadia, H. K.; Siegel, S. J. Poly Lactic-Co-Glycolic Acid (PLGA) as Biodegradable Controlled Drug Delivery Carrier. *Polymers (Basel).* **2011**, *3* (3), 1377–1397. https://doi.org/10.3390/polym3031377.

(64)   Lagreca, E.; Onesto, V.; Di Natale, C.; La Manna, S.; Netti, P. A.; Vecchione, R. Recent Advances in the Formulation of PLGA Microparticles for Controlled Drug Delivery. *Prog. Biomater.* **2020**, *9* (4),

153–174. https://doi.org/10.1007/s40204-020-00139-y.

(65)   Liu, S.; Qin, S.; He, M.; Zhou, D.; Qin, Q.; Wang, H. Current Applications of Poly(Lactic Acid) Composites in Tissue Engineering and Drug Delivery. *Compos. Part B Eng.* **2020**, *199* (May). https://doi.org/10.1016/j.compositesb.2020.108238.

(66)   Anderson, J. M.; Shive, M. S. Biodegradation and Biocompatibility of PLA and PLGA Microspheres. *Adv. Drug Deliv. Rev.* **2012**, *64* (SUPPL.), 72–82. https://doi.org/10.1016/j.addr.2012.09.004.

(67)   Pulivendala, G.; Bale, S.; Godugu, C. Inhalation of Sustained Release Microparticles for the Targeted Treatment of Respiratory Diseases. *Drug Deliv. Transl. Res.* **2020**, *10* (2), 339–353. https://doi.org/10.1007/s13346-019-00690-7.

(68)   Di, A.; Zhang, S.; Liu, X.; Tong, Z.; Sun, S.; Tang, Z.; Chen, X. D.; Wu, W. D. Microfluidic Spray Dried and Spray Freeze Dried Uniform Microparticles Potentially for Intranasal Drug Delivery and Controlled Release. *Powder Technol.* **2021**, *379*, 144–153. https://doi.org/10.1016/j.powtec.2020.10.061.

(69)   Li, T.; Liu, B.; Jiang, Y.; Lou, Y.; Chen, K.; Zhang, D. L-Polylactic Acid Porous Microspheres Enhance the Mechanical Properties and in Vivo Stability of Degummed Silk/Silk Fibroin/Gelatin Scaffold. *Biomed. Mater.* **2021**, *16* (1). https://doi.org/10.1088/1748-605X/abca11.

(70)   Hu, X.; He, J.; Yong, X.; Lu, J.; Xiao, J.; Liao, Y.; Li, Q.; Xiong, C.

Biodegradable Poly (Lactic Acid-Co-Trimethylene Carbonate)/Chitosan Microsphere Scaffold with Shape-Memory Effect for Bone Tissue Engineering. *Colloids Surfaces B Biointerfaces* **2020**, *195* (May), 111218. https://doi.org/10.1016/j.colsurfb.2020.111218.

(71) Zhang, J.; Wang, J.; Qiao, F.; Liu, Y.; Zhou, Y.; Li, M.; Ai, M.; Yang, Y.; Sui, L.; Zhou, Z. Polymeric Non-Spherical Coarse Microparticles Fabricated by Double Emulsion-Solvent Evaporation for Simvastatin Delivery. *Colloids Surfaces B Biointerfaces* **2021**, *199* (December 2020). https://doi.org/10.1016/j.colsurfb.2021.111560.

(72) Amer, M. H.; Rose, F. R. A. J.; Shakesheff, K. M.; Modo, M.; White, L. J. Translational Considerations in Injectable Cell-Based Therapeutics for Neurological Applications: Concepts, Progress and Challenges. *npj Regen. Med.* **2017**, *2* (1), 23. https://doi.org/10.1038/s41536-017-0028-x.

(73) Zheng, H.; Du, W.; Duan, Y.; Geng, K.; Deng, J.; Gao, C. Biodegradable Anisotropic Microparticles for Stepwise Cell Adhesion and Preparation of Janus Cell Microparticles. *ACS Appl. Mater. Interfaces* **2018**, *10* (43), 36776–36785. https://doi.org/10.1021/acsami.8b14884.

(74) Makadia, H. K.; Siegel, S. J. Poly Lactic-Co-Glycolic Acid (PLGA) as Biodegradable Controlled Drug Delivery Carrier. *Polymers (Basel).* **2011**, *3* (3), 1377–1397. https://doi.org/10.3390/polym3031377.

(75) Butreddy, A.; Gaddam, R. P.; Kommineni, N.; Dudhipala, N.; Voshavar, C. Plga/Pla-Based Long-Acting Injectable Depot Microspheres in Clinical

Use: Production and Characterization Overview for Protein/Peptide Delivery. *Int. J. Mol. Sci.* **2021**, *22* (16). https://doi.org/10.3390/ijms22168884.

(76)   Thissen, H.; Chang, K.-Y.; Tebb, T. A.; Tsai, W.-B.; Glattauer, V.; Ramshaw, J. A. M.; Werkmeister, J. A. Synthetic Biodegradable Microparticles for Articular Cartilage Tissue Engineering. *J. Biomed. Mater. Res. Part A* **2006**, *77A* (3), 590–598. https://doi.org/10.1002/jbm.a.30612.

(77)   Custõdio, C. A.; Santo, V. E.; Oliveira, M. B.; Gomes, M. E.; Reis, R. L.; Mano, J. F. Functionalized Microparticles Producing Scaffolds in Combination with Cells. *Adv. Funct. Mater.* **2014**, *24* (10), 1391–1400. https://doi.org/10.1002/adfm.201301516.

(78)   Neto, M. D.; Oliveira, M. B.; Mano, J. F. Microparticles in Contact with Cells: From Carriers to Multifunctional Tissue Modulators. *Trends Biotechnol.* **2019**, *37* (9), 1011–1028. https://doi.org/10.1016/j.tibtech.2019.02.008.

(79)   Maciel, M. M.; Correia, T. R.; Henriques, M.; Mano, J. F. Microparticles Orchestrating Cell Fate in Bottom-up Approaches. *Curr. Opin. Biotechnol.* **2022**, *73*, 276–281. https://doi.org/10.1016/j.copbio.2021.09.008.

(80)   Oliveira, M. B.; Mano, J. F. High-Throughput Screening for Integrative Biomaterials Design: Exploring Advances and New Trends. *Trends*

Biotechnol. **2014**, *32* (12), 627–636. https://doi.org/10.1016/j.tibtech.2014.09.009.

(81)   Santos-Vizcaino, E.; Salvador, A.; Vairo, C.; Igartua, M.; Hernandez, R. M.; Correa, L.; Villullas, S.; Gainza, G. Overcoming the Inflammatory Stage of Non-Healing Wounds: In Vitro Mechanism of Action of Negatively Charged Microspheres (NCMS). *Nanomaterials* **2020**, *10* (6), 1–14. https://doi.org/10.3390/nano10061108.

(82)   García Cruz, D. M.; Sardinha, V.; Escobar Ivirico, J. L.; Mano, J. F.; Gómez Ribelles, J. L. Gelatin Microparticles Aggregates as Three-Dimensional Scaffolding System in Cartilage Engineering. *J. Mater. Sci. Mater. Med.* **2013**, *24* (2), 503–513. https://doi.org/10.1007/s10856-012-4818-9.

(83)   Oliveira, M. B.; Mano, J. F. Polymer-Based Microparticles in Tissue Engineering and Regenerative Medicine. *Biotechnol. Prog.* **2011**, *27* (4), 897–912. https://doi.org/10.1002/btpr.618.

(84)   Smith, D.; Herman, C.; Razdan, S.; Abedin, M. R.; Stoecker, W. Van; Barua, S. Microparticles for Suspension Culture of Mammalian Cells. *ACS Appl. Bio Mater.* **2019**, *2* (7), 2791–2801. https://doi.org/10.1021/acsabm.9b00215.

(85)   Lee, J. H.; Lee, C. S.; Cho, K. Y. Enhanced Cell Adhesion to the Dimpled Surfaces of Golf-Ball-Shaped Microparticles. *ACS Appl. Mater. Interfaces* **2014**, *6* (19), 16493–16497.

https://doi.org/10.1021/am505997s.

(86) Zhang, D.; Zheng, H.; Geng, K.; Shen, J.; Feng, X.; Xu, P.; Duan, Y.; Li, Y.; Wu, R.; Gou, Z.; Gao, C. Large Fuzzy Biodegradable Polyester Microspheres with Dopamine Deposition Enhance Cell Adhesion and Bone Regeneration in Vivo. *Biomaterials* **2021**, *272* (August 2020), 1–11. https://doi.org/10.1016/j.biomaterials.2021.120783.

(87) Park, J. S.; Yang, H. N.; Jeon, S. Y.; Woo, D. G.; Na, K.; Park, K.-H. H. Osteogenic Differentiation of Human Mesenchymal Stem Cells Using RGD-Modified BMP-2 Coated Microspheres. *Biomaterials* **2010**, *31* (24), 6239–6248. https://doi.org/10.1016/j.biomaterials.2010.05.002.

(88) Holland, T. A.; Tabata, Y.; Mikos, A. G. In Vitro Release of Transforming Growth Factor-β1 from Gelatin Microparticles Encapsulated in Biodegradable, Injectable Oligo(Poly(Ethylene Glycol) Fumarate) Hydrogels. *J. Control. Release* **2003**, *91* (3), 299–313. https://doi.org/https://doi.org/10.1016/S0168-3659(03)00258-X.

(89) Hüsler, A.; Haas, S.; Parry, L.; Romero, M.; Nisisako, T.; Williams, P.; Wildman, R. D.; Alexander, M. R. Effect of Surfactant on: Pseudomonas Aeruginosa Colonization of Polymer Microparticles and Flat Films. *RSC Adv.* **2018**, *8* (28), 15352–15357. https://doi.org/10.1039/c8ra01491d.

(90) Dundas, A. A.; Cuzzucoli Crucitti, V.; Haas, S.; Dubern, J. F.; Latif, A.; Romero, M.; Sanni, O.; Ghaemmaghami, A. M.; Williams, P.; Alexander, M. R.; Wildman, R.; Irvine, D. J. Achieving Microparticles with Cell-

Instructive Surface Chemistry by Using Tunable Co-Polymer Surfactants. *Adv. Funct. Mater.* **2020**, *30* (36). https://doi.org/10.1002/adfm.202001821.

(91)   Hook, A. L.; Chang, C.-Y. Y.; Yang, J.; Atkinson, S.; Langer, R.; Anderson, D. G.; Davies, M. C.; Williams, P.; Alexander, M. R. Discovery of Novel Materials with Broad Resistance to Bacterial Attachment Using Combinatorial Polymer Microarrays. *Adv. Mater.* **2013**, *25* (18), 2542–2547. https://doi.org/10.1002/adma.201204936.

(92)   Hook, A. L.; Anderson, D. G.; Langer, R.; Williams, P.; Davies, M. C.; Alexander, M. R. High Throughput Methods Applied in Biomaterial Development and Discovery. *Biomaterials* **2010**, *31* (2), 187–198. https://doi.org/10.1016/J.BIOMATERIALS.2009.09.037.

(93)   Magennis, E. P.; Hook, A. L.; Davies, M. C.; Alexander, C.; Williams, P.; Alexander, M. R. Engineering Serendipity: High-Throughput Discovery of Materials That Resist Bacterial Attachment. *Acta Biomater.* **2016**, *34*, 84–92. https://doi.org/10.1016/j.actbio.2015.11.008.

(94)   Hook, A. L.; Chang, C.-Y. Y.; Yang, J.; Luckett, J.; Cockayne, A.; Atkinson, S.; Mei, Y.; Bayston, R.; Irvine, D. J.; Langer, R.; Anderson, D. G.; Williams, P.; Davies, M. C.; Alexander, M. R.; Roger, B.; Irvine, D. J.; Langer, R.; Anderson, D. G.; Williams, P.; Davies, M. C.; Alexander, M. R. Combinatorial Discovery of Polymers Resistant to Bacterial Attachment. *Nat. Biotechnol.* **2012**, *30* (9), 868.

https://doi.org/10.1038/nbt.2316.

(95) Carpenter, J.; Khang, D.; Webster, T. J.; Ya, G.; Xue, X.; Collier, P.; Clarke, P. Functions The in Fl Uence of Nanotexturing of Poly (Lactic-Co-Glycolic Acid) Fi Lms upon Human Ovarian Cancer Cell Attachment. **2016**.

(96) Kim, M. R.; Lee, S.; Park, J. K.; Cho, K. Y. Golf Ball-Shaped PLGA Microparticles with Internal Pores Fabricated by Simple O/W Emulsion. *Chem. Commun.* **2010**, *46* (39), 7433–7435. https://doi.org/10.1039/c0cc01738h.

(97) Wang, Y.; Shang, L.; Chen, G.; Shao, C.; Liu, Y.; Lu, P.; Rong, F.; Zhao, Y. Pollen-Inspired Microparticles with Strong Adhesion for Drug Delivery. *Appl. Mater. Today* **2018**, *13*, 303–309. https://doi.org/10.1016/j.apmt.2018.09.016.

(98) Hussain, M.; Xie, J.; Hou, Z.; Shezad, K.; Xu, J.; Wang, K.; Gao, Y.; Shen, L.; Zhu, J. Regulation of Drug Release by Tuning Surface Textures of Biodegradable Polymer Microparticles. *ACS Appl. Mater. Interfaces* **2017**, *9* (16), 14391–14400. https://doi.org/10.1021/acsami.7b02002.

(99) Sahoo, S. K.; Panda, A. K.; Labhasetwar, V. Characterization of Porous PLGA/PLA Microparticles as a Scaffold for Three Dimensional Growth of Breast Cancer Cells. *Biomacromolecules* **2005**, *6* (2), 1132–1139. https://doi.org/10.1021/bm0492632.

(100) Liu, S.; Cai, M.; Deng, R.; Wang, J.; Liang, R.; Zhu, J. Fabrication of

Porous Polymer Microparticles with Tunable Pore Size and Density through the Combination of Phase Separation and Emulsion-Solvent Evaporation Approach. *Korea Aust. Rheol. J.* **2014**, *26* (1), 63–71. https://doi.org/10.1007/s13367-014-0007-3.

(101) Kirby, G. T. S.; White, L. J.; Rahman, C. V; Cox, H. C.; Qutachi, O.; Rose, F. R. A. J.; Hutmacher, D. W.; Shakesheff, K. M.; Woodruff, M. A. PLGA-Based Microparticles for the Sustained Release of BMP-2. *Polymers (Basel).* **2011**, *3* (1), 571–586.

(102) Lu, L.; Yaszemski, M. J.; Mikos, A. G. TGF-β1 Release from Biodegradable Polymer Microparticles: Its Effects on Marrow Stromal Osteoblast Function. *J. Bone Jt. Surg. - Am. Vol.* **2001**, *83* (SUPPL. 1 II).

(103) Rosca, I. D.; Watari, F.; Uo, M. Microparticle Formation and Its Mechanism in Single and Double Emulsion Solvent Evaporation. *J. Control. Release* **2004**, *99* (2), 271–280. https://doi.org/10.1016/j.jconrel.2004.07.007.

(104) O'Donnell, P. B.; McGinity, J. W. Preparation of Microspheres by the Solvent Evaporation Technique. *Adv. Drug Deliv. Rev.* **1997**, *28*, 25–42.

(105) Lee, B. K.; Yun, Y.; Park, K. PLA Micro- and Nano-Particles. *Advanced Drug Delivery Reviews*. 2016. https://doi.org/10.1016/j.addr.2016.05.020.

(106) Li, M.; Rouaud, O.; Poncelet, D. Microencapsulation by Solvent Evaporation: State of the Art for Process Engineering Approaches. *Int. J. Pharm.* **2008**, *363* (1–2), 26–39.

https://doi.org/10.1016/j.ijpharm.2008.07.018.

(107) Tice, T. R.; Gilley, R. M. Preparation of Injectable Controlled-Release Microcapsules by a Solvent-Evaporation Process. *J. Control. Release* **1985**, *2* (C), 343–352. https://doi.org/10.1016/0168-3659(85)90056-2.

(108) Kirby, G. T. S.; White, L. J.; Rahman, C. V.; Cox, H. C.; Rose, F. R. A. J.; Hutmacher, D. W.; Shakesheff, K. M.; Woodruff, M. A. PLGA-Based Microparticles for the Sustained Release of BMP-2. *Eur. Cells Mater.* **2011**, *22* (SUPPL.3), 24. https://doi.org/10.3390/polym3010571.

(109) Lee, S. C.; Oh, J. T.; Jang, M. H.; Chung, S. Il. Quantitative Analysis of Polyvinyl Alcohol on the Surface of Poly(D,L-Lactide-Co-Glycolide) Microparticles Prepared by Solvent Evaporation Method: Effect of Particle Size and PVA Concentration. *J. Control. Release* **1999**, *59* (2), 123–132. https://doi.org/10.1016/S0168-3659(98)00185-0.

(110) Meng, F. T.; Ma, G. H.; Qiu, W.; Su, Z. G. W/O/W Double Emulsion Technique Using Ethyl Acetate as Organic Solvent: Effects of Its Diffusion Rate on the Characteristics of Microparticles. *J. Control. Release* **2003**, *91* (3), 407–416. https://doi.org/10.1016/S0168-3659(03)00273-6.

(111) Bahl, Y.; Sah, H. Dynamic Changes in Size Distribution of Emulsion Droplets during Ethyl Acetate-Based Microencapsulation Process. *AAPS PharmSciTech* **2000**, *1* (1). https://doi.org/10.1007/bf02830520.

(112) Sah, H. Microencapsulation Techniques Using Ethyl Acetate as a

Dispersed Solvent: Effects of Its Extraction Rate on the Characteristics of PLGA Microspheres. *J. Control. Release* **1997**, *47* (3), 233–245. https://doi.org/10.1016/S0168-3659(97)01647-7.

(113) Chung, T. W.; Huang, Y. Y.; Liu, Y. Z. Effects of the Rate of Solvent Evaporation on the Characteristics of Drug Loaded PLLA and PDLLA Microspheres. *Int. J. Pharm.* **2001**, *212* (2), 161–169. https://doi.org/10.1016/S0378-5173(00)00574-3.

(114) Xu, Q.; Hashimoto, M.; Dang, T. T.; Hoare, T.; Kohane, D. S.; Whitesides, G. M.; Langer, R.; Anderson, D. G.; David, H. Preparation of Monodisperse Biodegradable Polymer Microparticles Using a Microfluidic Flow-Focusing Device for Controlled Drug Delivery. *Small* **2009**, *5* (13), 1575–1581. https://doi.org/10.1002/smll.200801855.

(115) Baret, J. C. Surfactants in Droplet-Based Microfluidics. *Lab Chip* **2012**, *12* (3), 422–433. https://doi.org/10.1039/c1lc20582j.

(116) Dendukuri, D.; Doyle, P. S. The Synthesis and Assembly of Polymeric Microparticles Using Microfluidics. *Adv. Mater.* **2009**, *21* (41), 4071–4086. https://doi.org/10.1002/adma.200803386.

(117) Nunes, J. K.; Tsai, S. S. H.; Wan, J.; Stone, H. A. Dripping and Jetting in Microfluidic Multiphase Flows Applied to Particle and Fibre Synthesis. *J. Phys. D. Appl. Phys.* **2013**, *46* (11). https://doi.org/10.1088/0022-3727/46/11/114002.

(118) Cubaud, T.; Mason, T. G. Capillary Threads and Viscous Droplets in

Square Microchannels. *Phys. Fluids* **2008**, *20* (5). https://doi.org/10.1063/1.2911716.

(119) Kim, J. H.; Jeon, T. Y.; Choi, T. M.; Shim, T. S.; Kim, S. H.; Yang, S. M. Droplet Microfluidics for Producing Functional Microparticles. *Langmuir* **2013**, *30* (6), 1473–1488. https://doi.org/10.1021/la403220p.

(120) Sahin, S.; Bliznyuk, O.; Rovalino Cordova, A.; Schroën, K. Microfluidic EDGE Emulsification: The Importance of Interface Interactions on Droplet Formation and Pressure Stability. *Sci. Rep.* **2016**, *6*. https://doi.org/10.1038/srep26407.

(121) Ekanem, E. E.; Nabavi, S. A.; Vladisavljević, G. T.; Gu, S. Structured Biodegradable Polymeric Microparticles for Drug Delivery Produced Using Flow Focusing Glass Microfluidic Devices. *ACS Appl. Mater. Interfaces* **2015**, *7* (41), 23132–23143. https://doi.org/10.1021/acsami.5b06943.

(122) Yobas, L.; Martens, S.; Ong, W. L.; Ranganathan, N. High-Performance Flow-Focusing Geometry for Spontaneous Generation of Monodispersed Droplets. *Lab Chip* **2006**, *6* (8), 1073–1079. https://doi.org/10.1039/b602240e.

(123) Atencia, J.; Beebe, D. J. Controlled Microfluidic Interfaces. *Nature* **2005**, *437* (7059), 648–655. https://doi.org/10.1038/nature04163.

(124) Anna, S. L. Droplets and Bubbles in Microfluidic Devices. *Annu. Rev. Fluid Mech.* **2016**, *48* (1). https://doi.org/10.1146/annurev-fluid-122414-

034425.

(125) Ong, W. L.; Hua, J.; Zhang, B.; Teo, T. Y.; Zhuo, J.; Nguyen, N. T.; Ranganathan, N.; Yobas, L. Experimental and Computational Analysis of Droplet Formation in a High-Performance Flow-Focusing Geometry. *Sensors Actuators, A Phys.* **2007**, *138* (1), 203–212. https://doi.org/10.1016/j.sna.2007.04.053.

(126) Bruijn De et al. (12) United States Patent. US 8609737B2, 2013. https://doi.org/10.1016/j.(73).

(127) Liu, S.; Qin, S.; He, M.; Zhou, D.; Qin, Q.; Wang, H. Current Applications of Poly(Lactic Acid) Composites in Tissue Engineering and Drug Delivery. *Compos. Part B Eng.* **2020**, *199* (July). https://doi.org/10.1016/j.compositesb.2020.108238.

(128) Annunziata, M.; Nastri, L.; Cecoro, G.; Guida, L. The Use of Poly-D, L-Lactic Acid (PDLLA) Devices for Bone Augmentation Techniques: A Systematic Review. *Molecules* **2017**, *22* (12). https://doi.org/10.3390/molecules22122214.

(129) Algahtani, M. S.; Scurr, D. J.; Hook, A. L.; Anderson, D. G.; Langer, R. S.; Burley, J. C.; Alexander, M. R.; Davies, M. C. High Throughput Screening for Biomaterials Discovery. *J. Control. Release* **2014**, *190*, 115–126. https://doi.org/10.1016/j.jconrel.2014.06.045.

(130) Patel, A. K.; Tibbitt, M. W.; Celiz, A. D.; Davies, M. C.; Langer, R.; Denning, C.; Alexander, M. R.; Anderson, D. G. High Throughput

Screening for Discovery of Materials That Control Stem Cell Fate. *Curr. Opin. Solid State Mater. Sci.* **2016**, *20* (4), 202–211. https://doi.org/10.1016/j.cossms.2016.02.002.

(131) Vallieres, C.; Hook, A. L.; He, Y.; Crucitti, V. C.; Figueredo, G.; Davies, C. R.; Burroughs, L.; Winkler, D. A.; Winkler, D. A.; Winkler, D. A.; Winkler, D. A.; Wildman, R. D.; Irvine, D. J.; Alexander, M. R.; Avery, S. V. Discovery of (Meth)Acrylate Polymers That Resist Colonization by Fungi Associated with Pathogenesis and Biodeterioration. *Sci. Adv.* **2020**, *6* (23), 1–13. https://doi.org/10.1126/sciadv.aba6574.

(132) Mei, Y.; Saha, K.; Bogatyrev, S. R.; Yang, J.; Hook, A. L.; Kalcioglu, Z. I.; Cho, S. W.; Mitalipova, M.; Pyzocha, N.; Rojas, F.; Van Vliet, K. J.; Davies, M. C.; Alexander, M. R.; Langer, R.; Jaenisch, R.; Anderson, D. G. Combinatorial Development of Biomaterials for Clonal Growth of Human Pluripotent Stem Cells. *Nat. Mater.* **2010**, *9* (9), 768–778. https://doi.org/10.1038/nmat2812.

(133) Celiz, A. D.; Harrington, H. C.; Hook, A. L. High Throughput Assessment and Chemometric Analysis of the Interaction of Epithelial and Fibroblast Cells with a Polymer Library. *Appl. Surf. Sci.* **2014**, *313*, 926–935. https://doi.org/10.1016/j.apsusc.2014.06.111.

(134) Nasir, A.; Thorpe, J.; Burroughs, L.; Meurs, J.; Pijuan-Galito, S.; Irvine, D. J.; Alexander, M. R.; Denning, C. Discovery of a Novel Polymer for Xeno-Free, Long-Term Culture of Human Pluripotent Stem Cell

Expansion. *Adv. Healthc. Mater.* **2021**, *10* (6), 1–7. https://doi.org/10.1002/adhm.202001448.

(135) Latif, A. Developing Stromal Instructive Niches to Promote Wound Healing. **2021**, No. March.

(136) Wollman, A. J. M.; Nudd, R.; Hedlund, E. G.; Leake, M. C. From Animaculum to Single Molecules: 300 Years of the Light Microscope. *Open Biology*. Royal Society of London April 29, 2015. https://doi.org/10.1098/rsob.150019.

(137) Wang, G.; Fang, N. *Detecting and Tracking Nonfluorescent Nanoparticle Probes in Live Cells*, 1st ed.; Elsevier Inc., 2012; Vol. 504. https://doi.org/10.1016/B978-0-12-391857-4.00004-5.

(138) Davidson, M. W.; Mortimer, A. Optical Microscopy. *Encycl. Imaging Sci. Technol.* **2002**, *2* (1106–1141), 120. https://doi.org/10.1016/B0-12-369401-9/00579-9.

(139) Abdullah, A.; Mohammed, A. Scanning Electron Microscopy (SEM): A Review Scanning Electron Microscopy (SEM): A Review. *Int. Conf. Hydraul. Pneum.* **2019**, No. January, 1–9.

(140) Vernon-Parry, K. D. Scanning Electron Microscopy : An Introduction. *Analysis* **2000**, *13* (4), 40–44.

(141) Zhou, W.; Apkarian, R.; Wang, Z. L.; Joy, D. Fundamentals of Scanning Electron Microscopy (SEM). *Scanning Microsc. Nanotechnol. Tech. Appl.* **2007**, 1–40. https://doi.org/10.1007/978-0-387-39620-0_1.

(142) Groeber, M. A.; Haley, B. K.; Uchic, M. D.; Dimiduk, D. M.; Ghosh, S. 3D Reconstruction and Characterization of Polycrystalline Microstructures Using a FIB-SEM System. *Mater. Charact.* **2006**, *57* (4–5), 259–273. https://doi.org/10.1016/j.matchar.2006.01.019.

(143) KIZILYAPRAK, C.; DARASPE, J.; HUMBEL, B. M. Focused Ion Beam Scanning Electron Microscopy in Biology. *J. Microsc.* **2014**, *254* (3), 109–114. https://doi.org/10.1111/jmi.12127.

(144) Young, R. J.; Moore, M. V. Dual-Beam (FIB-SEM) Systems Techniques and Automated Applications. In *Introduction to Focused Ion Beams: Instrumentation, Theory, Techniques and Practice*; Springer US, 2005; pp 247–268. https://doi.org/10.1007/0-387-23313-X_12.

(145) Fearn, S. Introduction. *An Introd. to Time-of-Flight Second. Ion Mass Spectrom. its Appl. to Mater. Sci.* **2015**. https://doi.org/10.1088/978-1-6817-4088-1ch1.

(146) Dundas, A. A.; Kern, S.; Cuzzucoli Crucitti, V.; Scurr, D. J.; Wildman, R.; Irvine, D. J.; Alexander, M. R. A New Particle Mounting Method for Surface Analysis. *Surf. Interface Anal.* **2022**, *54* (4), 374–380. https://doi.org/10.1002/sia.7010.

(147) Chernov, N.; Lesort, C. Least Squares Fitting of Circles. *J. Math. Imaging Vis.* **2005**, *23* (3), 239–252. https://doi.org/10.1007/s10851-005-0482-8.

(148) Al-Sharadqah, A.; Chernov, N. Error Analysis for Circle Fitting Algorithms. *Electron. J. Stat.* **2009**, *3*, 886–911.

https://doi.org/10.1214/09-EJS419.

(149) Pratt, V. Direct Least-Squares Fitting of Algebraic Surfaces. *Comput. Graph. (ACM).* **1987**, *21* (4), 145–152.

(150) Chernov, N. Circle Fite (Taubin Method).

(151) Chernov, N. Circle Fit (Pratt method).

(152) Chernov, N. Circle Fit (Kasa method) https://www.mathworks.com/matlabcentral/fileexchange/22642-circle-fit-kasa-method.

(153) H.M., B.; Jun, M. J.; Bender, E.; Maurer, G. Interfacial Tensions in Binary and Ternary Liquid-Liquid Systems. *Chem. Eng. Sci.* **1990**, *45* (1), 275–286. https://doi.org/10.1016/0009-2509(90)87099-E.

(154) Apostoluk, W.; Drzymała, J. An Improved Estimation of Water-Organic Liquid Interfacial Tension Based on Linear Solvation Energy Relationship Approach. *J. Colloid Interface Sci.* **2003**, *262* (2), 483–488. https://doi.org/10.1016/S0021-9797(03)00115-2.

(155) Shahid, M. Z.; Usman, M. R.; Akram, M. S.; Khawaja, S. Y.; Afzal, W. Initial Interfacial Tension for Various Organic-Water Systems and Study of the Effect of Solute Concentration and Temperature. *J. Chem. Eng. Data* **2017**, *62* (4), 1198–1203. https://doi.org/10.1021/acs.jced.6b00703.

(156) Farah, S.; Anderson, D. G.; Langer, R. Physical and Mechanical Properties of PLA, and Their Functions in Widespread Applications — A

Comprehensive Review. *Adv. Drug Deliv. Rev.* **2016**, *107*, 367–392. https://doi.org/10.1016/j.addr.2016.06.012.

(157) Yu, B.; Meng, L.; Fu, S.; Zhao, Z.; Liu, Y.; Wang, K.; Fu, Q. Morphology and Internal Structure Control over PLA Microspheres by Compounding PLLA and PDLA and Effects on Drug Release Behavior. *Colloids Surfaces B Biointerfaces* **2018**, *172* (July), 105–112. https://doi.org/10.1016/j.colsurfb.2018.08.037.

(158) Spetz, M. R.; Isely, C.; Gower, R. M. Effect of Fabrication Parameters on Morphology and Drug Loading of Polymer Particles for Rosiglitazone Delivery. *J. Drug Deliv. Sci. Technol.* **2021**, *65* (June). https://doi.org/10.1016/j.jddst.2021.102672.

(159) Hayduk, W.; Laudie, H. Prediction of Diffusion Coefficients for Nonelectrolytes in Dilute Aqueous Solutions. *AIChE J.* **1974**, *20* (3), 611–615. https://doi.org/10.1002/aic.690200329.

(160) Rickard, D. L.; Mcintosh, T. Rickard PhD 2011 Multiphase, Multicomponent Systems.

(161) Rostam, H. M.; Fisher, L. E.; Hook, A. L.; Burroughs, L.; Luckett, J. C.; Figueredo, G. P.; Mbadugha, C.; Teo, A. C. K.; Latif, A.; Kämmerling, L.; Day, M.; Lawler, K.; Barrett, D.; Elsheikh, S.; Ilyas, M.; Winkler, D. A.; Alexander, M. R.; Ghaemmaghami, A. M. Immune-Instructive Polymers Control Macrophage Phenotype and Modulate the Foreign Body Response In Vivo. *Matter* **2020**, *2* (6), 1564–1581.

https://doi.org/10.1016/j.matt.2020.03.018.

(162) Magennis, E. P.; Hook, A. L.; Williams, P.; Alexander, M. R. Making Silicone Rubber Highly Resistant to Bacterial Attachment Using Thiol-Ene Grafting. *ACS Appl. Mater. Interfaces* **2016**, *8* (45), 30780–30787. https://doi.org/10.1021/acsami.6b10986.

(163) Nisisako, T.; Torii, T.; Higuchi, T. Novel Microreactors for Functional Polymer Beads. *Chem. Eng. J.* **2004**, *101* (1–3), 23–29. https://doi.org/10.1016/j.cej.2003.11.019.

(164) Zhou, Z.; Ruiz Cantu, L.; Chen, X.; Alexander, M. R.; Roberts, C. J.; Hague, R.; Tuck, C.; Irvine, D.; Wildman, R. High-Throughput Characterization of Fluid Properties to Predict Droplet Ejection for Three-Dimensional Inkjet Printing Formulations. *Addit. Manuf.* **2019**, *29* (January), 100792. https://doi.org/10.1016/j.addma.2019.100792.

(165) Krishne Gowda, V.; Brouzet, C.; Lefranc, T.; Söderberg, L. D.; Lundell, F. Effective Interfacial Tension in Flow-Focusing of Colloidal Dispersions: 3-D Numerical Simulations and Experiments. *J. Fluid Mech.* **2019**, *876*, 1052–1076. https://doi.org/10.1017/jfm.2019.566.

(166) Funfschilling, D.; Debas, H.; Li, H. Z.; Mason, T. G. Flow-Field Dynamics during Droplet Formation by Dripping in Hydrodynamic-Focusing Microfluidics. *Phys. Rev. E - Stat. Nonlinear, Soft Matter Phys.* **2009**, *80* (1), 2–5. https://doi.org/10.1103/PhysRevE.80.015301.

(167) Abate, A. R.; Poitzsch, A.; Hwang, Y.; Lee, J.; Czerwinska, J.; Weitz, D.

A. Impact of Inlet Channel Geometry on Microfluidic Drop Formation. *Phys. Rev. E - Stat. Nonlinear, Soft Matter Phys.* **2009**, *80* (2), 1–5. https://doi.org/10.1103/PhysRevE.80.026310.

(168) Sigma Aldrich. HMDA SDS https://www.sigmaaldrich.com/GB/en/sds/aldrich/246816 (accessed Jun 26, 2022).

(169) Nosenko, M. A.; Moysenovich, A. M.; Zvartsev, R. V.; Arkhipova, A. Y.; Zhdanova, A. S.; Agapov, I. I.; Vasilieva, T. V.; Bogush, V. G.; Debabov, V. G.; Nedospasov, S. A.; Moisenovich, M. M.; Drutskaya, M. S. Novel Biodegradable Polymeric Microparticles Facilitate Scarless Wound Healing by Promoting Re-Epithelialization and Inhibiting Fibrosis. *Front. Immunol.* **2018**, *9* (December), 1–11. https://doi.org/10.3389/fimmu.2018.02851.

(170) Kendall, R. T.; Feghali-Bostwick, C. A. Fibroblasts in Fibrosis: Novel Roles and Mediators. *Front. Pharmacol.* **2014**, *5 MAY* (May), 1–13. https://doi.org/10.3389/fphar.2014.00123.

(171) Hannan, R. T.; Peirce, S. M.; Barker, T. H. Fibroblasts: Diverse Cells Critical to Biomaterials Integration. *ACS Biomater. Sci. Eng.* **2018**, *4* (4), 1223–1232. https://doi.org/10.1021/acsbiomaterials.7b00244.

(172) Darby, I. A.; Laverdet, B.; Bonté, F.; Desmoulière, A. Fibroblasts and Myofibroblasts in Wound Healing. *Clin. Cosmet. Investig. Dermatol.* **2014**, *7*, 301–311. https://doi.org/10.2147/CCID.S50046.

(173) Latif, A.; Fisher, L. E.; Dundas, A. A.; Cuzzucoli Crucitti, V.; Imir, Z.; Lawler, K.; Pappalardo, F.; Muir, B. W.; Wildman, R.; Irvine, D. J.; Alexander, M. R.; Ghaemmaghami, A. M. Microparticles Decorated with Cell-Instructive Surface Chemistries Actively Promote Wound Healing. *Adv. Mater.* **2022**, *2208364*. https://doi.org/10.1002/adma.202208364.

(174) Herrmann, J.; Bodmeier, R. Somatostatin Containing Biodegradable Microspheres Prepared by a Modified Solvent Evaporation Method Based on W/O/W-Multiple Emulsions. *Int. J. Pharm.* **1995**, *126* (1–2), 129–138. https://doi.org/10.1016/0378-5173(95)04106-0.

(175) Spetz, M. R.; Isely, C.; Gower, R. M. Effect of Fabrication Parameters on Morphology and Drug Loading of Polymer Particles for Rosiglitazone Delivery. *J. Drug Deliv. Sci. Technol.* **2021**, *65* (July). https://doi.org/10.1016/j.jddst.2021.102672.

(176) Jeyanthi, R.; Thanoo, B. C.; Metha, R. C.; DeLuca, P. P. Effect of Solvent Removal Technique on the Matrix Characteristics of Polylactide/Glycolide Microspheres for Peptide Delivery. *J. Control. Release* **1996**, *38* (2–3), 235–244. https://doi.org/10.1016/0168-3659(95)00125-5.

(177) Crotts, G.; Park, T. G. Preparation of Porous and Nonporous Biodegradable Polymeric Hollow Microspheres. *J. Control. Release* **1995**, *35* (2–3), 91–105. https://doi.org/10.1016/0168-3659(95)00010-6.

(178) Zhang, T.; Li, M.; Wang, X.; Zhou, Z.; Yuan, W.; Ma, J. Facile Synthesis

of Polylactide Coarse Microspheres as Artificial Antigen-Presenting Cells. *Chem. Commun.* **2018**, *54* (80), 11356–11359. https://doi.org/10.1039/C8CC04958K.

(179) Doolittle, A. K. *The Technology of Solvents and Plasticizers*; Wiley: New York, 1954.

(180) Freytag, T.; Dashevsky, A.; Tillman, L.; Hardee, G. E.; Bodmeier, R. Improvement of the Encapsulation Efficiency of Oligonucleotide-Containing Biodegradable Microspheres. *J. Control. Release* **2000**, *69* (1), 197–207. https://doi.org/10.1016/S0168-3659(00)00299-6.

(181) Yap, S. F.; Adams, M. J.; Seville, J. P. K.; Zhang, Z. Single and Bulk Compression of Pharmaceutical Excipients: Evaluation of Mechanical Properties. *Powder Technol.* **2008**, *185* (1), 1–10. https://doi.org/10.1016/j.powtec.2007.09.005.

(182) Sun, G.; Zhang, Z. Mechanical Strength of Microcapsules Made of Different Wall Materials. *Int. J. Pharm.* **2002**, *242* (1–2), 307–311. https://doi.org/10.1016/S0378-5173(02)00193-X.

Appendix 1: Interfacial Tension Analysis

Appendix 1A: ImageJ script for interface images, pre-processing:

```
1  // IFT image analysis processing
2  // Utilising edge detection
3  // 09/10/2018
4  setBatchMode(true);
5
6  path= getDirectory("Choose a directory of Material");
7  pathSave= getDirectory("Choose a directory to save to");
8  list= getFileList(path); // file selection and directory to save, taken from original macro
9
10 for(i=0;i<list.length;i++){
11 open(path+list[i]);  // repeat for all images in the folder
12
13 FileName=getTitle();
14 makeRectangle(246, 17, 264, 462);
15 run("Crop"); // crop first using area from setup and to crop off text
16 run("Median...", "radius=2");
17 run("Find Edges");
18 run("Invert"); // black on white so have thin edge (if not get thicker line or skeletonise selects wrong)
19 run("Auto Threshold", "method=Default white");
20 setOption("BlackBackground", false);
21 run("Skeletonize"); // applies threshold and thins
22 run("Invert");// return to white on black for analysis
23
24  SaveName = replace(FileName,".TIFF","_processed.TIFF");
25
26      saveAs("tiff", pathSave+SaveName);
27      close();
28
29 }
30
31 waitForUser("Completed");
```

Appendix 1B: Crop fractions applied to an example image.

1.6% HPhOPA mPEGMA HMDA
Set 1, Image G

Crop fractions, centred on the
image mid point from 0.1 to 1.
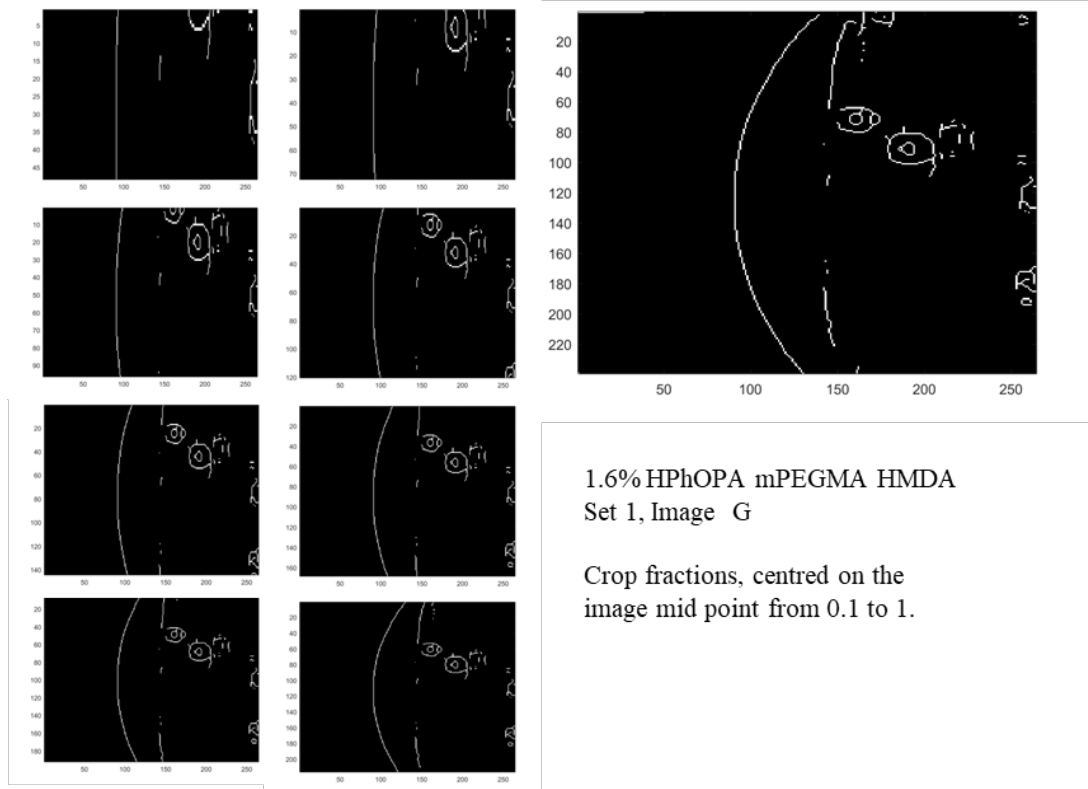
Appendix 1C: Interfacial analysis script – MATLAB

```matlab
% Interfacial tension measurements from images from the
micropipette
% station.

% Input: Processed Images of boundary. Using on screen
positioning images
% are precut the to region of interest.
% Output: Graph with tension value. Values of radius.
clear all
%% Read in data

% Read in images
 folder_path = uigetdir;
%
% Get list of file names in chosen folder
Files = dir(fullfile(folder_path,'*.tif'));
File_names = {Files.name};

%Set up array to hold data.
radiiFinal = zeros(length(File_names),1);

% Read in pressures
```

```matlab
[fileNameEx, pathNameEx] = uigetfile('*.xlsx');

for filecount = 1:length(File_names)
origImage =
imread(fullfile(folder_path,char(File_names(filecount))));


%% Identify area

% Precropped to area of interest. Based on positioning when
taking images.

imageSize = size(origImage);
wallEdge = 1; % set up initialls so if there are no walls
found, can still be identified later. Stop errors.
n=1;
ind=1; % edge position index count
 for n=1:(imageSize(1)-1)
     if origImage(n,4) ~= origImage(n+1,4)
     wallEdge(ind) = n;
     ind = ind+1;
     end
 end
% Find boundaries above and below centre.
% Use last boundary index in first half. Use first boundary of
second half.
% If the are no walls: take the centre as the centre, use the
whole image.

firstBound = 1; % set as limits first, so if not found it will
be these. Will over write with real values
secondBound = imageSize(1);
m=1;
l=1; p=1;
noBounds = size(wallEdge);
for m = 1:noBounds(2)
    if wallEdge(m)< imageSize(1)/2
        firstBound(l) = wallEdge(m);
        l=l+1;
    elseif wallEdge(m) > imageSize(1)/2
        secondBound(p) = wallEdge(m);
        p=p+1;
%     else
%         firstBound = 1;
%         secondBound = imageSize(1); Moved as if it doesnt
meet one of the
%         above conditions it will remain empty.
    end
end


% From here, cut down some more to avoid edges near the wall.
%% Repeated croppping
firstBoundInner = max(firstBound);
secondBoundInner = min(secondBound); % coordinates of full area
set by walls

% Use various crop sizes to find most reliable
differenceGap = (secondBoundInner-firstBoundInner);
```

```matlab
centre = firstBoundInner +(differenceGap/2);
crop = 1;
for x = 0.2:0.1:1

space = x*(differenceGap/2);
upperCrop = floor(centre-space); lowerCrop =
floor(centre+space);

cutImage = origImage(upperCrop:lowerCrop, 1:imageSize(2));

%% Save boundary coordinates
finalBoundary = cutImage; % imcomplement(cutImage);

noPixels = size(finalBoundary);
edgeCoor = zeros(noPixels(1),2);
c=1; % column number
r=1; %row number
    for r=1:noPixels(1) % row number
       for c = 1:(noPixels(2)-10)
        if finalBoundary(r,c) ~= 0 %&& cutImage(r,(c+5)) ~= 0
            edgeCoor(r,1) = r;
            edgeCoor(r,2) = c;
                break
        end
       end
    end


%% Fit circle to the coordinates

XY = [edgeCoor(:,2) edgeCoor(:,1)];

% try and catch so if there is noise or too flat etc and the
fit wont work.
% it will export a NaN to the array.
%Call pratt fit
try
    par = prattfit(XY);
catch
    par = NaN;
end

radiusCi = par(3); % radius for this crop.
radius(crop) = radiusCi;
crop = crop+1;
end


% remove extreme outlyers.
avgRadFul = median(radius);
spread = std(radius);

ri=1; % radius index in array
radLast = size(radius);
%Rvalue = radius(radLast(2));
radiiSensible = 0;
q = 1;
for ri=1:(radLast(2))
```

```matlab
        if abs(radius(ri)-avgRadFul) <= spread
            %save radii that arent outside range
            radiiSensible(q) = radius(ri);
            q=q+1;
        end

    end



% compare to taking the median value
radiusMed = median(radius);
Rvalue = mean(radiiSensible);



radiiFinal(filecount) = Rvalue;

medRadii(filecount) = radiusMed;

% try clearing variables relating to cropping to stop incorrect
boundaries.
%
clear wallEdge noBounds firstBound secondBound firstBoundInner
secondBoundInner
clear differenceGap centre space upperCrop lowerCrop origImage
radiiSensible radiiLimited
end

%% Analysis
%Convert from pixels to microns!!!!
%Averaging 2.87 pixels per micron from scale.
pixUm = 2.88;%%%%%%%%%%%%%%%%%%
radiiUm = radiiFinal/pixUm;

% Read pressures
pressData = xlsread(fileNameEx);
%asign variables
pressCmH20 = pressData(:,1);
%Convert Pressure to Nm-2
press = 98.0665.*pressCmH20;
%Pressure error % pressure error more realistic is 0.05cm not
0.01
n = length(pressCmH20);
pressErr = 98.0665.*0.1.*(ones(n,1));

%Inverse of Rc in m
rCm = radiiUm./1e6;
invRc = 1./rCm;

% applying the fit
datFit = NonLinearModel.fit(invRc, press, 'y ~ b0*x + b1',
[0.08 -1000]);
% extract coefficients and errors from table
fitInfoTab = datFit.Coefficients;
%convert table to array
fitInfo = table2array(fitInfoTab);
% extract individual coeffs.
```

```matlab
grad = fitInfo(1,1);
gradSE = fitInfo(1,2);
int = fitInfo(2,1);
intSE = fitInfo(2,2);
%grad = 0.02253; int = 219.4;

% creat fit line for plotting
lobf = (grad.*invRc)+int;
%extract and calculate for IFT
intfTens = (grad/2)*1000;
errintfTens = (gradSE/2)*1000;
%% Plot

figure
errorbar(invRc, press, pressErr, 'kx');
hold on
plot(invRc, lobf, 'k-');


%Label with file
title(['Interfacial Tension of '  char(fileNameEx)]);
ylabel('Pressure, Nm^{-2}');
xlabel('1/Rc, Inverse Radius of Curvature, m^{-1}');

finalValue = ['Surface Tension = ', num2str(intfTens), ' \pm ',
num2str(errintfTens), 'mNm^{-1}'];
%text position relativ to data.
highPress = max(press); highInvRc = max(invRc);
text((min(invRc)),(max(press)), finalValue, 'FontSize', 10,
'Color', 'k');
legend('Data', 'Fitted Data', 'Location', 'SouthEast');
```

Appendix 1D: Fitting function - Pratt Circle Fit[151]


```matlab
function par = prattfit(XY)
%Pratt Function to fit a cricle
%

%     Circle fit by Pratt
%       V. Pratt, "Direct least-squares fitting of algebraic
surfaces",
%        Computer Graphics, Vol. 21, pages 145-152 (1987)
%
%     Input:  XY(n,2) is the array of coordinates of n points
x(i)=XY(i,1), y(i)=XY(i,2)
%
%     Output: Par = [a b R] is the fitting circle:
%                         center (a,b) and radius R


n = size(XY,1);      % number of data points

centroid = mean(XY);   % the centroid of the data set

%     computing moments (note: all moments will be normed, i.e.
divided by n)
```

```
Mxx=0; Myy=0; Mxy=0; Mxz=0; Myz=0; Mzz=0;

for i=1:n
    Xi = XY(i,1) - centroid(1);  %  centering data
    Yi = XY(i,2) - centroid(2);  %  centering data
    Zi = Xi*Xi + Yi*Yi;
    Mxy = Mxy + Xi*Yi;
    Mxx = Mxx + Xi*Xi;
    Myy = Myy + Yi*Yi;
    Mxz = Mxz + Xi*Zi;
    Myz = Myz + Yi*Zi;
    Mzz = Mzz + Zi*Zi;
end

Mxx = Mxx/n;
Myy = Myy/n;
Mxy = Mxy/n;
Mxz = Mxz/n;
Myz = Myz/n;
Mzz = Mzz/n;

%    computing the coefficients of the characteristic
polynomial

Mz = Mxx + Myy;
Cov_xy = Mxx*Myy - Mxy*Mxy;
Mxz2 = Mxz*Mxz;
Myz2 = Myz*Myz;

A2 = 4*Cov_xy - 3*Mz*Mz - Mzz;
A1 = Mzz*Mz + 4*Cov_xy*Mz - Mxz2 - Myz2 - Mz*Mz*Mz;
A0 = Mxz2*Myy + Myz2*Mxx - Mzz*Cov_xy - 2*Mxz*Myz*Mxy +
Mz*Mz*Cov_xy;
A22 = A2 + A2;

epsilon=1e-12;
ynew=1e+20;
IterMax=20;
xnew = 0;

%    Newton's method starting at x=0

for iter=1:IterMax
    yold = ynew;
    ynew = A0 + xnew*(A1 + xnew*(A2 + 4.*xnew*xnew));
    if (abs(ynew)>abs(yold))
        disp('Newton-Pratt goes wrong direction: |ynew| >
|yold|');
        xnew = 0;
        break;
    end
    Dy = A1 + xnew*(A22 + 16*xnew*xnew);
    xold = xnew;
    xnew = xold - ynew/Dy;
    if (abs((xnew-xold)/xnew) < epsilon), break, end
    if (iter >= IterMax)
```

```
        disp('Newton-Pratt will not converge');
        xnew = 0;
    end
    if (xnew<0.)
        fprintf(1,'Newton-Pratt negative root:  x=%f\n',xnew);
        xnew = 0;
    end
end

%    computing the circle parameters

DET = xnew*xnew - xnew*Mz + Cov_xy;
Center = [Mxz*(Myy-xnew)-Myz*Mxy , Myz*(Mxx-xnew)-
Mxz*Mxy]/DET/2;

par = [Center+centroid , sqrt(Center*Center'+Mz+2*xnew)];

end    %    CircleFitByPratt
```

Appendix 2: Dissolution and Diffusion Analysis

Appendix 2A Drop Dissolution Analysis

```
% Dissolution video analysis

% Take video of bubbled/droplets on the end of the pipette
and track change
% in radius over time.
clear all
%% Read in video/image

% [inputfile,inputpath]=uigetfile('*.avi');
% fullVideo = VideoReader(fullfile(inputpath,inputfile));

% % ask for frame rate and number of frames as different
between videos.
% %Taken from substrack creation in imageJ.
```

```matlab
imFile = uigetfile('*.tif');
testImage = imread(imFile);

noFrames = str2double(inputdlg('Enter Number of Frames '
));%%%%change based on stack
frameRate = str2double(inputdlg('Enter Frame Rate '));%fps
%one frame at a time
% index to cycle through frames
radii=zeros(1, noFrames);
%Entre radius range from first and last substack frames,
measured in pixels
% from imageJ
radiusRange = str2double(inputdlg({'Min R  ', 'Max R  '},
'Radius Range'));
% choose sensitivity
houghSens = 0.97;%str2double(inputdlg({'Choose level of
sensitivity '}));


for k=1:noFrames %8th frame is fully formed. Account for
this in plot.

% Extract frames.
% videoFrame = readFrame(fullVideo);
% grayVideoFrame = rgb2gray(videoFrame);
% Read in test image
imagesc(grayVideoFrame);


%% Pre/processing
% change type
%dubFrame = double(videoFrame);
% Apply median Filter.
%medFilIm = medfilt2(rgb2gray(testImage));
medFilIm = medfilt2(grayVideoFrame);
figure
imagesc(medFilIm);
%Threshold Image
binIm = imbinarize(medFilIm);
figure
imagesc(binIm)

% Fill centre
negIm = imcomplement(binIm);
fillBin = imfill(negIm, 'holes');
figure
imshow(fillBin)

% Hough

[centres, radius] = imfindcircles(fillBin,[radiusRange(1)
radiusRange(2)], 'ObjectPolarity', 'bright',
'Sensitivity', houghSens);
```

```
Draw on circles
viscircles(centres, radius,'EdgeColor','b');

%save radius for that frame
%add a try and catch to make more robust. If out of foucus
or no visible
%drop then the timing will be preserved.
noRadius = isempty(radius);
if noRadius == 1;
    radius = NaN;
else
radii(k) = radius(1);
end

end
%% Time dependence
radiium = radii./2.88;
time = (0:1/frameRate:(noFrames-1)/frameRate);

plot(time, radiium, 'kx');
title('Dissolution of X in Water');
xlabel('Time, seconds');
ylabel('Droplet Radius, \mu m');
%
% Must cut to beginning of dissolution. Do so in
conversion video
```

Appendix 2B Fitting Dissolution and Calculation of EP model

```
%% Linearise and fit the data.
% Using a separate script so that the NaN frames can be
removed from the
% fit manually (quicker and allows checks)
% Data can all be saved into the same sheet for use in
prism etc. for final
% graphs.
close all
%% Read in data


[fileNameEx, pathNameEx] = uigetfile('*.xlsx');
dissolutionDataIn =  xlsread(fileNameEx);

timeCrop = dissolutionDataIn(2:51,4); % 1 and 2 for full,
4 and 5 for crop
```

```matlab
radiiCrop = dissolutionDataIn(2:51,5);
time = dissolutionDataIn(:,1);
%% Plot dissolution curve305

plot(timeCrop, radiiCrop, 'kx');
title('Dissolution of xxx');
xlabel('Time, seconds');
ylabel('Droplet Radius, \mu m');

%% Linearisation

r0 = radiiCrop(1);
linR = (r0.^2)-(radiiCrop.^2);

figure
plot(timeCrop, linR, 'ko');
title('Linearised dissolution of xxx');
xlabel('Time, seconds');
ylabel('Ro^2 - R^2');

dissFit = NonLinearModel.fit(timeCrop, linR, 'y ~ b0*x +
b1', [5 0]);
dissFitTab = dissFit.Coefficients;
dissFitArr = table2array(dissFitTab);

grad = dissFitArr(1,1)
gradSE = dissFitArr(1,2)
int = dissFitArr(2,1); intSE = dissFitArr(2,2);
%grad = 61.94; int = -0.2344;

rho = 1323;%mg/ml
cs = 17.22;%mg/ml
f = 0;

D = ((grad.*rho)./(2.*cs))./(1e8)
errD = ((rho/(2*cs))*gradSE)/1e8
%convert um^2/s to cm^2/s is 1e-8

% plot
lobf = (grad.*timeCrop)+int;
hold on
plot(timeCrop, lobf, 'k-');


%% Predicitve model

% time = dissolutionDataIn(:,1); % 1 and 2 for full, 4 and
5 for crop
% radii = dissolutionDataIn(:,2);

% need SI units
% Dm = D*1e8;
```

```
% Extend time to zero point Assume zero will be reached by
1.5*initial
% length

% r0 = radii(2);
% rho = 1323;%mg/ml
% cs = 17.22;%mg/ml
% f = 0;

% rPred2 = (r0^2)-(2*Dm*cs*time/rho);
% for unknown Cs and D directly input gradient


% pad out Radii with NaN to be able to plot
timePad = zeros((floor(length(timeCrop)*1.5)),1);
timePad(1 :(length(timeCrop))) = timeCrop;
timePad((length(timeCrop)+1):end) = NaN;

radPad = zeros((floor(length(timeCrop)*1.5)),1);
radPad(1: (length(timeCrop))) = radiiCrop;
radPad((length(timeCrop)+1):end) = NaN;

% timePred = 0-length timepad
timePred =  timeCrop(1) + (0:(length(timePad)-
1))*1;%%%%%%%%%%%%
rPred2 = (r0^2)-(grad*time);
rPred = sqrt(rPred2);

figure
plot(time, rPred, 'r--')
hold on
plot(timePad, radPad, 'kx');
```

Appendix 2C: Calculation of Activity based EP and Corresponding Profile.

```
%% Read in data
clear all

% [fileNameEx, pathNameEx] = uigetfile('*.xlsx');
% dissolutionDataIn =  xlsread(fileNameEx);

dissolutionDataIn =  xlsread('10% PLA EA Vid 5.xlsx');

timeCrop = dissolutionDataIn(:,1);
radiiCrop = dissolutionDataIn(:,2);


%% Known parameters
```

```matlab
% Constants
RPip = 8.5e-6; % pipette radius - take from imageJ
rho =902;%1323;%mg/ml Denisty
Cs = 83;% 17.22;%mg/ml Saturation concentration
D = 0.894e-9; % diffusion coccicitent.
dt = 1; % time interval - 1 second
f=0;
concStock = 10; % use for calculating the concentration
after formation
concStart = 10; % hard code in as set value - assuming
conc remains constant during formation.

% Varible/data sourced
radiiCropm = radiiCrop.*1e-6;
[r0, r0Place] = max(radiiCropm); % starting radius after
formation, the largest.
tOff = timeCrop(r0Place); % t offset, time taken for drop
to be formed. Start of official dissolution.




%% complete radius prediction time step of 0.01 seconds

%concStart=1.4357; %hard value until better calculation
from lost volumes

stepSize = 0.01; % 100 per second
timePred = tOff: stepSize: max(timeCrop);

% set up arrays
conc = zeros(1,length(timePred)); conc(1) = concStart;
fI = zeros(1,length(timePred)); % set arrays needed for
loop to the size of the prediction.
rPred = zeros(1,length(timePred));
rPred(1) = r0;


for n = 2:length(timePred)-1

% instantaneous concentration
conc(n) = concStart*(r0.^3)./(rPred(n-1).^3); % true
radius for calcula5ting conc

%fI(n) =  3.312e-5.*(conc(n).^2) -  0.01833.*(conc(n))
+1.441; % 2nd order
%fI/conc fit

%fI(n)= -0.0134.*(conc(n)) +1.296; % linear fI/conc fit
%EA

fI(n)= -0.01144.*(conc(n)) +1.237;
```

```
rPred(n) = rPred(n-1)-
stepSize*((r0+sqrt((r0^2)+(RPip^2)))/(2*r0))*(D*Cs*(fI(n)-
f)/rho)*((1/rPred(n-
1))+(1/sqrt(pi*D*(tOff+timePred(n))))));

end
%% Plot measured data and predictive fitting

 plot(timeCrop, radiiCropm, 'xk');
 hold on
 plot(timePred(1:length(timePred)-1),
rPred(1:length(timePred)-1), '-r')
 xlabel('time,s')
 ylabel('radius, m')
```

Appendix 2D: Simplex Fitting of EP parameters

```
clear all


dissolutionDataIn =  xlsread('1% PLA in EA Video 1
data.xlsx');

time = dissolutionDataIn(:,1);
radii = dissolutionDataIn(:,2);
pars = zeros;
fit = zeros;


% Input values for this file

rPip     = 8.5e-6;   % pipette radius - take from imageJ
rho      = 902;  % mg/ml Denisty
Cs       = 83; % mg/ml Saturation concentration
D        = 1.23;%1.236; % cm2/s diffusion coefficitent.
f        = 0.0;   % Stauration of continuous phase with
solvent
concStock = 1;   % mg/mL Concentration of polymer in
solvent

% Set these to 1 to fit or 0 to fix

fit(1) = 0;
fit(2) = 0;
fit(3) = 0;
fit(4) = 0;
fit(5) = 0;
fit(6) = 1;
```

```
TINY = 1E-20;
ftol = 1E-15;

NMAX = 10000;

pars(1) = rPip;
pars(2) = rho;
pars(3) = Cs;
pars(4) = D;
pars(5) = f;
pars(6) = concStock;

ndim = 0;
p = zeros(7);

for i = 1:6
  if (fit(i) == 1)
    ndim = ndim + 1;
    p(1, ndim) = pars(i);
  end
end

for i = 2:ndim+1
  for j = 1:ndim
    p(i, j) = p(1, j);
  end
end

for i = 1:ndim
  p(i+1, i) = p(i+1, i) / 2.0;
  if (p(i+1, i) == 0.0)
    p(i+1, i) = 1.0;
  end
end

y = zeros;
psum = zeros;

for i = 1:ndim+1
  for j = 1:ndim
    psum(j) = p(i, j);
  end
  y(i) = funk(time, radii, fit, pars, psum);
end

yy = zeros;
in = 1;

for i = 1:6
  if (fit(i) == 0)
    yy(i) = pars(i);
  else
    yy(i) = p(1, in);
```

```matlab
    in = in + 1;
  end
  if (yy(i) == 0.0)
    yy(i) = 1.0E-15;
  end
end

fileID = fopen('start.txt', 'w');
fprintf(fileID, '%6s %12s\n', 'time', 'radii');
for i = 1:length(time)
  fprintf(fileID, '%6.2f %12.6f\n', time(i), radii(i));
end
fclose(fileID);

mpts = ndim + 1;

nfunk = 0;
for j = 1:ndim
  sum = 0.0;
  for i = 1:mpts
    sum = sum + p(i, j);
  end
  psum(j) = sum;
end

while true
  ilo = 1;
  if (y(1) > y(2))
    ihi = 1;
    inhi = 2;
  else
    ihi = 2;
    inhi = 1;
  end

  for i = 1:mpts
    if (y(i) <= y(ilo))
      ilo = i;
    end
    if (y(i) > y(ihi))
      inhi = ihi;
      ihi = i;
    elseif (y(i) > y(inhi)) && (i ~= ihi)
      inhi = i;
    end
  end

  rtol = 2.0 * abs(y(ihi) - y(ilo)) / (abs(y(ihi)) +
abs(y(ilo)) + TINY);

  if (rtol < ftol)
    temp = y(1);
    y(i) = y(ilo);
```

```
      y(ilo) = temp;
      for i = 1:ndim
        temp = p(1, i);
        p(1, i) = p(ilo, i);
        p(ilo, i) = p(1, i);
      end
      break
    end

    if (nfunk >= NMAX)
      break
    end

    nfunk = nfunk + 2;

    [ytry, p, y, psum] = amotry(time, radii, fit, pars, p,
y, psum, ihi, -1.0);

    if (ytry <= y(ilo))
      [ytry p, y, psum] = amotry(time, radii, fit, pars, p,
y, psum, ihi, 2.0);
    elseif (ytry >= y(inhi))
      ysave = y(ihi);
      [ytry, p, y, psum] = amotry(time, radii, fit, pars, p,
y, psum, ihi, 0.5);
      if (ytry >= ysave)
        for i = 1:mpts
          if (i ~= ilo)
            for j = 1:ndim
              p(i, j) = 0.5 * (p(i, j) + p(ilo, j));
              psum(j) = p(i, j);
            end
            y(i) = funk(time, radii, fit, pars, psum);
          end
        end
        nfunk = nfunk + ndim;

        for j = 1:ndim
          sum = 0.0;
          for i = 1:mpts
            sum = sum + p(i, j);
          end
          psum(j) = sum;
        end
      end
    else
      nfunk = nfunk - 1;
    end
end

yy = zeros;
in = 1;
```

```matlab
for i = 1:6
  if (fit(i) == 0)
    yy(i) = pars(i);
  else
    yy(i) = p(1, in);
    in = in + 1;
  end
  if (yy(i) == 0.0)
    yy(i) = 1.0E-15;
  end
end

[rmsRs, timepred, rpred] = dissFitAssess(time, radii,
abs(yy(1)) * 1.0E-6, abs(yy(2)), abs(yy(3)), abs(yy(4)) *
1.0E-9, abs(yy(5)), abs(yy(6)));

fileID = fopen('prediction.txt', 'w');
fprintf(fileID, '%6s %12s\n', 'time', 'radii');
for i = 1:length(timepred)-1
  fprintf(fileID, '%6.2f %12.6f\n', timepred(i), rpred(i)
* 1.0E6);
end
fclose(fileID);

fprintf('%6s %11.0f\n', 'Iter', nfunk);
fprintf('%6s %11.ff\n\n', 'RMS', rmsRs);
fprintf('%6s %11.5f %6s\n', 'rPip', yy(1), 'um');
fprintf('%6s %11.5f %6s\n', 'rho', yy(2), 'mg/mL');
fprintf('%6s %11.5f %6s\n', 'Cs', yy(3), 'mg/mL');
fprintf('%6s %11.5f %6s\n', 'D', yy(4), 'cm2/s');
fprintf('%6s %11.5f\n', 'f', yy(5));
fprintf('%6s %11.5f %6s\n', 'Conc', yy(6), 'mg/mL');
```

Appendix 3: Supplementary Figures

Appendix 3A: Interfacial tension of HMDA/DCM for different DCM volume fractions